ABSTRACT

Title: COMPARISON BETWEEN PARTICLE IMAGE VELOCIMETRY DATA AND COMPUTATIONAL FLUID DYNAMICS SIMULATIONS FOR AN IN-LINE SLOT AND TOOTH ROTOR-STATOR MIXER

Author: Jung W. Kim
Master of Science, 2015

Directed by: Professor Richard V. Calabrese
Department of Chemical and Biomolecular Engineering

Rotor-stator mixers have a broad spectrum of applications in chemical, petrochemical and pharmaceutical processes since they produce the high shear fields for emulsification and dispersion processes. To assess device performance and quantify mixing and dispersion capabilities, analyzing the velocity field data due to the rotor-stator interactions is crucial. Experimental 2-D velocity data have previously been acquired using Particle Image Velocity (PIV) for an in-line IKA prototype mixer which contains single rows of 12 rotor teeth and 14 stator teeth. The working fluid was water in turbulent flow. In this thesis, the development and validation of a Computational Fluid Dynamics (CFD) model is reported along with the comparison between the CFD and PIV data.

The CFD model geometry and mesh were developed within ANSYS Workbench with a fully transient sliding mesh 3-D RANS simulations performed with Fluent using the realizable k-ϵ turbulence model. To begin, the effect of mesh density and wall treatment were systematically tested to optimize the CFD simulation settings. With respect to post processing, the numerical data were sampled in a stator slot at 9 rotor tooth positions on a grid that closely mimicked that for PIV data acquisition. The

comparisons were made for three different rotor speeds (10, 20, and 26 revolutions per second) but at the same volumetric throughput (1.3 liters per second).

The study of near-wall modelling options considered Non-Equilibrium Wall Functions (NEWF) and Enhanced Wall Treatment (EWT). Both produced similar results but EWT showed advantage in computational efficiency. In the mesh independence study, 3 mesh levels were created with approximately 2, 6, and 16 million cells. The study revealed that the mesh level with 6 million cells was sufficient to insure grid independence at reasonable accuracy.

The CFD and PIV data compared favorably in many aspects. On average, CFD predicted the location of mixing layer and rotor tip vortices within 6.0% of the stator slot width compared to the PIV data. CFD also successfully identified 23 out of 27 (85.1%) mixing layer and rotor tip vortices captured by PIV. Differences were observed as well. The CFD simulations consistently yielded higher velocity magnitude (~20% on average), especially near the slot exit, where the stator slot adjoins the volute region. Despite the differences, the results show that CFD simulations can be used to gain knowledge of flow structure and device performance. The potential reasons for model and data mismatch are discussed and methods to improve the comparison are suggested for future studies.

COMPARISON BETWEEN PARTICLE IMAGE VELOCIMETRY DATA AND COMPUTATIONAL FLUID DYNAMICS SIMULATIONS FOR AN IN-LINE SLOT AND TOOTH ROTOR-STATOR MIXER

By

Jung W. Kim

Thesis submitted to the Faculty of the Graduate School of the
University of Maryland, College Park in partial fulfillment
of the requirements for the degree of
Master of Science

2015

Advisory Committee:

Professor Richard V. Calabrese, Chair

Professor Kenneth T. Kiger

Professor Srinivasa R. Raghavan

Contents

A. List of Table

B. List of Figures

1. Introduction

With their ability to create high shear fields, rotor-stator mixers have a wide spectrum of applications in chemical and engineering processes. To better understand the system and quantify its mixing ability, analyzing the flow field created by the mixer is crucial. In this study, the flow fields collected from the results of earlier experimental measurements using particle image velocimetry (PIV) are compared with computational fluid dynamics (CFD) simulations for an IKA prototype slot and tooth rotor-stator mixer.

The IKA prototype mixer is an in-line slot and tooth rotor-stator design. Rotor-stator mixers are known for their high shear fields, compact design, and well-controlled mixing environment (BanaszekC, 2009). The advantages originates from the close tolerance of the shear gap and the geometry of the rotor and stator. The design of rotor-stator mixers are currently based on the intuition and experience of the mixing industry. However, further research into the flow fields through their complex geometries is required for rotor-stator mixers to reach their full potential. Identifying the flow patterns and shear and dissipation fields can be a significant benefit in revealing their characteristics and efficiencies as mixers (RodgersThomas, 2011).

1.1 Experiment and simulation data

Experimental measurements such as PIV have a longer history and better established reliability than CFD simulation do, but they are often difficult to acquire in complex geometries. Although CFD shares its rapid growth with developing computer technology and contains undeniable potential, CFD involves numerical approximations to the Navier-Stokes equations that may result in non-physical or inaccurate flow solutions (FordMD, 2008). Therefore, the comparison between CFD and PIV can be valuable. Experimental flow field data have

previously been acquired for the prototype rotor-stator mixer using PIV. In this study, the accuracy of CFD is assessed by comparing its result to the PIV data for the mixer.

1.2 Recent CFD studies of Rotor-Stator Mixers

There have been various CFD studies of rotor-stator mixers that compared the CFD and experimental data. Generally, CFD data compared well with the experimental data in terms of flow patterns. A study with RANS equations, k-ε turbulence model, fully transient sliding mesh, and enhanced wall functions in ANSYS Fluent successfully predicted major flow patterns captured by Laser Doppler Anemometry (LDA) (PacekA, BakerM, UtomoA, 2007). Studies also reported that the results of comparisons in identical settings can vary depending on the speed of the rotor and the geometry of the mixer (UtomoAdi, BakerMichael, PacekAndrzej, 2008). It was often observed that CFD produces lower jet maximum velocity emerging from stator slots when compared to the experimental data collected by LDA. The lower maximum velocity in CFD was demonstrated in both laminar (BaraillerFabien, MouradHeniche, PhilippeTanguy, 2006) and turbulent (PacekA, BakerM, UtomoA, 2007) regimes.

There was a CFD study conducted for the same IKA prototype mixer as this study (KoDerrick, 2013). In the study, ANSYS Fluent was used to gather 3-D simulation data with RANS equation, k-ε turbulence model, and non-equilibrium wall function. The focus of the study was to develop a reliable CFD model of the mixer. It focused on investigating mesh refinement, especially in the shear gap, necessary to acquire accurate flow characteristics. It was conducted in high and low operating conditions. The high scenario used rotor speed of 30 rps and flow rate of 2.54 L/s, while the low scenario used 5 rps and 0.315 L/s. The author recommended validating its established model by comparing its data to the PIV data as a future project.

1.3 Geometry of the Mixer

Figure 1 presents a picture of the IKA prototype mixer. The flow, fed by a pump, enters through the axially-directed inlet pipe. The fluid then goes through twelve rotor slots and fourteen stator slots while the rotor spins at high velocity. The complex rotor-stator interactions and close tolerances create an intense shear field which dissipates throughout the fluid causing mixing, dispersion, and/or emulsification. The fluid then flows around the volute region and exits through the outlet pipe.

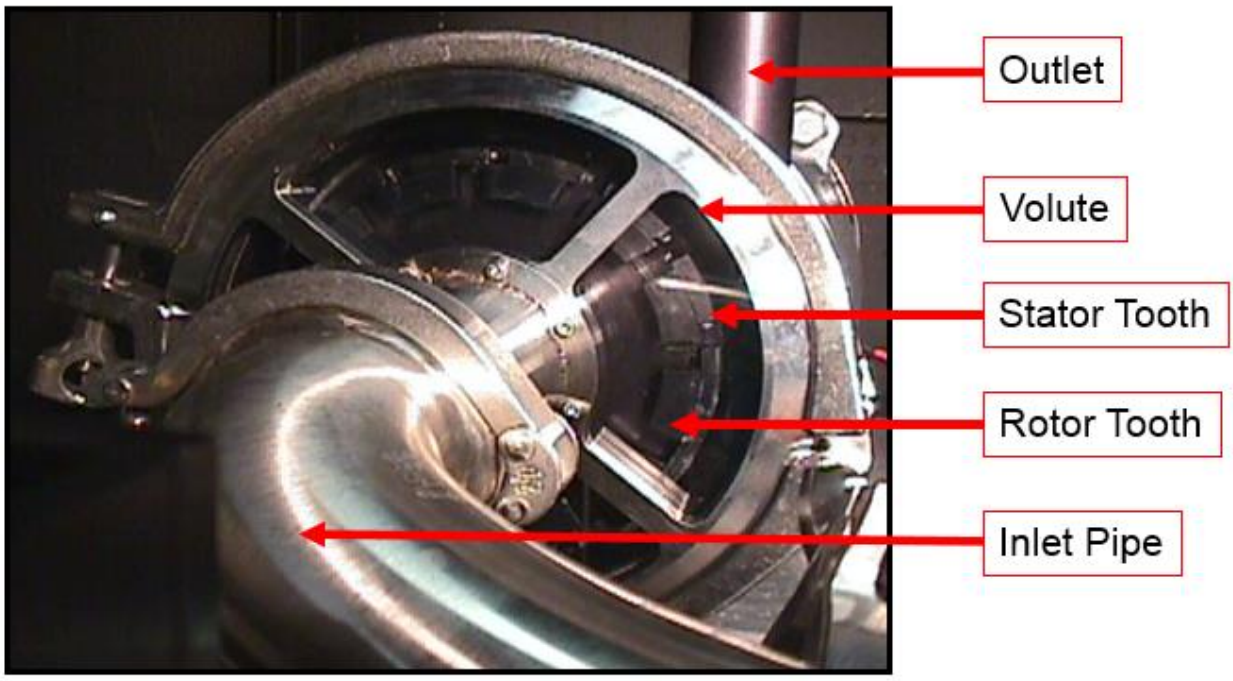

Figure 1. Geometry of an IKA prototype mixer

Figure 2 shows detailed dimensions for the mixer. The inlet pipe is 60mm in diameter while the rotor and stator are 70.5 and 77mm in outer diameter, respectively. The slots on both the rotor and stator are 10mm wide. The rotor and stator have 12 and 14 slots respectively. There is a 5 mm shear gap between the rotor and the stator.

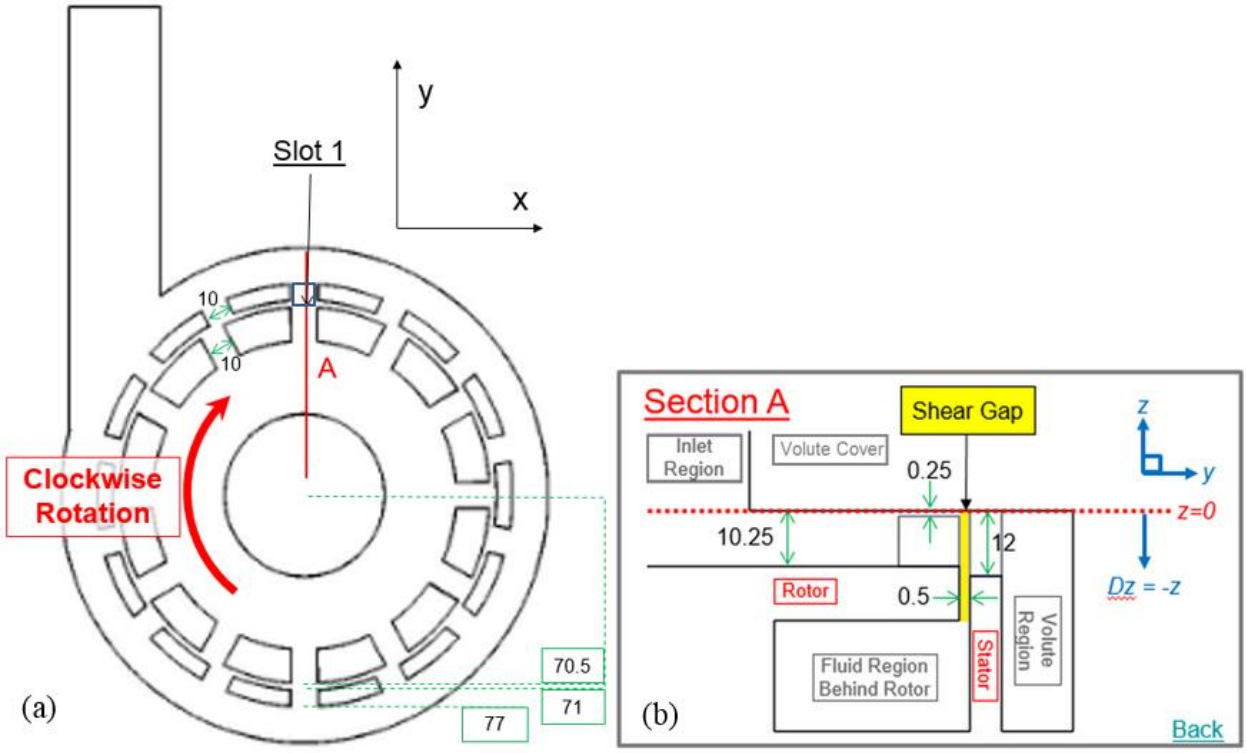

Figure 2. Dimensions of an IKA Prototype Mixer

As the main purpose of this study is to compare the results of the CFD simulations to those of the PIV measurements, the observations of the CFD simulations focused on the region where the PIV data were acquired. The location is the stator slot which is located at the greatest value of y and parallel to the outlet pipe. It is referred to as 'Slot 1' in Figure 2(a) and for the rest of this thesis. Note that the Cartesian coordinate system is used; the horizontal and vertical directions of Figure 2(a) are represented by x and y axes, respectively. The rotor and stator are centered on the z-axis. The depth into the mixer from the volute cover is represented by the negative direction of the z axis, with the location of the volute cover at z = 0.

1.4 Operating Conditions of CFD and PIV

The operating conditions of CFD simulation were also set to match the ones of PIV. The PIV measurements in the IKA prototype mixer that were performed by Karl Kevala

(unpublished) were made at three different rotor rotation speeds (N): 10, 20, and 26 revolutions per second (rps). The volumetric flow rate (Q_v) was fixed at 1.3 liter per second (L/s), enforced by an external pump; the mixer does not impart any radial momentum to the flow, making it a poor design to function as a pump on its own.

Table 1. Operating scenarios adopted in PIV study

N, Rotor Angular Speed (rps)	V_{tip}, Rotor Tip Speed (m/s)	N_{sh}, Shearing Number
10	4.4	5.69
20	8.9	11.5
26	11.5	14.9

*Shearing Number (N_{sh}) = V_{tip}/V_{slot}

1.5 Overview of PIV

PIV is a popular visualization and optical data acquisition technique for various types of fluid movements. Minute and easily visible particles called tracers are dispersed into the targeted flow field, visualizing it without significantly affecting the flow. Figure 3 is an illustration of the PIV technique.

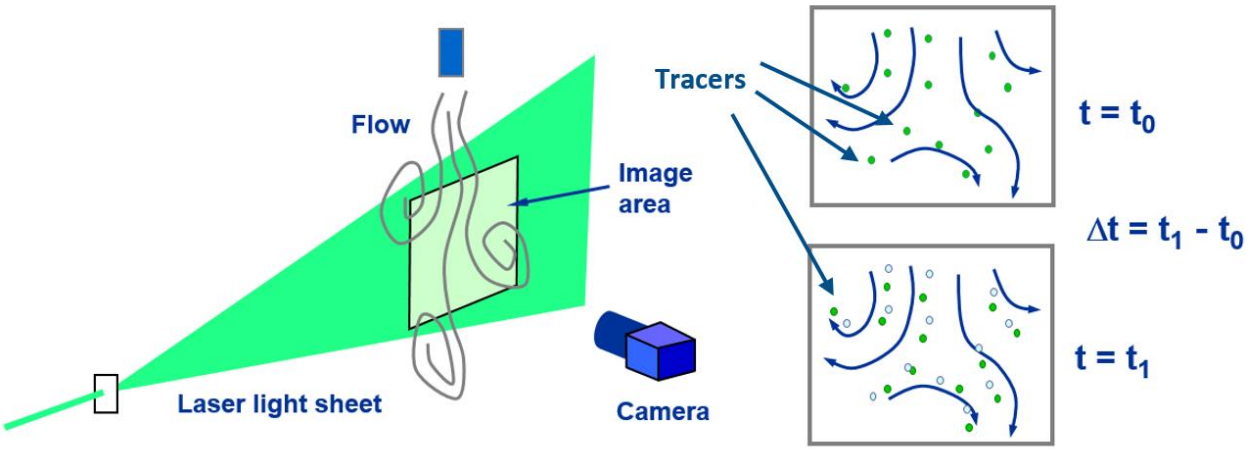

Figure 3. Overview of PIV

An optical arrangement with a camera and laser light source illuminating a plane captures two images shortly after each other (at t_0 and t_1), revealing the movement of tracer particles. By dividing the displacement of the particles between the subsequent images by Δt, the velocity at each point in the flow field can be calculated. As indicated in previous sections, all PIV measurements were taken in Slot 1, using an acrylic volute cover for optical access (see Figure 4). A Sumtak optical encoder coupled with LaVision pulse timing unit was used to measure the rotational rate of the rotor. A Kodak ES 1.0 CCD camera with 1018 x 1008 pixels was used to capture images, while a Surelite PIV-I Nd-YAG pulse laser was used to illuminate the target area.

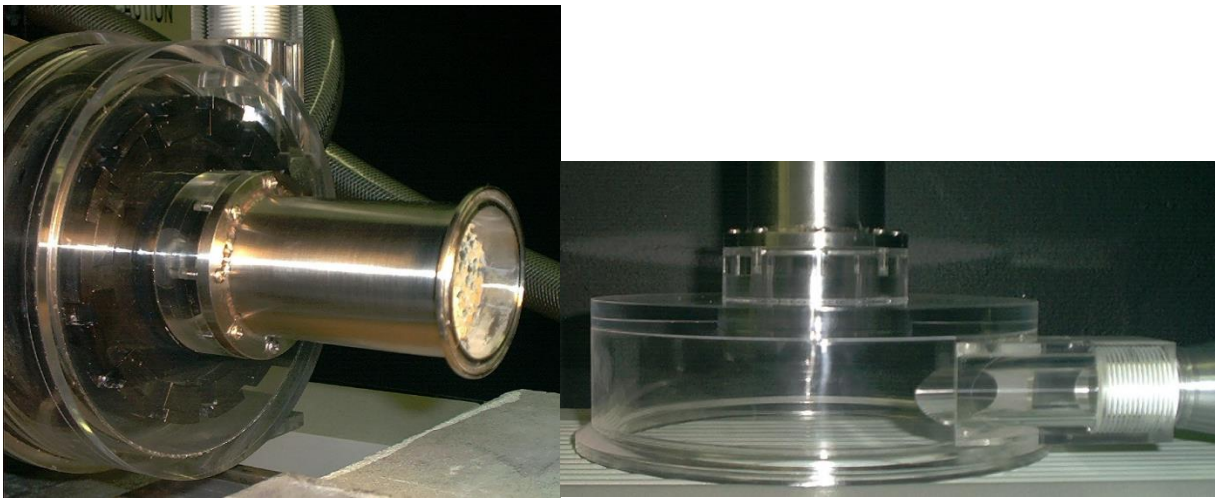

Figure 4. Transparent volute cover for PIV measurement with IKA prototype mixer

1.6 Layout of Thesis

Before the final CFD simulations were run, two preliminary studies were conducted to configure the mesh density and near-wall modeling settings (Chapter 3). The purpose of these studies was to accomplish resource-efficient simulation without sacrificing refinement in the results. Mesh density is a significant factor to achieve such a goal; while a fine mesh increases a simulation's capacity of achieving highly accurate results, so does its cell count which hinders overall computational time. In this preliminary study, three simulations were run, each with difference only in the mesh density in the shear gap and stator slot. The results were compared to determine at which mesh level a mesh-independent solution was reached.

The wall function can also affect simulation efficiency in a significant manner, especially for a turbulent model with a confined geometry (Charles, Abid, & Anderson, 1992). Two simulations were run with identical conditions except for the choice of wall function: Enhanced Wall Treatment (EWT) and Non-Equilibrium Wall Function (NEWF). Time and accuracy costs were analyzed to decide which wall function to use for the main simulations.

After the preliminary studies were conducted, the simulations were run for the comparison between CFD and PIV (Chapter 4). For qualitative comparison, side-by-side velocity plots were created; CFD and PIV velocity plots of identical conditions were created on Slot 1 at the plane of z= -0.005m (Figure 2) and placed next to each other. The goal of the comparison was to locate flow features that were found in both the PIV measurements and the CFD simulation. The features of interest are the mixing layer, mixing layer vortex, recirculation region, rotor tip vortex, and stator slot radial jet. Figure 5, 6, and 7 display sample mean velocity vector plots of a stator slot and a rotor slot with the aforementioned features (See Figure 2 for the stator and rotor slot locations). In Figure 5, momentum is being transferred from the rotating rotor tooth to the rotor and stator slots. In the process, high velocity difference and shear are created, especially in the layer between the rotor and stator slots. The outcome is a mixing layer that is shown in the light blue circle.

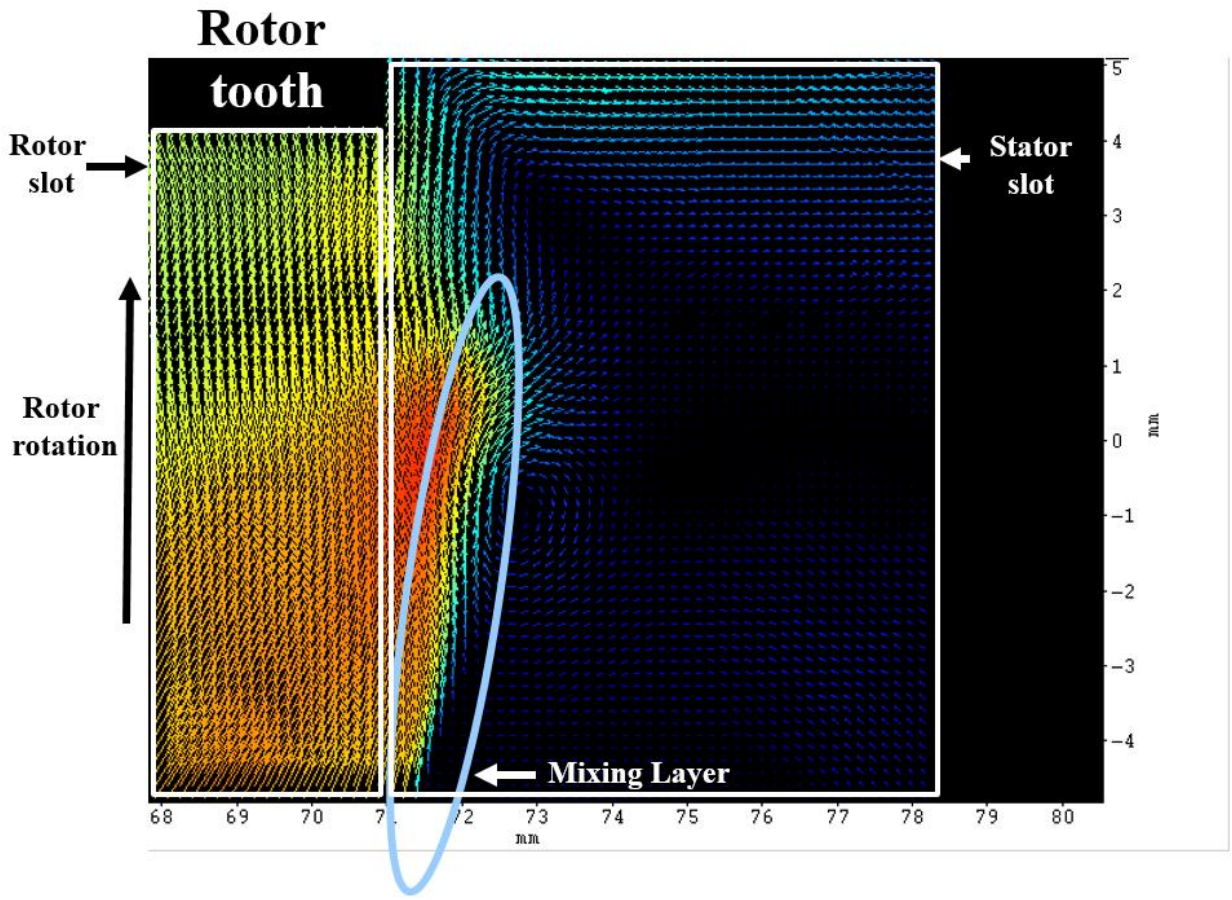

Figure 5. Sample PIV measurements, with a mixing layer circled in light blue.

A high speed movement of the rotor can create rotation within a mixing layer. Such feature is called mixing layer vortex, which is shown in Figure 6.

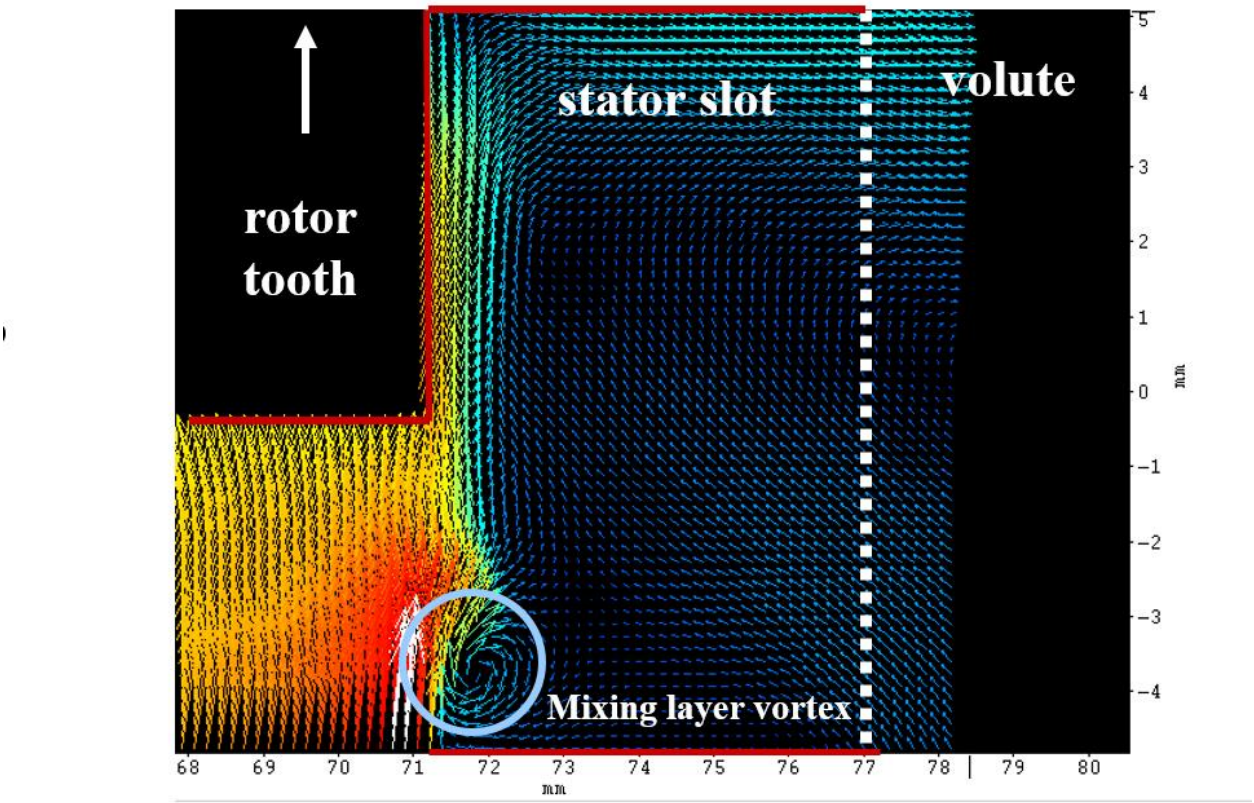

Figure 6. Sample PIV measurements with a mixing layer vortex circled in light blue

A rotor tooth vortex is another type of vortex that is sometimes observed next to a rotor tooth, as shown in Figure 7. An easy way to distinguish a mixing layer vortex from a rotor tip vortex is to see whether the vortex is located next to a rotor tooth or a rotor slot.

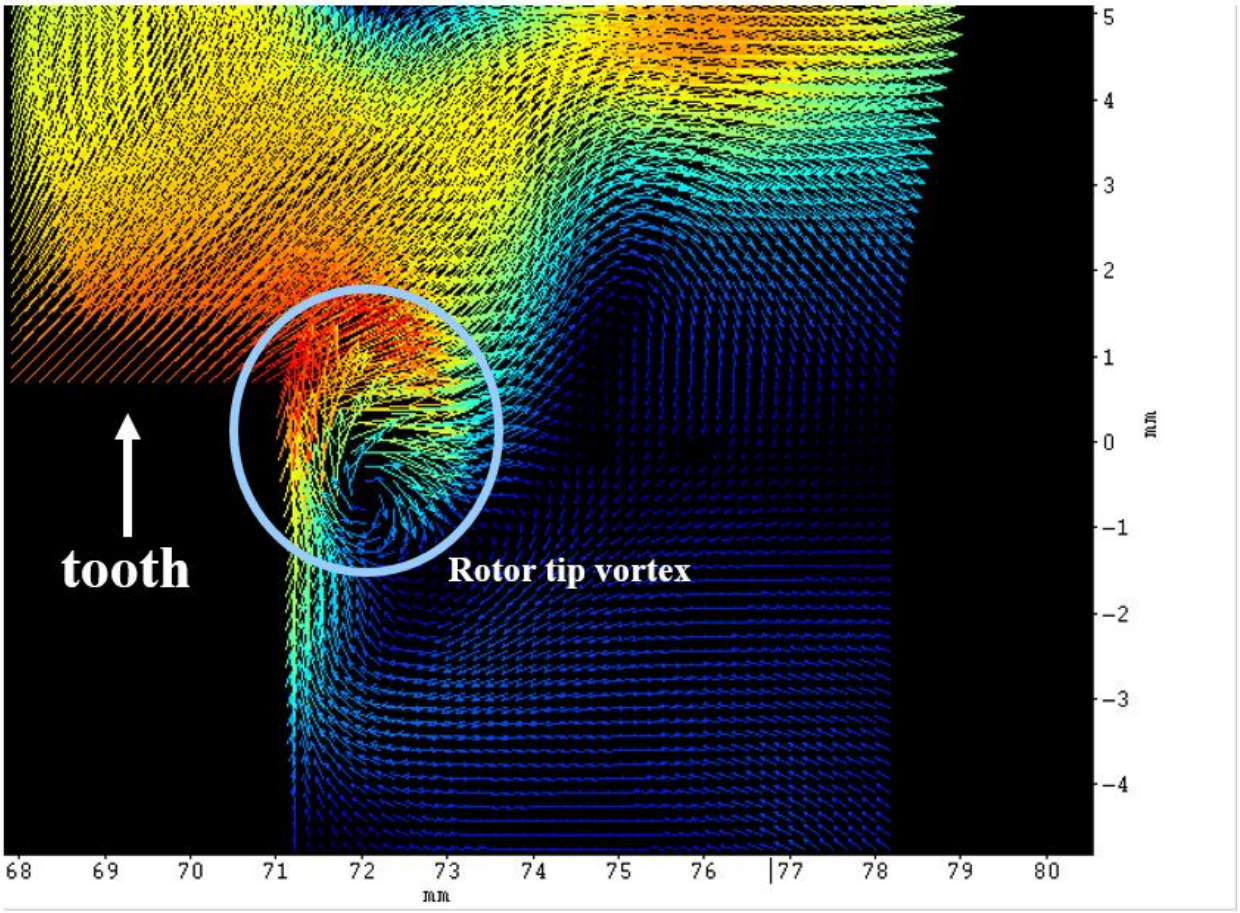

Figure 7. Sample PIV measurement with a rotor tip vortex circled in light blue.

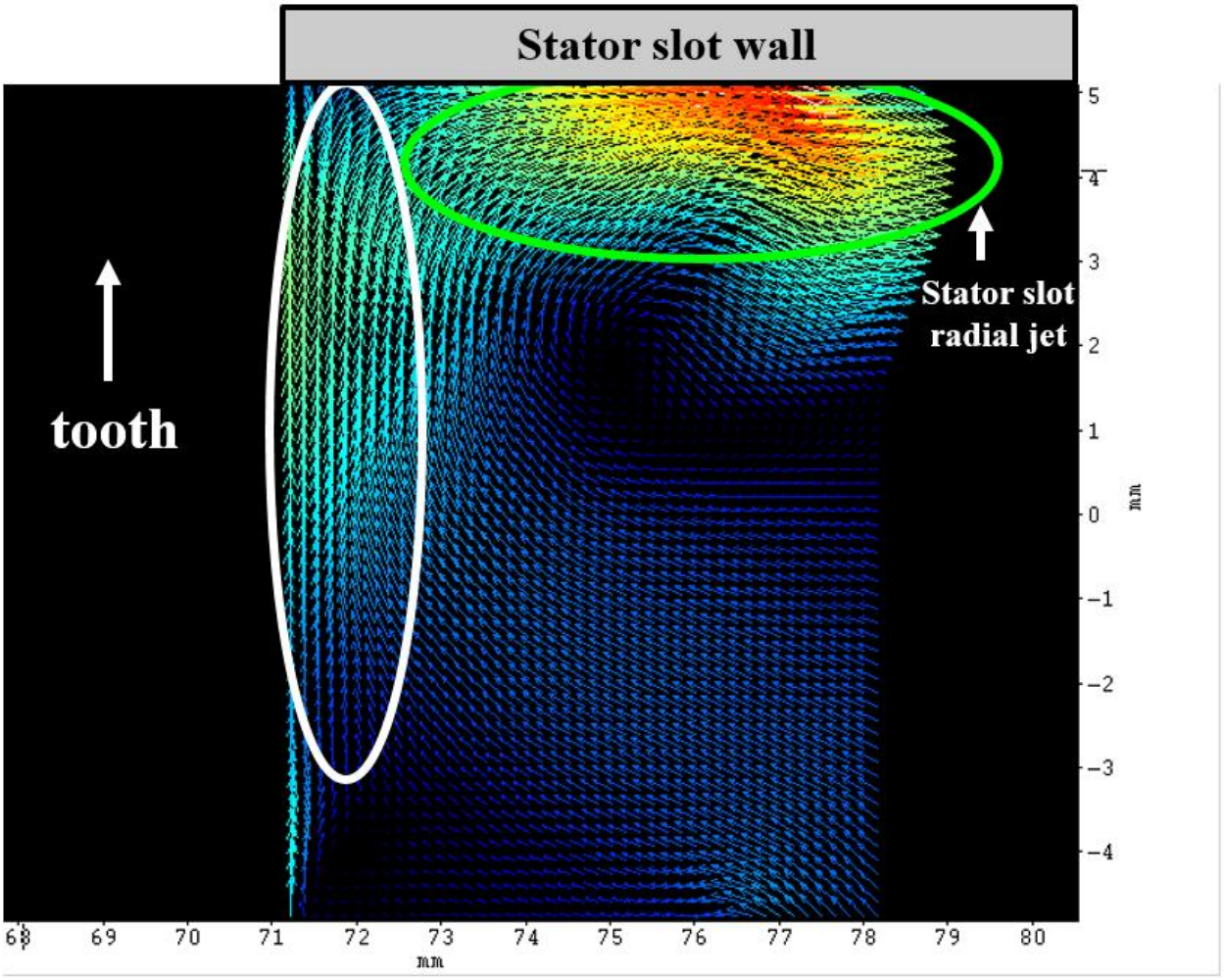

Figure 8. Sample PIV measurement with stator slot radial jet circled in green.

In Figure 8, the tooth is moving up and creating a flow in that direction as shown in the white circle. The flow then collide with the stator slot wall, creating a high speed lateral jet that is called stator slot radial jet (circled in green). As it can be seen in the figure, the collision causes sudden change in flow velocity which can affect mixing significantly.

Locating and comparing these flow features in PIV and CFD results is a useful qualitative comparison method. As a more quantitative set of metrics, the locations of the flow features, velocity magnitudes, and strain rates from the CFD and PIV data were also calculated and

compared (Chapter 4). From the qualitative and quantitative comparisons, conclusions are drawn and future work is suggested (Chapter 5).

2. CFD Background, Approach, and Numerical Condition

This study concerns the turbulent flow of water in a slot and tooth rotor-stator mixer geometry. Modern CFD simulation software provides a number of options to choose for both turbulence and near-wall modeling, each with its own strengths and weaknesses. Choosing appropriate options for modeling is one of the most crucial factors in obtaining successful results. It is desirable to achieve refinement in the results, but the project has to be performed with reasonable computational resources. Our purpose in setting up the conditions was to find optimal balance between accuracy and practicality. Not all decisions were dictated by this argument however, as the geometry or fluid properties became a more prominent factor in some cases.

2.1. CFD Software Package

For the CFD operations, ANSYS products were used. DesignModeler was used to build the geometry of the mixer, which Meshing based on for mesh generation. After the geometry and mesh of the mixer were completed, they were imported to Fluent for configuring simulation parameters and running the simulations.

2.2. Turbulence Modeling

It is well documented that turbulence and its state of chaotic property changes is crucial in achieving homogenization of fluids as mixing requires energy (PollmanAllert, 2009). The statement accentuates the importance of turbulence modeling in CFD simulation of a mixer.

2.2.1. Reynolds Averaged Navier-Stokes (RANS) equations

With the currently available computing power, solving the entire turbulence spectrum with the Navier-Stokes equations down to the smallest scale of turbulence is impractical. Instead,

this study used the Reynolds Averaged Navier-Stokes (RANS) equations. RANS formalism utilizes time-averaging of the Navier-Stokes equation terms, which helps in reducing the computational burden in CFD. In many cases, RANS modeling is adequate to capture the main flow structures of importance and is thus widely adopted for practical application in engineering. However, it would not be suitable for identifying random motions or turbulent fluctuations in smaller scales.

The RANS equation achieve the time-averaging by separating the instantaneous solution variables into the time-averaged terms and fluctuating components. For example, for an exact term f = f(t),

$$f = \bar{f} + f'$$

where $\bar{f}$ is a time-averaged term of f and f' is the fluctuation component. $\bar{f}$ is defined as,

$$\bar{f} = \frac{1}{T}\int_{t0-\frac{T}{2}}^{t0+\frac{T}{2}} f(t).$$

The function, f, can be velocity components, pressure or other scalar quantities. Navier-Stokes equations are,

$$\frac{\partial u}{\partial x} + \frac{\partial v}{\partial y} + \frac{\partial w}{\partial z} = 0 \ (continuity)$$

$$\frac{\partial u_x}{\partial t} + \frac{\partial}{\partial x}({u_x}^2) + \frac{\partial}{\partial y}(u_x u_y) + \frac{\partial}{\partial z}(u_x u_z)$$

$$= -\frac{1}{\rho}\frac{\partial P}{\partial x} + \nu\left(\frac{\partial^2 u_x}{\partial x} + \frac{\partial^2 u_x}{\partial y} + \frac{\partial^2 u_x}{\partial z}\right) \ (x - momentum)$$

$$\frac{\partial u_y}{\partial t} + \frac{\partial}{\partial x}(u_x u_y) + \frac{\partial}{\partial y}({u_y}^2) + \frac{\partial}{\partial z}(u_y u_z)$$

$$= -\frac{1}{\rho}\frac{\partial P}{\partial y} + \nu\left(\frac{\partial^2 u_y}{\partial x} + \frac{\partial^2 u_y}{\partial y} + \frac{\partial^2 u_y}{\partial z}\right)(y - momentum)$$

$$\frac{\partial u_z}{\partial t} + \frac{\partial}{\partial x}(u_x u_z) + \frac{\partial}{\partial y}(u_z u_y) + \frac{\partial}{\partial z}({u_z}^2)$$

$$= -\frac{1}{\rho}\frac{\partial P}{\partial y} + \nu\left(\frac{\partial^2 u_z}{\partial x} + \frac{\partial^2 u_z}{\partial y} + \frac{\partial^2 u_z}{\partial z}\right)(z - momentum)$$

**The gravity term is neglected since density is constant in this problem.*

Where P is pressure, u_i are velocity components, ν is kinematic viscosity. The x, y, and z momentum equations are often expressed in generalized form as the following.

$$\frac{\partial \mathrm{u}_i}{\partial \mathrm{t}} + \frac{\partial}{\partial \mathrm{x}_i}(\mathrm{u}_i \mathrm{u}_j) = -\frac{1}{\rho}\frac{\partial \mathrm{P}}{\partial \mathrm{x}_i} + \nu\left(\frac{\partial^2 \mathrm{u}_i}{\partial \mathrm{x}} + \frac{\partial^2 \mathrm{u}_i}{\partial \mathrm{y}} + \frac{\partial^2 \mathrm{u}_i}{\partial \mathrm{z}}\right)$$

When the Navier-Stokes equations' exact flow variables are substituted by the time-averaged terms and fluctuating components, the following equations emerge as RANS equations.

$$\frac{\partial \overline{\mathrm{u}_x}}{\partial x} + \frac{\partial \overline{\mathrm{u}_y}}{\partial y} + \frac{\partial \overline{\mathrm{u}_z}}{\partial z} = 0$$

$$\frac{\partial \overline{u_x}}{\partial t} + \frac{\partial}{\partial x}(\overline{{u_x}^2}) + \frac{\partial}{\partial y}(\overline{u_x u_y}) + \frac{\partial}{\partial z}(\overline{u_x u_z})$$

$$= -\frac{1}{\rho}\frac{\partial \bar{P}}{\partial x} + \nu\left(\frac{\partial^2 \overline{u_x}}{\partial x} + \frac{\partial^2 \overline{u_x}}{\partial y} + \frac{\partial^2 \overline{u_x}}{\partial z}\right) - \frac{\partial}{\partial \mathrm{x}}(\overline{{u_x}' {u_x}'}) - \frac{\partial}{\partial \mathrm{x}}(\overline{{u_x}' {u_y}'})$$

$$- \frac{\partial}{\partial \mathrm{x}}(\overline{{u_y}' {u_z}'})$$

$$\frac{\partial \overline{u_y}}{\partial t} + \frac{\partial}{\partial x}(u_y u_x) + \frac{\partial}{\partial y}\left(\overline{u_y}^2\right) + \frac{\partial}{\partial z}\left(\overline{u_y u_z}\right)$$

$$= -\frac{1}{\rho}\frac{\partial \bar{P}}{\partial y} + \nu\left(\frac{\partial^2 \overline{u_y}}{\partial x} + \frac{\partial^2 \overline{u_y}}{\partial y} + \frac{\partial^2 \overline{u_y}}{\partial z}\right) - \frac{\partial}{\partial \mathrm{y}}\left(\overline{u_y{}' u_x{}'}\right) - \frac{\partial}{\partial \mathrm{y}}\left(\overline{u_y{}' u_y{}'}\right)$$

$$- \frac{\partial}{\partial \mathrm{y}}\left(\overline{u_y{}' u_z{}'}\right)$$

$$\frac{\partial \overline{u_z}}{\partial t} + \frac{\partial}{\partial x}(u_z u_x) + \frac{\partial}{\partial y}\left(u_z u_y\right) + \frac{\partial}{\partial z}\left(\overline{u_z}^2\right)$$

$$= -\frac{1}{\rho}\frac{\partial \bar{P}}{\partial z} + \nu\left(\frac{\partial^2 \overline{u_z}}{\partial x} + \frac{\partial^2 \overline{u_z}}{\partial y} + \frac{\partial^2 \overline{u_z}}{\partial z}\right) - \frac{\partial}{\partial \mathrm{z}}\left(\overline{u_z{}' u_x{}'}\right) - \frac{\partial}{\partial \mathrm{z}}\left(\overline{u_z{}' u_y{}'}\right)$$

$$- \frac{\partial}{\partial \mathrm{z}}\left(\overline{u_z{}' u_z{}'}\right).$$

Notice additional terms (last three terms of the momentum equations) are generated when the velocity variables are time-averaged. The terms, composed with the fluctuation terms, are called Reynolds stresses and they represent the effect of turbulence. The Navier-Stokes equations now become a closure problem – the additional terms must be modeled for the equations to be closed.

2.2.2. Realizable k-ϵ Turbulence Model

The k-ϵ model provides closure to RANS equations by introducing two semi-empirical transport equations that provide modelling for the Reynolds stress. The model introduces two key variables: turbulent kinetic energy (k) and turbulence dissipation rate (ϵ). ANSYS Fluent theory guide expresses the equations as the following.

$$\frac{\partial}{\partial \mathrm{t}}(\rho k) + \frac{\partial}{\partial \mathrm{x}_j}\left(\rho k u_j\right) = \frac{\partial}{\partial \mathrm{x}_j}\left(\left(\mu + \frac{\mu_t}{\sigma_k}\right)\frac{\partial \mathrm{k}}{\partial \mathrm{x}_j}\right) + G_k + G_b - \rho\epsilon - Y_M + S_K$$

$$\frac{\partial}{\partial \mathrm{t}}(\rho\epsilon) + \frac{\partial}{\partial \mathrm{x}_j}(\rho\epsilon u_j) = \frac{\partial}{\partial \mathrm{x}_j}\left(\left(\mu + \frac{\mu_t}{\sigma_k}\right)\frac{\partial \epsilon}{\partial \mathrm{x}_j}\right) + \rho C_1 S_\epsilon + \rho C_2 + \frac{\epsilon^2}{k + \sqrt{\nu\epsilon}} - C_{1\epsilon}\frac{\epsilon}{k}C_{3\epsilon}G_b + S_\epsilon$$

where

$$\mathrm{C}_1 = \max\left(0.43, \frac{\eta}{\eta + 5}\right), \eta = S\frac{k}{\epsilon}, S = \sqrt{2S_{ij}S_{ij}}$$

G_k and G_b represent the turbulence kinetic energy generation caused by the mean velocity gradients and buoyance, respectively. Y_M is the fluctuating dilatation term, while C_2 and $C_{1\epsilon}$ are constants. σ_k and σ_ϵ are Prandtl numbers for k and ϵ. Finally, S_k and $S\epsilon$ are the source terms.

The model retains reasonable modeling accuracy while keeping its robustness and practicality. The model is called 'realizable' because epsilon is derived from an exact equation rather than from physical reasoning, as in the standard k-epsilon turbulence model. The k-ϵ model's accurate prediction of jet spreading rates and superior performance for rotating flows with strong adverse pressure gradients and recirculation makes it suitable choice for the IKA prototype mixer (LaunderB & SharmaB, 1974). Its weaknesses include insensitivity in critical pressure gradient or boundary layer separation, rendering it inappropriate for some external geometries, but it has shown promising results for internal structures (WilcoxDavid, 1998).

ANSYS recommends using the realizable k-ϵ option, reporting substantial improvement over the standard k-ϵ model. It was found that the ϵ value from an exact equation for the transport of the mean-square vorticity fluctuation was resolved for the model, which should prevent the round-jet anomaly that sometimes occurs in the standard k-ϵ model (Shih, 1995).

2.3. Near-wall Modeling

The significance of near-wall modeling does not only originate from the fact that the IKA prototype mixer has only an internal geometry. The crucial calculations of CFD – velocity field, shear and dissipation rate, moment values, and power number –all depend on the way modeling captures the fluid's interaction with the various rotating and stationary surfaces.

2.3.1. Near-wall Region: Near-wall Model and Wall Functions

The near-wall region can be subdivided into three layers, depending on a non-dimensional wall distance for a wall-bounded flow y^+, which can be defined as following (AmanoR, 1983),

$$y^+ = {u_* y}/{\nu}$$

where ν is the kinematic viscosity, y the distance to the nearest wall, and u_* the friction velocity on the nearest wall. Friction velocity, which is also called shear velocity, is defined as

$$u_* = \sqrt{{\tau}/{\rho}}\,.$$

The three layers are,

–Viscous sublayer: near-wall, dominated by viscosity ($y^+<5$)

–Fully-turbulent layer: outer layer, turbulence plays a major role ($60<y^+$)

–Buffer layer (blending region): affected by both viscosity and turbulence ($5<y^+<60$).

The near-wall region is highly dynamic where the velocity profile transitions from a linear shear flow to a turbulent profile. In order to accurately capture the transition using near-wall modeling, a high mesh density is required in the near-wall region (Figure 9, right). Although this is a logical solution, it also dramatically increases the computing time since the total cell quantity directly correlates to the number of required calculations. The wall function approach

(Figure 9, left) attempts to circumvent the disadvantages of near-wall modeling by utilizing a collection of semi-empirical formulas. By using wall functions, the mesh does not need to be resolved as finely in the near-wall region, but the accuracy of the solution in the region may depend on factors such as the geometry, sizing, etc.

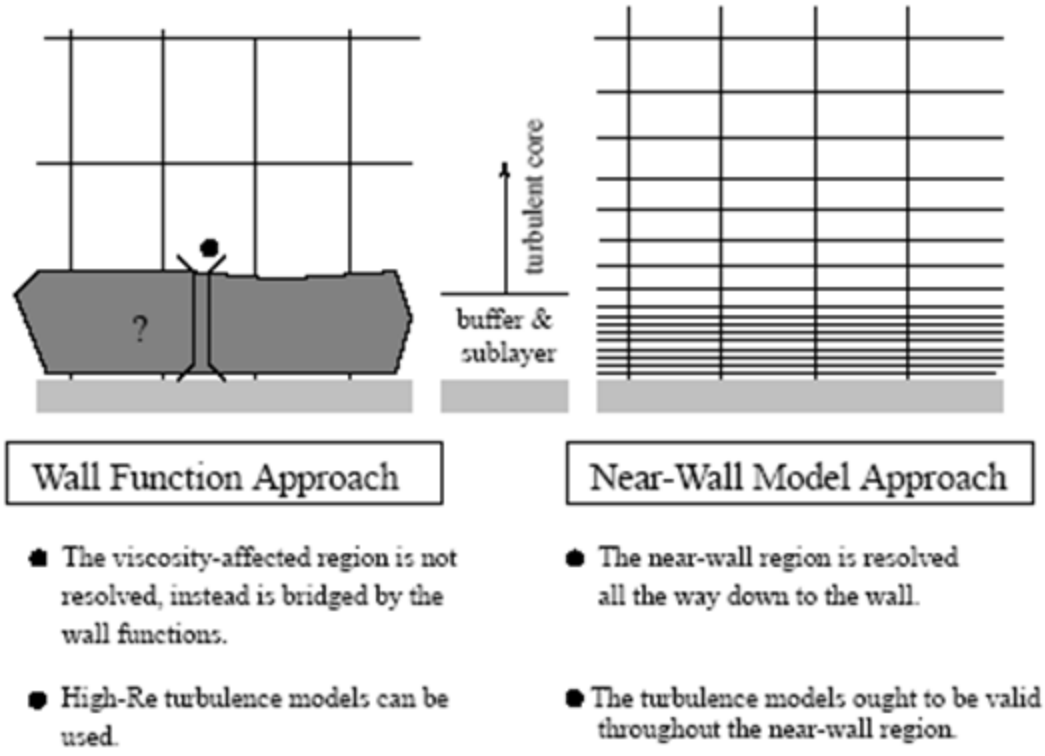

Figure 9. Wall Function and Near-wall modeling (ANSYS,INC., 2013)

2.3.2. Non-Equilibrium Wall Function (NEWF)

Even though the wall function's practical strength is appealing, it is not without its shortcomings. Wall functions are developed in part from experimental measurements and therefore work better in some flows and worse in others. For example, standard wall functions are severely compromised when the flows have a strong pressure gradient. Non-equilibrium wall functions (NEWF) attempt to overcome the issue by partially accounting for the effects of pressure gradients and departure from equilibrium. ANSYS recommends NEWF for geometries

like the IKA mixer, where the mean flow and turbulence change abruptly and pressure gradient is severe. NEWF does have difficulty in capturing flows of the following conditions:

- Pervasive low-Reynolds number or near-wall effects
- Blowing or suction (significant transpiration)
- Boundary layer separations
- Strong body forces (buoyancy driven flows)

Fortunately, the IKA mixer is not subjected to any of the item in the list, so the theoretical basis of the method appears suitable for the simulation.

2.3.3. Enhanced Wall Treatment (EWT)

Enhanced wall treatment (EWT) is another development in the effort to achieve accurate results without losing practicality. Unlike with other wall functions EWT will produce the same result as the traditional near-wall modeling if the mesh is sufficiently fine to resolve the near-wall region. The advantage of EWT appears when the near-wall mesh density is lower; it attempts to retain the accuracy of resolving the entire near-wall region. It combines near-wall modeling and wall function approaches in the sense that,

- The whole domain of fluid is subdivided into a viscosity-affected region and a fully-turbulent region
- In the turbulent region, the realizable k-e model is used
- In the viscosity affected region, the one-equation model of Wolfstein is used.

On the surface, NEWF and EWT were both were developed to serve the same purpose. However, the approaches were made from different basis with different algorithms. Therefore, it is difficult to predict which of the two methods will be superior in practicality and accuracy.

Numerous factors, such as geometry or other simulation settings, can favor one model over the other. A comparison of results using the two methods is made in Chapter 3.

2.4. Computational Mesh

The geometry of the IKA prototype mixer was imported to ANSYS Workbench for mesh development. Several levels of mesh were generated. The initial mesh, referred to in this study as mesh level 1, had relatively uniform cell size throughout the domain. The main goal of the first level mesh was to model the entire geometry using hexahedral cells. This introduced the necessity of dividing the domain into numerous smaller parts, which exposed more geometrical elements to the user's mesh specifications, and reduced the usage of automatic mesh generation. Figure 10 shows the overview of mesh level 1, with Slot 1 marked with a red box.

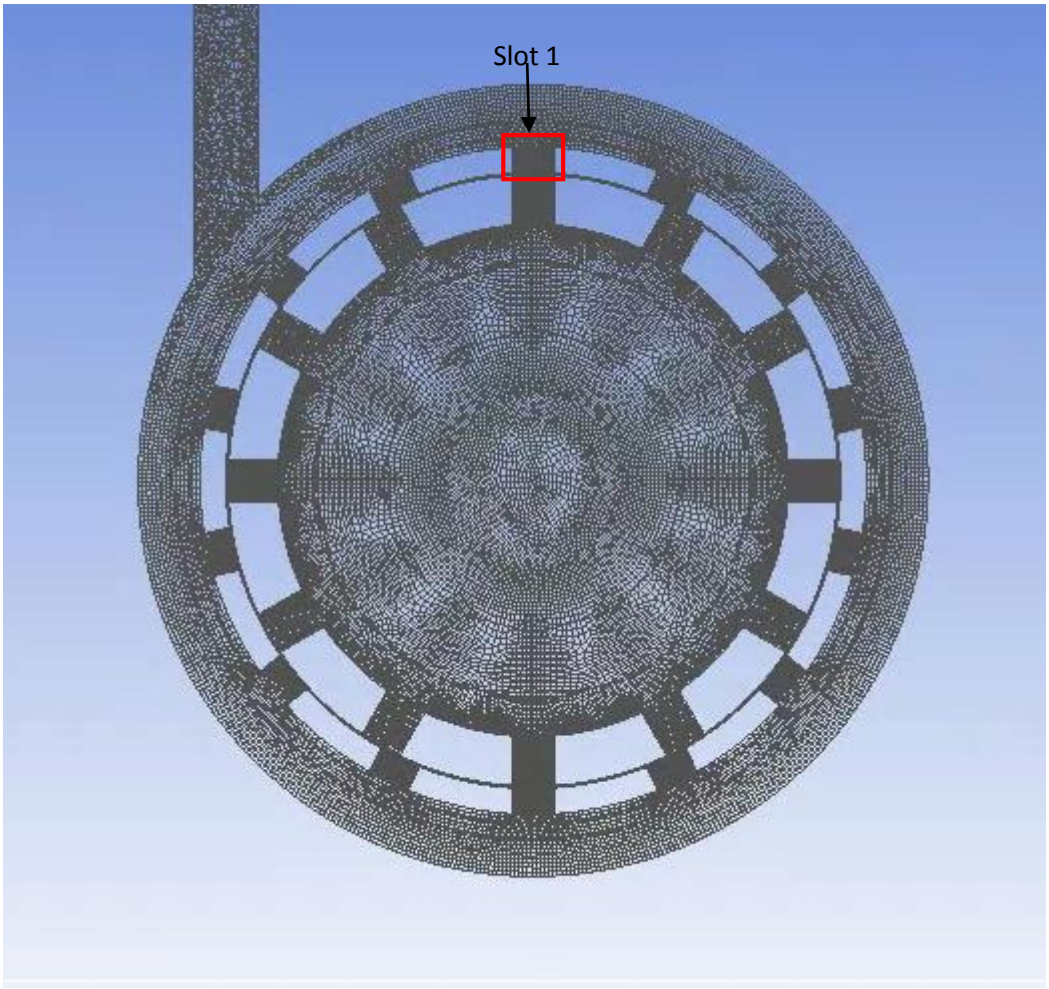

Figure 10. Overview of mesh level 1

Mesh level 1 was used as a basis to create mesh levels 2 and 3. A higher mesh level has higher mesh density in key areas such as in the vicinity of Slot 1 and in the shear gap. This was achieved by using the Adapt function in Fluent. Figure 11 is a graphical representation of mesh variation of the shear gap for different levels.

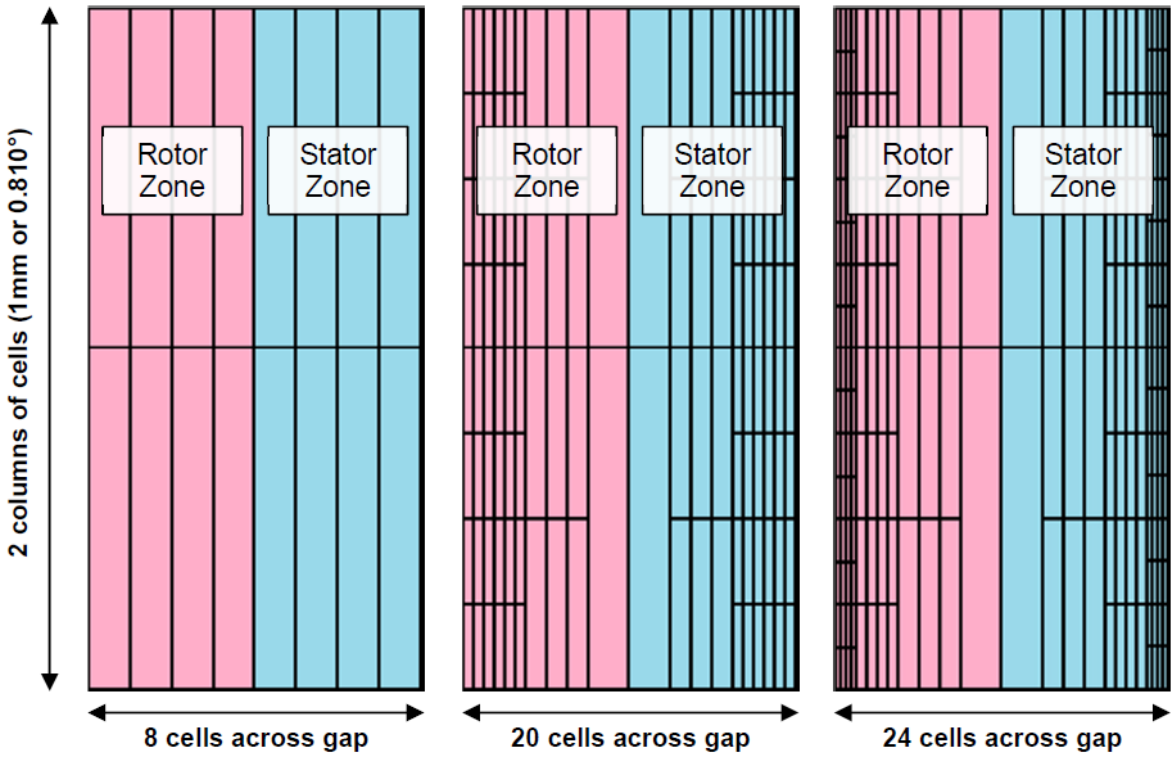

Figure 11. Mesh density variation among different levels in shear gap

Figure 12, Figure 13, and Figure 14 are screenshots of the shear gap and Slot 1 for mesh level 1, 2, and 3, respectively. The mesh specifications of the different mesh levels are listed in Table 2.

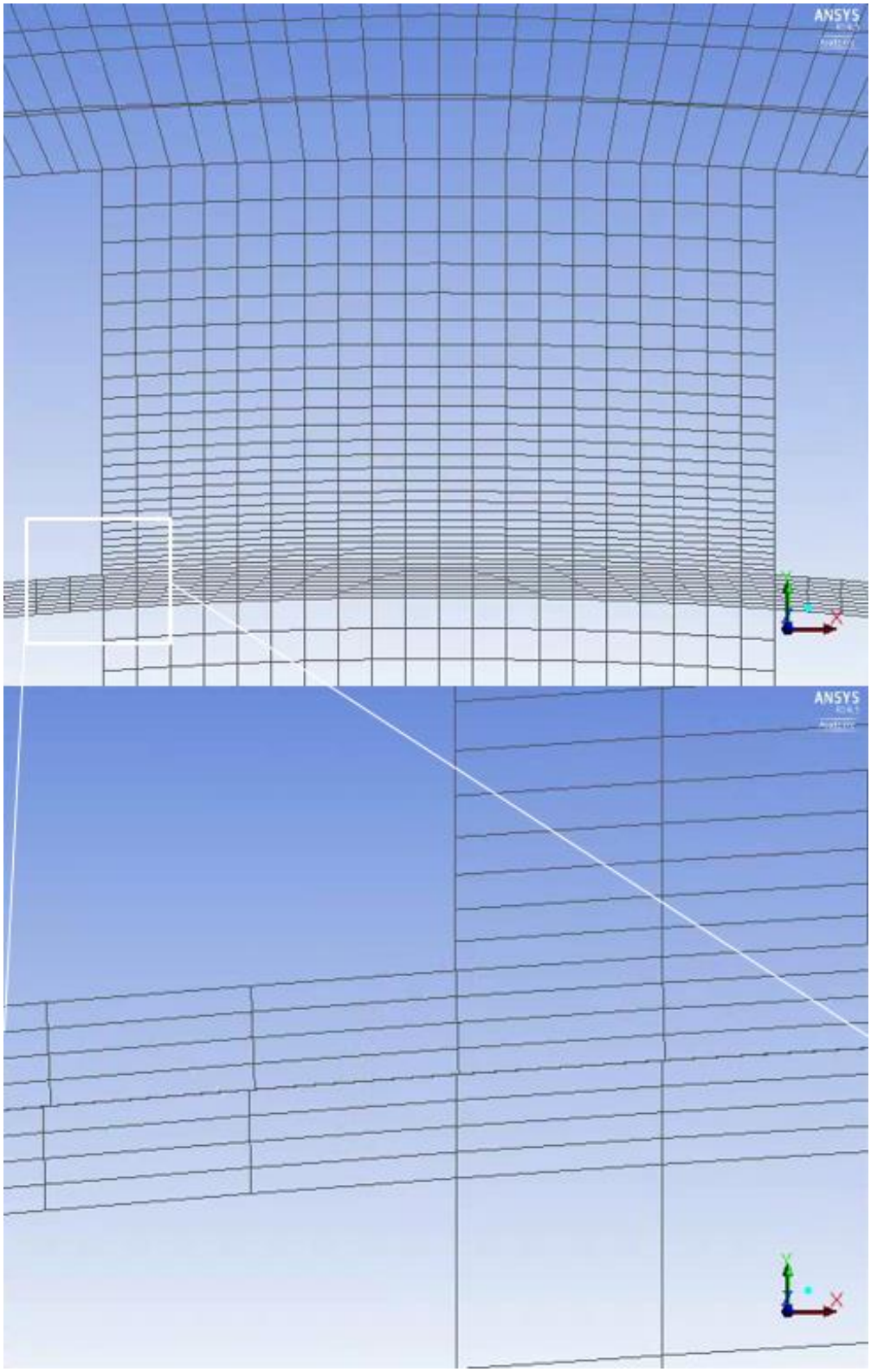

Figure 12. Mesh level one: the shear gap and Slot 1

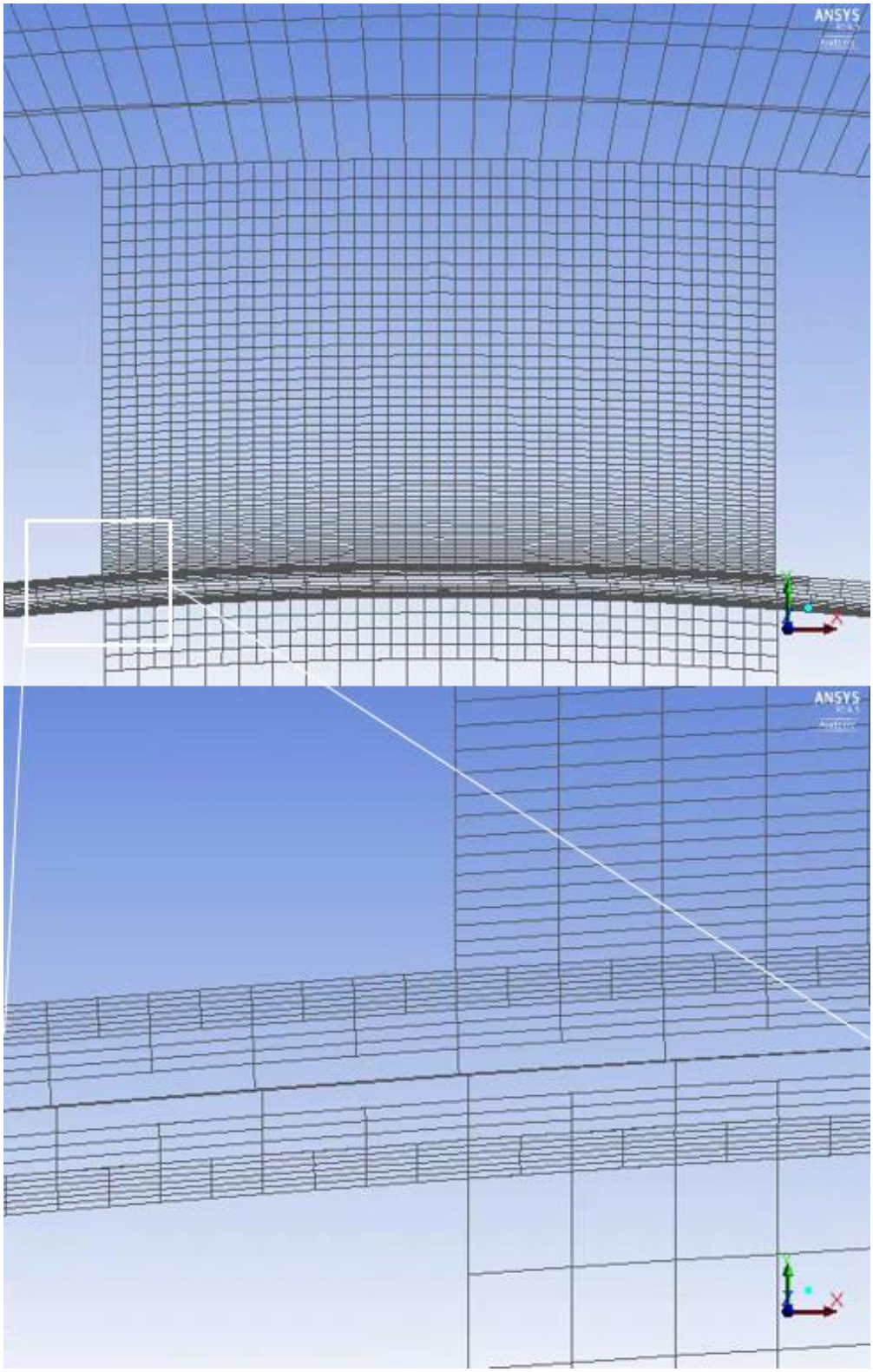

Figure 13. Mesh level two: the shear gap and Slot 1

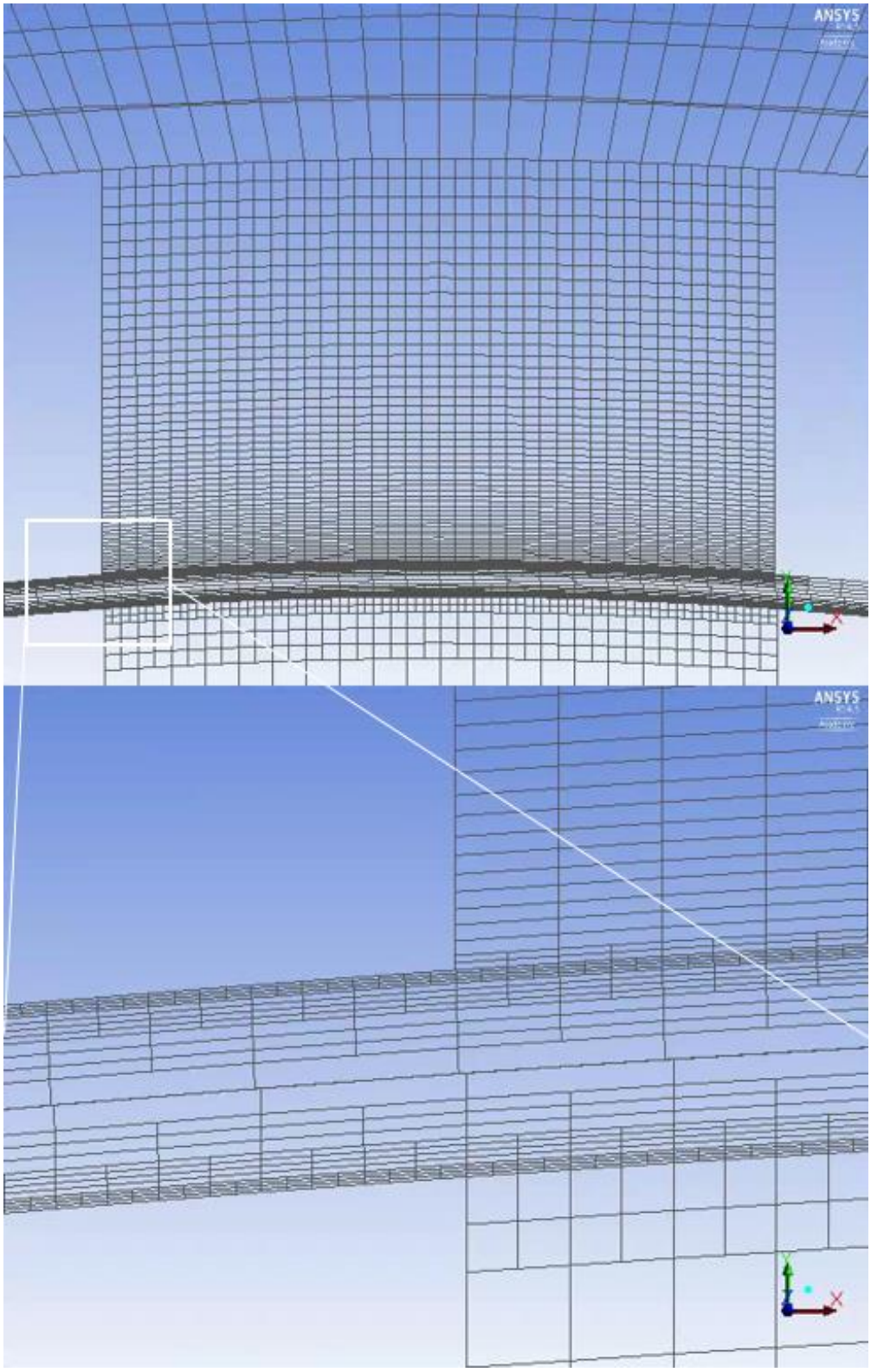

Figure 14. Mesh level three: the shear gap and Slot 1

Table 2. Specification of the three mesh levels

Mesh Level	Total Cells	Cells in Stator Zone	Cells in Rotor Zone	Computation Time*
1	2.08 mil	0.918 mil	0.878 mil	22 hours
2	6.66 mil	3.92 mil	3.33 mil	90 hours
3	15.9 mil	7.80 mil	6.85 mil	250 hours

*Per revolution. Computer specifications is listed in Chapter 2.5

Note that, between mesh levels two and three, the only difference is the mesh densities in the shear gap. Between levels one to two, however, the difference in mesh density lies both in the shear gap and the Slot 1. Such choice was made from an understanding that the shear gap directly upstream of Slot 1 is a highly dynamic region of flow; even when the slot is completely closed, there is a leakage flow around the rotor teeth. The mesh density in Slot 1 for levels two and three is comparable to the density of the PIV grid used to develop the experimental PIV data. The computation time varied as the total cell numbers change in a linear fashion. At mesh level three, the simulation was already taking about a week and half to complete one revolution. Although creating a further-refined mesh in Slot 1 was not performed in this study, it may produce positive effects to the results and is suggested as a future project.

2.4.1 Mesh zone configuration in ANSYS Fluent

The IKA prototype mixer geometry has one rotating mesh zone (rotor) and all other mesh zones (stator, volute region, etc) stay stationary. It is necessary for the zones to be configured accordingly for ANSYS Fluent to properly simulate the zonal relative motions. There are two methods to configure the mesh movement: multiple reference frame (MRF) and sliding mesh models.

In an MRF modeling, each cell zone is configured with its rotational speed. Using the data and moving reference frame equations, a steady-state approximation is made (LuoJ, IssaR, GosmanA, 1994). Since this approach is not transient, there is no relative motion of rotating mesh zones. On the other hand, sliding mesh modeling creates movements in rotating zones and transient solutions. Compared to steady-state MRF, solving a sliding mesh model is more expensive computationally. However, considering the importance of the interaction between the rotor and stator zones in this simulation, sliding mesh modeling is a clearly more appropriate choice. Understanding the practical advantage of MRF, it was used to create initial conditions for sliding mesh simulations, as that was deemed more practical compared to using the sliding mesh modeling from ground up.

2.5. Computer specifications

For the CFD simulation, two computers were used in a parallel configuration. Each machine housed two quad core Xeon CPUs, which resulted in a system with sixteen cores. The CFD programs were run in a Linux-based Centos 6 x86-64 operating system. The following table describes detailed specifications of each machine.

Table 3. Specifications of Computers Used for the CFD Simulation.

Mainboard	Asus Z8PE-D12 Dual LGA1366 Xeon Motherboard
CPU	2 x Intel Xeon Quad Core E5520 2.26Ghz 1333MHz
RAM	12 x 4GB DIMMS DDR3 1066 Memory
OS	Centos 6 x86-64
Hard Drive	Seagate Barracuda 7200 rpm 32MB Cache SATA

2.6. Convergence Verification Method

Each simulation, with different mesh level and rotor speed scenario, was considered to be completed only when it reached convergence. The convergence process was gradual and visual inspection alone was determined not to sufficient for verification. Therefore, two lines parallel to the y axis were drawn in the radial direction at the center of stator-slot 1 at two different depths. One line is nearer to the volute cover (z = -2mm, the axis described in Figure 2), and the other is placed approximately in the middle between the volute cover and the stator wall (z = -7mm). Figure 15 graphically shows where the two lines are located.

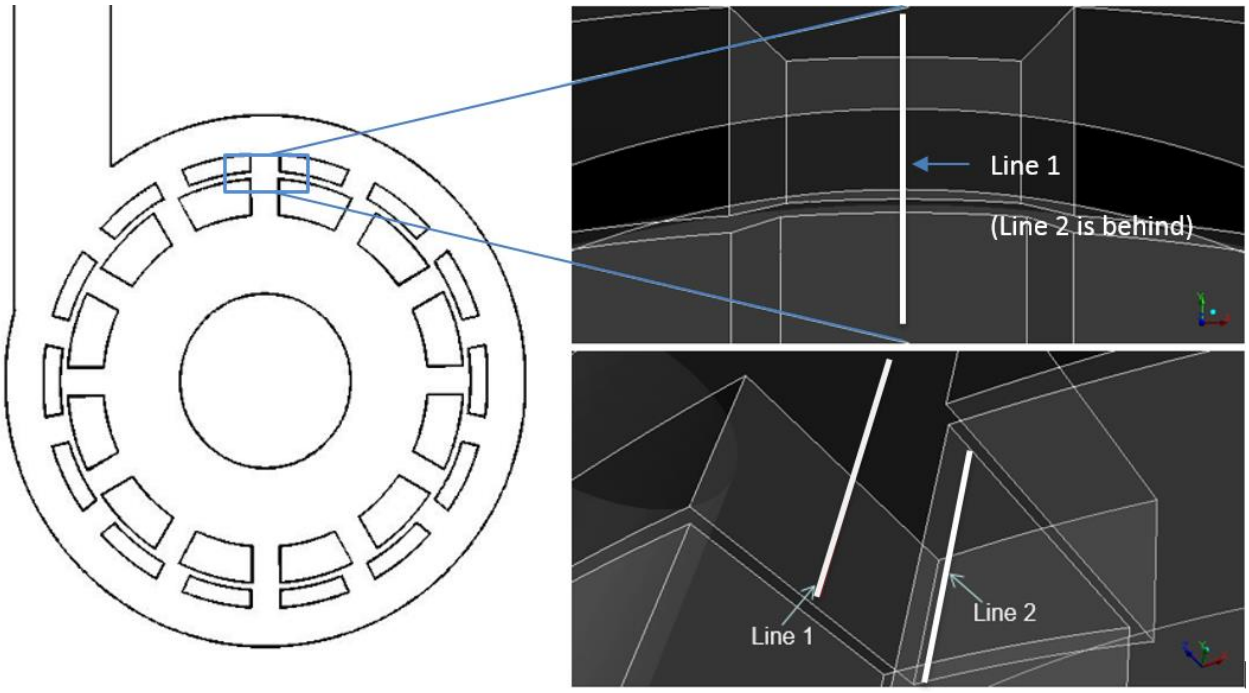

Figure 15. Locations of the Convergence Verification lines

Flow velocity data in the x, y, and z directions were collected from each cell along the two lines. To justify a simulation's convergence at a certain revolution n, the data for the last two revolutions (n-1 and n) were compared. By subtracting x, y, and z velocity components of the

two revolutions, a difference vector was created for each cell along the two lines, which was then used to generate a percent difference calculation.

For example, consider a cell *i* on one of the two lines. Its reported velocity vector for revolution n will be expressed as,

$$V_i^n = \left(v_{xi}^n, v_{yi}^n, v_{zi}^n\right),$$

where x_i^n, y_i^n, and z_i^n are the x, y, and z velocity components. The velocity components for the previous revolution n-1 can be written as,

$$V_i^{n-1} = (v_{xi}^{n-1}, v_{yi}^{n-1}, v_{zi}^{n-1}).$$

The difference vector $\underline{d}$ is created by subtracting the two vectors.

$$\underline{d} = V_i^n - V_i^{n-1}$$

From the difference vector, percent difference of each component is calculated as,

$$\%d_i = \left(\left|\frac{d_x}{v_{xi}^n}\right|, \left|\frac{d_y}{v_{yi}^n}\right|, \left|\frac{d_z}{v_{zi}^n}\right|\right) \times 100(\%)$$

where d_x, d_y, and d_z are the x,y, and z components of $\underline{d}$. Percent difference, $\%d$, is calculated for every cell on the two lines. Then, the average percent difference, $\%d_{avg,}$ is calculated along the two lines as follows,

$$\%d_{avg} = \frac{\sum_{i=1}^{j} \%d_i}{j},$$

where *j* is the total number of cells over the two lines.

The convergence of a simulation was claimed to occur when the average percent difference for x, y, and z along the two lines (Figure 15) became less than 3%. Table 4 shows how many revolutions were required for a mesh level to satisfy such condition in each rotor speed scenario using RANS simulation with realizable k-ϵ turbulence model and Enhanced Wall Treatment. All simulations have the same throughput of 1.3 L/s. The table, however, is not a representation of a scenario's ability to converge because each has different initial conditions (as described in 2.7 Simulation Scheme). It can be observed, however, that within the same mesh level, the 10 rps scenario requires significantly more amount of revolutions than the others because its starting point is from a different rotor speed scenario.

Table 4. Number of Revolutions Required for Convergence in each Rotor speed scenario

	Mesh level 1	Mesh level 2	Mesh level 3
10 rps	13	8	5
20 rps	10	6	4
26 rps	9	7	4

Some of the simulations were run for extended periods past its convergence to observe how $\%d_{avg}$ value varies after the 3% threshold is reached. The percent difference values varied minutely and remained steadily between 2% and 3% after they initially reach the threshold. This behavior was displayed throughout different mesh settings and rotor speed scenarios; for instance, mesh level 2 was run twelve revolutions past the convergence without the $\%d_{avg}$ going below 2%. An in-depth observation of the data revealed the cause of the fluctuation to be the

slight movements in vortices' locations between subsequent revolutions – even though RANS simulation does not show fluctuations in the results, minute movement in the vortex center locations were still observed. Near the center of a vortex, cells have near zero velocity magnitudes. This results in significantly exaggerate variation in terms of percent difference of the magnitude.

2.7. Simulation Scheme

Mesh level 1 was constructed in ANSYS Workbench and was taken to Fluent. Initial calculations were performed with the Multiple Reference Frame (MRF) technique to generate the data that were consequently used as an initial condition for the RANS sliding mesh simulation. The following table shows the residual monitor settings for the simulations.

Table 5. Residual Settings for RANS simulation

	Continuity	X-velocity	Y-velocity	Z-velocity	K	ϵ
Residual value	1e-04	1e-05	1e-05	1e-05	1e-05	5e-05

The first simulation was conducted with the 10 rps rotor speed scenario. When the model was converged, the data were used as an initial setting for the 20 rps rotor speed scenario, and so on for the 26 rps scenario. When the all three velocity simulations are completed in mesh level 1, the data were taken as the initial settings for each rotor speed scenario in mesh level 2, and so on.

2.8 Notations of the Rotor Positions

The velocity data of Slot 1 are reported in the form of vector velocity plots in result sections. The data are collected in different rotor speed scenarios and rotor positions. In Figure 16, angular notations of the rotor are demonstrated.

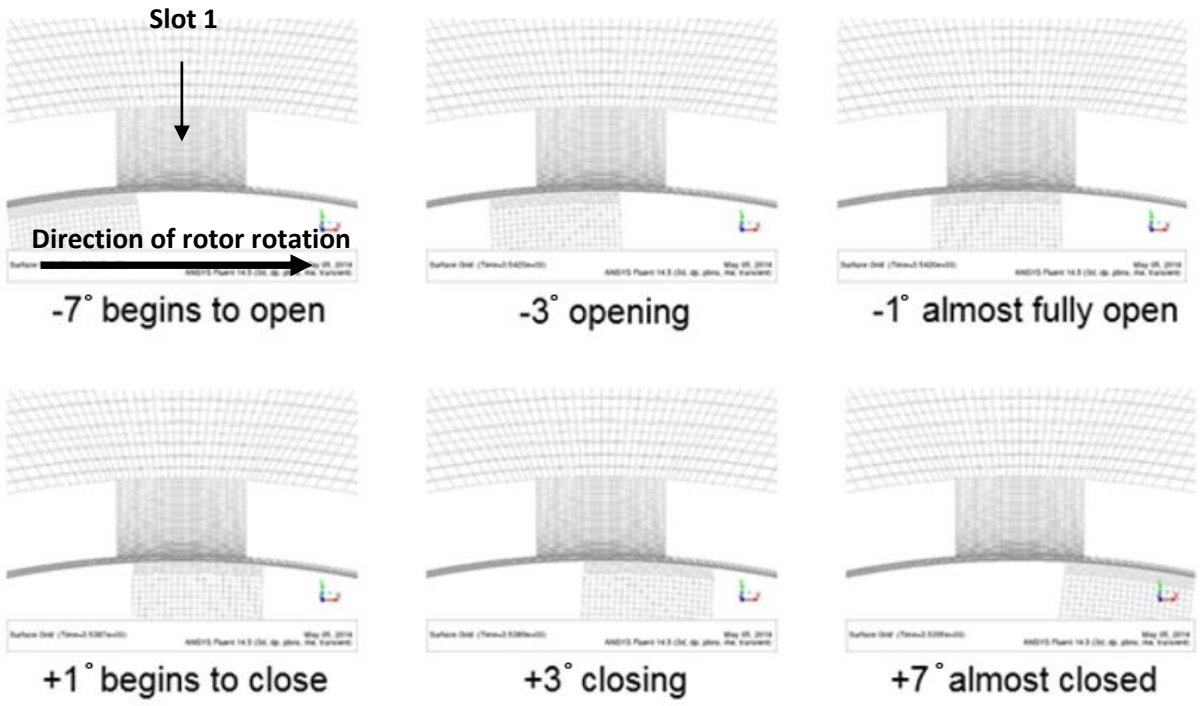

Figure 16. The Angular Notation of Slot One

The θ = 0° position is when the rotor and stator slots are perfectly aligned. Negative or positive degree values of the angle position, θ, represent how many degrees of rotation the rotor made in counter clockwise or clockwise direction from the θ = 0° position. Slot 1 is considered fully closed when it is completely blocked by a rotor tooth, and completely open when the rotor and stator slots are perfectly aligned. The slot starts to open and completely closes at approximately -8° and +8°, respectively.

2.9 Summary

In this chapter, the background and configuration information that will be significant for the CFD simulation were introduced. In the following chapters, the execution of the CFD simulation and its comparison to the PIV data of the IKA prototype in-line mixer will be discussed.

3. Preliminary Study

3.1. Mesh Independence Study

In order for a CFD simulation to provide a realistic representation of the fluid dynamics, maintaining reasonable mesh density is crucial. High mesh density alone, however, does not guarantee accurate result; mesh uniformity also needs to be considered in mesh design, as it creates discrepancies such as spatial truncation error (FletcherC., 1994). With these considerations, the mesh level 1 was generated using hexahedral elements which makes it easier to achieve higher orthogonality and better aspect ratio of neighboring cells compared to using tetrahedral elements. Since mesh level 2 and 3 were generated using the Adapt function based on a hexahedral mesh, they share similar mesh uniformity (Figure 11). However, the mesh density and the computation time per revolution varies dramatically from one level to another, as was described in Table 2. This preliminary study was an effort to determine if using mesh level three, with approximately three times longer computation time than level two, is necessary for the main purpose of PIV to CFD comparison.

The simulations were run at 10 rps rotor angular rotor speed scenario using identical simulation parameters except for the mesh density, on the same computer platform (specification described in Table 3). Figure 17, 14, and 15 reports results for the mesh level 1, 2, and 3, respectively.

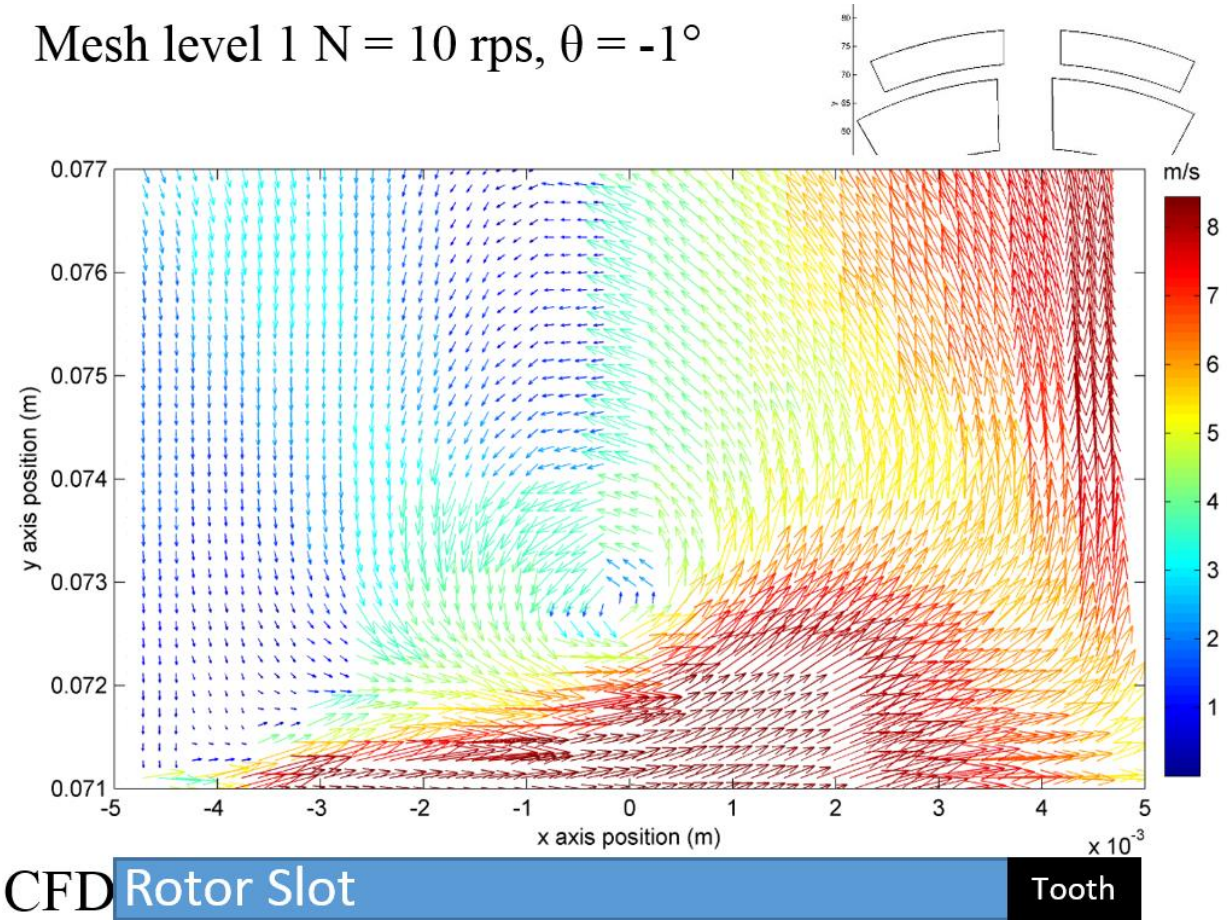

Figure 17. Flow Field from Mesh Level 1 at -1° Rotor Position, N = 10 rps

Compared to the following figures generated by the denser mesh levels, it is easily seen that the mesh level 1 is unable to generate a smooth vector field; there are patches of vectors that have the same velocity data due to the coarse mesh. As a result, it creates uneven transition from one region to another. Such a result is unsuitable for an adequate comparison to the resolved experimental flow data captured by the PIV measurements. This was an expected result as the first level was meant to be used as a base model to build the finer models.

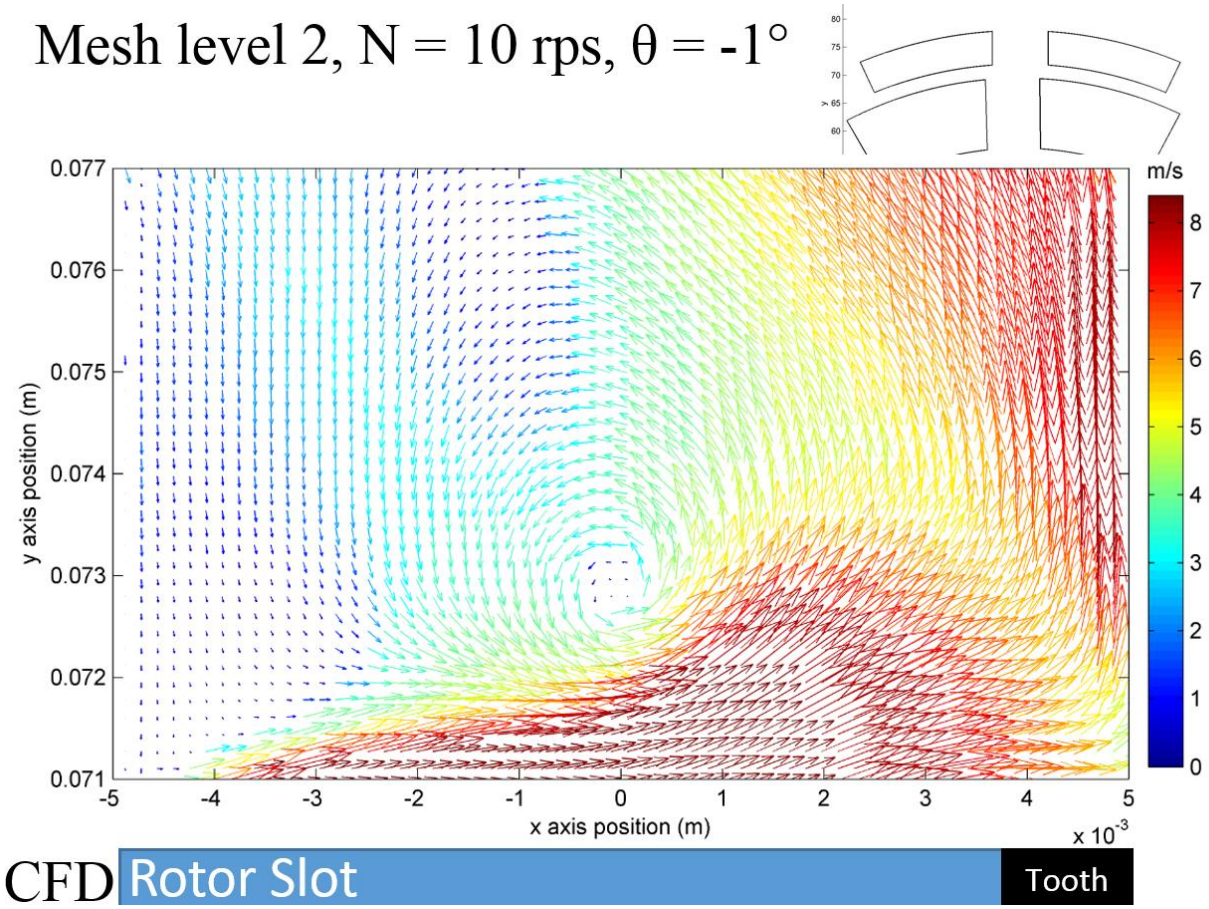

Figure 18. Flow Field from Mesh Level 2 at, N = 10 rps, θ = -1° Rotor Position

Figure 18 does much better job in creating smoother, more realistic flow field in Slot 1. The patches of arrows that cause abrupt transition are not present anymore. The flow fields of level one and level two show strong similarity in terms of general flow direction and the location of the mixing vortex. This indicates level one can be used as reliable as level two to predict the locations of major flow features with great robustness. For this particular study, however, level one mesh is too coarse to create smooth vector fields since the mesh is not as dense as the one used in the PIV study.

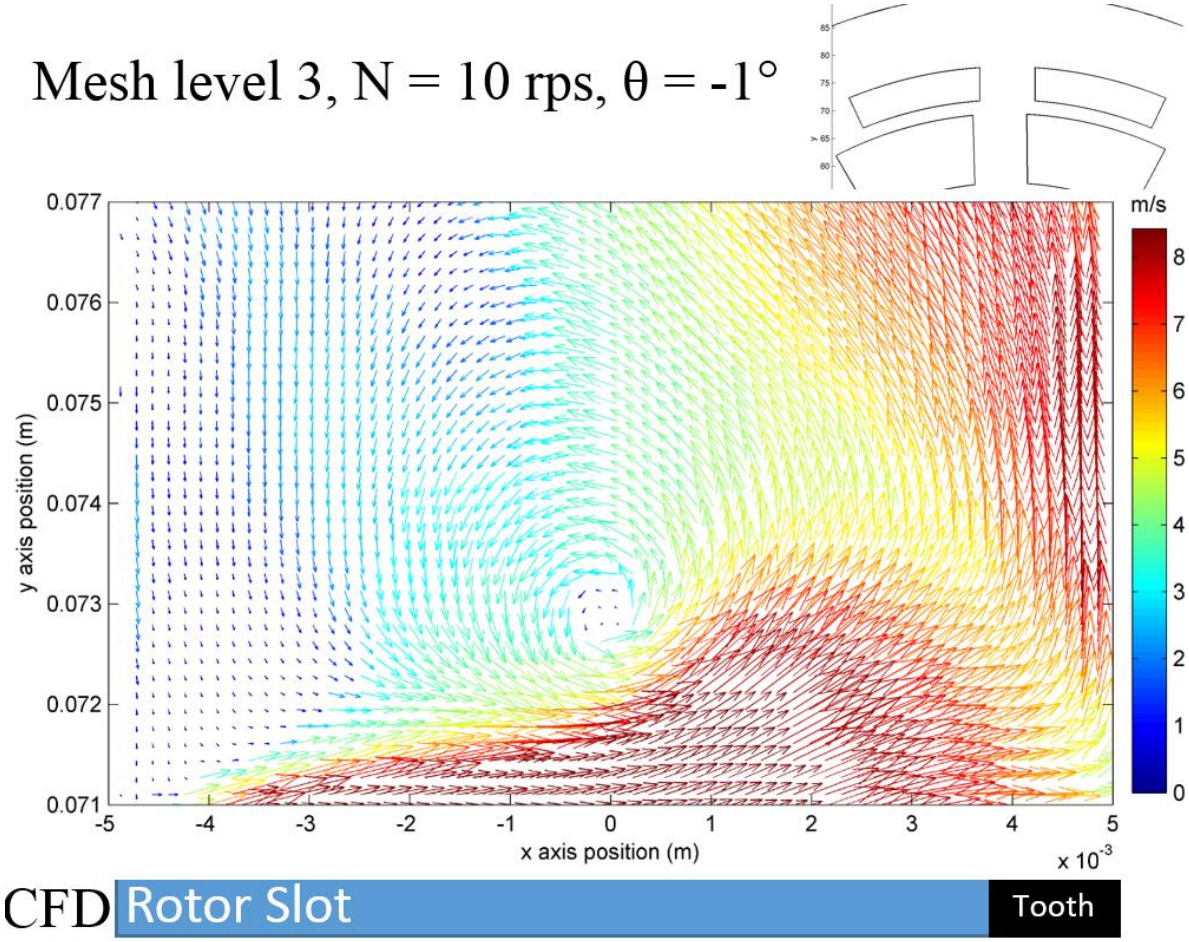

Figure 19. Flow Field of Mesh Level 3 at -1° Rotor Position

Figure 19 shows what mesh level three result for the same location. There is no visually apparent difference between the vector fields created by mesh level two and three. For more in-depth comparison, the results for mesh levels 2 and 3 are compared throughout the nine different angular rotor positions of Figure 16: -7°, -5°, -3°, -1°, +1°, +3°, +5°, +7°, and +9°. Figure 20 and Figure 21 compare the vector mean velocity fields at the θ = -5° and +3° rotor positions. The two figures show that the mesh level 2 and 3 are very similar, with predicted mixing layer vortex (at θ = -5°) and rotor tip vortex (at θ = +3°) in close proximities.

As a quantitative comparison, the average difference in the vortex center locations, vector direction and vector magnitude were calculated. The comparison was conducted between mesh level 1 and 2 and between 2 and 3 in order to show that the mesh independence has been reached at mesh level 2. For the vortex center location calculation, each vortex's center location for two mesh levels are subtracted at each of the nine rotor positions and averaged. The value was then normalized by the slot width (10mm) and reported as a percentage value. For the vector direction and magnitude calculation, the difference percentage was calculated by using the same method as in *Section 2.6*.

Table 6. Results comparison among the three mesh levels

Averaged difference* between level 1 and 2	Averaged difference* between level 1 and 2	Averaged difference* between level 2 and 3
Vortex center location	2.9% of the slot width**	0.21% of the slot width
Vector (on the field) direction	7.8%	1.7%
Vector magnitude	14%	2.3%

*Averaged over 9 different angular positions

Mesh level 2 compares much better with the higher mesh level than the mesh level 1. Also considering that the level 2 and 3 comparison produced differences that are within the convergence requirement, it was determined to be a reasonable balance between accuracy and practicality and thus adopted for the main CFD to PIV comparisons.

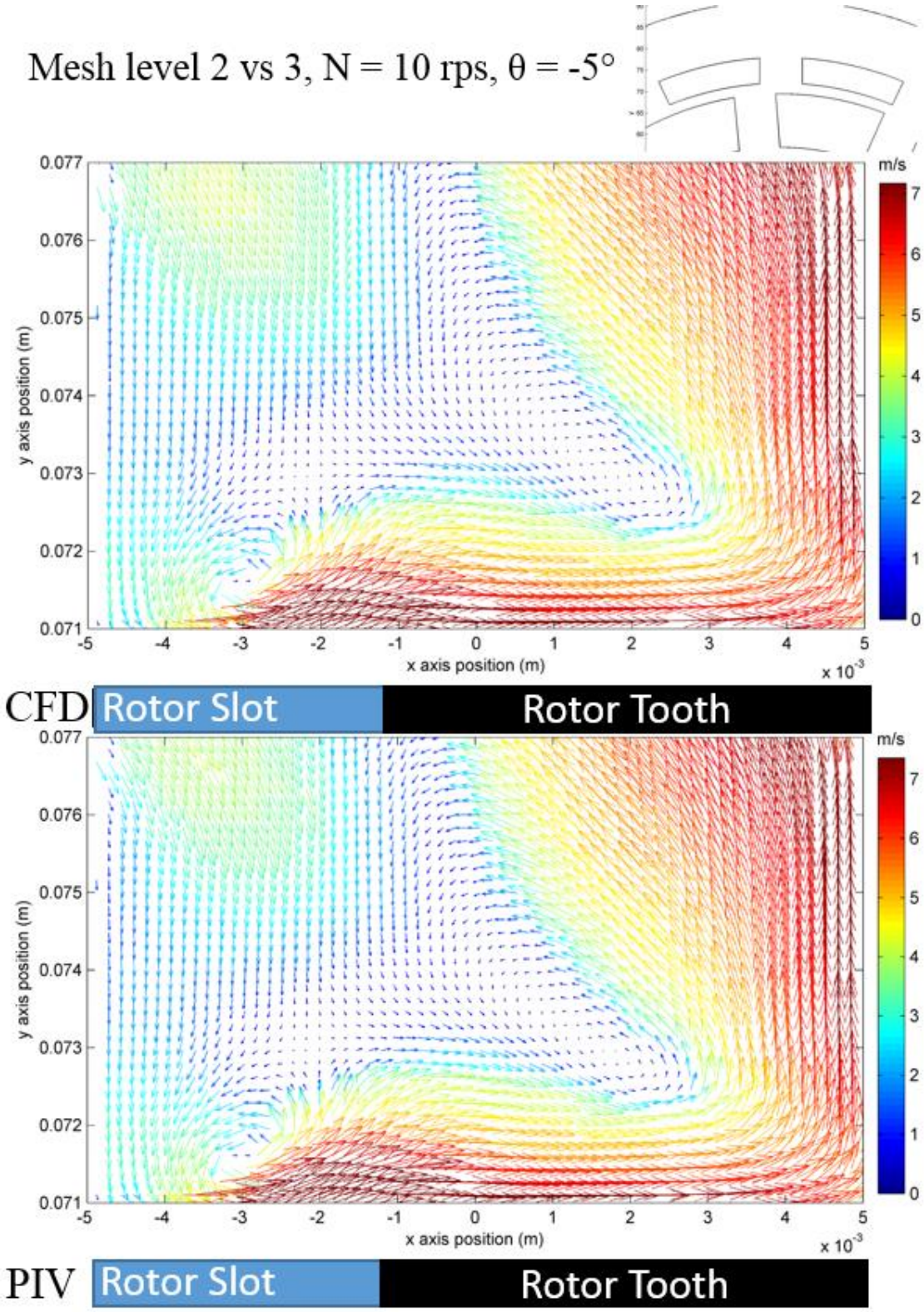

Figure 20. Mean velocity field comparison between mesh Level 2 (top) and 3 (bottom): -5° Rotor Position, 10 rps rotor velocity

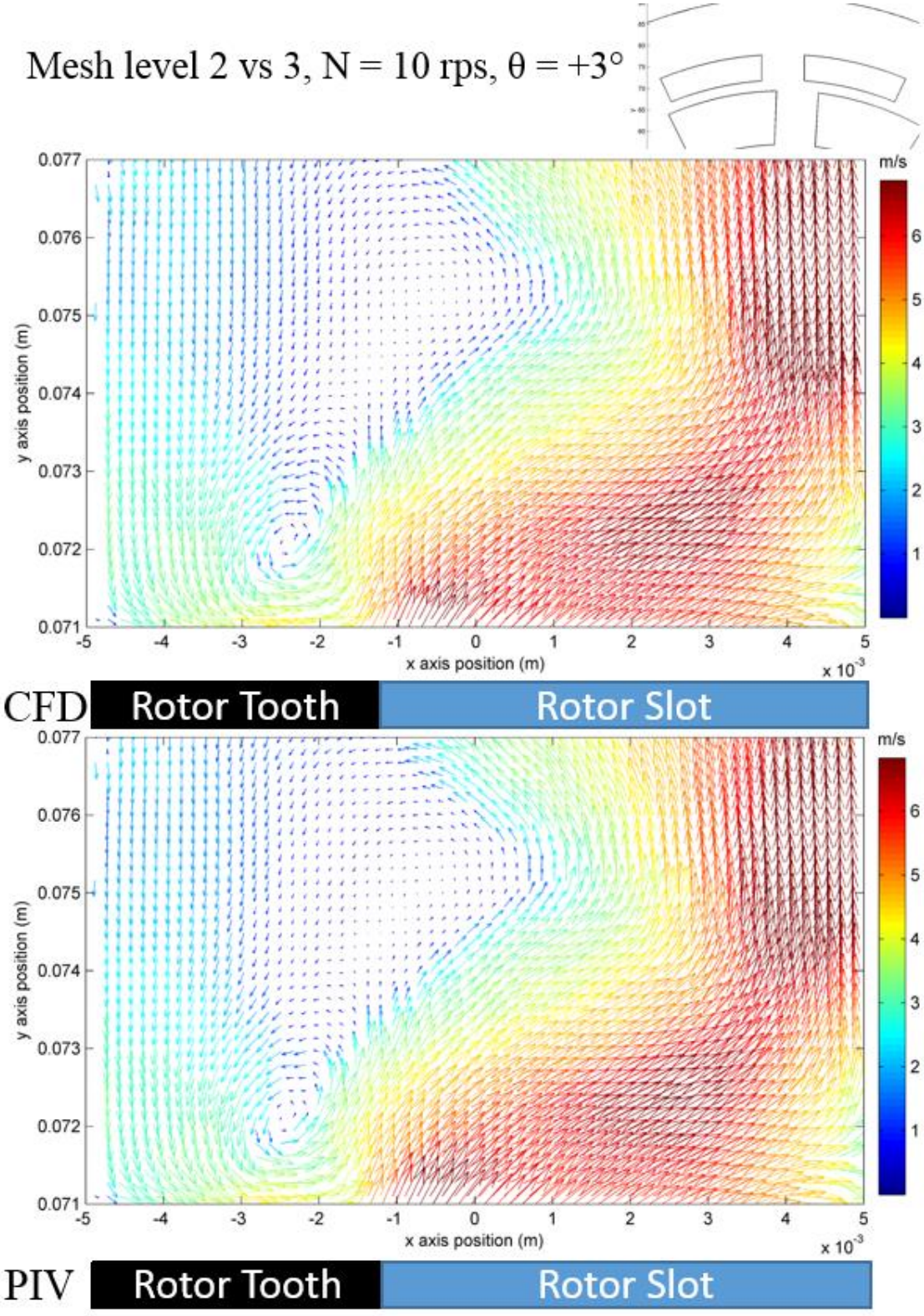

Figure 21. Mean velocity field comparison between mesh Level 2 (top) and 3 (bottom): +3° Rotor Position, 10 rps

3.2. Wall Treatment: EWT and NEWF Comparison

The near-wall modeling comparison tests were conducted in a similar fashion to the mesh independence study. The objective was to identify the wall treatment that offered the better balance between practicality and accuracy. Two level 1 models, one with the EWT and the other with the NEWF wall treatment option, were run at a rotor speed of 10 rps with otherwise identical settings. Table 7 describes how the two methods compared in terms of three calculation metrics. The statistical data provided in the table are gathered over fifteen rotor revolutions of the simulation.

Table 7. Statistics of the Wall Modeling Performance over 15 Rotor Revolutions

	NEWF	EWT
Iterations Required per Timestep	52	86
Time per Iteration	2.42 seconds	2.04 seconds
Time per Revolution	25.2 hours	35.1 hours

The results appear to support the advantages claimed for the EWT option (2.3.3 Enhanced Wall Treatment (EWT)). On average, EWT reached the time step convergence criterion in 60% of the iterations required by NEWF. However, the additional equations in EWT calculation do require a longer calculation time per iteration (approximately 19% more on average). However, even with the increased calculation time, EWT completed a revolution in approximately 28% less time than NEWF. Over the 15 revolution period, EWT and NEWF steadily completed each revolution in around 25 and 35 hours, respectively.

Even though the EWT's advantage in performance is established, it would be considered an unsuitable choice if its results were inaccurate. Therefore, the results of the two wall treatments were compared to determine whether there was a significant difference in the flow fields; if the two make different predictions, one must be more accurate than the other. The following figures report the comparisons at -6°, +1°, and +5° rotor positions.

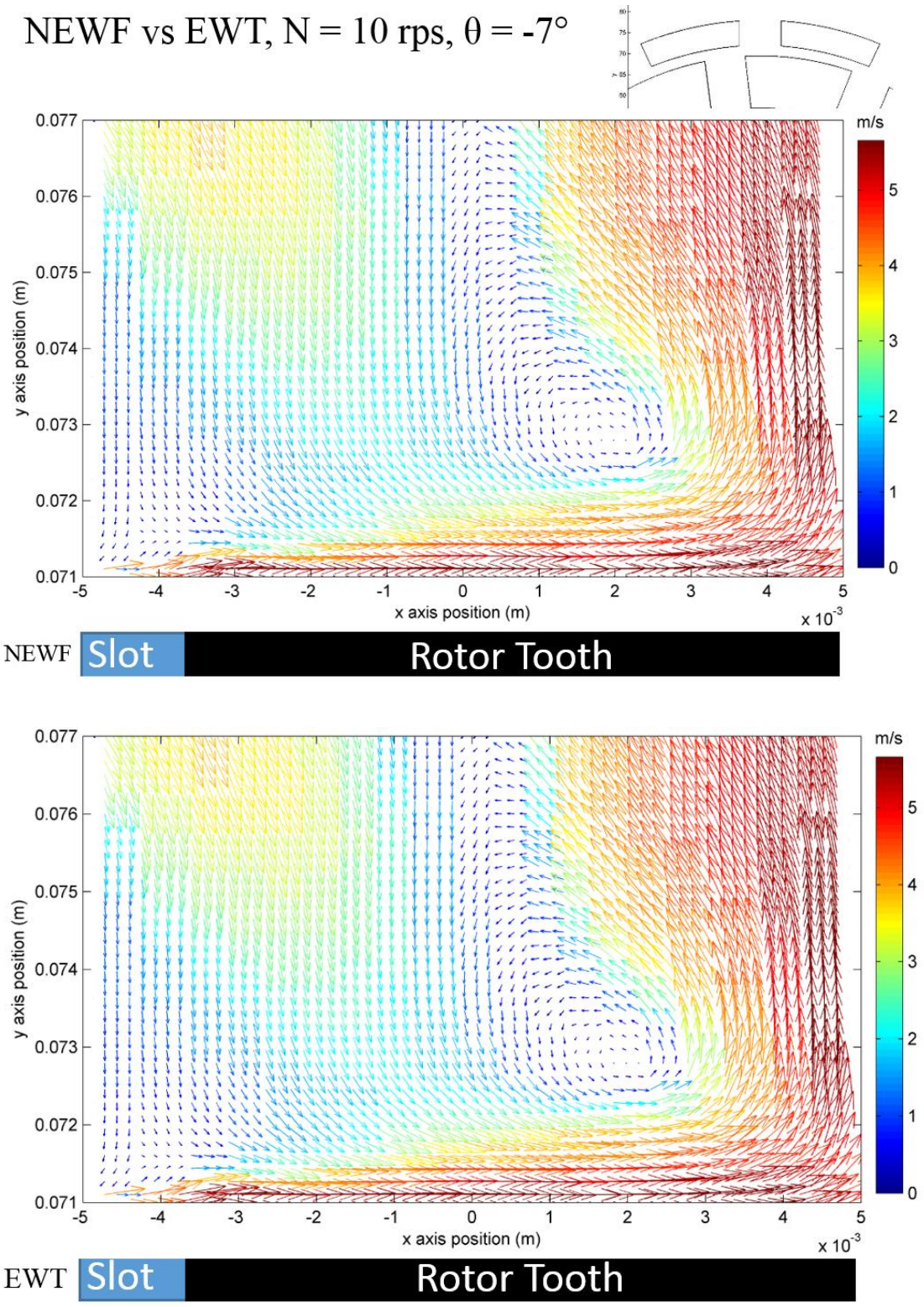

Figure 22. Mean velocity field comparison: NEWT (top) and EWF (bottom), θ = -7° rotor position, N= 10 rps, mesh level 1

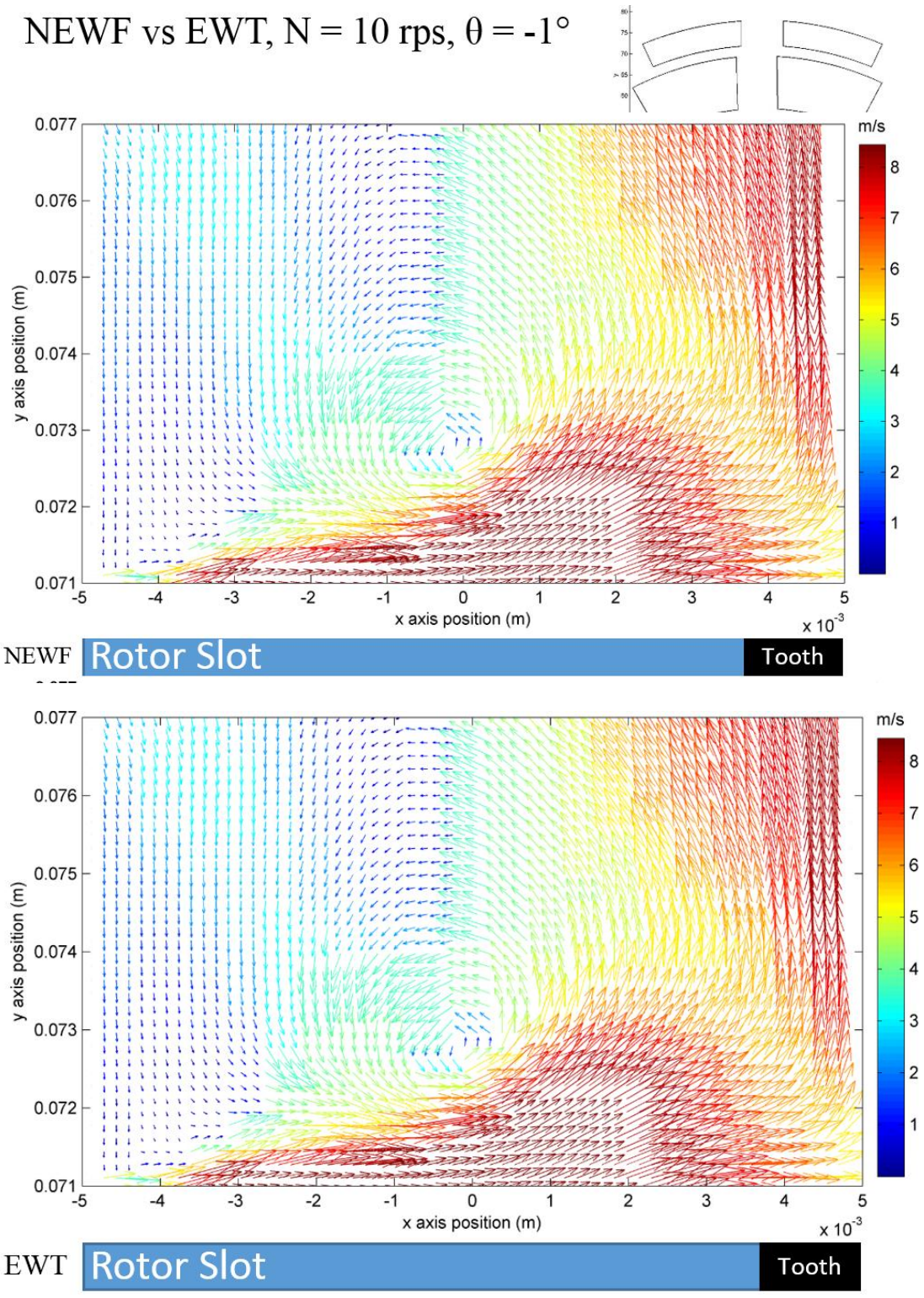

Figure 23. Mean velocity field comparison: NEWT (top) and EWF (bottom), θ = -1° rotor position, N= 10 rps, mesh level 1

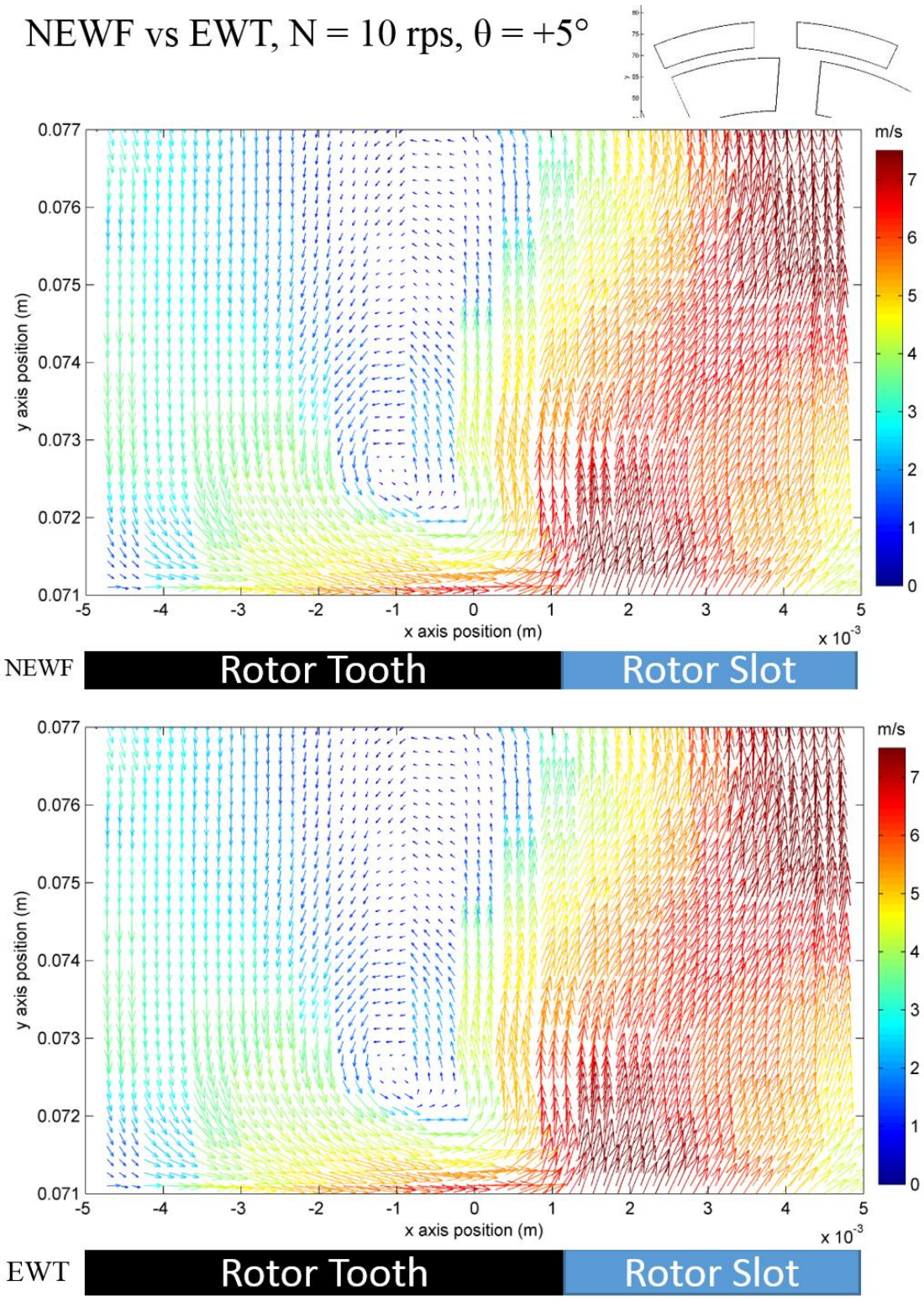

Figure 24. Mean velocity field comparison: NEWT (top) and EWF (bottom), θ = +5° rotor position, N= 10 rps, mesh level 1

The two vector fields show comparable flow patterns, especially the locations of the mixing layer vortices. In Slot 1, the difference in the magnitude of the mean velocity generated by the two wall functions averaged less than 6.8% over the whole plane. The difference originated from various regions of the field where NEWT reported stronger magnitude than EWT or vice versa. The directions of the vectors, by themselves, compared more favorably; when each vector's direction was cross compared between NEWF and EWT, the difference was determined to be less than 1%. The minimal nature of the difference in both vector directions and magnitude, it was determined that the choice of either near-wall method would not significantly affect in the CFD and PIV results comparison. The conclusion allowed us to take advantage of EWT's practical edge. As a conclusion of the preliminary studies, it was determined that level 2 mesh and EWT will be adopted for the rest of the study.

4. Comparison: CFD and PIV

The PIV data collected in the vicinity of Slot 1 at N = 10, 20, and 26 rps and at constant throughput of Q_v = 1.3 L/s, are compared to the mesh level 2 CFD simulations for rotor degree positions from -7° to +9° in 2° increments. In this chapter, representative mean velocity plots of Slot 1 at the depth of z = -0.005 m are introduced for in-depth comparison and analysis. A complete collection of the mean velocity plots are given in the appendix (Chapter 7.1) of this thesis. Originally, extending the domain of the plots and including the shear gap and rotor slot regions was considered, but doing so changed the scaling of the plots and ultimately make the flow feature and magnitude comparison more difficult between the PIV and CFD, especially with a color scaling option. The extended velocity plots without color scaling are included in Chapter 8.5.

4.1. CFD and PIV Mean Velocity Comparison

In general, the locations of vortices within the CFD simulations compare favourably with the ones captured by PIV. Figure 25 shows the mean velocity vector plot for CFD and PIV at N = 10 rps, and θ = +7° rotor position.

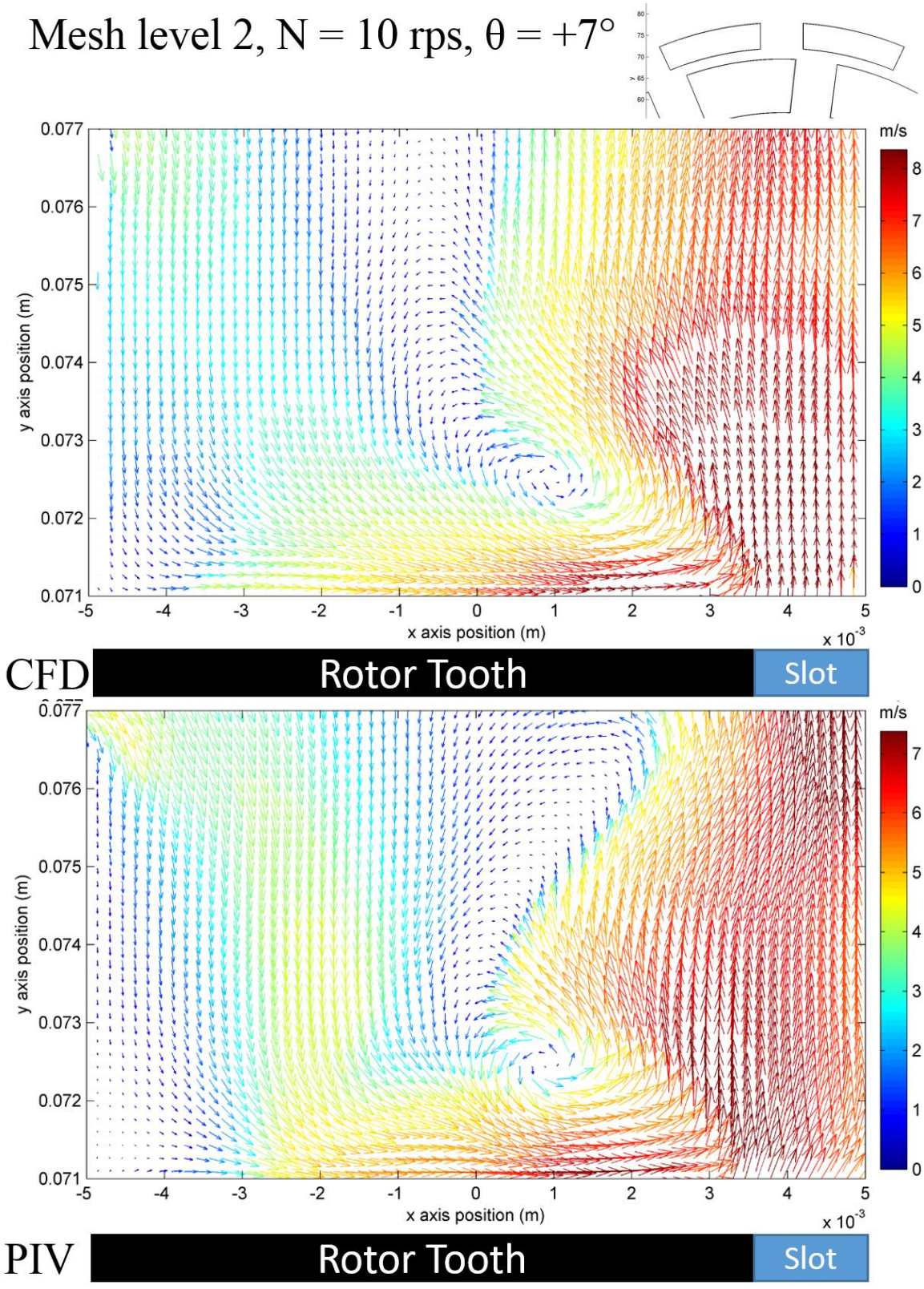

Figure 25. Mean velocity vector plots for CFD and PIV in Slot 1, N = 10rps, $\theta = +7°$

In this setting, CFD and PIV locate a rotor tooth vortex within a close proximity. The 2-D (x-y plane) distance of the two vortices is 0.181 mm, or 1.81 % of the 10mm slot width. Figure 26 shows the plots for CFD and PIV at a different rotor position ($\theta = -3°$), in which mixing layer vortices are captured.

Mesh level 2, N = 10 rps, θ = -3°

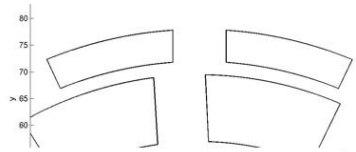

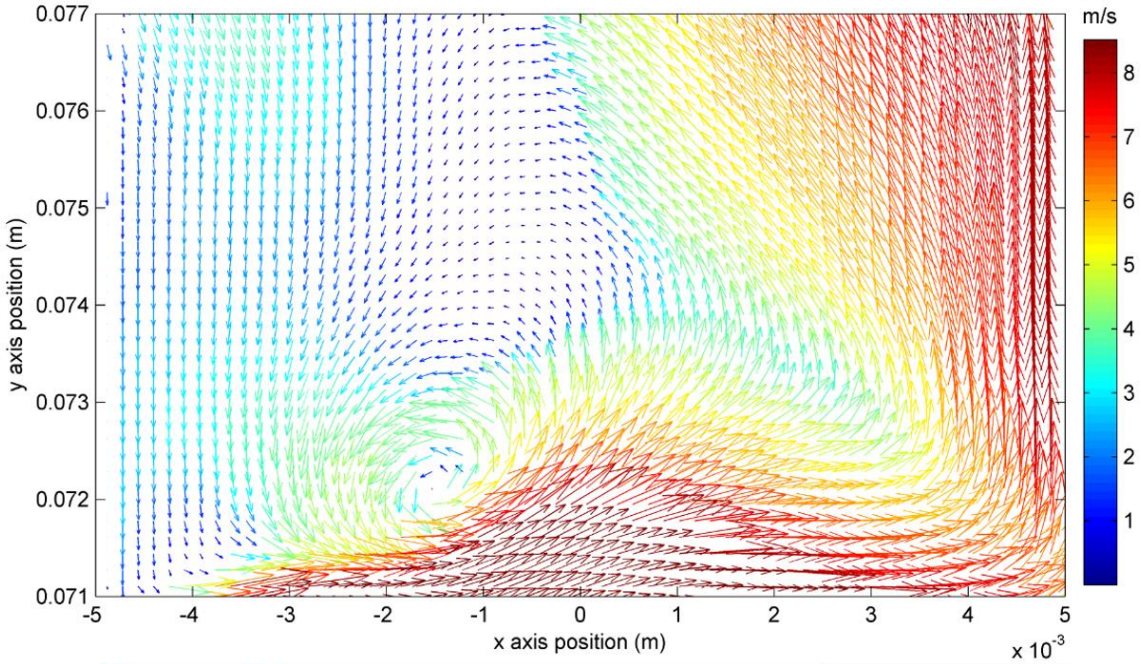

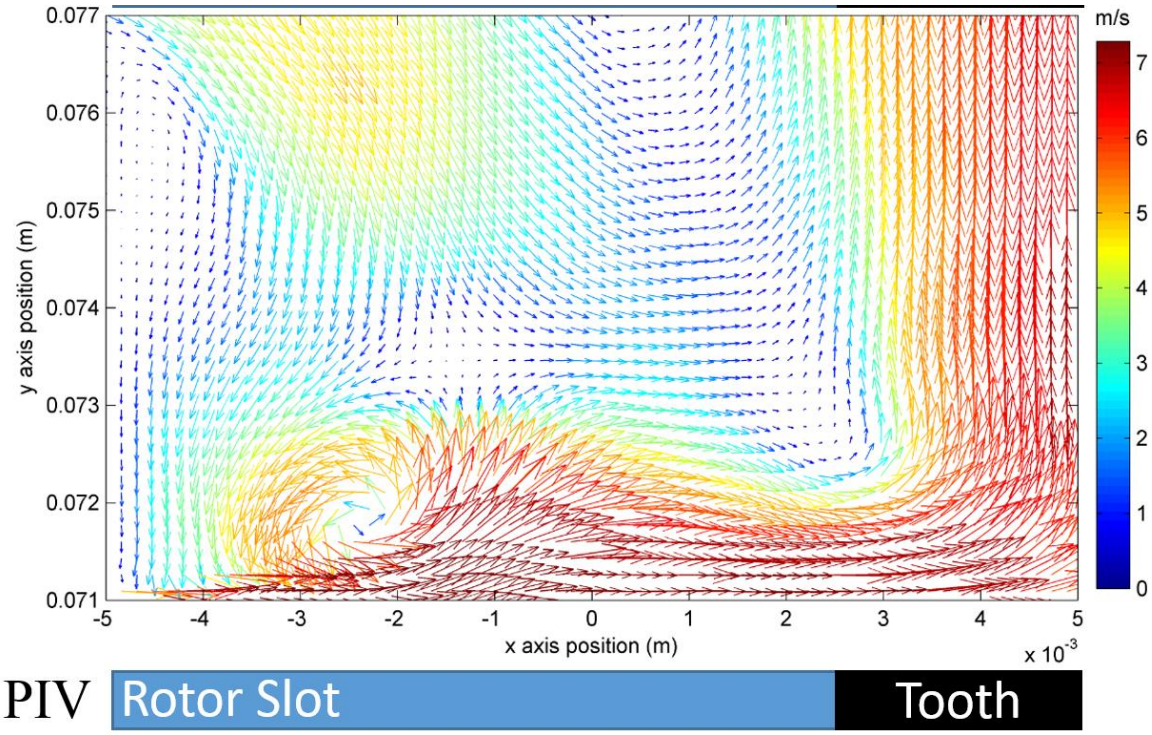

Figure 26. Mean velocity vector plots for CFD and PIV in Slot 1, N = 20rps, θ = -3°

In this case, the mixing layer vortex in CFD is located 0.831 mm away from the one in PIV, resulting in the vortex distance of 8.31% of the slot width. On average, locations of the two equivalent mixing layer or rotor tip vortices in CFD and PIV were within 7.54%, 5.50%, and 3.97% of the slot width (10mm) for the all three (N = 10, 20 and 26 rps) rotor speed scenarios, respectively. Table 8 reports the individual distance values between the vortices predicted by CFD and PIV in millimeters.

Table 8. The distance between mixing layer or rotor tooth tip vortices in CFD and PIV velocity plots in millimeters

	-7	-5	-3	-1	+1	+3	+5	+7	+9
10rps	0.481	0.871	2.11	2.18	0.741	0.0798, *m*	0.102	0.181	0.171
20rps	N/A*	0.187	0.512	1.01	0.803	0.195	0.831	0.198	0.8
26rps	N/A	*m***	0.712, *m*	0.495, *m*	0.195, *m*	0.303	N/A	0.371	0.315

*N/A: No vortex predicted by CFD nor PIV.
**m: CFD did not produce a vortex that is identified by PIV.

Overall, in all three rotor speed scenarios, CFD successfully predicted 23 out of 28 vortices in PIV (82.1%). Although the comparison in N = 26 rps recorded the lowest average vortices distance, the CFD simulation failed to predict 4 out of 10 vortices identified by PIV, as are indicated with *m* marks in Table 8. Considering such tendency is not shown in N = 10 and 20 rps settings, this may indicate the limitation of CFD or PIV methods in high rotor speed scenarios. It is worth noting that it was not possible to acquire data at N = 30 rps using PIV due to an excessive equipment vibration of the mixer and time-shift caused by the limitation in equipment responsiveness. This is the reason that N = 26 rps was chosen as the maximum rotor speed scenario. Figure 27 shows an example of a CFD plot at N = 26 rps not predicting a vortex that is

present in an equivalent PIV plot. In the figure, PIV captured a mixing layer vortex (circled in blue) which is not shown in the CFD plot. PIV also captured a vortex in recirculation region (circled in green in Figure 27) at 6 rotor positions at θ = -7, -5, -3, -1, +1, and +3 (see the appendix, Chapter 7.1, for the complete collection of velocity plots), none of which is captured by CFD. Considering that such feature was not found in the other rotor speed scenarios (N = 10 and 20 rps) of PIV data, it is questioned if some of the rotor tip and recirculation region vortices were created by the reported mechanical vibration. Further investigation on the PIV side of the study is required to evaluate the possibility.

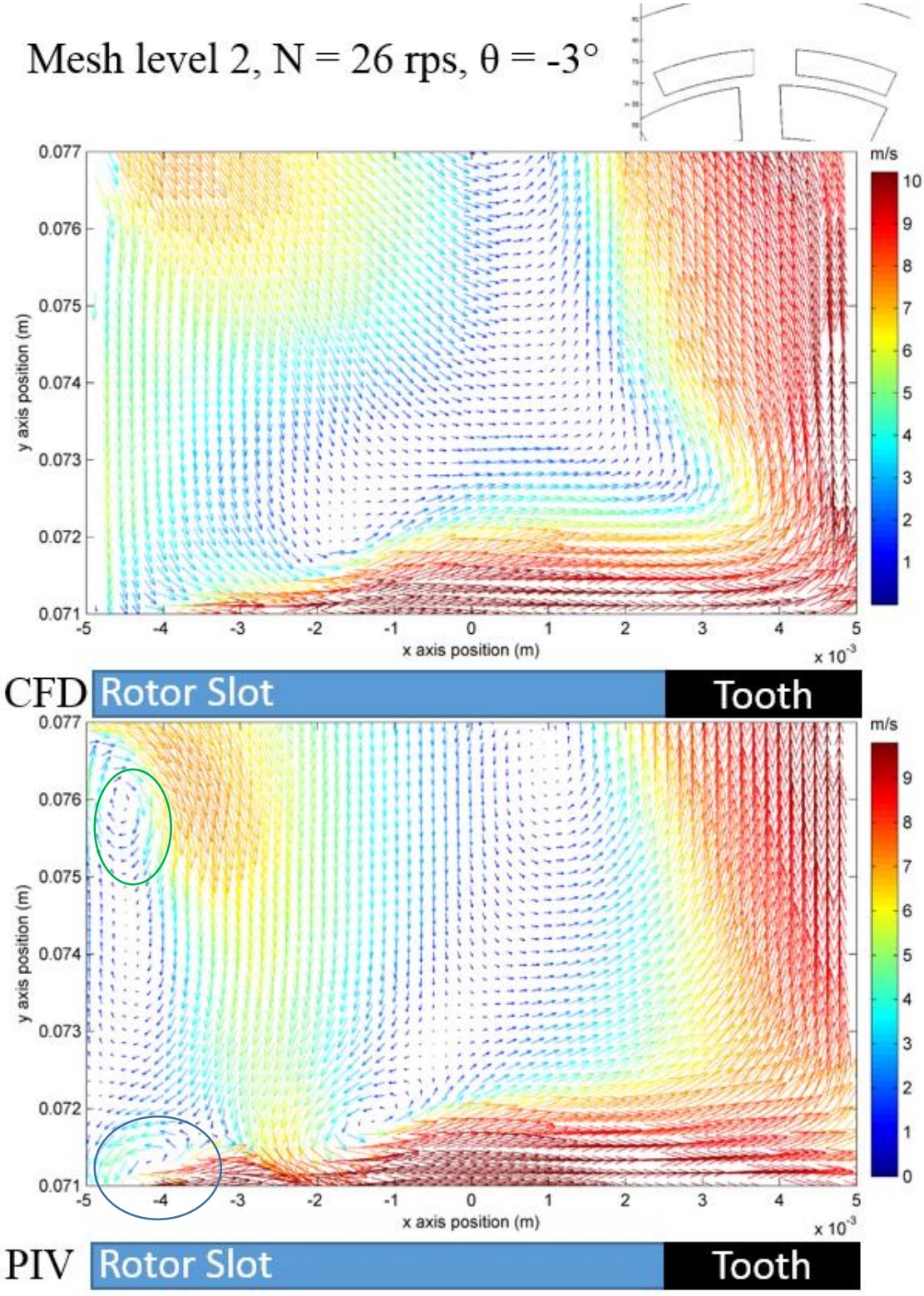

Figure 27. Mean velocity vector plots for CFD and PIV in Slot 1, N = 26 rps, θ = -3°

The vortex location is not the only aspect of poor comparison between PIV and CFD for N = 26 rps rotor speed scenario. Comparing the PIV data between N = 10 and 20 rps, it was established that the maximum velocity magnitudes in Slot 1 increase as the rotor speed increases. CFD data predicted the same tendency throughout all three rotor speed scenarios. For PIV, however, the maximum magnitude decreased from N = 20 rps to 26 rps at the rotor positions of θ = -7° and +9°. The unexpected result created a significant gap between CFD and PIV plots in maximum magnitude, as shown in Figure 28. The figure shows the mean velocity vector plots at θ = +9° rotor position. The maximum velocity magnitude for CFD is approximately 2.4 times greater than that for PIV.

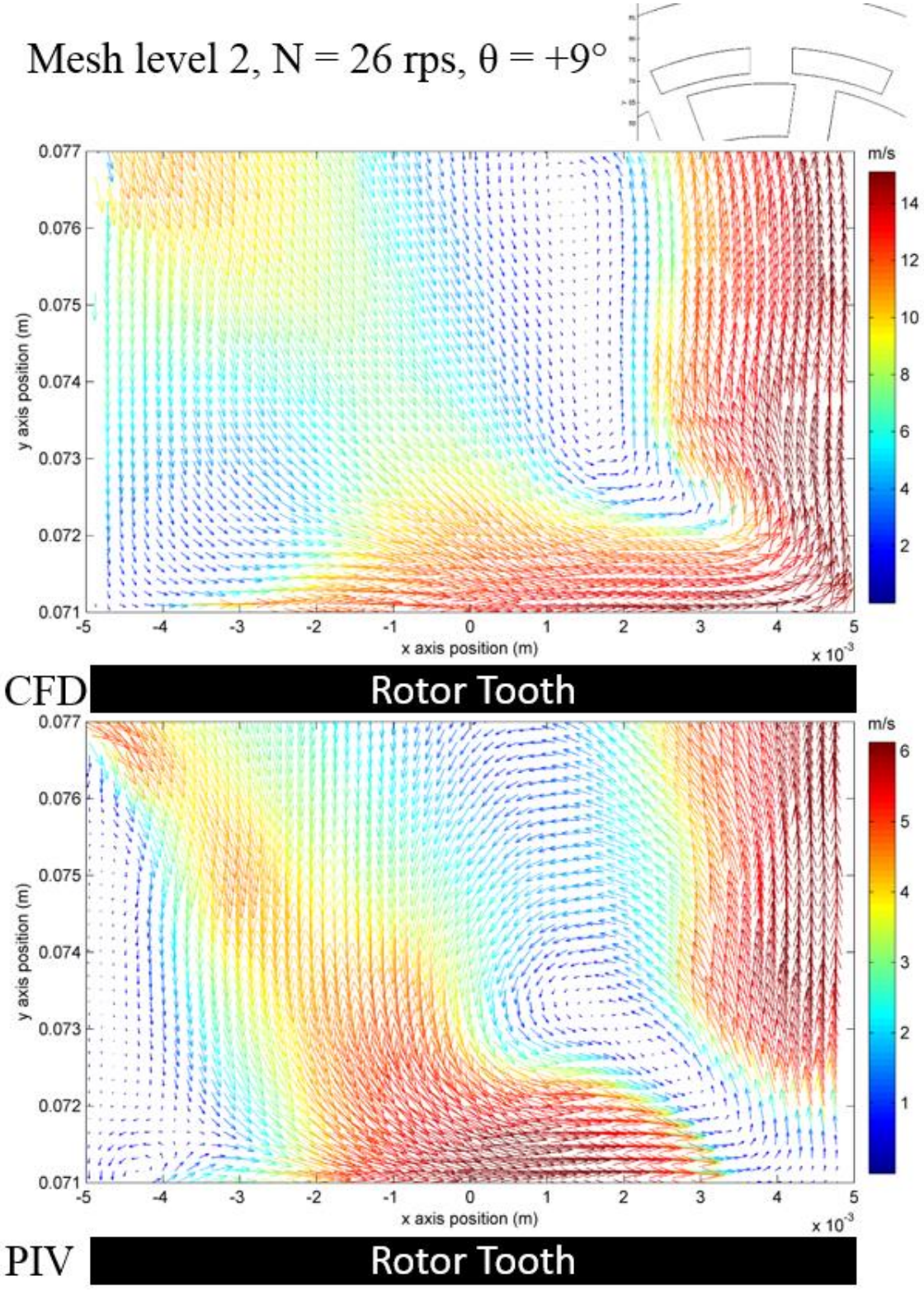

Figure 28. Mean velocity vector plots for CFD and PIV in Slot 1, N = 26 rps, θ = +9°

The difference in magnitude raised concerns and was followed up by a more profound analysis, which is reported in the following chapter.

4.1.1. Magnitude Difference Analysis

The difference in maximum velocity magnitude is also found in Figure 26 and Figure 27. In fact, the difference is consistently apparent throughout different rotor positions and rotor speed scenarios. The difference is much more pronounced towards the right side of Slot 1, from the rotor region where the fluid enters the stator slot, to the top area where the fluid exits into the volute region. This translates to higher flow rate in CFD than in PIV – the average y-velocity (radial direction) on the exit line (shown in Figure 29) of the slot for CFD is around three times greater than the one of PIV. The exit line is located at the same depth (z = -0.005 m) as the xy-plane where the mean velocity plots are generated, and the average y-velocity is measured by averaging the y-components of the vectors located on the exit line. Table 9 reports the details of average exit y-velocity comparison for N = 10, 20, and 26 rps.

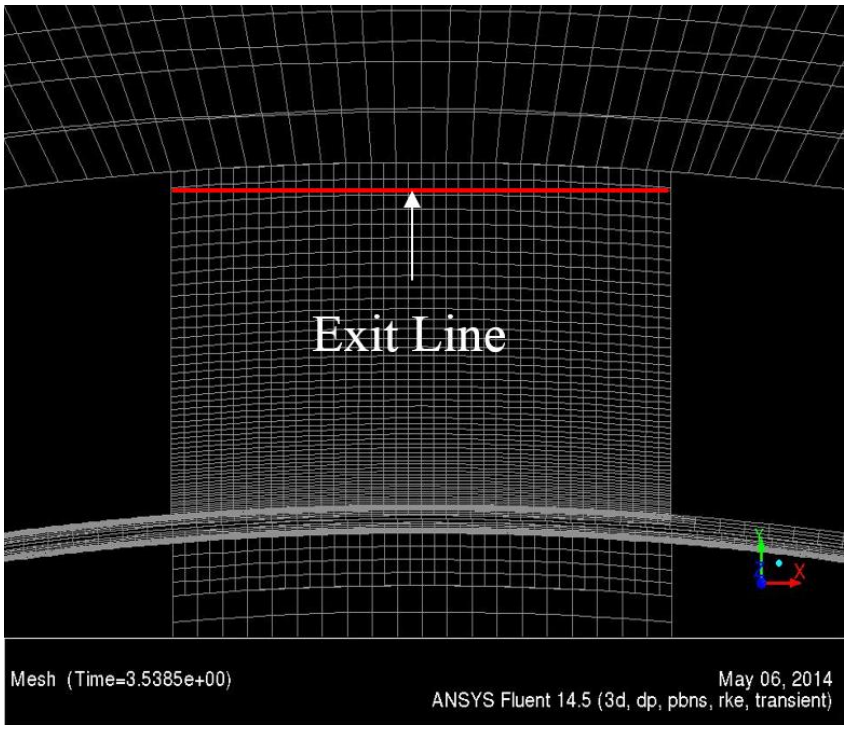

Figure 29. The exit line of Slot 1

Table 9. The Average Exit Y-Velocity Comparison for CFD and PIV

10rps, 1.3lps				
CFD		%	PIV	
Angular position	Radial Velocity (m/s)	difference	Angular position	Radial Velocity (m/s)
-7	0.676158	1086.013	-7	0.057011
-5	0.913316	759.1873	-5	0.1063
-3	1.087025	540.3683	-3	0.16975
-1	1.220076	377.338	-1	0.2556
1	1.450747	319.485	1	0.34584
3	1.719246	234.2561	3	0.51435
5	1.876122	200.218	5	0.62492
7	1.623364	148.4146	7	0.65349
9	1.030673	118.6409	9	0.4714
Average	**1.288525**	**262.5494**	**Average**	**0.355407**

20rps, 1.3lps				
CFD		%	PIV	
Angular position	Radial Velocity (m/s)	difference	Angular position	Radial Velocity (m/s)
-7	0.697459	578.3961	-7	0.1028
-5	0.763879	394.9647	-5	0.1543
-3	0.903563	427.0742	-3	0.1714
-1	1.079973	271.994	-1	0.2903
1	1.304923	304.1134	1	0.3229
3	1.473676	249.2041	3	0.422
5	1.647792	286.9327	5	0.4259
7	1.50114	275.1819	7	0.4001
9	0.926717	6464.081	9	0.0141
Average	**1.144347**	**347.0303**	**Average**	**0.255989**

26rps, 1.3lps				
CFD		%	PIV	
Angular position	Radial Velocity (m/s)	difference	Angular position	Radial Velocity (m/s)
-7	0.787217	172.6293	-7	0.28875
-5	0.846153	124.0634	-5	0.37764
-3	0.953498	103.2308	-3	0.46917
-1	1.086877	133.3806	-1	0.46571
1	1.266519	110.9037	1	0.60052
3	1.401215	130.9073	3	0.60683
5	1.562381	42.514	5	1.0963
7	1.439515	149.4438	7	0.57709
9	0.865596	744.6485	9	0.10248
Average	**1.13433**	**122.685**	**Average**	**0.509388**

Note that CFD averages exit y-velocity at ~1.2 m/s while the PIV averages at ~ 0.37 m/s over the rotation of position θ = -7° to +9°. The substantial difference in exit velocity between CFD and PIV raises concerns. Considering both models have the same set volumetric flow rate (Q_v = 1.3 L/s), such vast difference in average exit velocity is unexpected. If we assume, based on the

symmetric design of the mixer, that the Q_v is equally distributed over the 14 stator slots, Slot 1 should report an average exit radial velocity of 0.92 m/s over every 30° of rotor rotations. The CFD model's average value of ~1.2 m/s may be plausible considering the rotor and stator slots are at least partially aligned (Slot 1 is at least partially open) from -7° to +7° positions. But PIV averaged considerably lower exit velocity over the -7° to +9° rotor positions, which is bewildering because of the fact that the slot is completely closed outside of the -7° to +9° window and the Q_v will be considerably lower.

Among many possible causes of the difference, three are deemed most plausible and will be discussed in this section: velocity variation in z direction, leakage flow between the volute cover and the stator slot tooth, and mechanical vibration of the mixer at high rotation speed.

PIV data is only available in the xy-plane at one depth (z = -0.005 m), while the slot depth ranges from z = -0.002 m to -0.010 m (see Figure 2). Therefore, the CFD and PIV comparison was done in a single xy-plane. In the plane, continuous fluctuations in vortex positions are observed in both CFD and PIV. Due to the nature of a vortex, and how flows change their directions around it, even a very slight shift of its position can cause significantly different flow velocity in the area. Although the rotor movement is in the x-direction in Slot 1, shifts in vortex locations are seen in both x and y directions, and it is highly likely that the same occurred along the z-direction and created variation in the exit velocity at different depths. If the average exit velocity at one depth is lower than the average calculated from Q_v, it has to be greater than the average at other depths. According to the conservation of mass, this has to be the explanation of the PIV's low average exit velocity at z = -0.005 m. Otherwise, it raises questions if the 1.3 L/s flow rate was properly enforced for the PIV measurement.

Since the PIV data are not available at other depths, numerical data were collected from CFD to investigate how the flow in Slot 1 and the average exit y-velocity vary at different depths. An xz-plane is created into the exit line of Slot 1(Figure 29). Figure 30 shows the vector field plot of xz-plane along the exit line of Slot 1 at θ = +1° rotor position in N =10 rps setting.

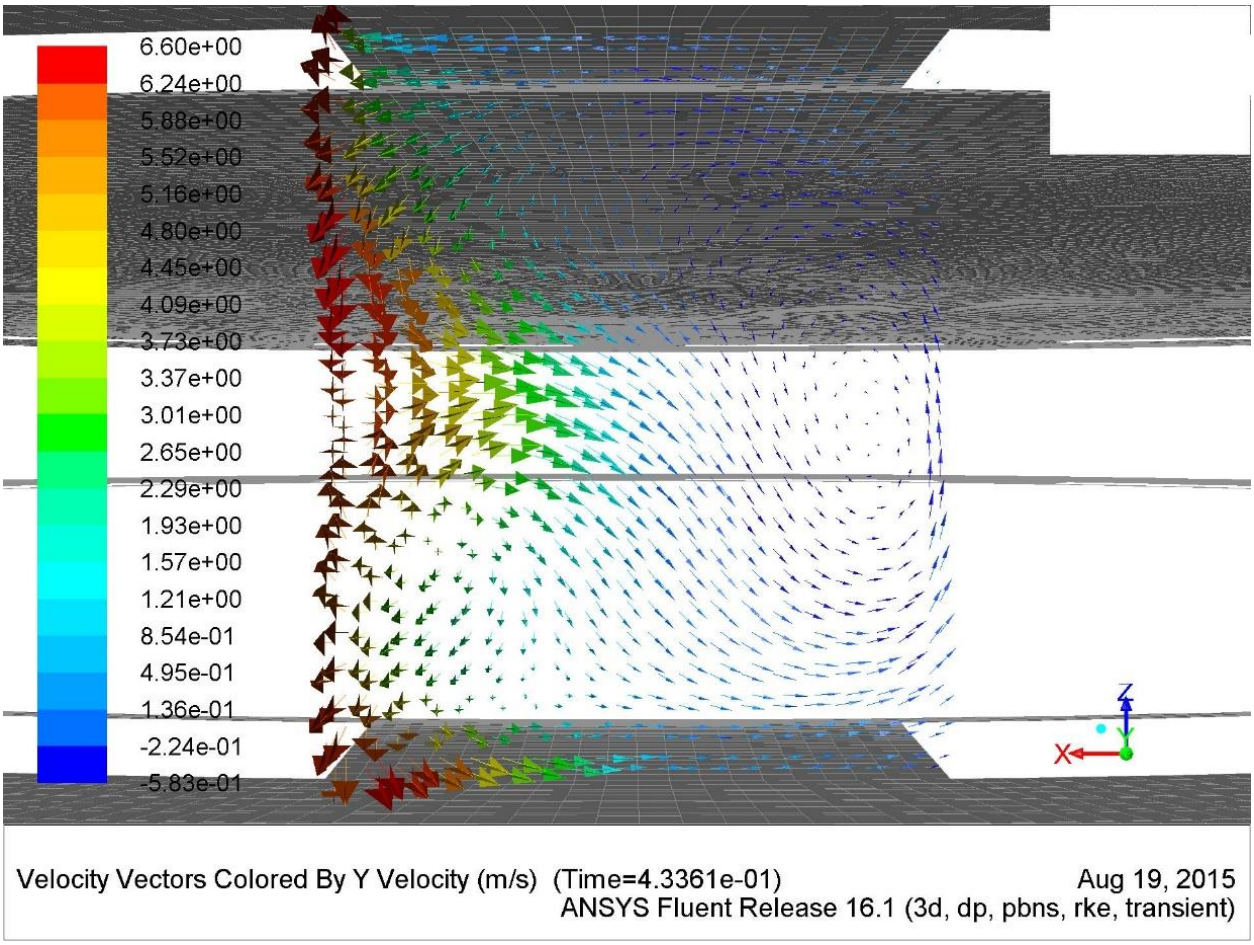

**Velocity vectors colored by y velocity magnitude.*

Figure 30. Velocity vector field in the XZ plane along the exit line of Slot 1 at θ = +1°, N =10 rps

First note how the magnitude is varying at different depths. In order to visualize the variation in the exit velocity, the vectors are colored by y-velocity (the radial element in Slot 1) magnitude. The difference is visually apparent by observing the colors. The direction of the vectors vary depending on the depth as well. The same plots are generated at each of the full 30° rotor rotation at N = 10 rps and presented in the appendix (Chapter 7.4).

*A *larger version of the same figure is presented in Appendix section. (Chapter 7.3)*

Figure 31 summarizes the 30 plots in a graph. It shows how the average exit y-velocity at different depths varies over the 30° of rotation. Note that the rotor rotation is periodic of 30 degrees – 23° is equivalent to -7°, 25° to -5°, and so on.

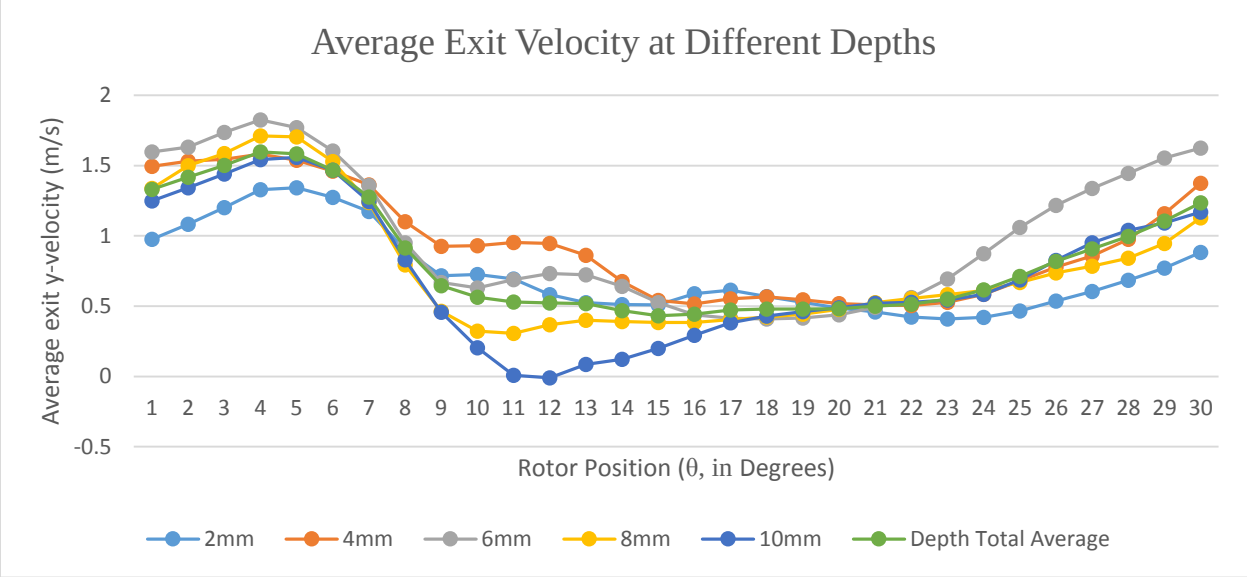

**A larger version of the same figure is presented in Appendix section. (Chapter 7.3)*

Figure 31. Average exit y-velocity at different depths

The chart clearly shows that the exit flow is significantly lower when the slot is completely closed (rotor positions θ = 10° to 20°). It is also apparent that there is a significant variation in the exit velocity at different depths. This, however, does not answer the low PIV average exit y-velocity. First, this result is gathered from CFD; it is not certain that the will be found if PIV measurements were made at different depths. Secondly, Figure 31 shows that the exit velocity at every depth fluctuates around the theoretical average exit value of 0.92 m/s over the 30 degrees of rotation. There is no depth that reports exit velocity that is consistently lower than the average

value. Therefore, the low mean exit velocity magnitude in Slot 1 seen in the PIV data are unexplainable with respect to the CFD results.

Another possible explanation of the low flow rate through the stator slot is potential flow leakage through gaps between the volute cover and the stator teeth. According to the design of the mixer, as shown in Figure 2(a), the mating between the volute cover and stator slots is supposed to be hydrodynamically sealed. However, the actual mixer can develop gaps in the region due to the manufacture craftsmanship, material imperfection or warping between the rotor teeth and the volute cover. The gaps will create leakage flow, which will lower Q_v through the stator slots. A CFD simulation revealed that the gap can significantly affect the results; when a case was run with a 0.25 mm gap between the stator and volute cover, 19% of the 1.3 L/s flow leaked through the gap, as shown in Figure 32.

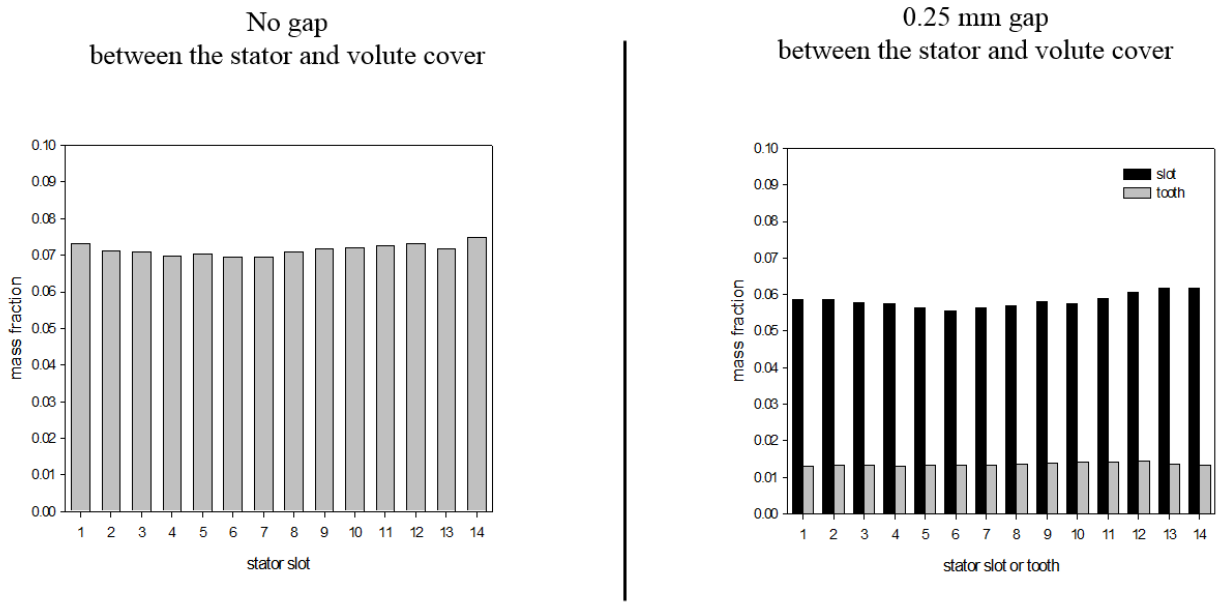

Figure 32. Volumetric flow rate with and without the 0.25mm gap between the stator and volute cover

Last potential cause is the mechanical vibration of the mixer at high rotation speed. It was already discussed in Chapter 4.1 as a cause of the poor comparison between CFD and PIV in N = 26 rps rotor speed scenario. It was explained that PIV measurement in N = 30 rps was attempted and withdrawn due to an excessive vibration of the mixer, reducing the maximum rotor speed scenario of this study to N = 26 rps. This is particularly plausible considering that the CFD and PIV comparison falters as the rotor speed increases. Both qualitative and quantitative comparisons report most favourably in N = 10 rps. It should also be pointed out that the PIV equipment caused an error and created nonsensical velocity data at $\theta = +5°$ (Appendix, Chapter 7.1).

Unfortunately, the investigation was not able to narrow down the cause of PIV's significantly lower velocity magnitude in Slot 1. It may be one of, or combinations of the three suggested explanations. To be more conclusive, additional PIV data are required for the IKA prototype in-line rotor stator mixer. Specifically, measuring the xy-plane velocity data at various other depths (from z = -0.002 m to 0.010 m), identifying gaps and leakage flow between the stator and the volute cover, and investigating the effect of mechanical vibration on the plane velocities, especially at high rotor speed scenarios will be highly helpful.

4.2. Mean Strain Rate Comparison

From the mean velocity data available in Slot 1 from CFD and PIV, the strain rate based on the velocity gradient is calculated and compared. Since the available data from PIV is 2-D, the two-by-two strain rate tensor, *S*, is calculated for the CFD and PIV as the following.

$$S = \begin{pmatrix} 2\frac{\partial u_x}{\partial x} & \frac{\partial u_x}{\partial y} + \frac{\partial u_y}{\partial x} \\ \frac{\partial u_x}{\partial y} + \frac{\partial u_y}{\partial x} & 2\frac{\partial u_y}{\partial y} \end{pmatrix}$$

Where u_x and u_y are x and y mean velocities. The diagonal cells of *S* are extension/compression rates and off-diagonal cells are shear rates. *m*, the magnitude of *S*, is calculated as the following and reported for each grid point.

$$m = \frac{1}{2}\sqrt{(S:S)}$$

Table 10 reports the average (m_{avg}), maximum (m_{max}), and minimum (m_{min}) of the double dot product in Slot 1 for the N = 10 rps scenario. Figure 33 shows CFD and PIV m_{avg} values of the table graphically.

Table 10. Statistics of D for Slot 1 in CFD and PIV (10rps)

Rotor position	-7	-5	-3	-1	1	3	5	7	9
m_{avg} (CFD)	6.59E+02	7.97E+02	9.76E+02	1.17E+03	1.48E+03	1.39E+03	1.20E+03	1.25E+03	1.43E+03
m_{avg} (PIV)	5.37E+02	6.59E+02	7.97E+02	9.76E+02	1.08E+03	1.23E+03	1.37E+03	1.24E+03	1.17E+03
m_{max} (CFD)	1.08E+04	9.17E+03	9.03E+03	1.14E+04	1.00E+04	9.30E+03	1.12E+04	1.16E+04	1.16E+04
m_{max} (PIV)	4.97E+03	1.08E+04	9.17E+03	9.03E+03	7.38E+03	6.84E+03	1.06E+04	1.32E+04	1.14E+04
m_{min} (CFD)	9.93E+00	3.11E+01	1.84E+01	5.75E+01	1.98E+01	2.95E+01	7.84E+00	2.97E+01	1.95E+01
m_{min} (PIV)	7.47E+00	9.93E+00	3.11E+01	1.84E+01	8.00E+01	8.39E+01	3.42E+01	6.20E+01	5.75E+01

*m values are in s^{-1}

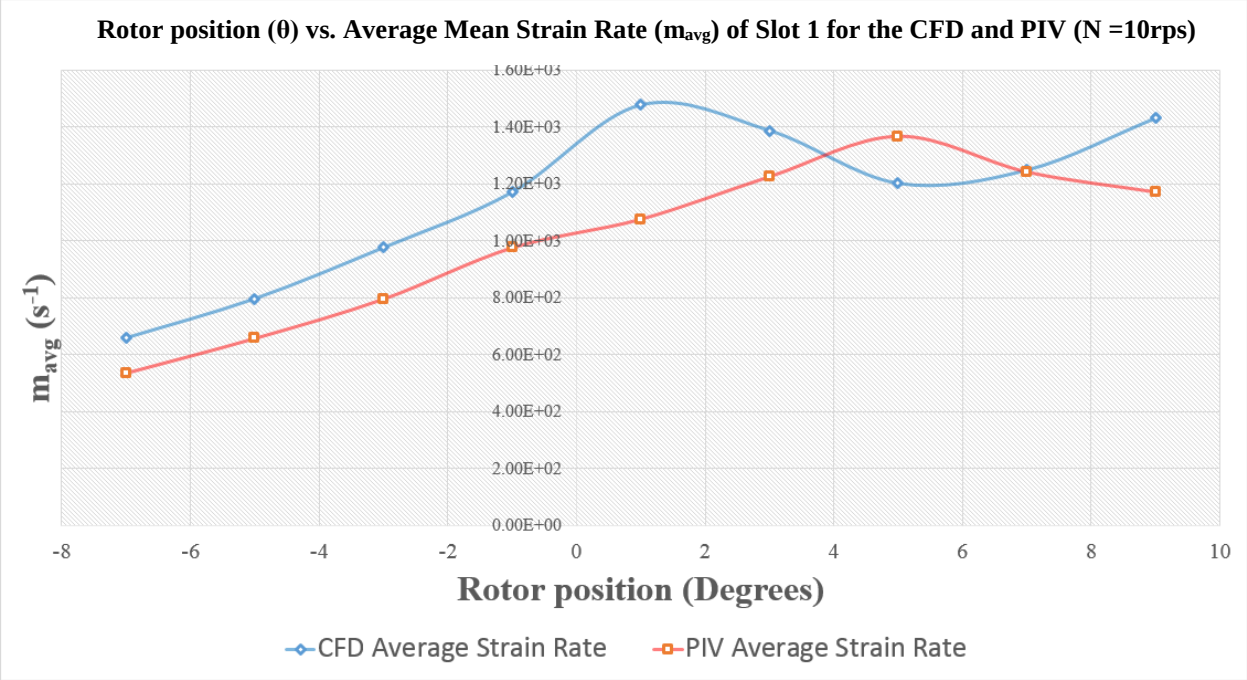

Figure 33. Rotor position vs. m_{avg} (10rps)

Note the increase in the magnitude of shear rate as the stator slot starts to open at θ = -7°. The increase continues beyond the θ = 0° position, which is when the stator slot is fully open (the slot and the rotor are completely aligned). Both CFD and PIV demonstrate the increase in a similar fashion; they both increase as the slot opens and level off past θ = 0° position. However, there is a difference in the peak m_{avg} value, which occurs at θ = +1° in CFD and θ = +5° in PIV. The m_{avg} value in CFD starts to oscillate as the slot starts to close, while that for PIV gradually increases

and starts to decrease after reaching its peak value. CFD gives a 15.7% higher m_{avg} than PIV over the 16° of rotor rotation.

The following figures and tables describe the strain rate magnitude in N = 20 and 26 rps rotor speed scenarios.

Table 11. Statistics of D for Slot 1 in CFD and PIV (N = 20rps)

Rotor position	-7	-5	-3	-1	+1	+3	+5	+7	+9
m_{avg} (CFD)	8.75E+02	9.42E+02	1.03E+03	1.30E+03	2.12E+03	2.18E+03	2.10E+03	1.82E+03	1.81E+03
m_{avg} (PIV)	7.94E+02	8.75E+02	9.42E+02	1.03E+03	1.29E+03	1.38E+03	1.40E+03	1.30E+03	1.30E+03
m_{max} (CFD)	1.04E+04	1.04E+04	1.15E+04	9.33E+03	1.94E+04	1.64E+04	1.57E+04	1.91E+04	2.18E+04
m_{max} (PIV)	5.05E+03	1.04E+04	1.04E+04	1.15E+04	1.28E+04	8.57E+03	1.16E+04	1.23E+04	9.33E+03
m_{min} (CFD)	2.85E+01	3.33E+01	2.93E+01	2.22E+01	3.58E+01	9.13E+00	1.92E+01	4.42E+01	7.01E+01
m_{min} (PIV)	4.54E+01	2.85E+01	3.33E+01	2.93E+01	1.50E+01	2.19E+01	1.70E+01	3.60E+01	2.22E+01

*m values are in s^{-1}

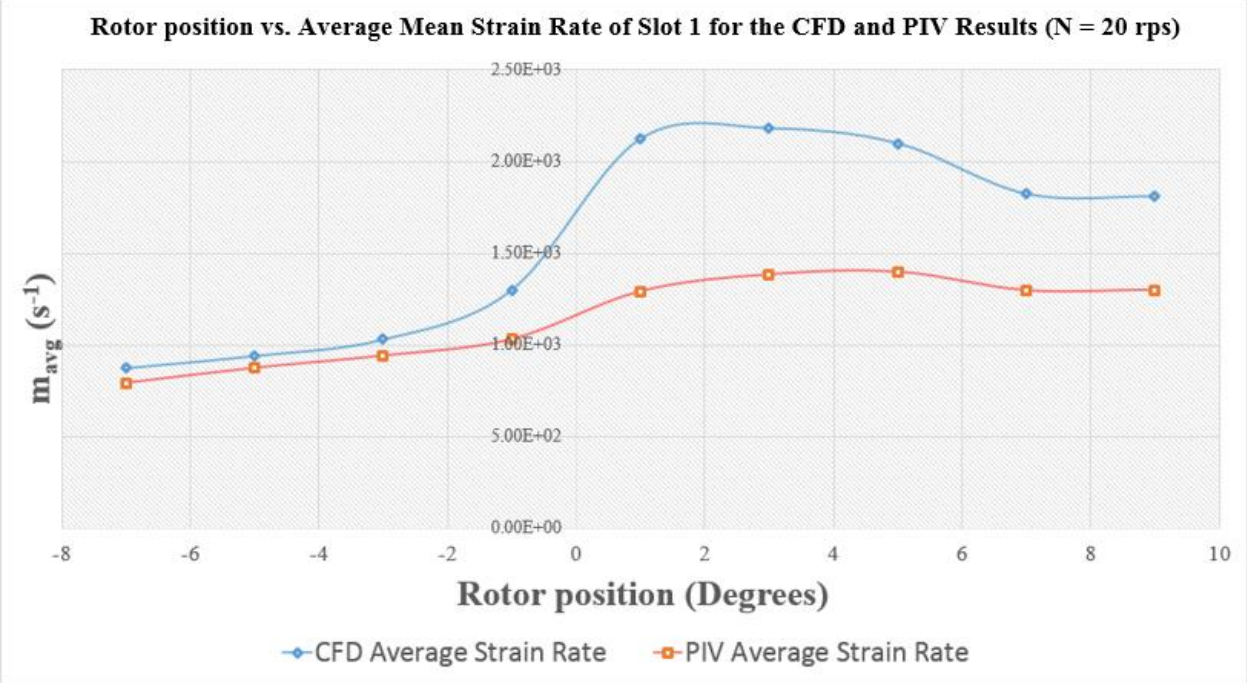

Figure 34. Rotor position vs. m_{avg} (N = 20 rps)

Table 12. Statistics of D for Slot 1 in CFD and PIV (N = 26 rps)

Rotor position	-7	-5	-3	-1	+1	+3	+7	+9
m_{avg} (CFD)	8.75E+02	9.42E+02	1.03E+03	1.30E+03	2.12E+03	2.18E+03	1.82E+03	1.81E+03
m_{avg} (PIV)	7.94E+02	8.75E+02	9.42E+02	1.03E+03	1.29E+03	1.38E+03	1.30E+03	1.30E+03
m_{max} (CFD)	1.04E+04	1.04E+04	1.15E+04	9.33E+03	1.94E+04	1.64E+04	1.91E+04	2.18E+04
m_{max} (PIV)	5.05E+03	1.04E+04	1.04E+04	1.15E+04	1.28E+04	8.57E+03	1.23E+04	9.33E+03
m_{min} (CFD)	2.85E+01	3.33E+01	2.93E+01	2.22E+01	3.58E+01	9.13E+00	4.42E+01	7.01E+01
m_{min} (PIV)	4.54E+01	2.85E+01	3.33E+01	2.93E+01	1.50E+01	2.19E+01	3.60E+01	2.22E+01

*m values are in s^{-1}. **rotor position +5 is omitted due to the error in PIV data.

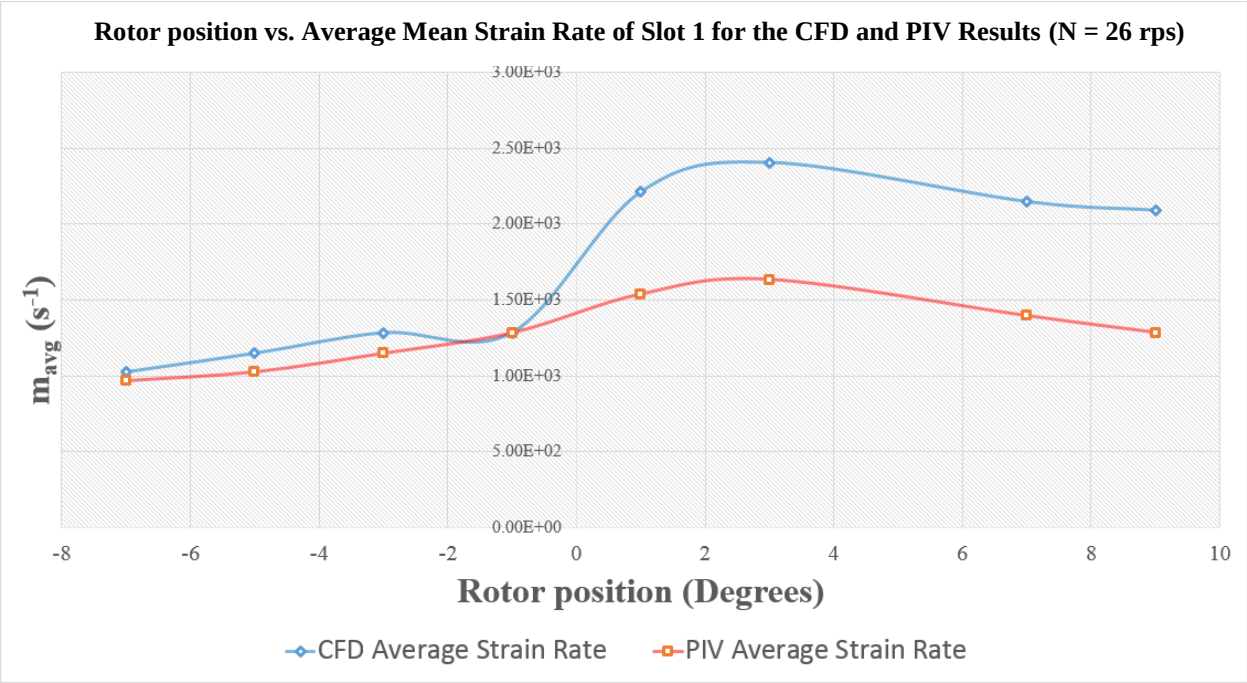

Figure 35. Rotor position vs. m_{avg} (N = 26 rps)

Compared to the values for N = 10 rps, the higher rotor speeds in N = 20 and 26 rps scenarios create higher m_{avg} for both CFD and PIV. CFD shows a significant increase in m values, 37.39% overall, as the rotor speed is doubled from N = 10 rps to 20 rps. The increase is especially evident at the rotor positions higher than 0°. For instance, the m_{avg} more than doubles over a mere 4° of rotation from -1° to +3°. The strain rate magnitude in PIV, however, reacts to the change in rotor speed in a less dynamic fashion. The m_{avg} value only increases by 9.12%

when the rotor speed doubles from N = 10 to 20 rps. Furthermore, the overall behavior shown in Figure 34 is similar to that for N = 10 rps, but is less dramatic; the PIV data show variation in the average strain rate magnitude over rotor positions at higher rotor speed.

The detailed velocity strain rate magnitude data of Slot 1 were analyzed to determine the cause of the difference in strain rate between CFD and PIV. The major contribution was from the stator slot radial jet (Figure 8) in the upper-right region of the slot. It was determined that both the velocity and strain rate data deviates as the rotation velocity increases and rotor positions increase beyond θ = 0°. This coincides with the rotor positions where the m_{avg} is critically different between CFD and PIV. Figure 36 and Figure 37 display and compare the mean velocity vector plots for level 2 mesh CFD and PIV at N = 20 rps, θ = +3° . We will focus on the upper-right region, which is marked with the red rectangle in the figures.

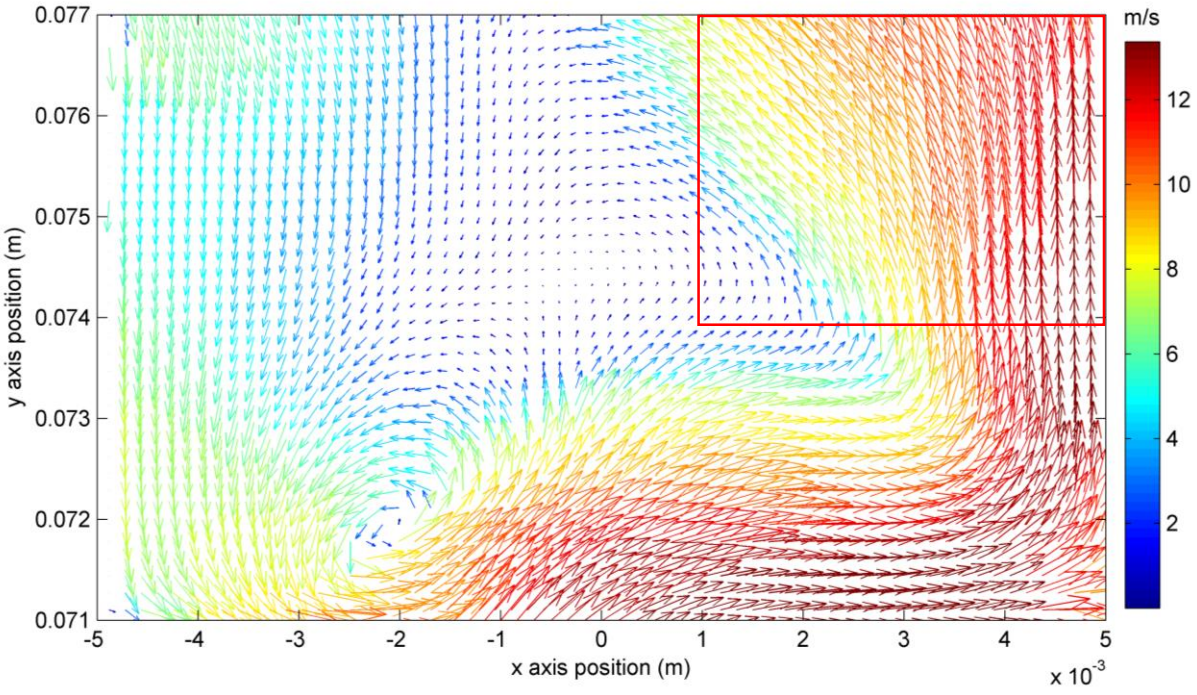

Figure 36. Flow comparison in upper-right region of Slot 1 at N = 20 rps, θ = +3° (CFD, mesh level 2)

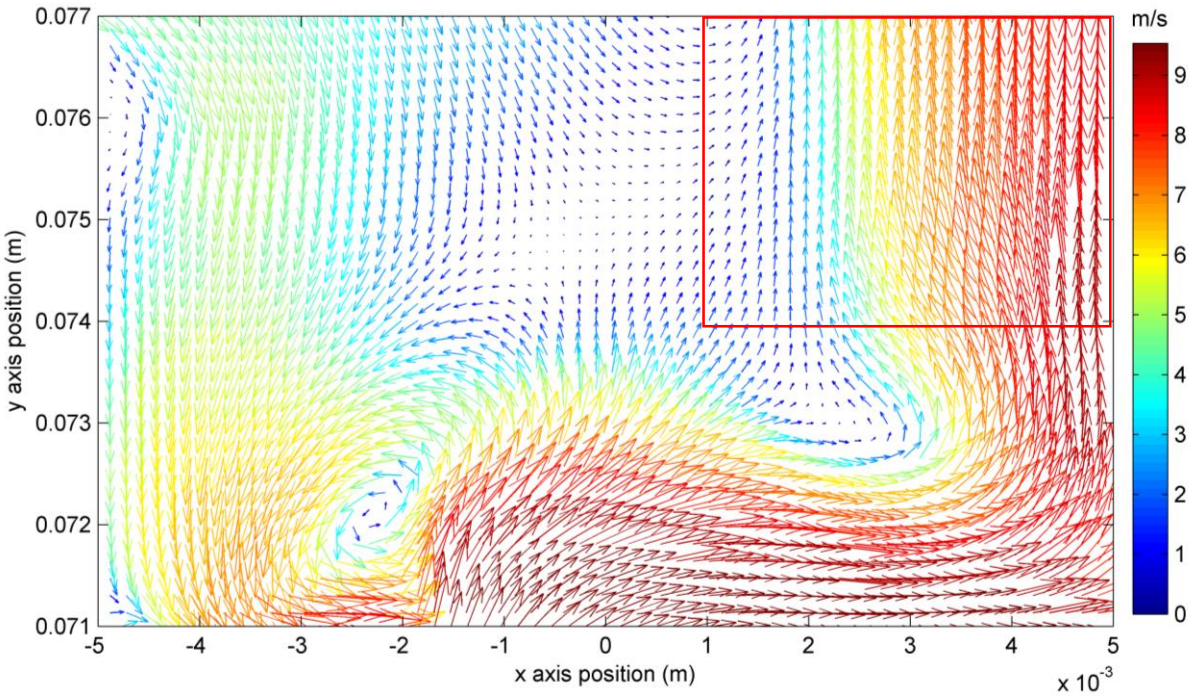

Figure 37. Flow comparison in upper-right region of Slot 1 at N = 20 rps, θ = +3° (PIV)

For the CFD results, as the rotor moves past the θ = 0° position, the flow in the upper-right region start to create lateral movement towards the negative x direction caused by the rotor rotation. In PIV, however, the flow in the region maintains to be mainly longitudinal in positive y direction, and lateral contribution to the flow remains insignificant.

The difference in vector directions in the upper-right region, along with the difference in overall magnitude (Chapter 4.1.1) contributes to the strain rate difference. Figure 38 summarizes the comparison between strain rate magnitude values of CFD and PIV. It shows the difference in magnitude and the % difference.

Rotor position (θ)	-7°	-5°	-3°	-1°	+1°	+3°	+5°	+7°	+9°
10rps CFD (1/s)	6.59E+02	7.97E+02	9.76E+02	1.17E+03	1.48E+03	1.39E+03	1.20E+03	1.25E+03	1.43E+03
10rps PIV (1/s)	5.37E+02	6.59E+02	7.97E+02	9.76E+02	1.08E+03	1.23E+03	1.37E+03	1.24E+03	1.17E+03
Magnitude difference (1/s)	1.21E+02	1.38E+02	1.80E+02	1.95E+02	4.01E+02	1.62E+02	1.65E+02	7.19E+00	2.60E+02
% difference	18.44	17.29	18.41	16.64	27.17	11.66	13.73	0.58	18.18
20rps CFD (1/s)	8.75E+02	9.42E+02	1.03E+03	1.30E+03	2.12E+03	2.18E+03	2.10E+03	1.82E+03	1.81E+03
20rps PIV (1/s)	7.94E+02	8.75E+02	9.42E+02	1.03E+03	1.29E+03	1.38E+03	1.40E+03	1.30E+03	1.30E+03
Magnitude difference (1/s)	8.15E+01	6.64E+01	8.94E+01	2.69E+02	8.31E+02	7.97E+02	7.01E+02	5.27E+02	5.09E+02
% difference	9.31	7.06	8.67	20.70	39.16	36.56	33.39	28.88	28.13
26rps CFD(1/s)	1.02E+03	1.15E+03	1.28E+03	1.28E+03	2.21E+03	2.40E+03	2.38E+03	2.15E+03	2.09E+03
26rps PIV(1/s)	9.65E+02	1.02E+03	1.15E+03	1.28E+03	1.54E+03	1.63E+03	N/A	1.39E+03	1.28E+03
Magnitude difference (1/s)	5.83E+01	1.23E+02	1.35E+02	1.80E+00	6.74E+02	7.71E+02	N/A	7.52E+02	8.06E+02
% difference	5.70	10.73	10.57	0.14	30.48	32.07	N/A	35.05	38.57

*the PIV data in θ = +5 rotor position, N = 26 rps is not available due to data corruption

Figure 38. Summary of strain rate magnitude in PIV and CFD

The % difference in strain rate magnitude clearly shows that the difference is higher when the rotor is in positive angular position and as the rotor speed increase from N = 10 to 26 rps. These are the same comparison characteristics that were observed and analyzed in CFD and PIV mean velocity comparison (Chapter 4.1.1).

5. Conclusion and Suggestion for Future Work

The main goal of this study was to further develop the CFD simulation of an IKA prototype in-line rotor stator mixer, and to compare its predictions to experimental mean velocity data acquired via 2-D PIV method. Both CFD and PIV data were collected in one of the stator slots (Slot 1, see Figure 2), for the operating conditions N = 10, 20, and 26 rps and Q_v = 1.3 L/s. The CFD simulations were run using the realizable k-ϵ turbulence model and a fully transient sliding mesh technique (Chapter 2).

Before the final CFD simulations were run, two preliminary studies were completed for the choices of mesh density and wall treatment. The following list summarizes the findings and conclusions of the mesh independence study (Chapter 3.1):

- The mesh levels were designed to minimize the computational cost without loss of accuracy in the final results.
- Three mesh levels 1, 2, and 3 were prepared, in the order of increasing mesh density.
- Mesh level 1,2, and 3, with 2.08, 6.66, and 15.9 million cells, take 22, 90, and 290 hours of computation time for one revolution, respectively, for a machine with 16 cores of Intel Xeon E5520 (Chapter 2.5)
- Mesh level 1 was determined to be too coarse to produce results in comparable grid density as the PIV data.
- The difference in results for mesh levels 2 and 3 indicated that mesh level 2 had better balance between accuracy and practicality (computational expense).

- Mesh level 3 only has increased mesh density in the shear gap region, which was a decision made due to the computational resource limitation. Creating another mesh level (e.g., mesh level 4), with increased mesh density in Slot 1, is suggested as a future project as it can possibly return more accurate CFD results.

After the mesh independence study, two wall functions of interest, Enhanced Wall Treatment (EWT) and Non-Equilibrium Wall Function (NEWF), were compared in accuracy and performance. From the comparison, the following conclusions were drawn (Chapter 3.2):

- EWT, being more computationally expensive, took longer time (2.42s) compared to NEWF (2.04s) per iteration on average.
- EWT reached convergence more efficiently. EWT required only ~52 iterations while NEWF took ~86 iterations for an advancement in time.
- The two methods produced minimal difference in the results (<1% in flow pattern, Figure 22, Figure 23).
- EWT, with the advantage in computational cost, was adopted for the final CFD simulation.

After the preliminary studies were completed, RANS CFD simulations of IKA prototype mixer at the PIV experimental conditions were run using the level 2 mesh and EWT. The CFD and PIV data were then compared. The following are the conclusions for the CFD to PIV comparison (Chapter 4):

- From the CFD and PIV velocity data, mean velocity vector plots (Chapter 4.1) and mean strain rates (Chapter 4.2) in Slot 1 were prepared and compared.

- In the mean velocity vector plots, two types of vortices were observed: a mixing layer vortex (Figure 6) and a rotor tip vortex (Figure 7). CFD and PIV results compare favorably with respect to the rotor tooth and mixing layer vortex locations at N = 10 and 20 rps. However, CFD fails to identify 4 out of 10 vortices that are captured in the PIV results at N = 26 rps. Overall, in all three rotor speed scenarios, CFD successfully predicted 23 out of 28 vortices in PIV (82.1%).

- The locations of the vortices that are identified both by CFD and PIV are well-matched. The center locations of the vortices predicted by CFD and PIV were, on average, 7.54%, 5.50%, and 3.97% of the slot width (10mm) apart from each other for the 10, 20, and 26 rps rotor speed scenarios, respectively.

- In general, CFD reported greater velocity magnitude in Slot 1 than PIV. The difference is especially apparent near the stator slot exit line (Figure 29). Over N = 10, 20, and 26 rps scenarios, PIV reported an average exit line y-velocity of 0.37m/s, while CFD did 1.2m/s (Table 9). This was concerning because both CFD and PIV data are collected for the same volumetric inlet flow rate (Q_v = 1.3 L/s) setting. From the Q_v, an average radial velocity at a stator exit was calculated to be 0.92m/s over the 30° period of rotor rotation. The PIV data are available from rotor position -7 to +9, during which the slot is at least partially open. It would be expected that the average output velocity to be greater than the average of 0.92 m/s over the period. In that sense, the CFD exit line y-velocity seemed plausible, but the PIV low exit line velocity required further analysis.

- To understand the significant difference in exit line y-velocity of Slot 1 at z = -0.005 m depth between CFD and PIV, three possible causes were suggested and discussed: velocity variation in the z direction (slot depth), leakage flow between the volute cover and the stator slot tooth, and mechanical vibration of the mixer at high rotation speed. (Chapter 4.1.1)

- With the PIV data only available at one depth (z = -0.005 m), the Slot 1 plots were generated in the xy-plane and the flow profile variation in the z-direction was not closely monitored. With the stator slot walls at z = -0.002 m and z = -0.010 m, it was highly likely that the flow varies in z-direction as well. If true, this would explain the low exit line y-velocity in PIV at z = -0.005 m. To validate the hypothesis, exit line y-velocity data at multiple depths were collected from CFD. The data did reveal that the exit line y-velocity does vary significantly with the depth. However, the velocity fluctuated above and below the predicted average value of 0.92m/s at all depths – there was no depth at which the exit velocity was uniformly lower, especially while the slot was open (θ = -7° to +7°). From that aspect, this hypothesis does not fully explain the lower exit velocity at z = -0.005 m depth in PIV because it is constantly lower than the average value by a significant margin.

- Another potential reason is a leakage flow through gaps between the volute cover and the stator teeth. The gaps can develop from the manufacturing process, material imperfection or warping during mixer operation. Even a small gap can cause a significant leakage; a CFD simulation was ran with a 0.25 mm gap between the stator and volute cover, and 19% of the inlet flow rate passed through the gap (Figure 32).

- The last potential cause discussed was mechanical vibration of the mixer. It was reported that at N = 30 rps rotor speed, the mixer developed a severe vibration, which was the reason the maximum rotor speed for PIV was limited at N = 26 rps. It is possible that the PIV measurements were still affected by the vibration at N = 26 rps setting. If true, this explains why CFD and PIV made poorer comparison in higher rotor speed scenarios.

- There can be numerous different factors that can cause differences between the data for CFD and PIV. The three suggested causes, however, are deemed to be an appropriate starting place for the future work to improve the comparison. It is suggested that the following additional PIV data be acquired for the IKA prototype in-line rotor stator mixer: measurement of the xy-plane velocity at various depths (from z = 0 to -0.012 m), close investigation of potential leakage flow between the stator teeth and the volute cover, and diagnosis of the impact of mechanical vibration at high rotor speeds.

6. Nomenclature

N	Rotor rotation speed
Q_v	Inlet volumetric flow rate
θ	Rotor angular position
y_+	Non-dimensional wall distance
u_*	Friction velocity
ν	Kinematic viscosity
$\underline{d}$	Difference vector
$\%d_{avg}$	Average percent difference
S	Strain rate tensor
m	Magnitude of strain rate tensor
P	Pressure

7. Appendix

7.1. CFD Mesh Level 2 vs. PIV XY-Plane Velocity Vector Plots of Slot 1

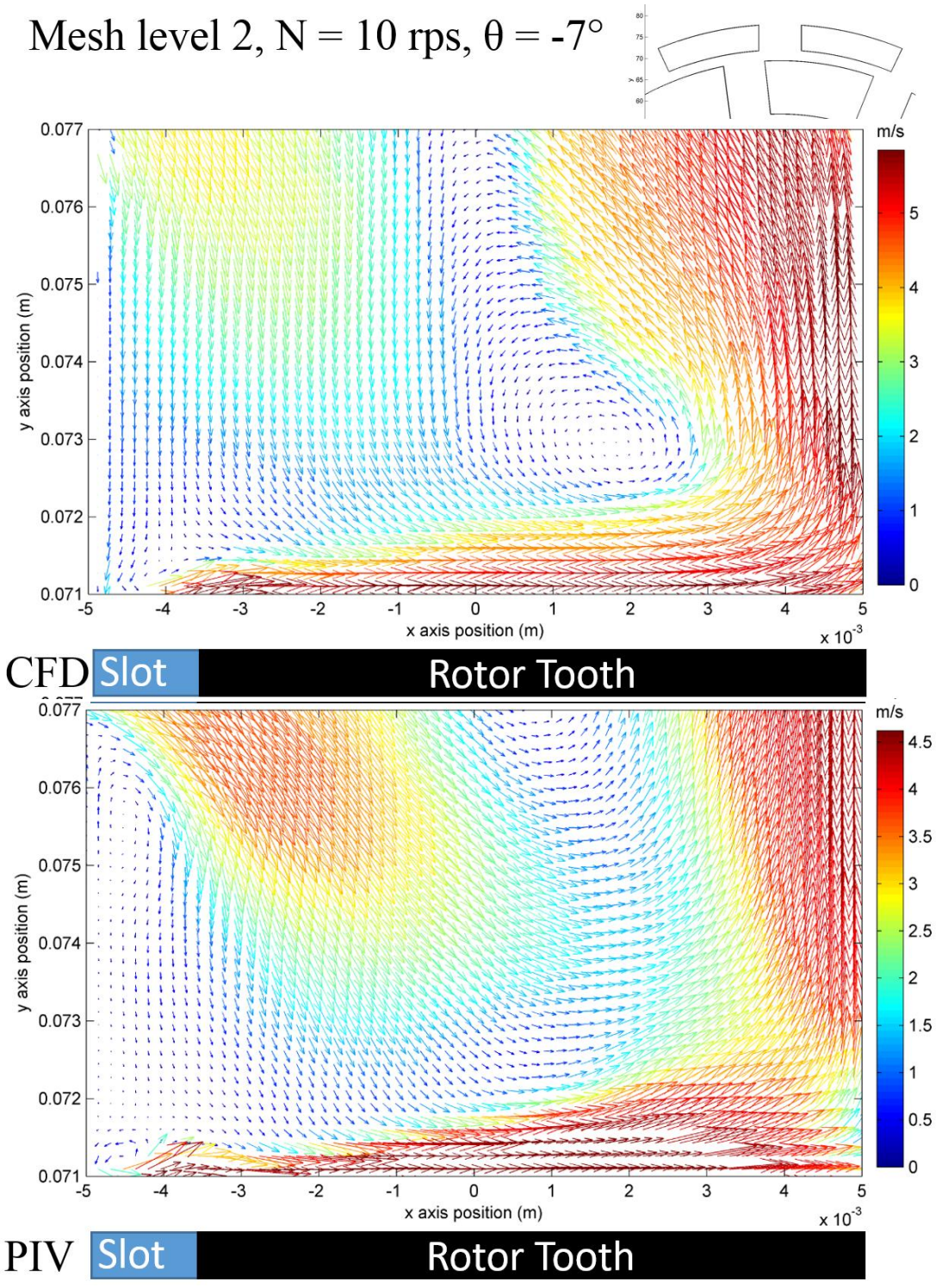

Mesh level 2, N = 10 rps, θ = -5°

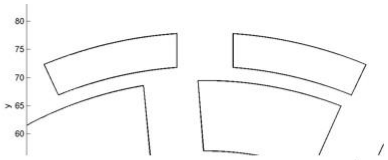

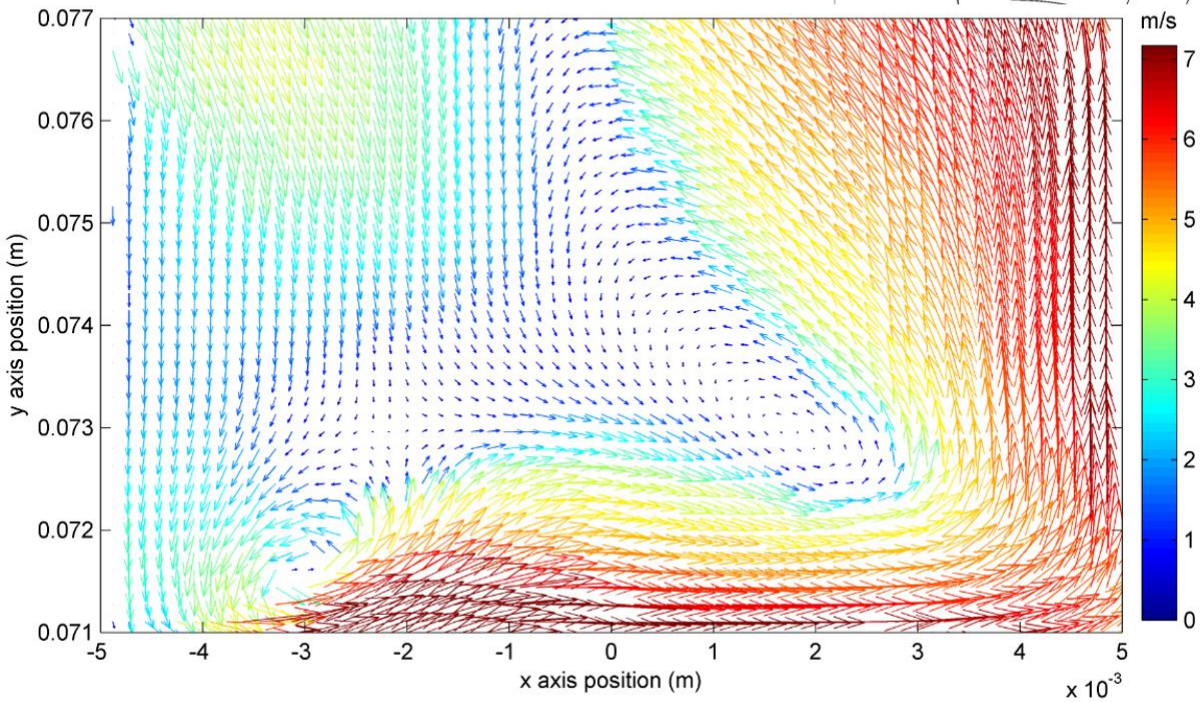

CFD Rotor Slot Rotor Tooth

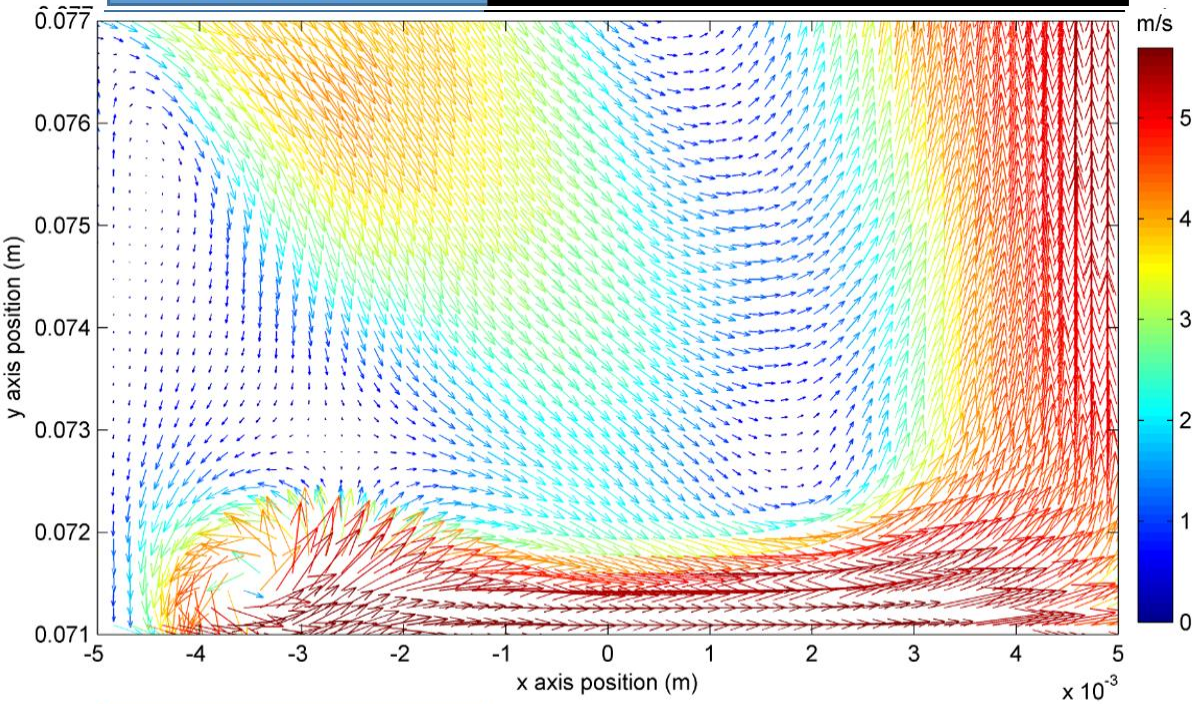

PIV Rotor Slot Rotor Tooth

Mesh level 2, N = 10 rps, θ = -3°

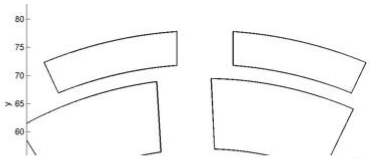

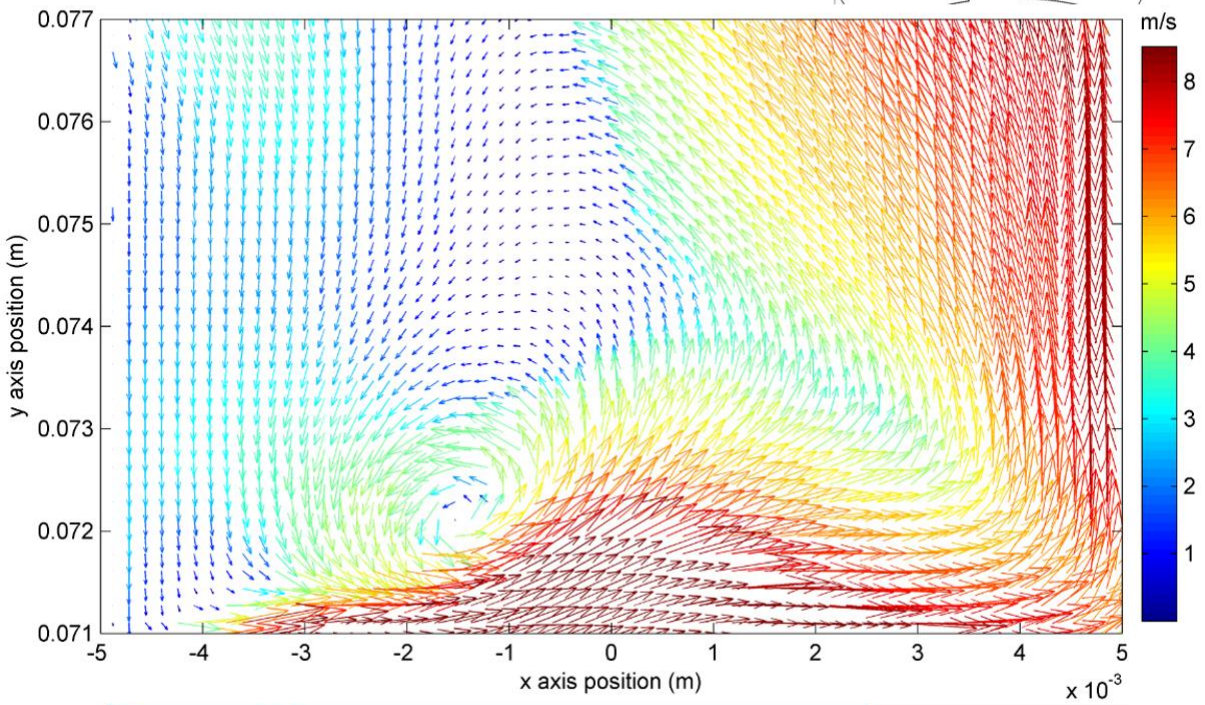

CFD Rotor Slot Tooth

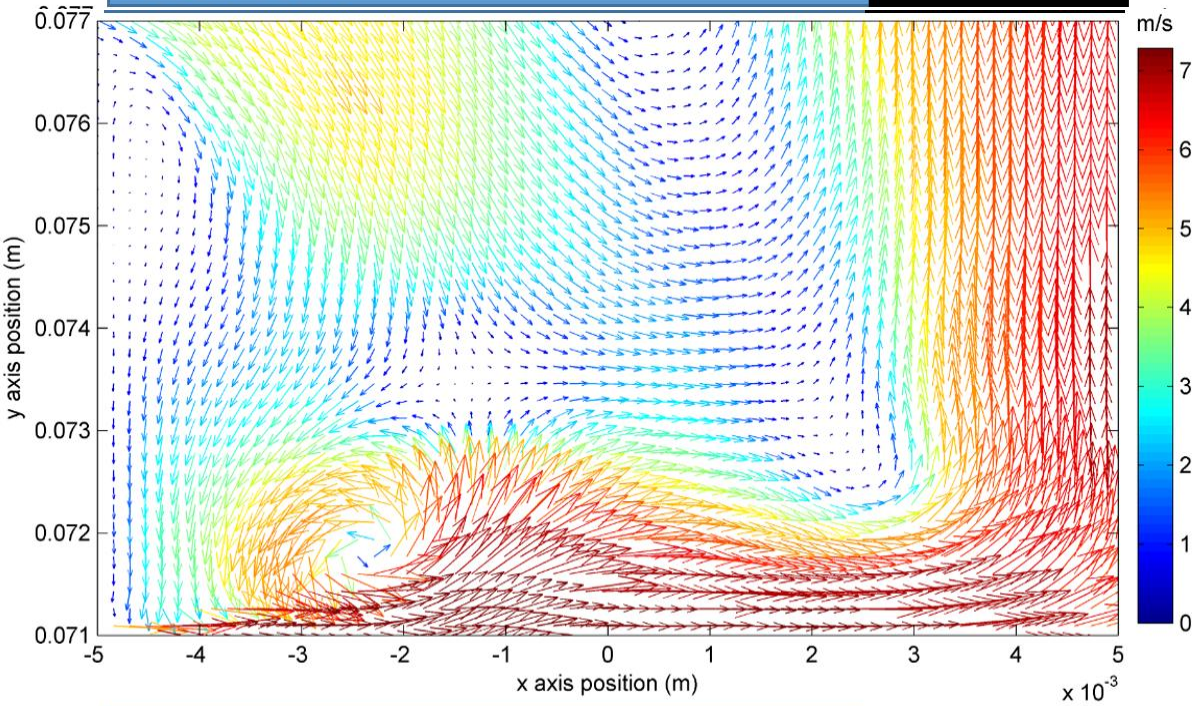

PIV Rotor Slot Tooth

Mesh level 2, N = 10 rps, θ = -1°

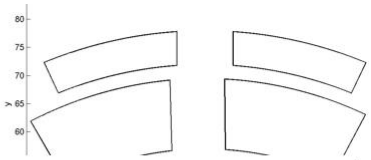

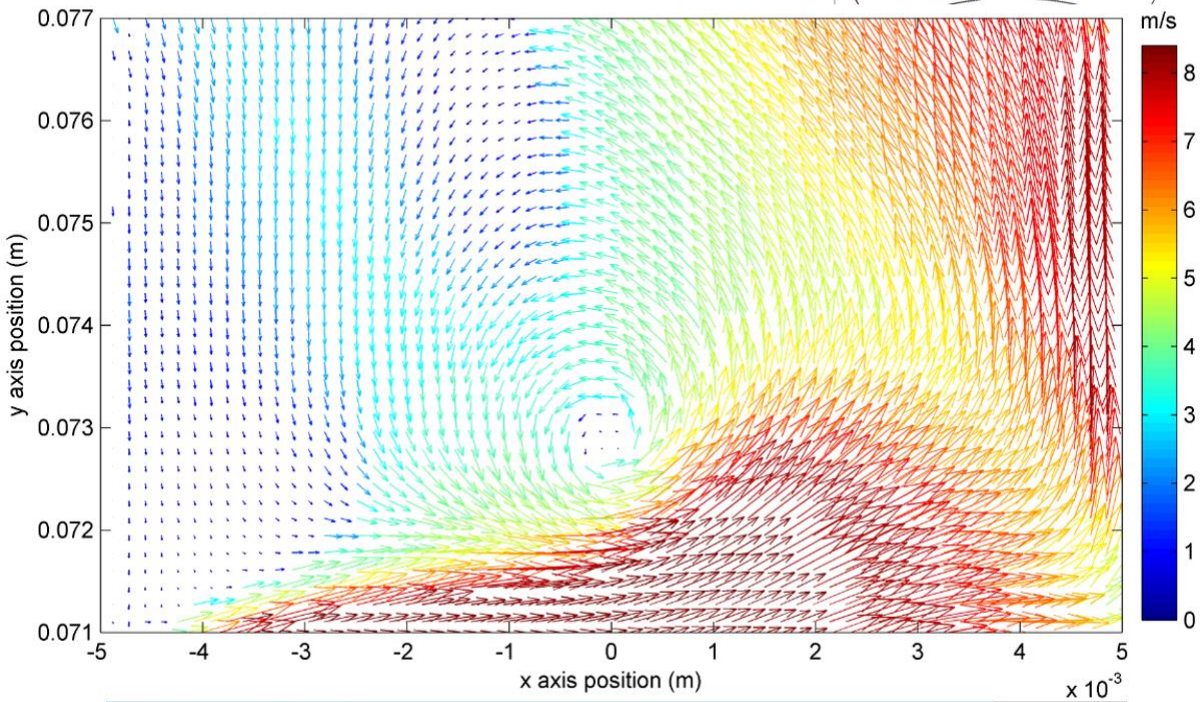

CFD Rotor Slot Tooth

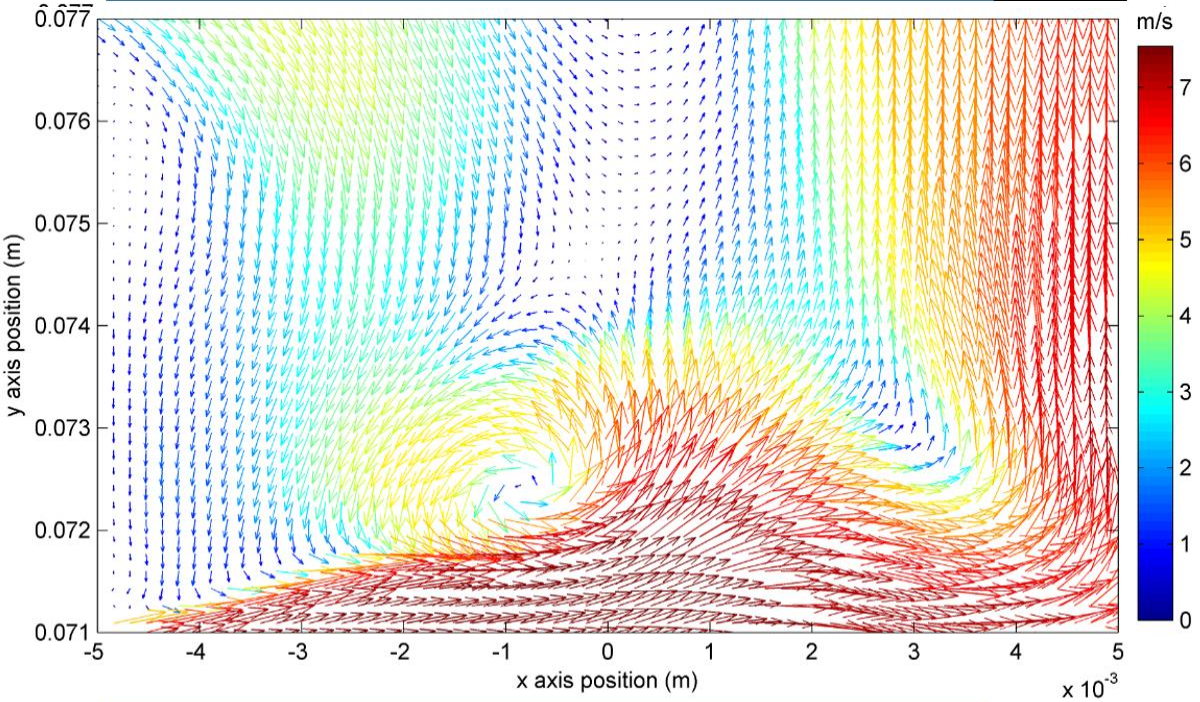

PIV Rotor Slot Tooth

Mesh level 2, N = 10 rps, θ = +1°

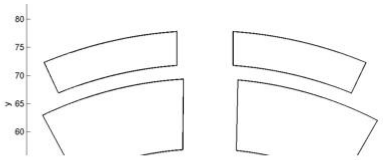

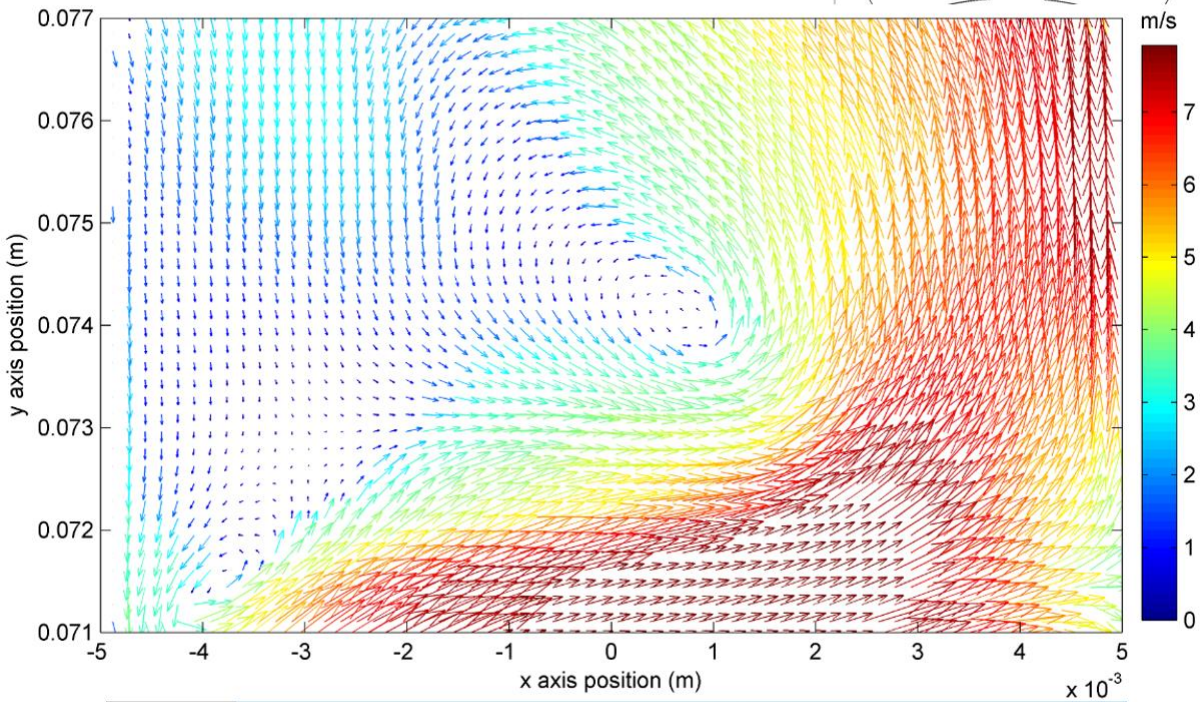

CFD

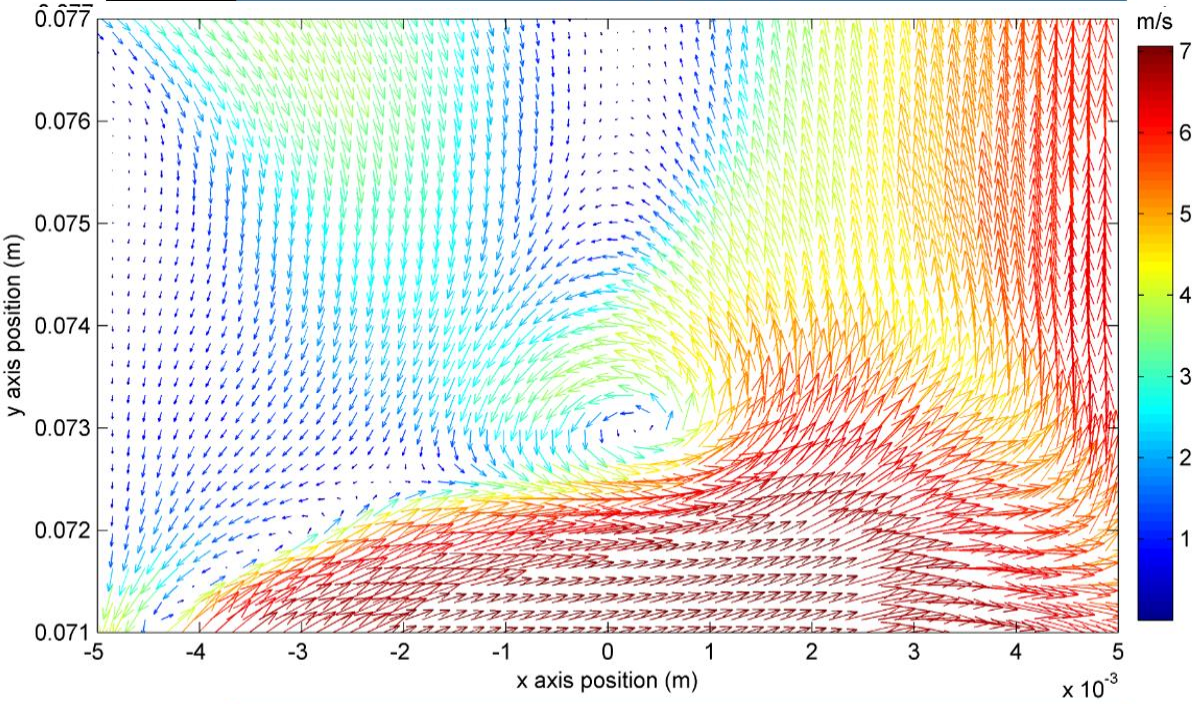

PIV

Mesh level 2, N = 10 rps, θ = +3°

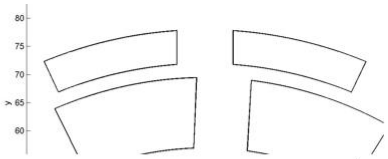

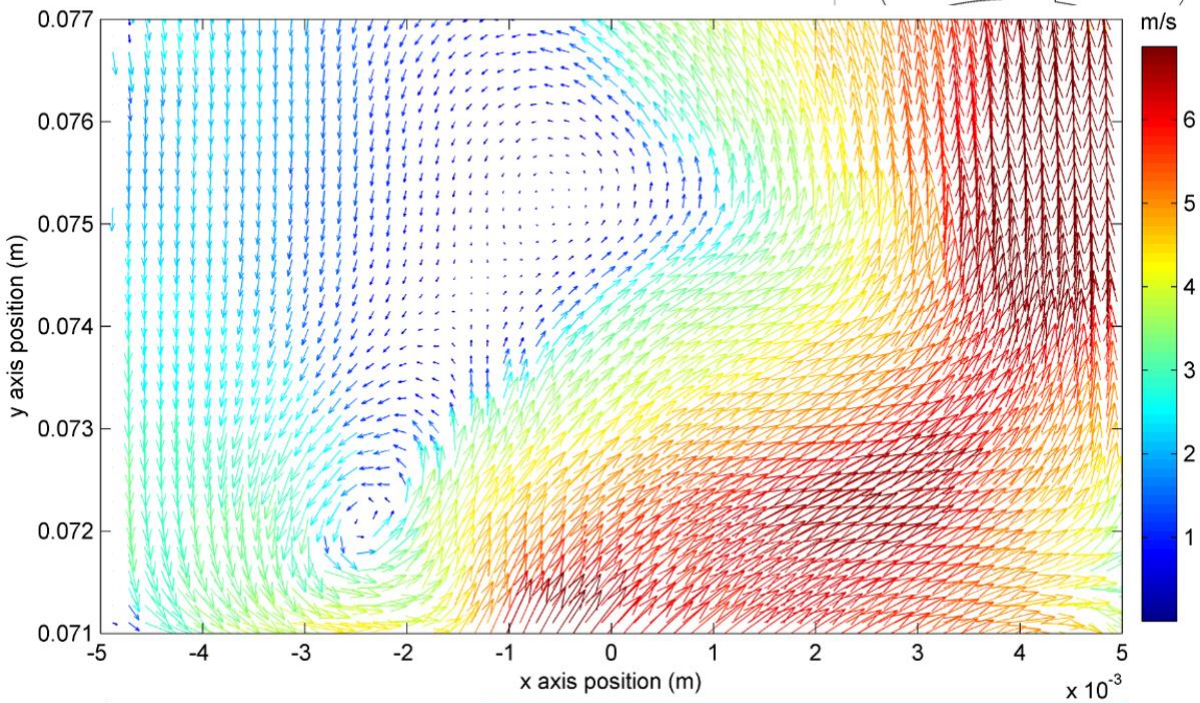

CFD Rotor Tooth Rotor Slot

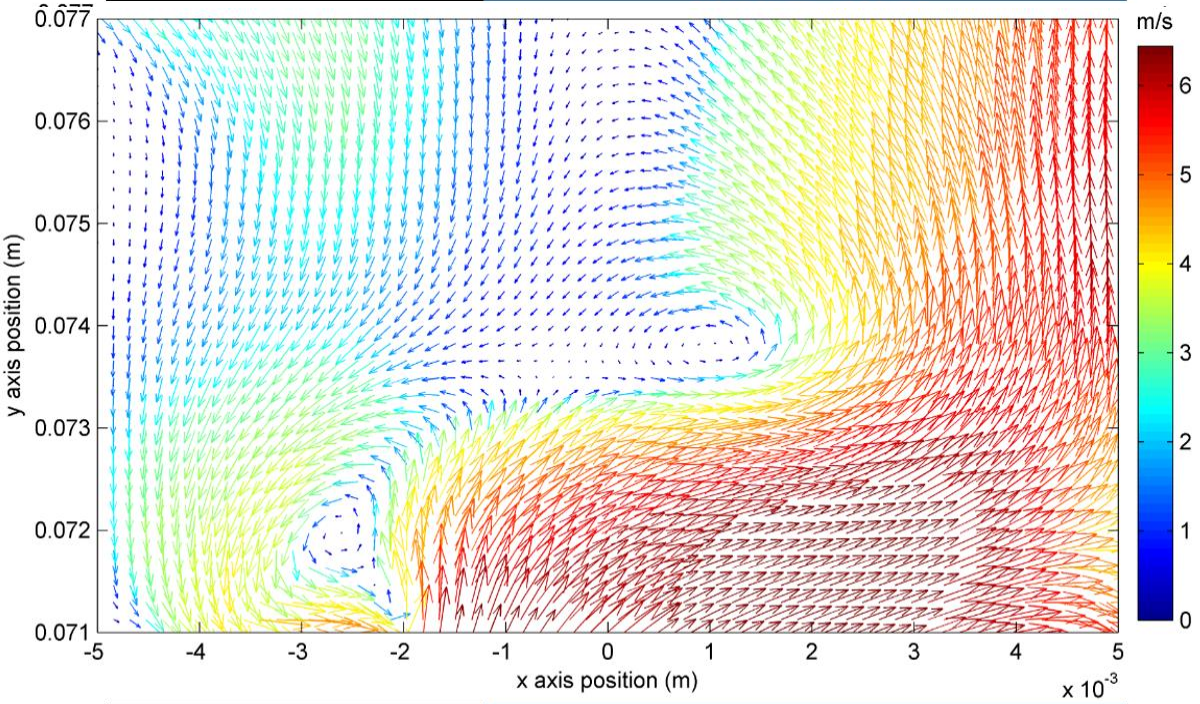

PIV Rotor Tooth Rotor Slot

Mesh level 2, N = 10 rps, θ = +5°

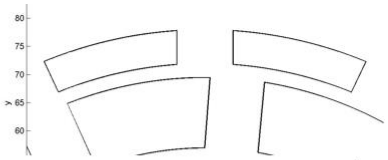

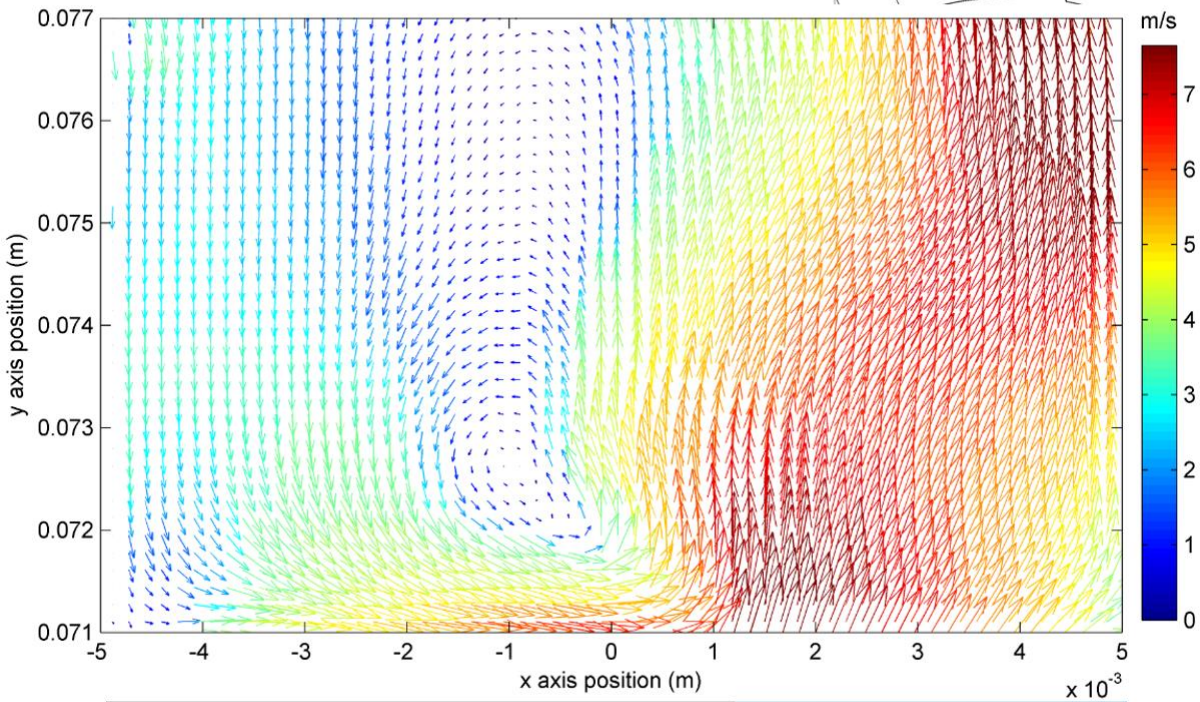

CFD

Rotor Tooth | Rotor Slot

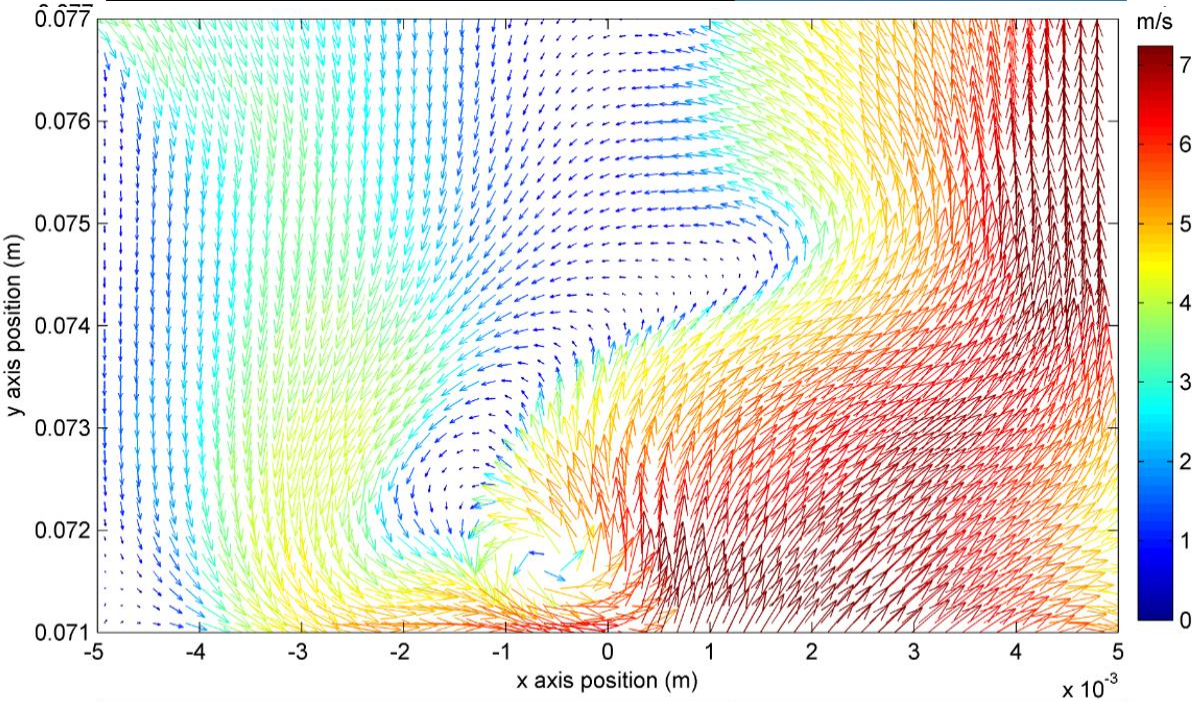

PIV

Rotor Tooth | Rotor Slot

Mesh level 2, N = 10 rps, θ = +7°

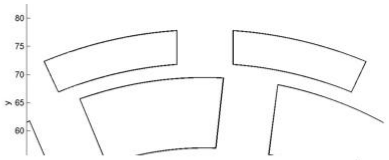

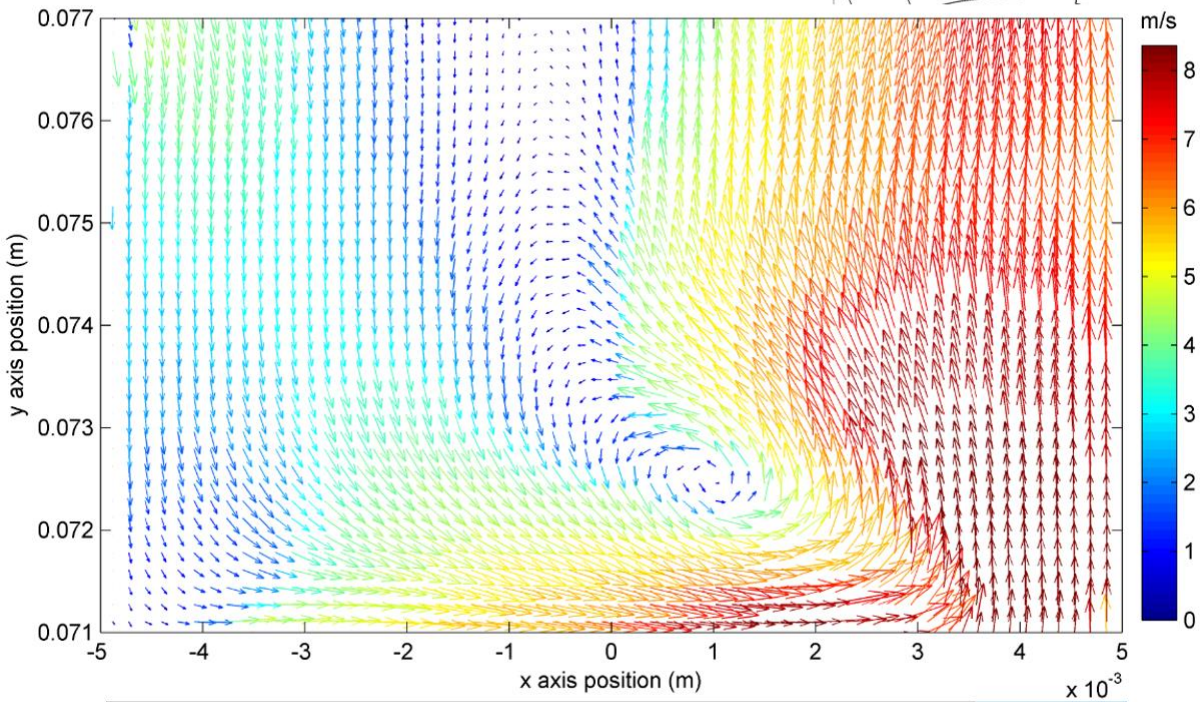

CFD

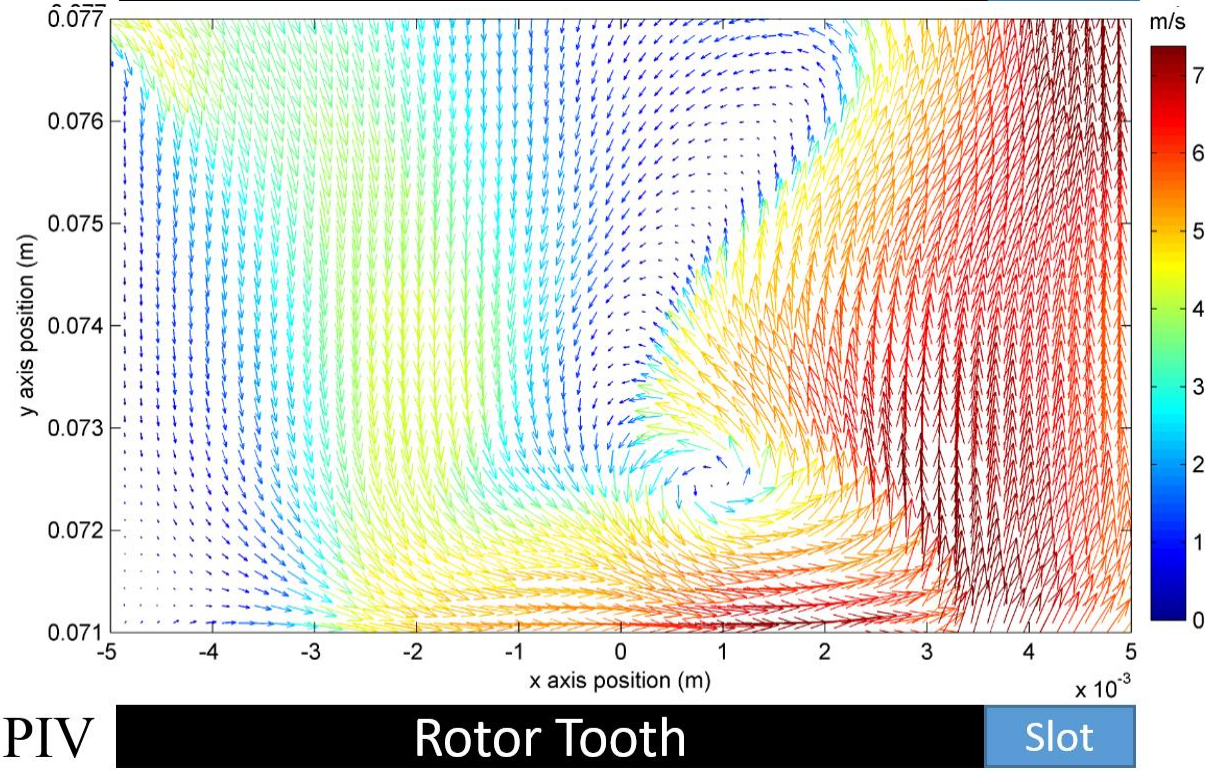

PIV

Mesh level 2, N = 10 rps, θ = +9°

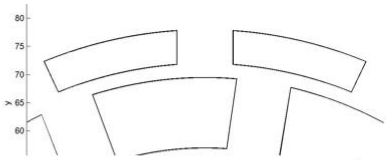

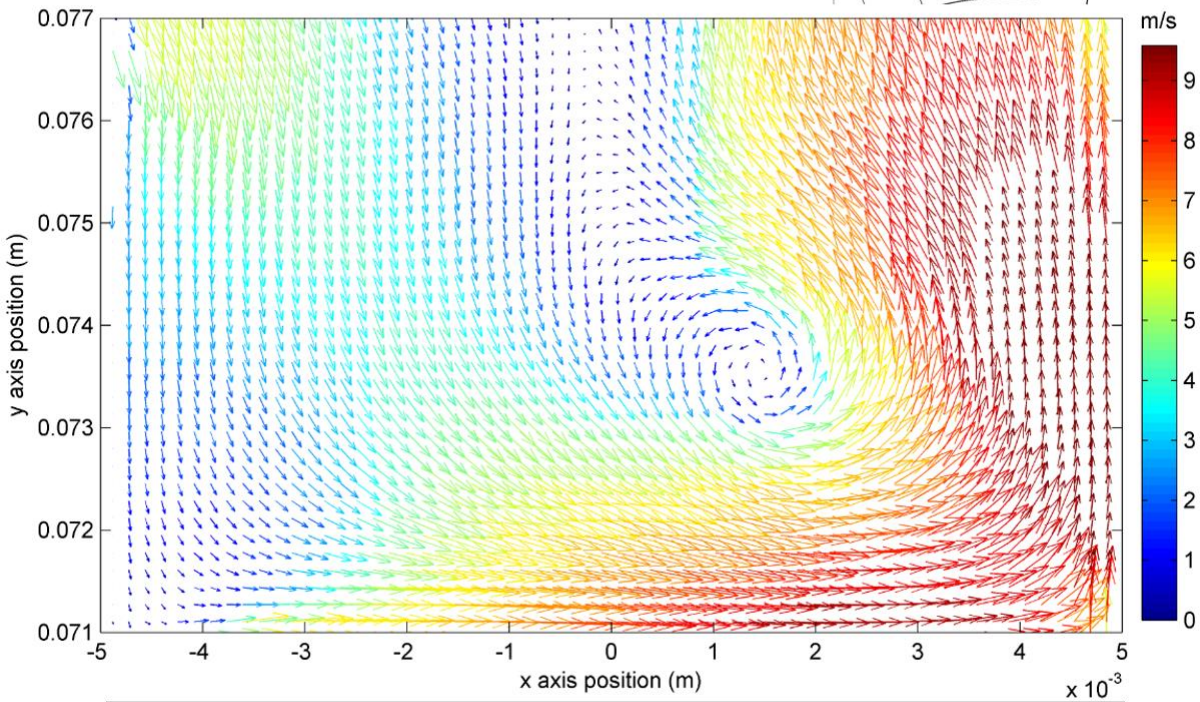

CFD Rotor Tooth

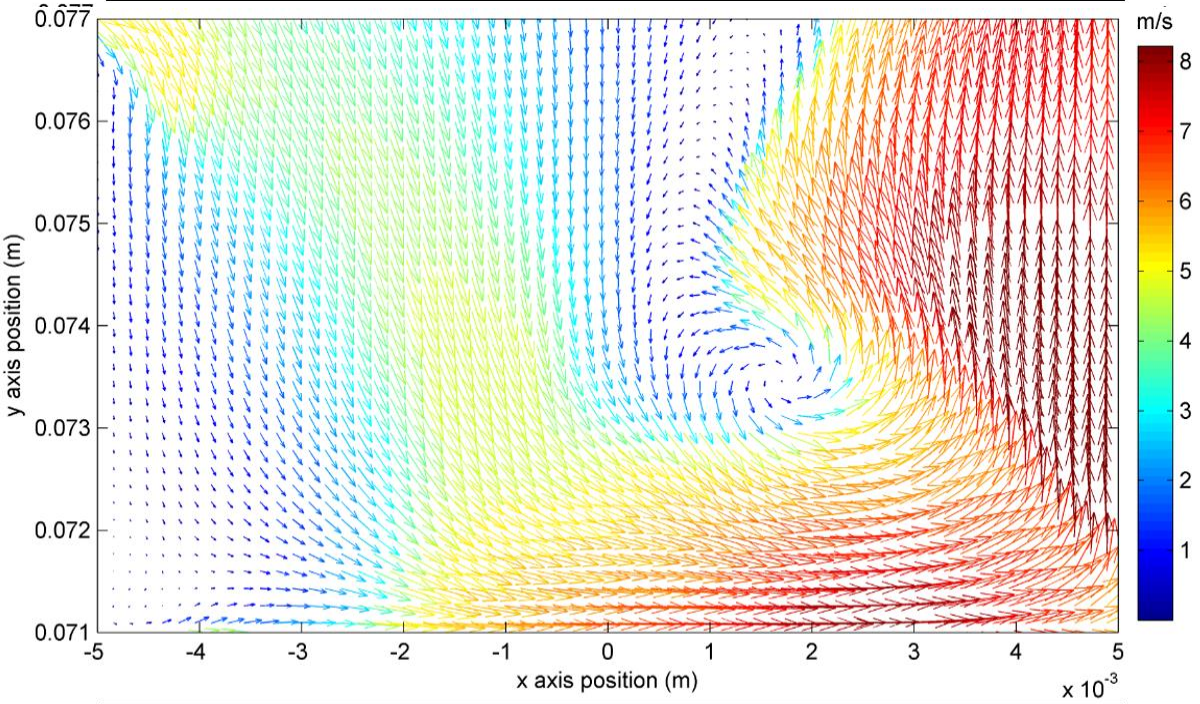

PIV Rotor Tooth

Mesh level 2, N = 20 rps, θ = -7°

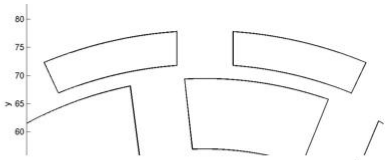

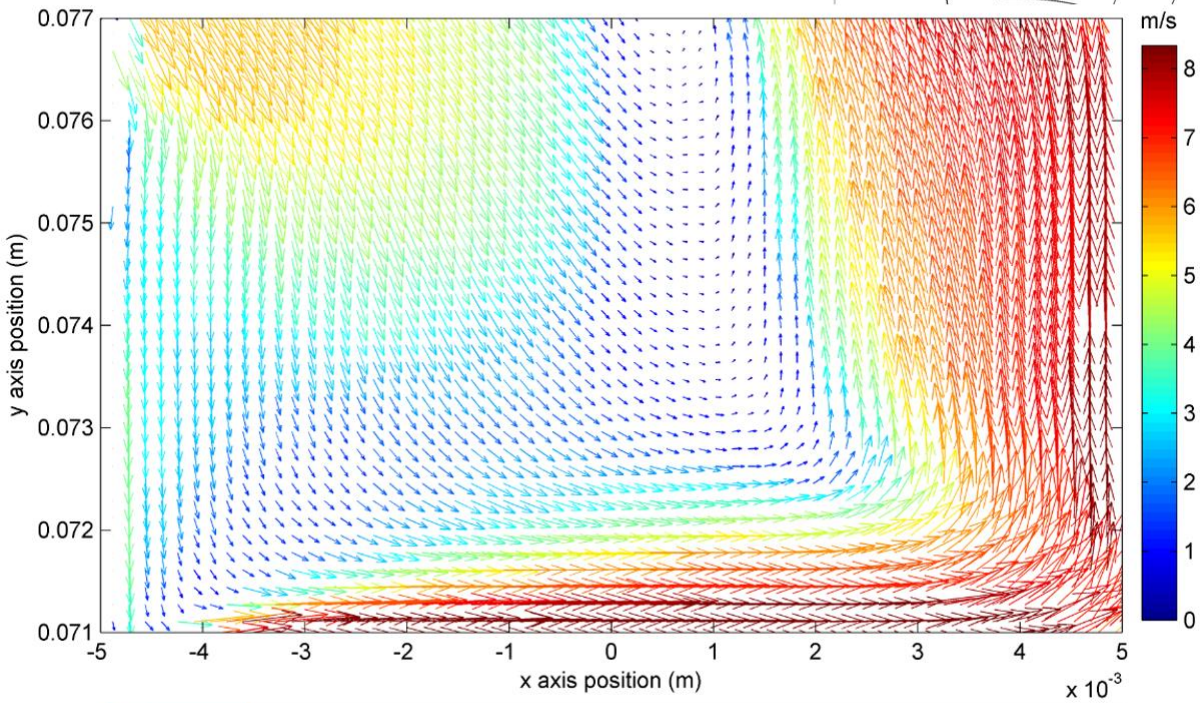

CFD Slot Rotor Tooth

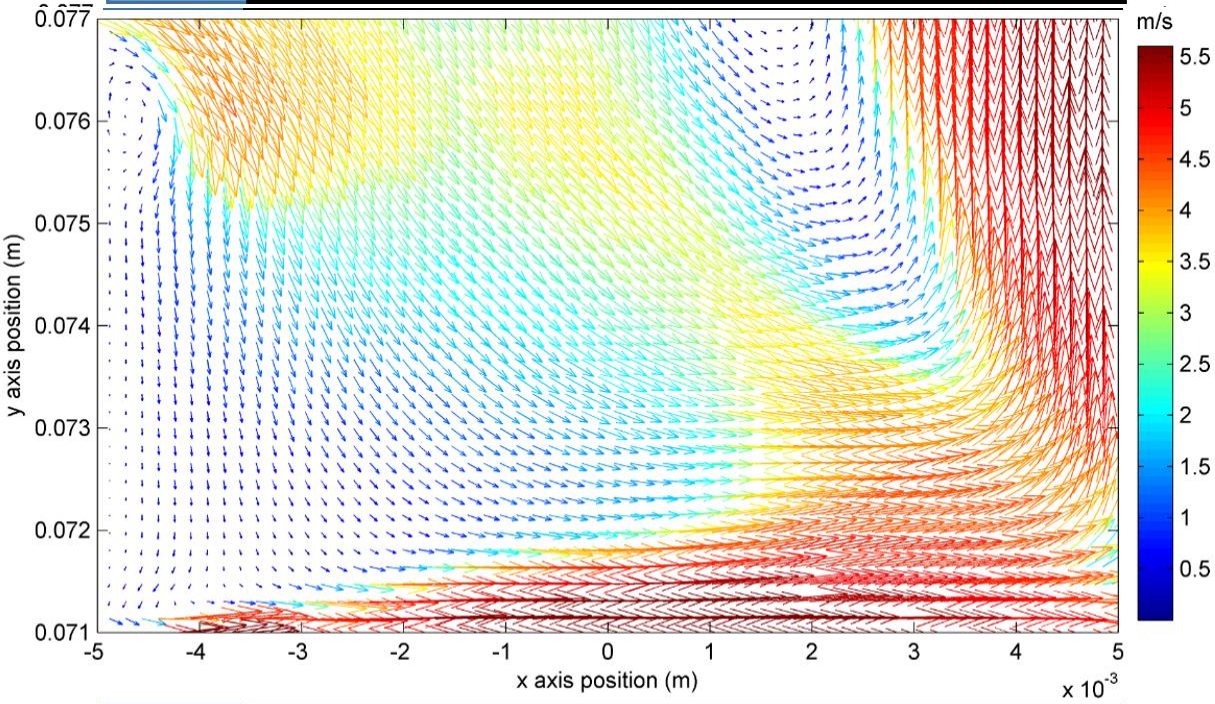

PIV Slot Rotor Tooth

Mesh level 2, N = 20 rps, θ = -5°

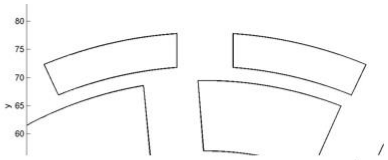

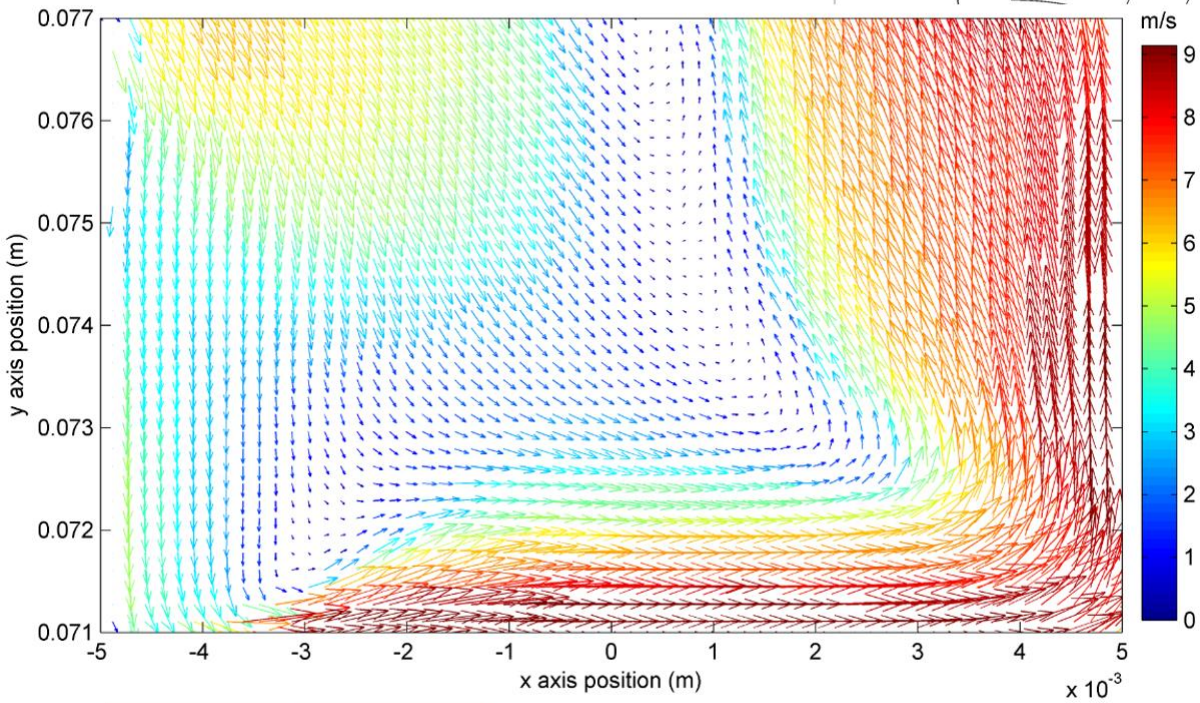

CFD Rotor Slot Rotor Tooth

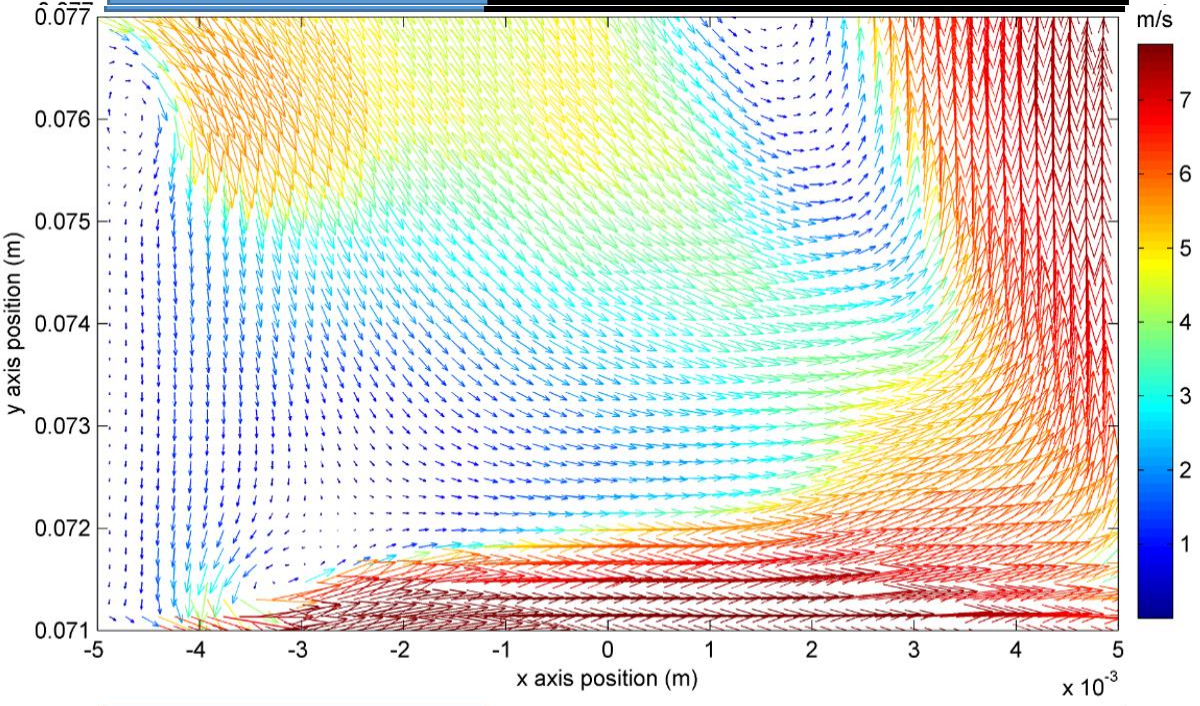

PIV Rotor Slot Rotor Tooth

Mesh level 2, N = 20 rps, θ = -3°

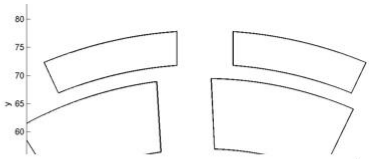

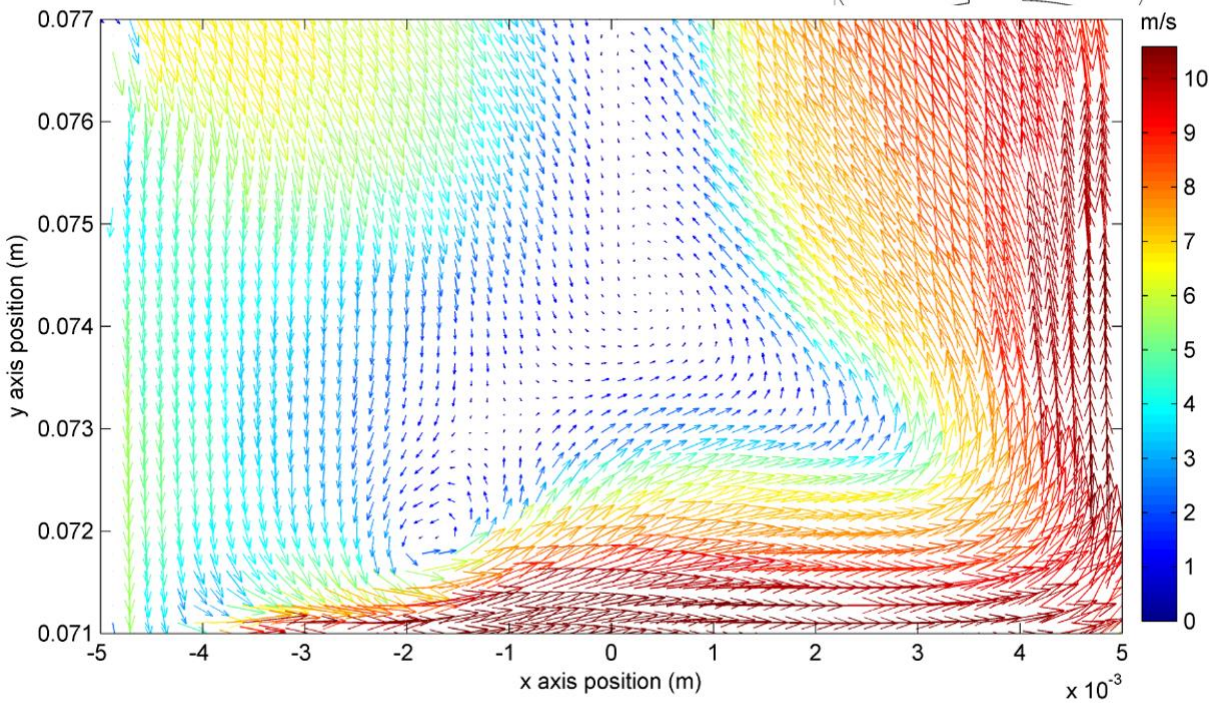

CFD Rotor Slot Tooth

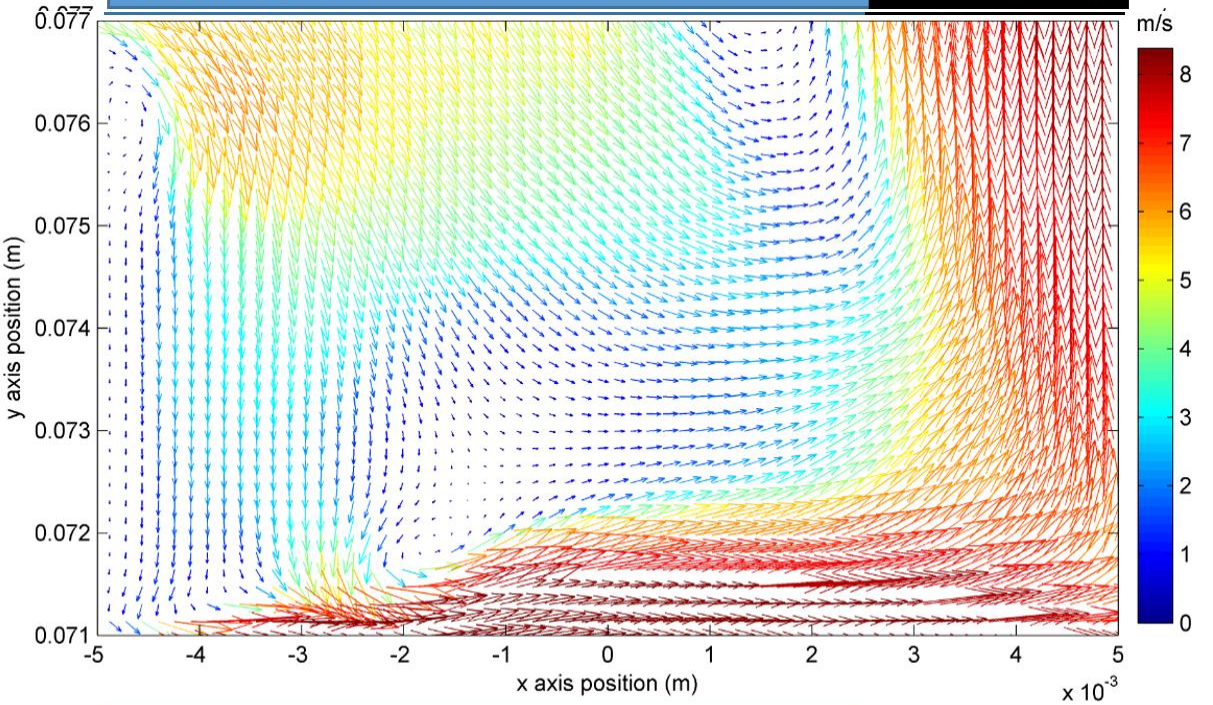

PIV Rotor Slot Tooth

Mesh level 2, N = 20 rps, θ = -1°

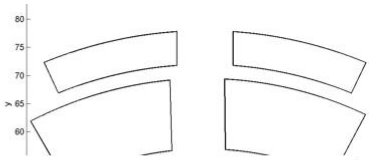

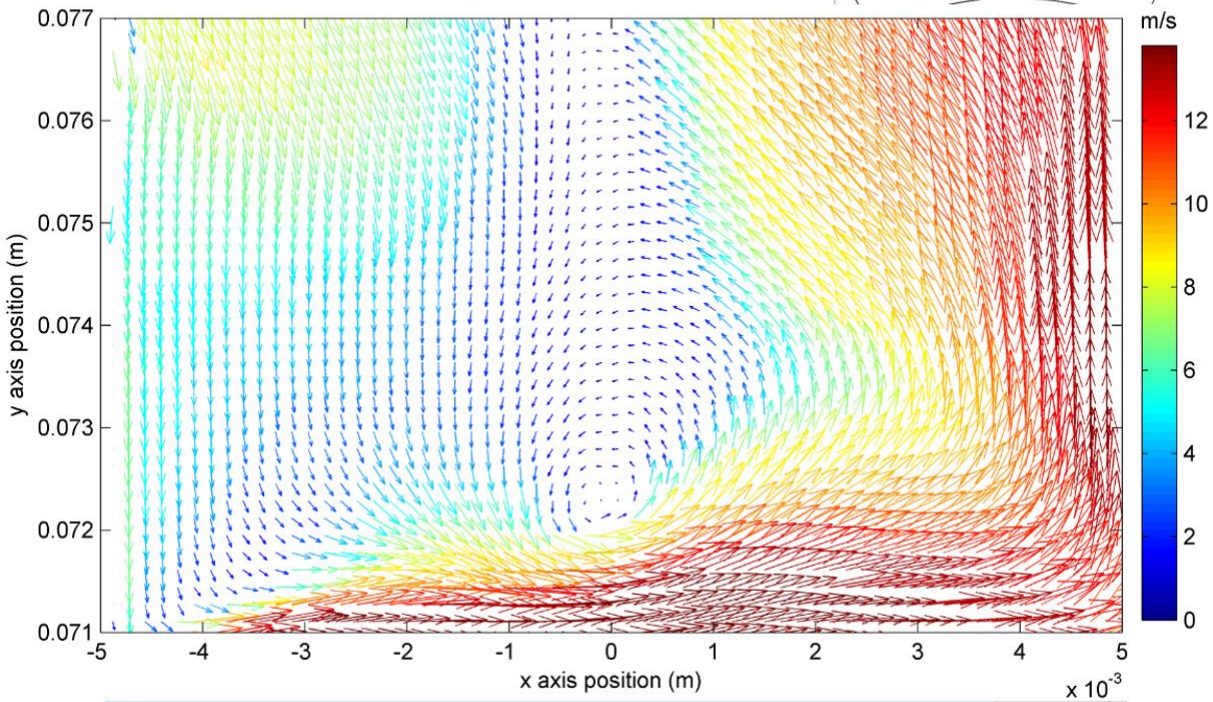

CFD Rotor Slot Tooth

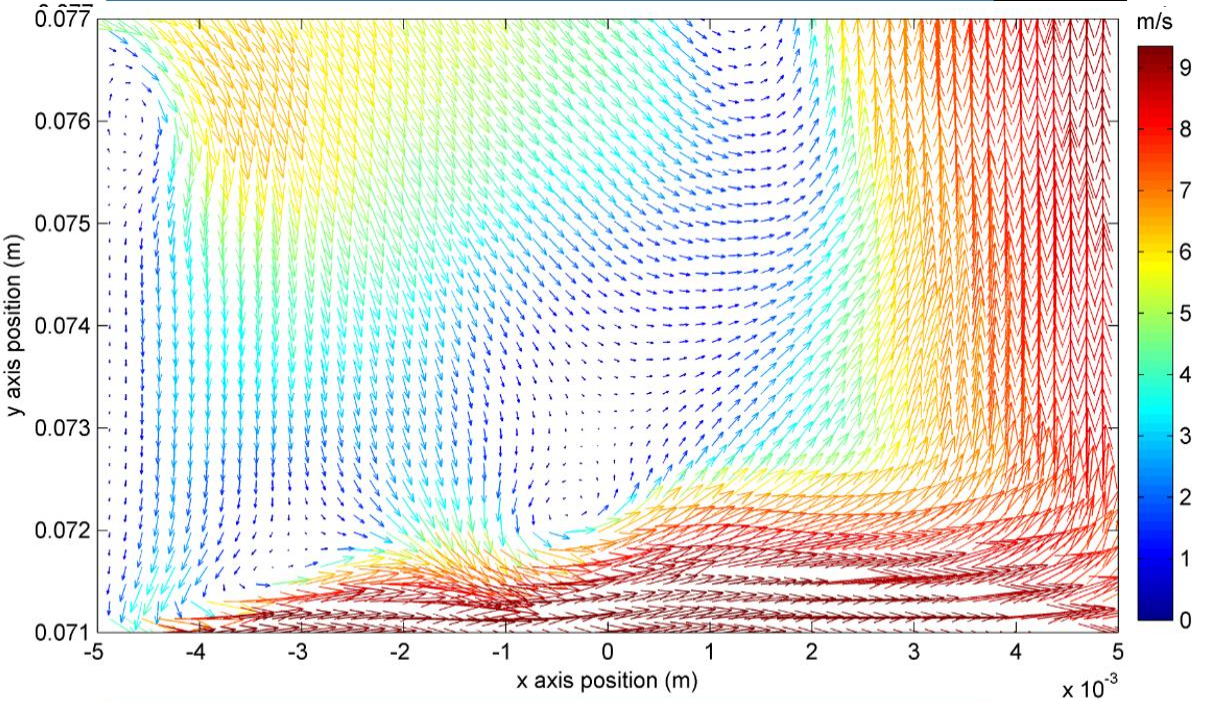

PIV Rotor Slot Tooth

Mesh level 2, N = 20 rps, θ = +1°

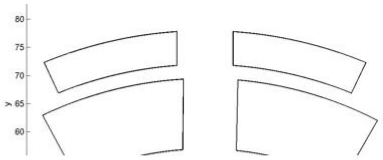

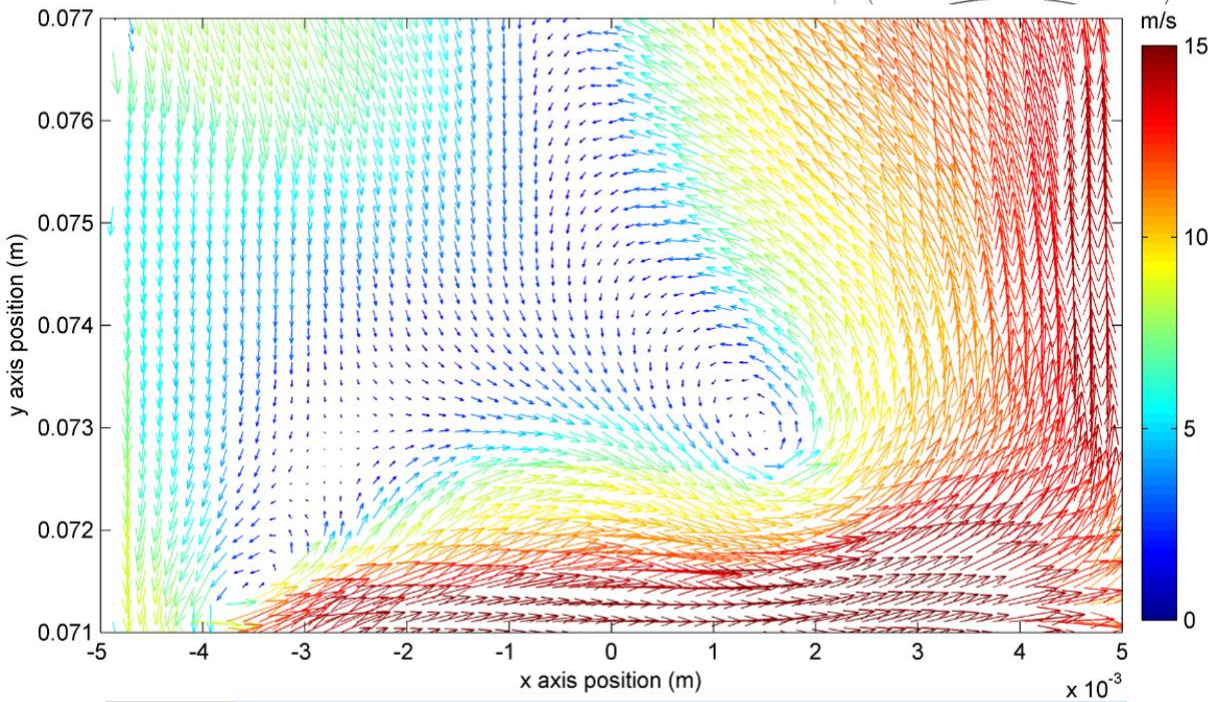

CFD

Tooth | Rotor Slot

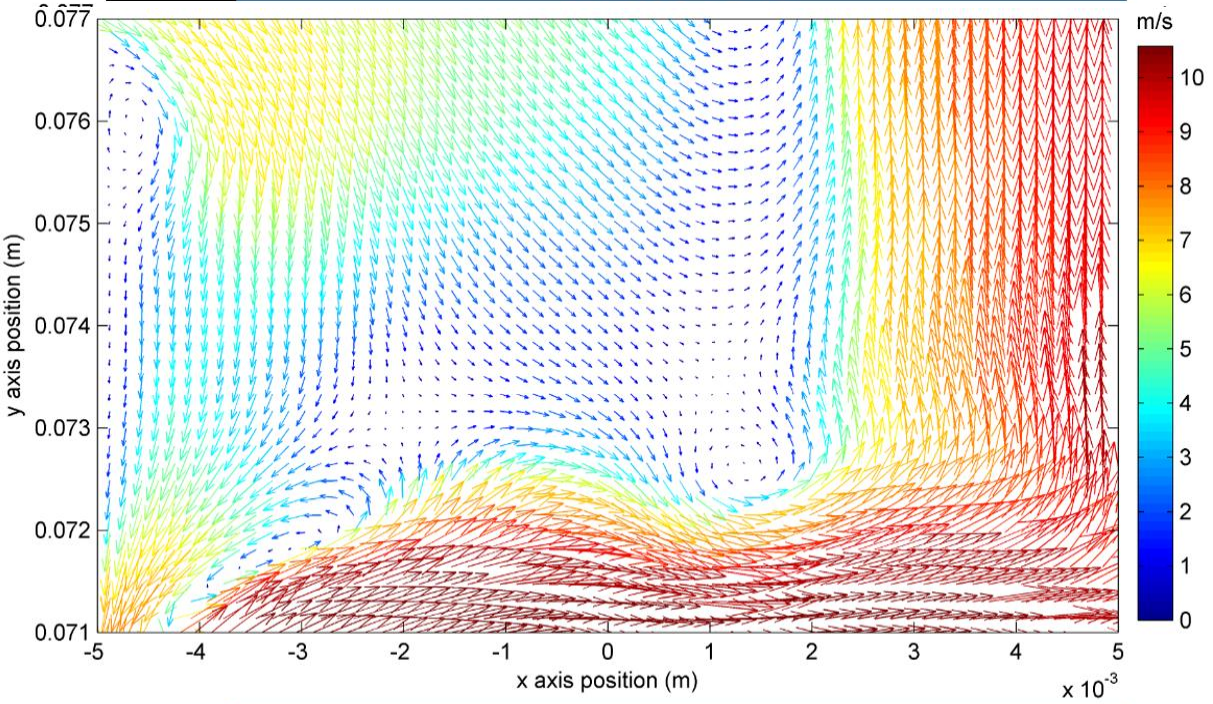

PIV

Tooth | Rotor Slot

Mesh level 2, N = 20 rps, θ = +3°

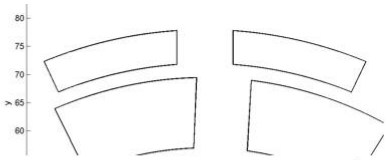

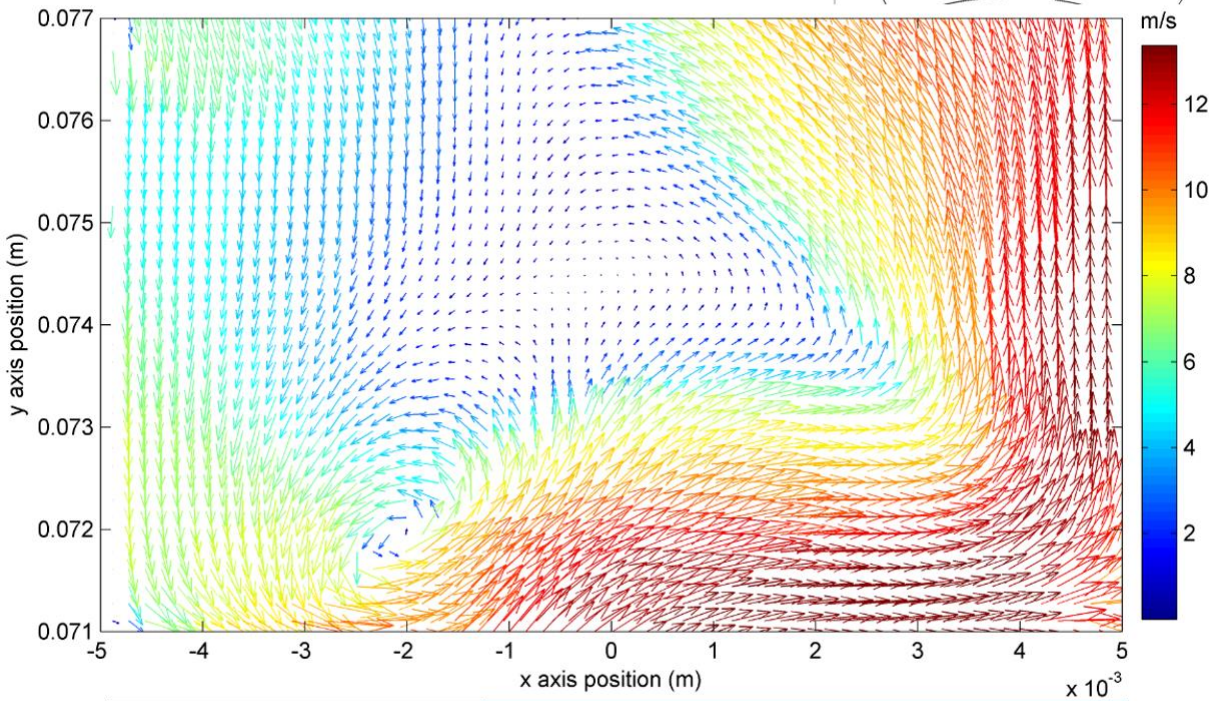

CFD Rotor Tooth Rotor Slot

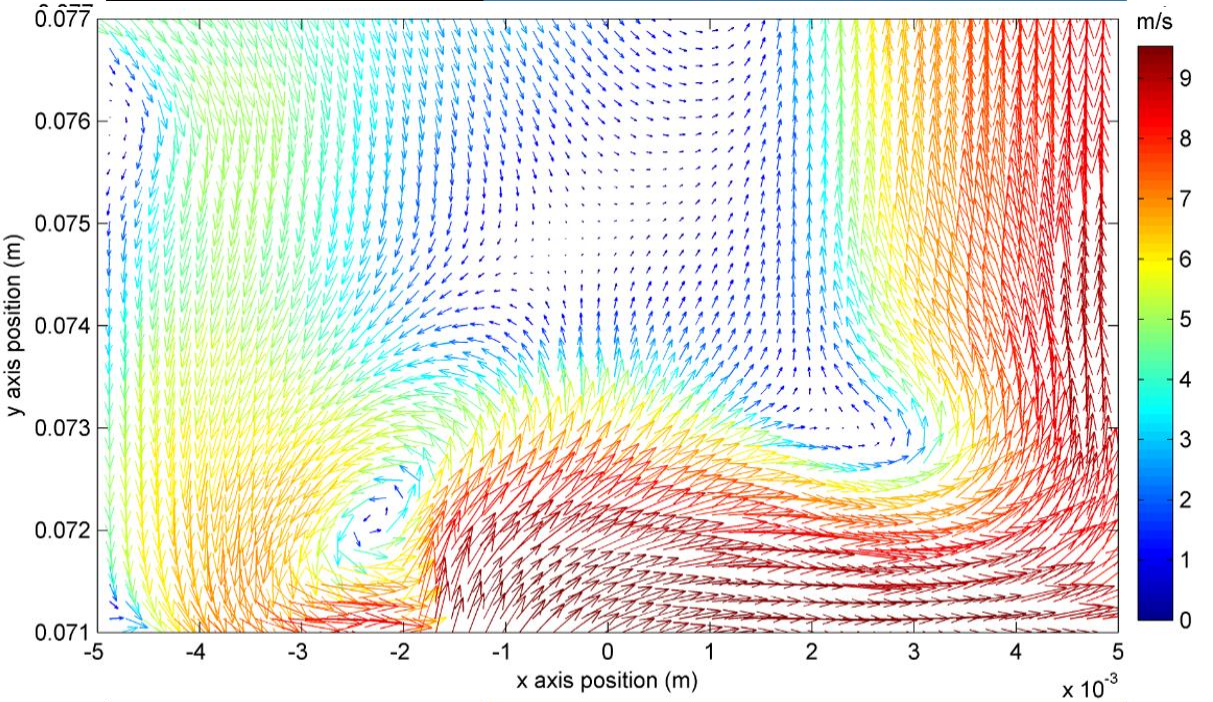

PIV Rotor Tooth Rotor Slot

Mesh level 2, N = 20 rps, θ = +5°

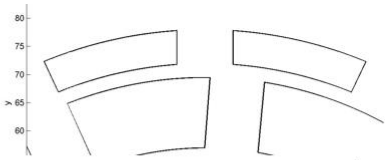

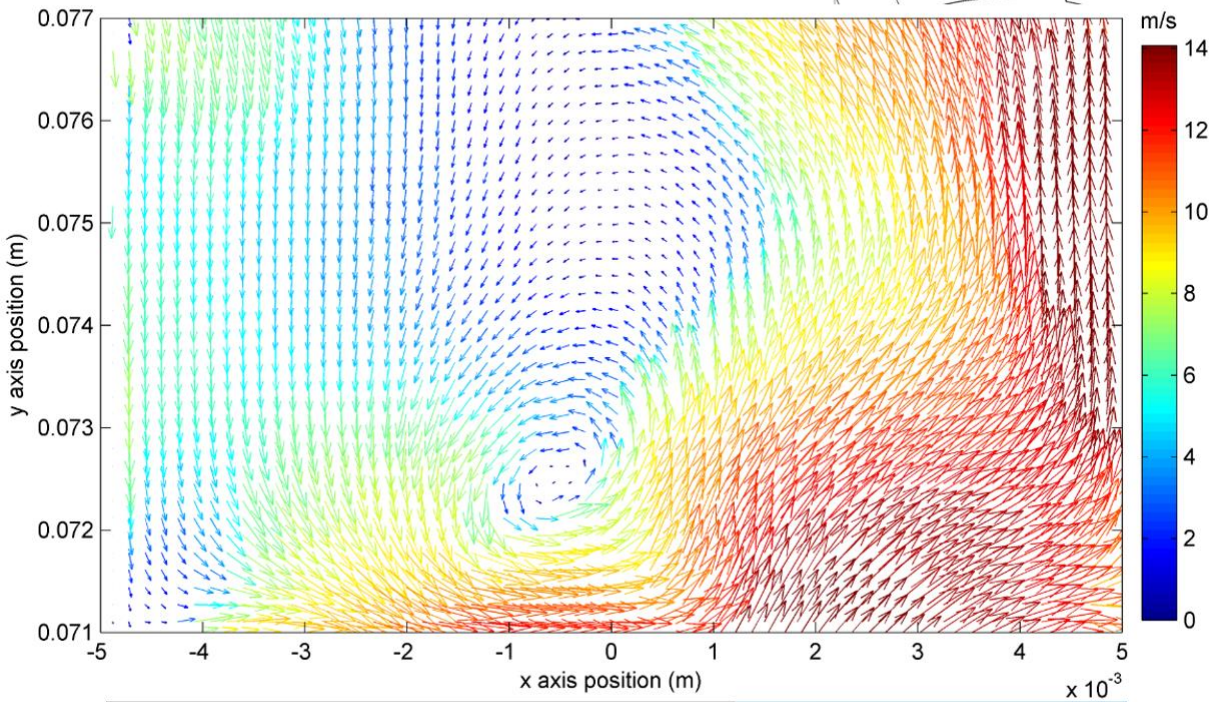

CFD

Rotor Tooth | Rotor Slot

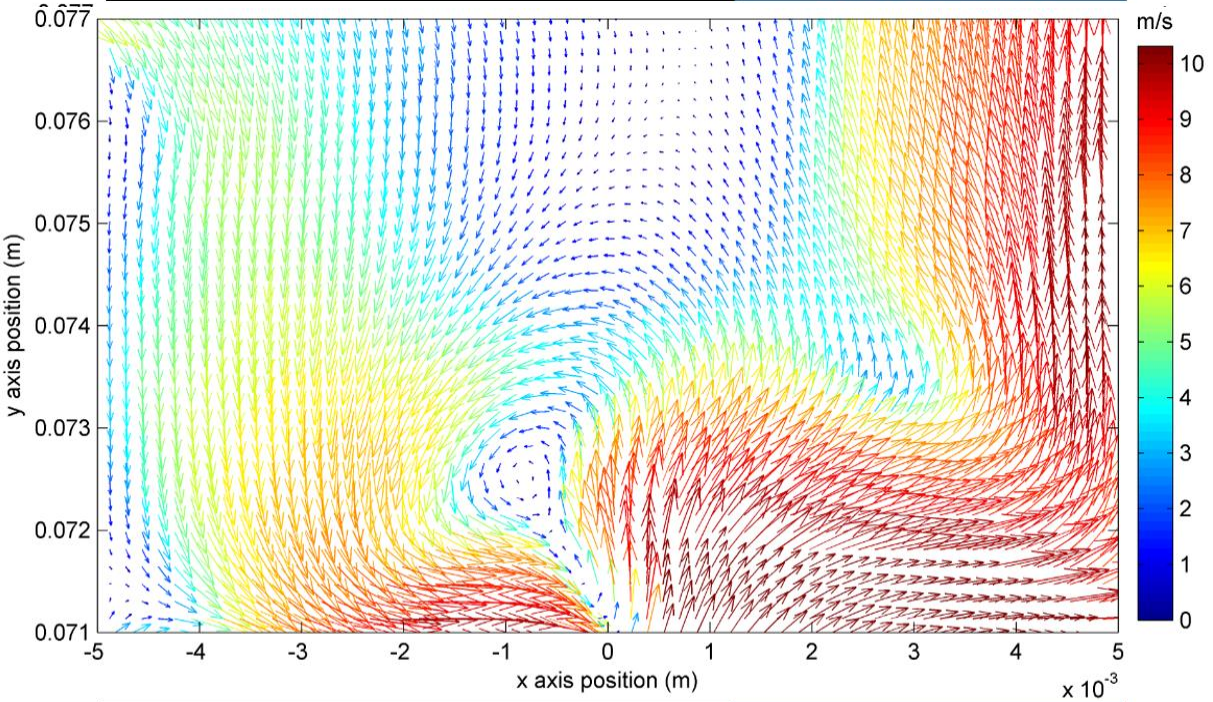

PIV

Rotor Tooth | Rotor Slot

Mesh level 2, N = 20 rps, θ = +7°

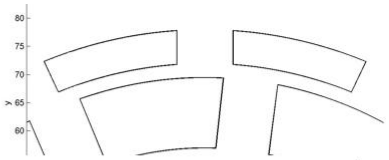

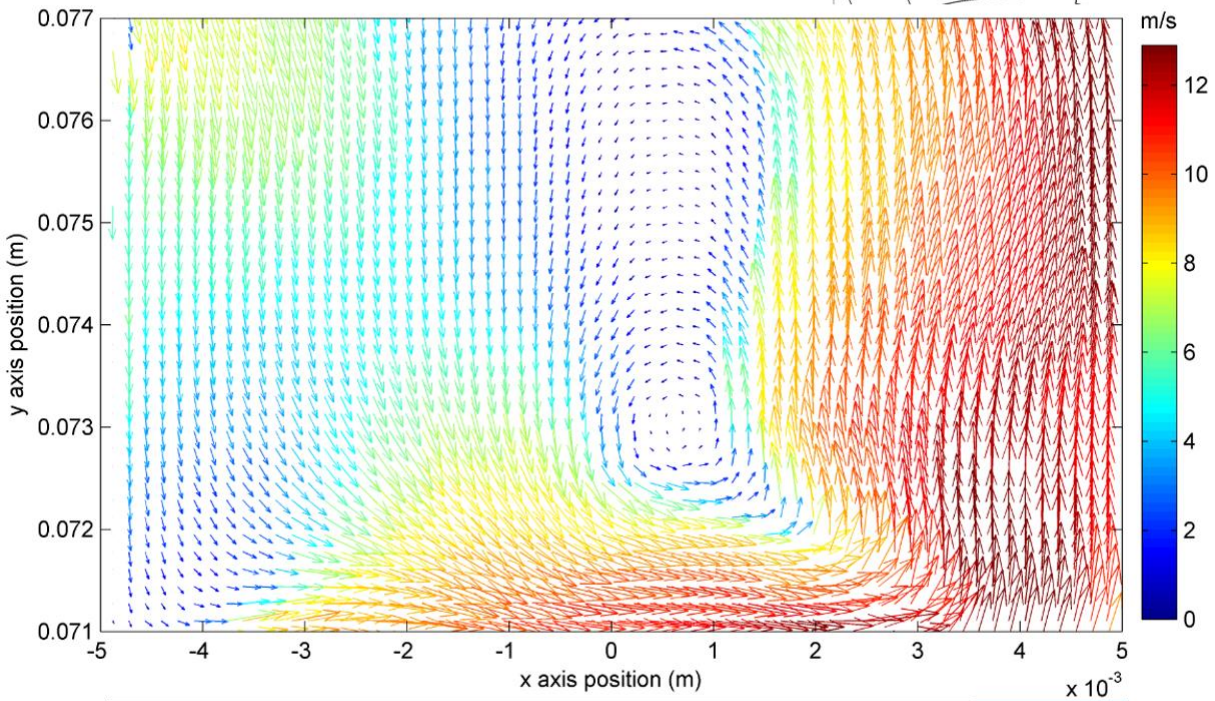

CFD

Rotor Tooth | Slot

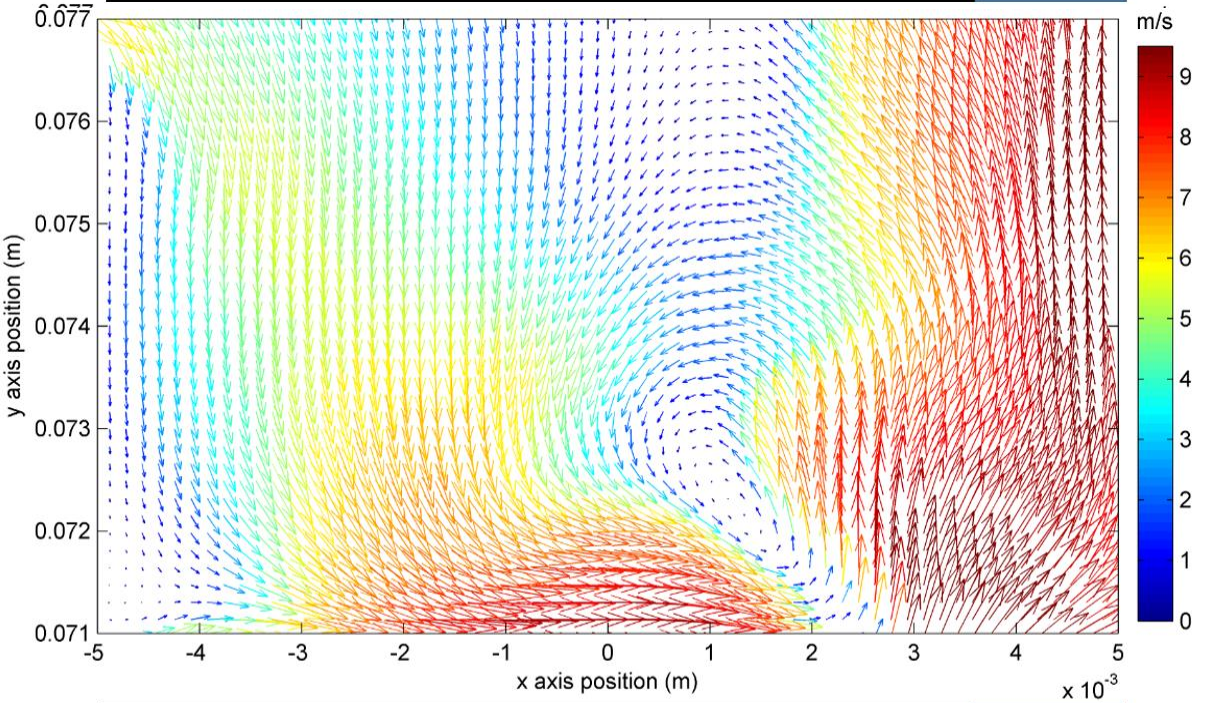

PIV

Rotor Tooth | Slot

Mesh level 2, N = 20 rps, θ = +9°

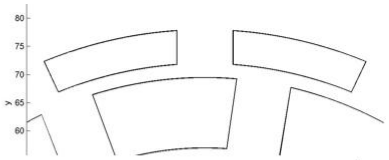

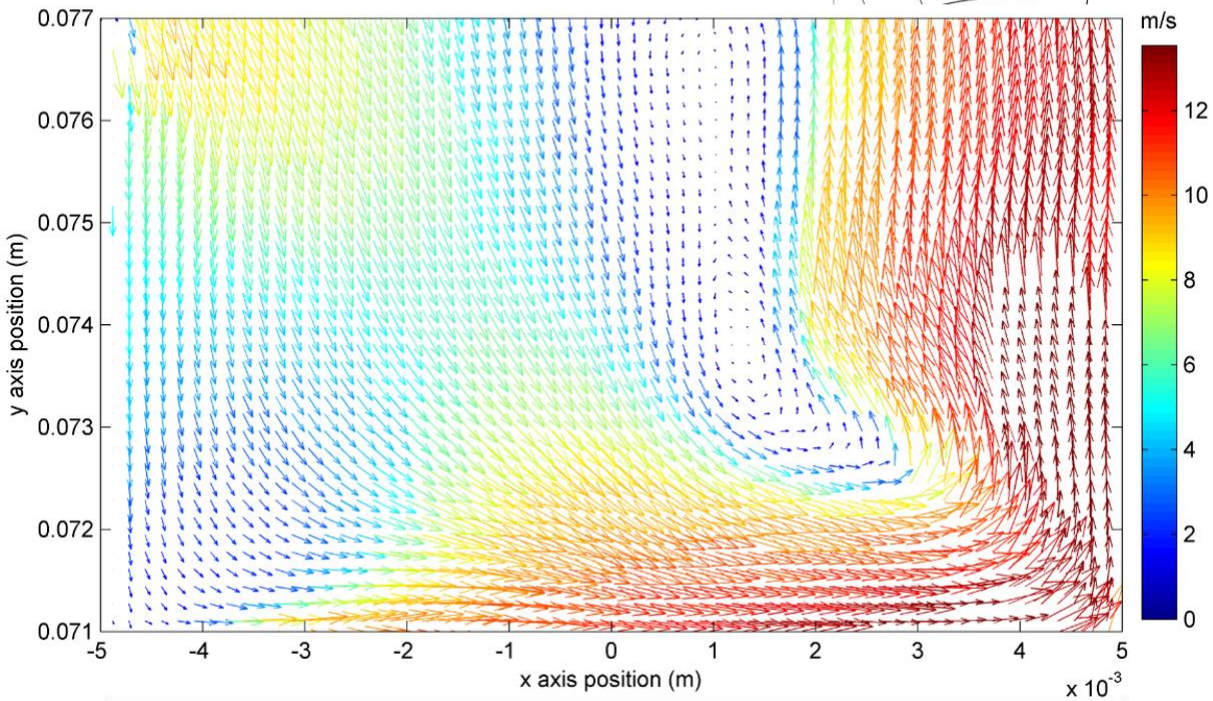

CFD

Rotor Tooth

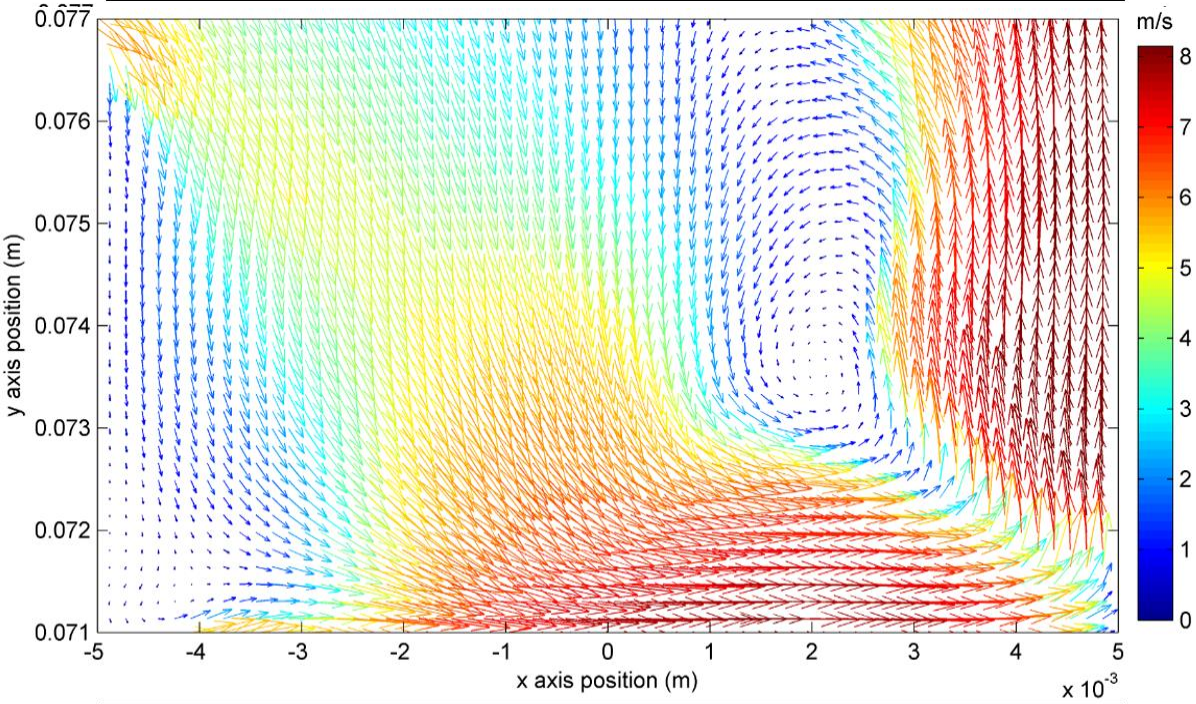

PIV

Rotor Tooth

Mesh level 2, N = 26 rps, θ = -7°

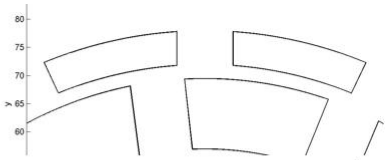

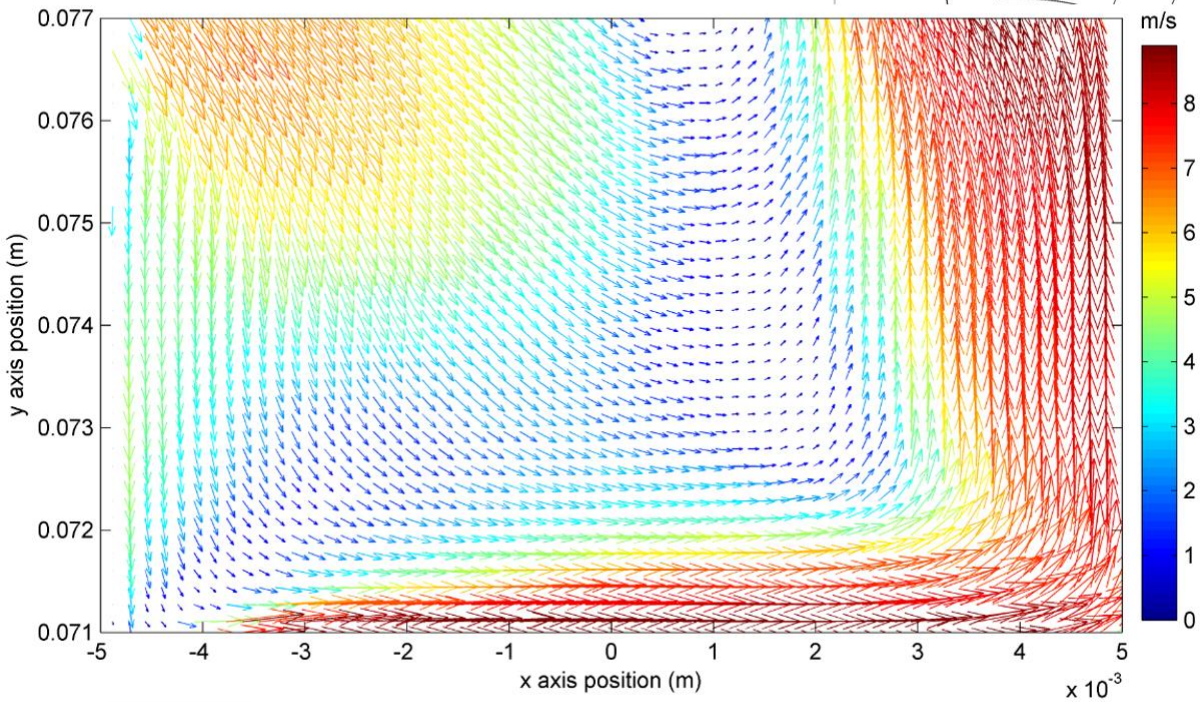

CFD Slot Rotor Tooth

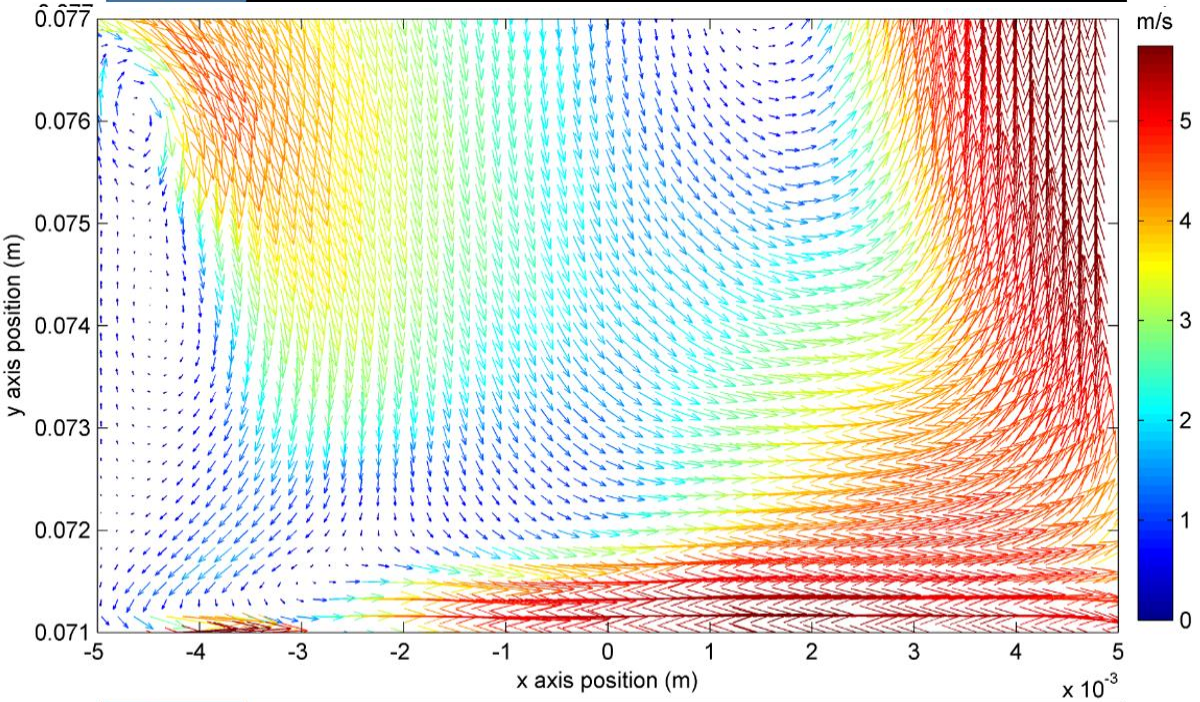

PIV Slot Rotor Tooth

Mesh level 2, N = 26 rps, θ = -5°

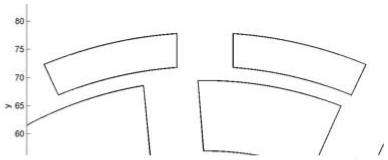

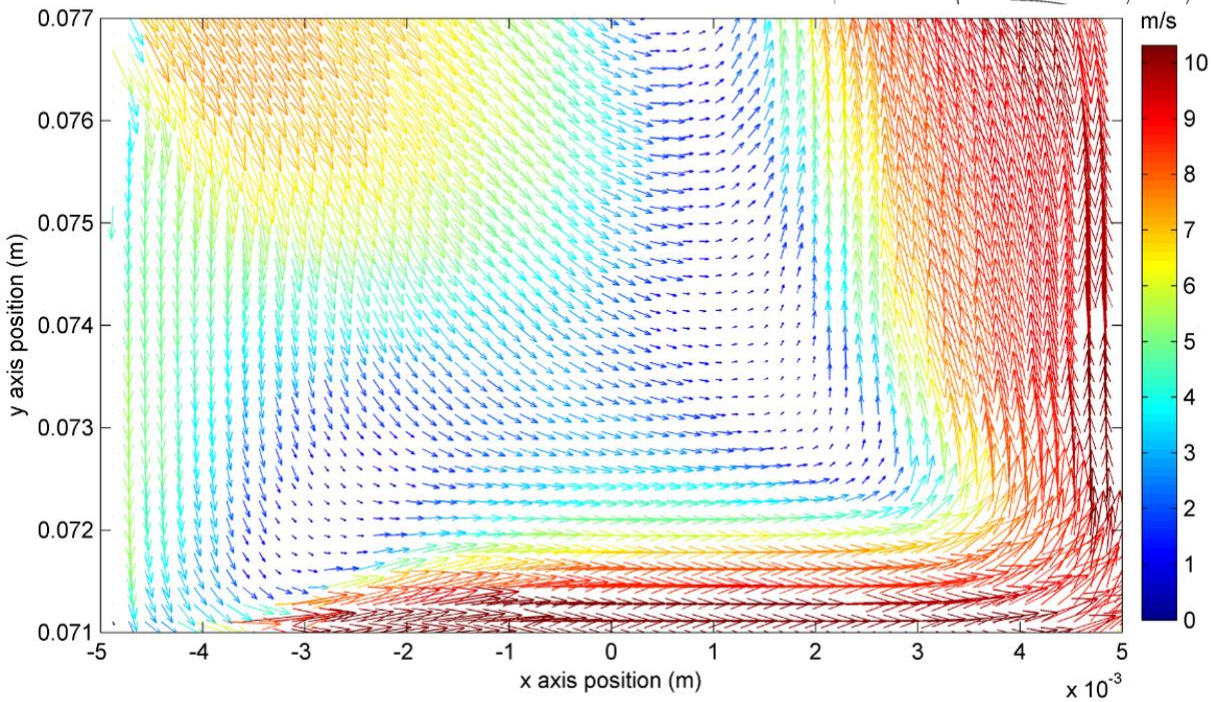

CFD Rotor Slot Rotor Tooth

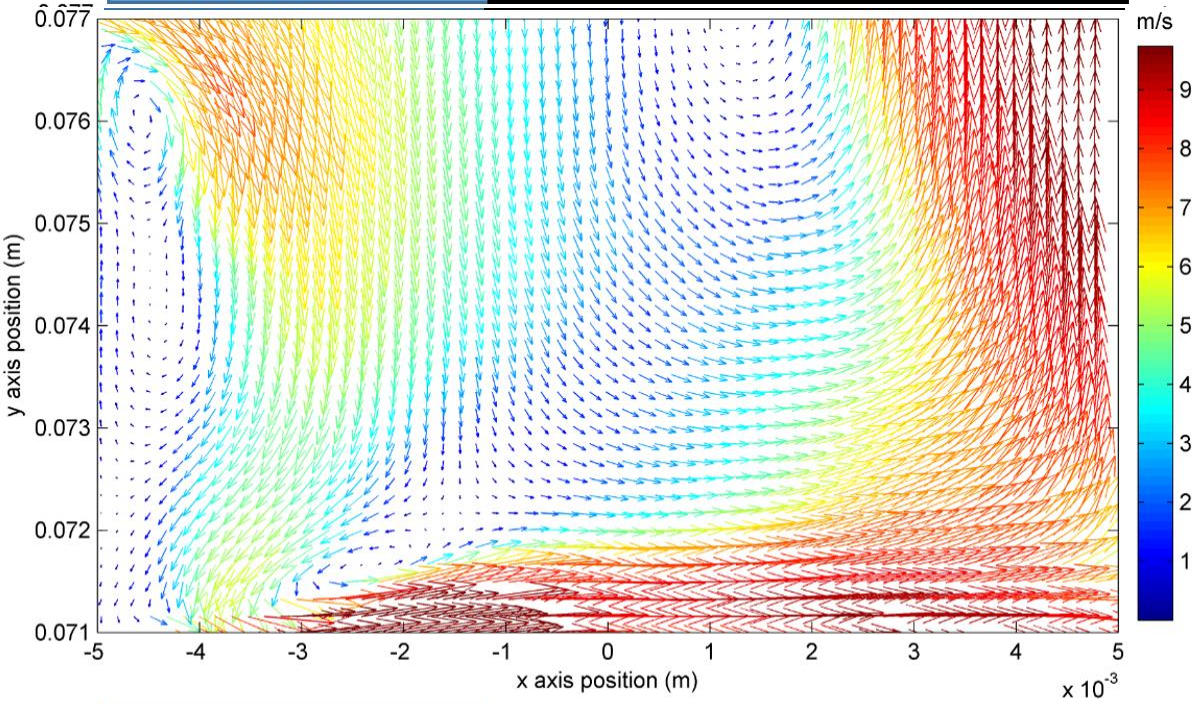

PIV Rotor Slot Rotor Tooth

Mesh level 2, N = 26 rps, θ = -3°

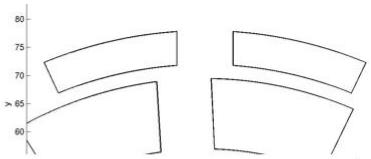

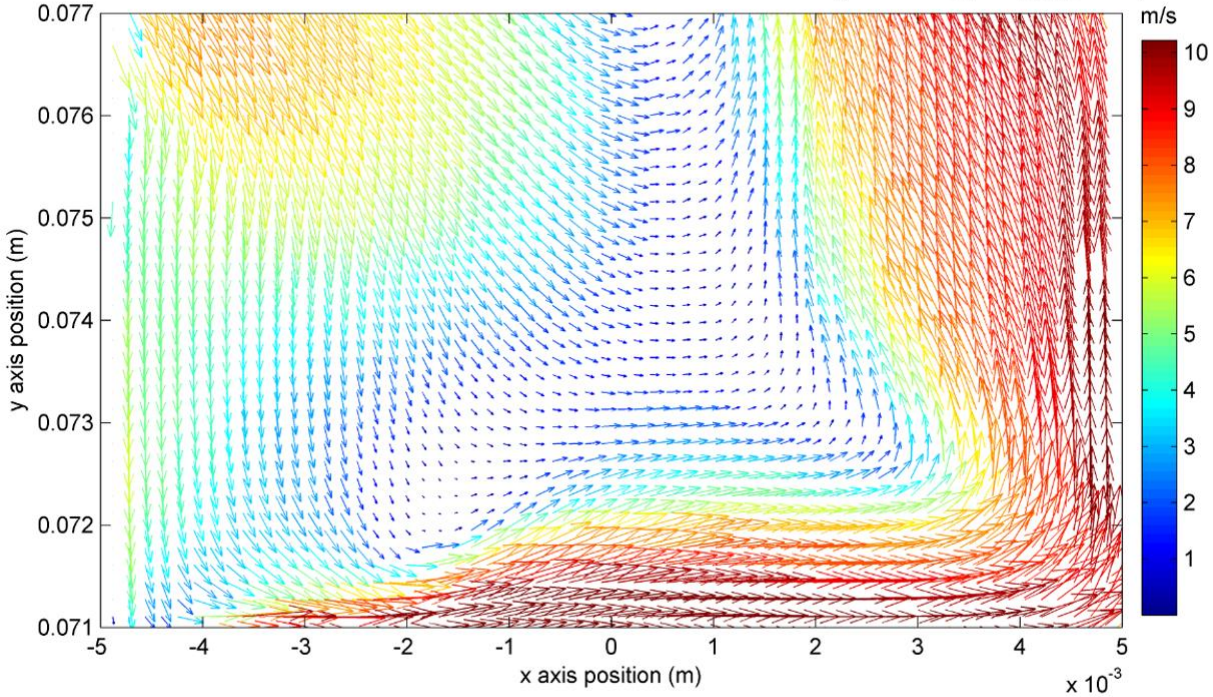

CFD Rotor Slot Tooth

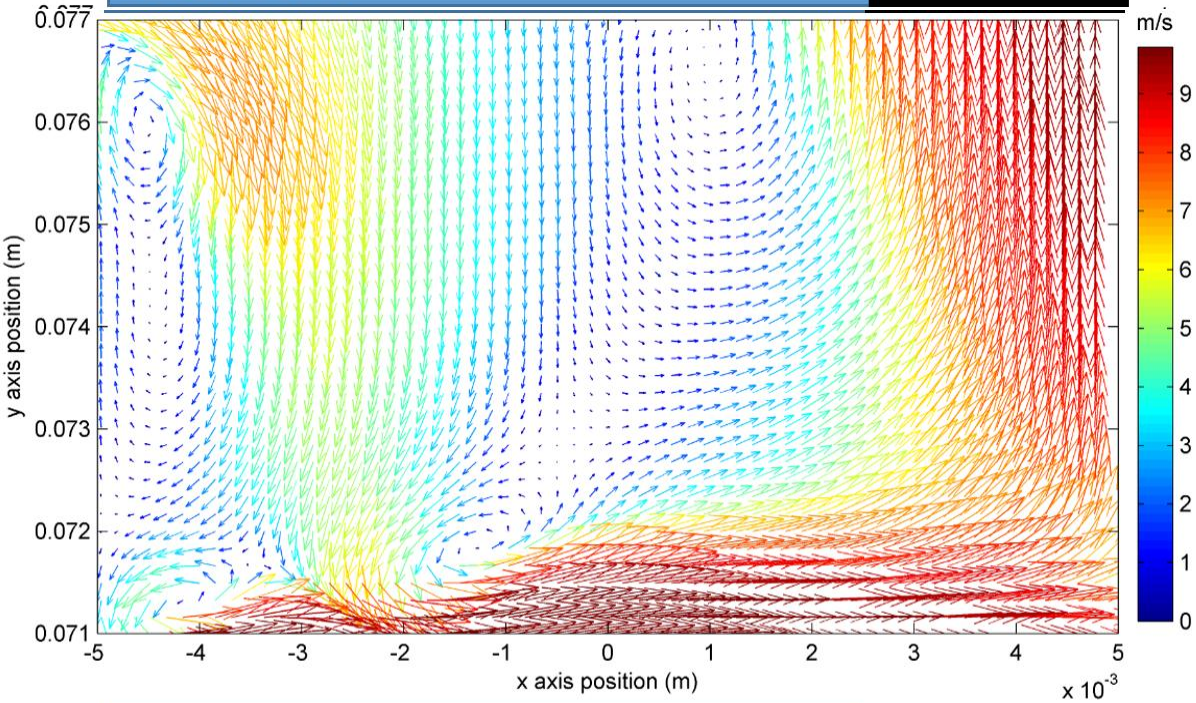

PIV Rotor Slot Tooth

Mesh level 2, N = 26 rps, θ = -1°

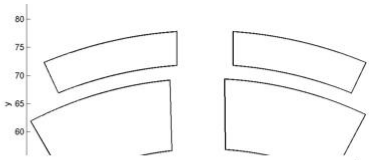

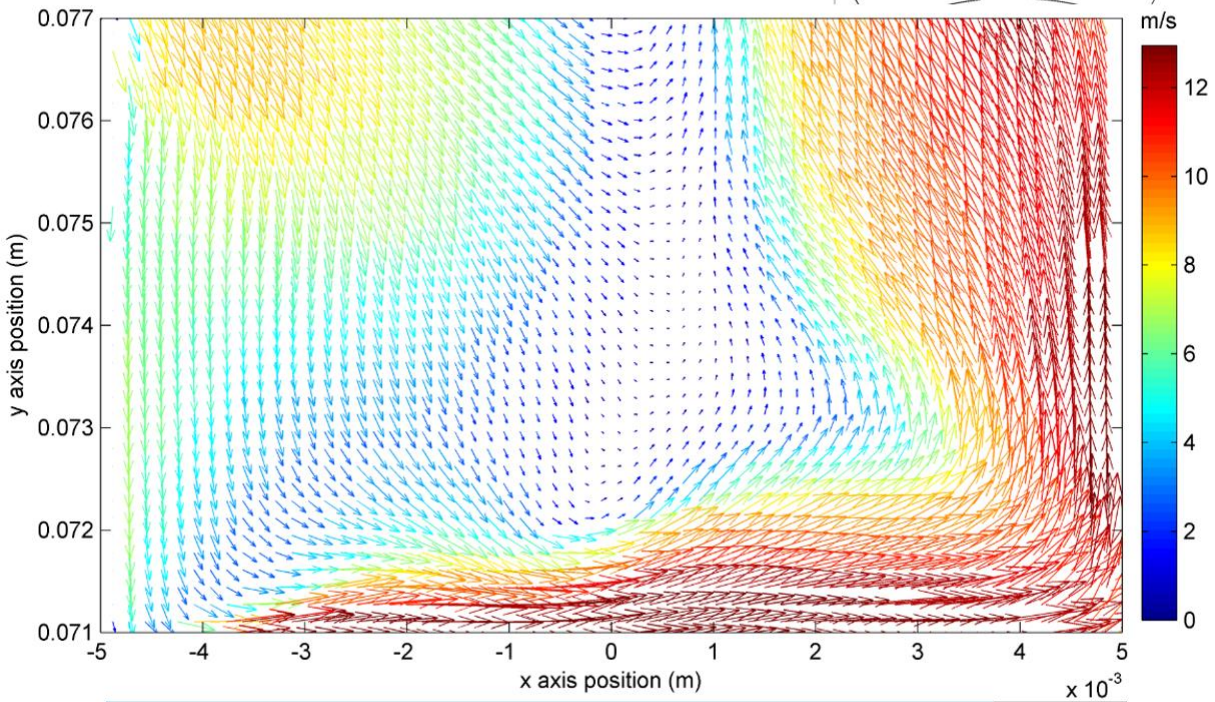

CFD Rotor Slot Tooth

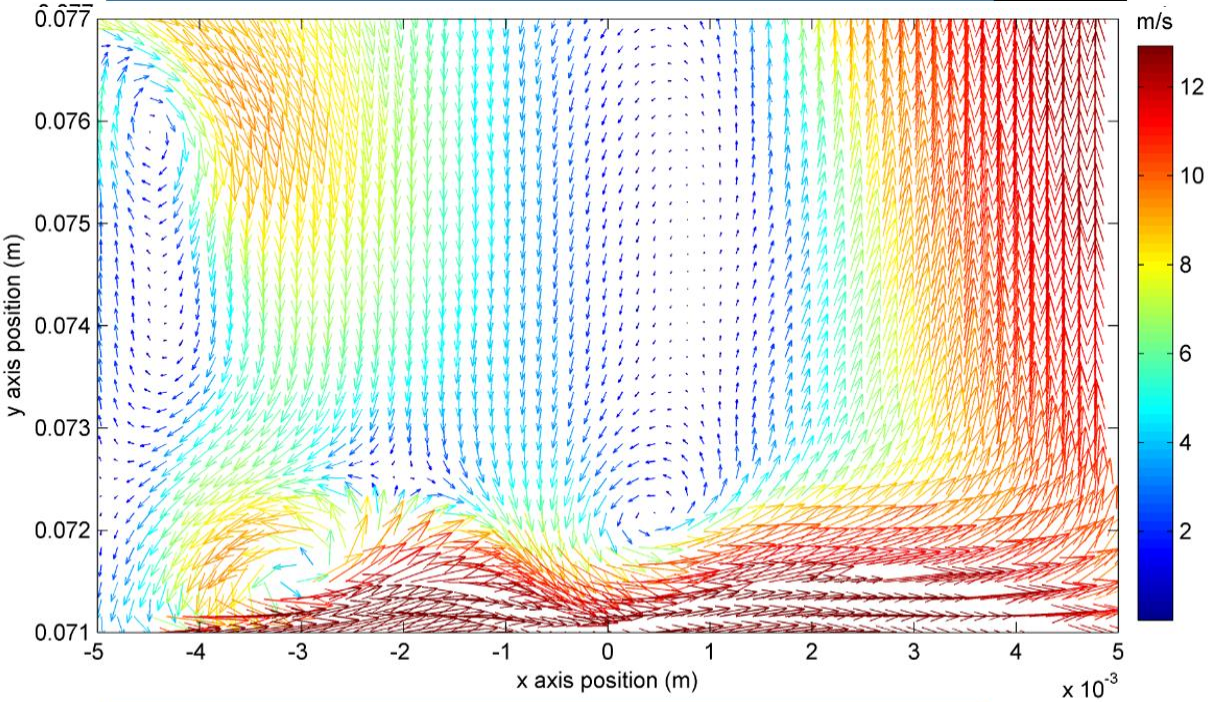

PIV Rotor Slot Tooth

Mesh level 2, N = 26 rps, θ = +1°

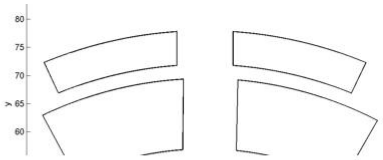

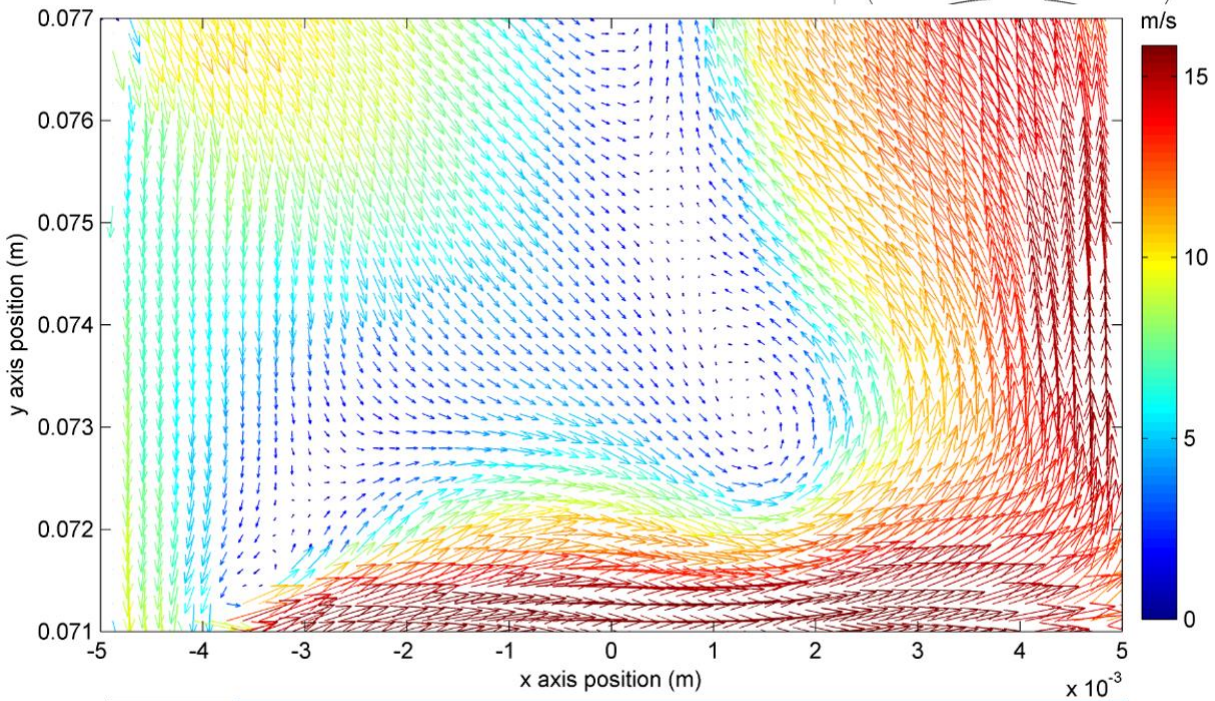

CFD

Tooth | Rotor Slot

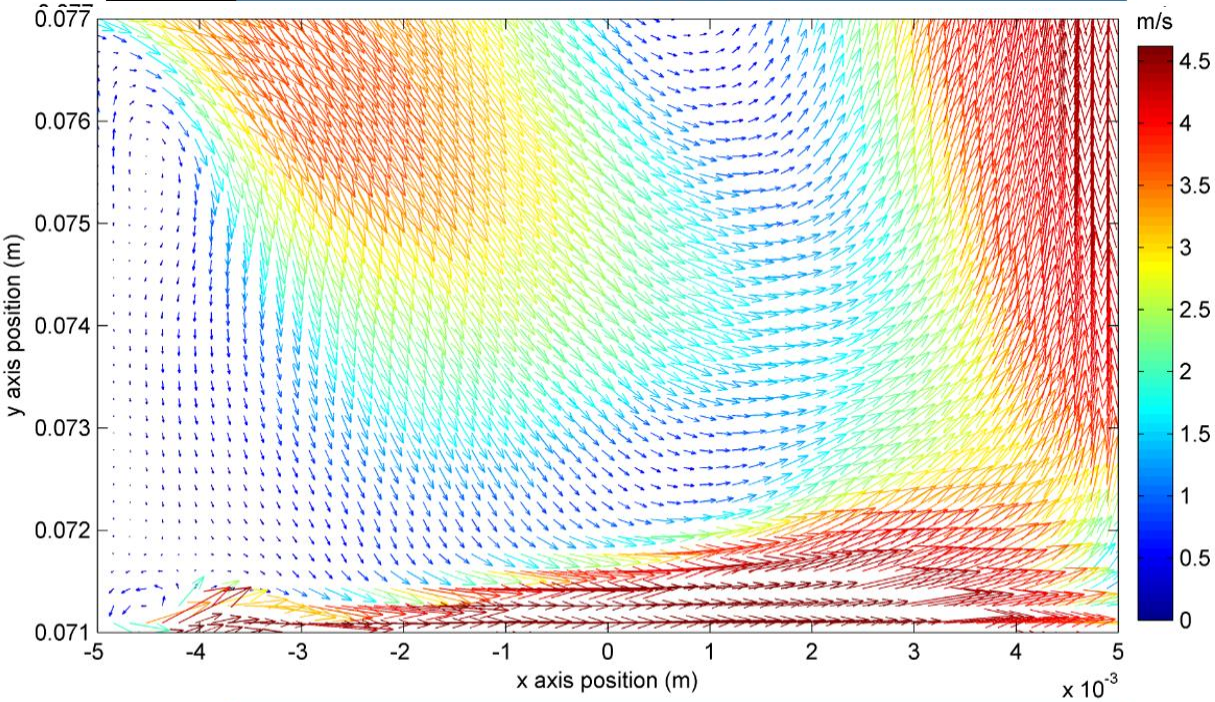

PIV

Tooth | Rotor Slot

Mesh level 2, N = 26 rps, θ = +3°

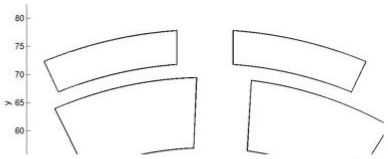

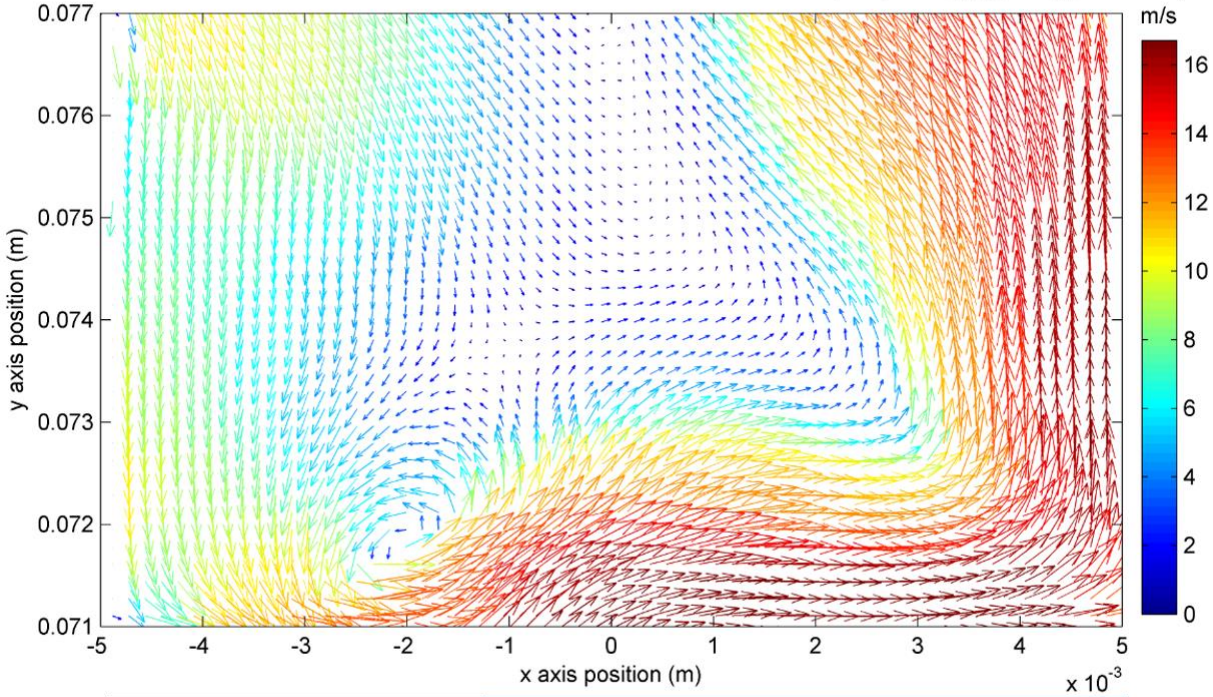

CFD Rotor Tooth Rotor Slot

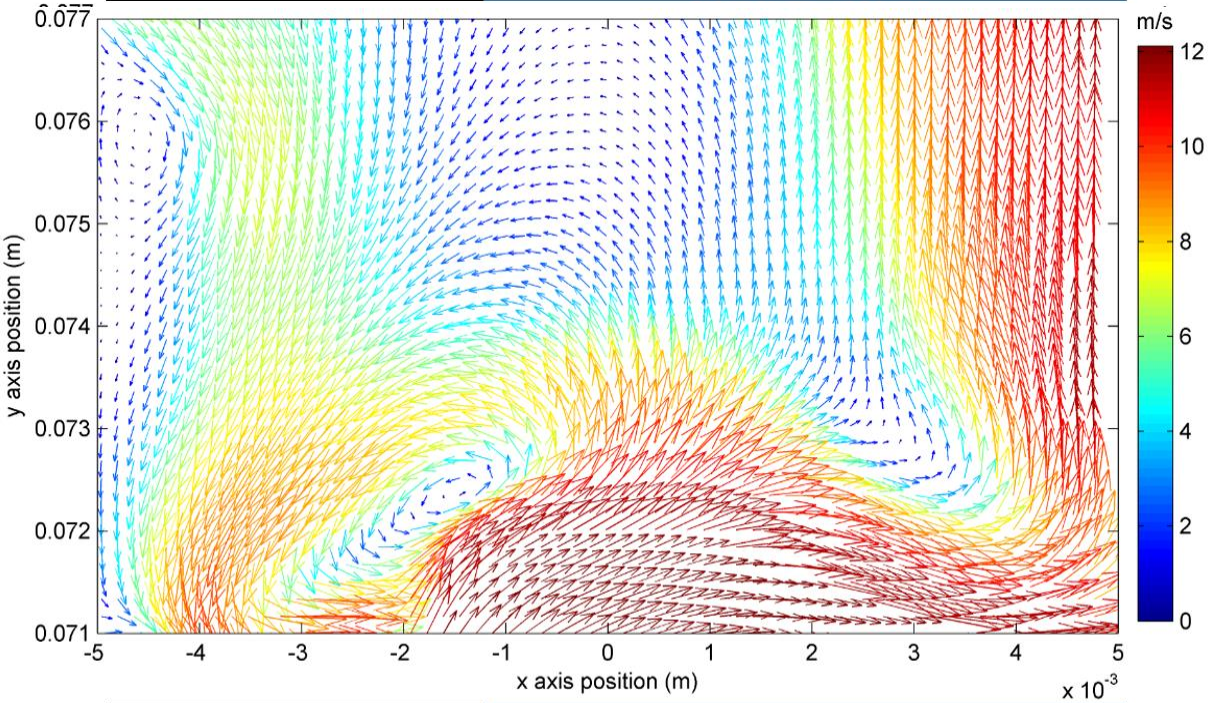

PIV Rotor Tooth Rotor Slot

Mesh level 2, N = 26 rps, θ = +5°

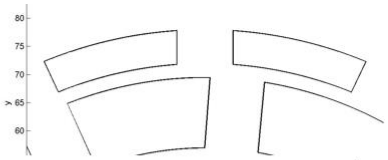

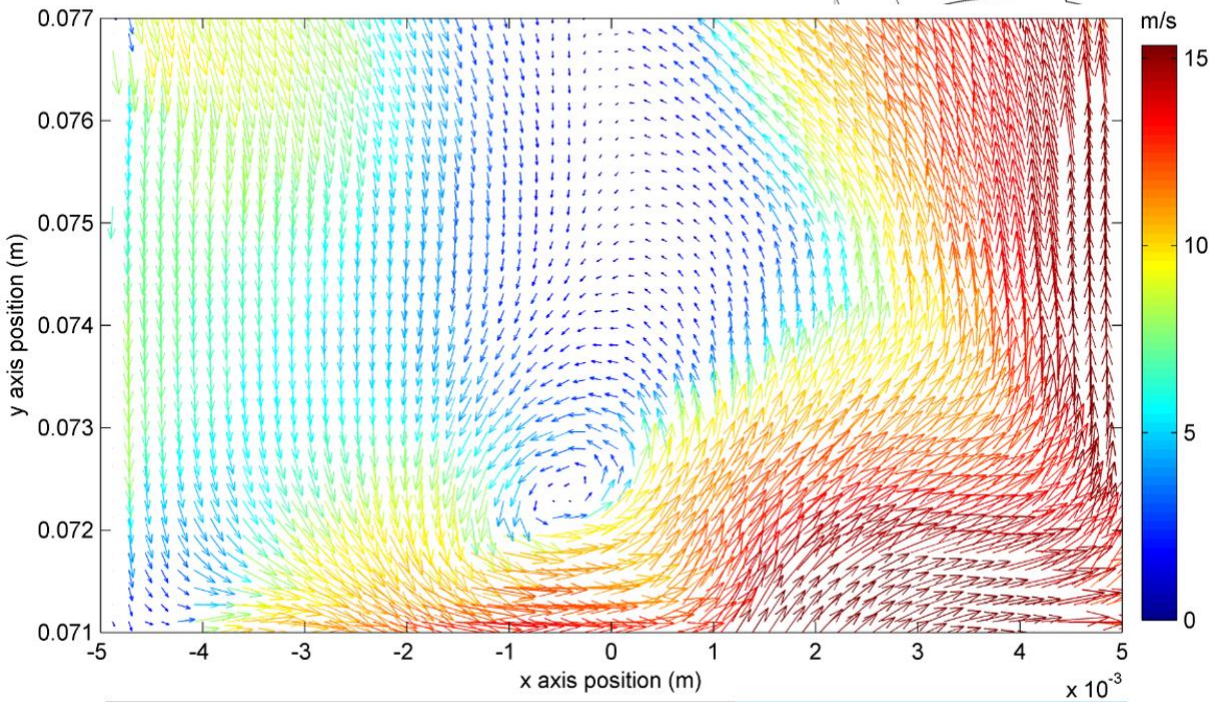

CFD

Rotor Tooth | Rotor Slot

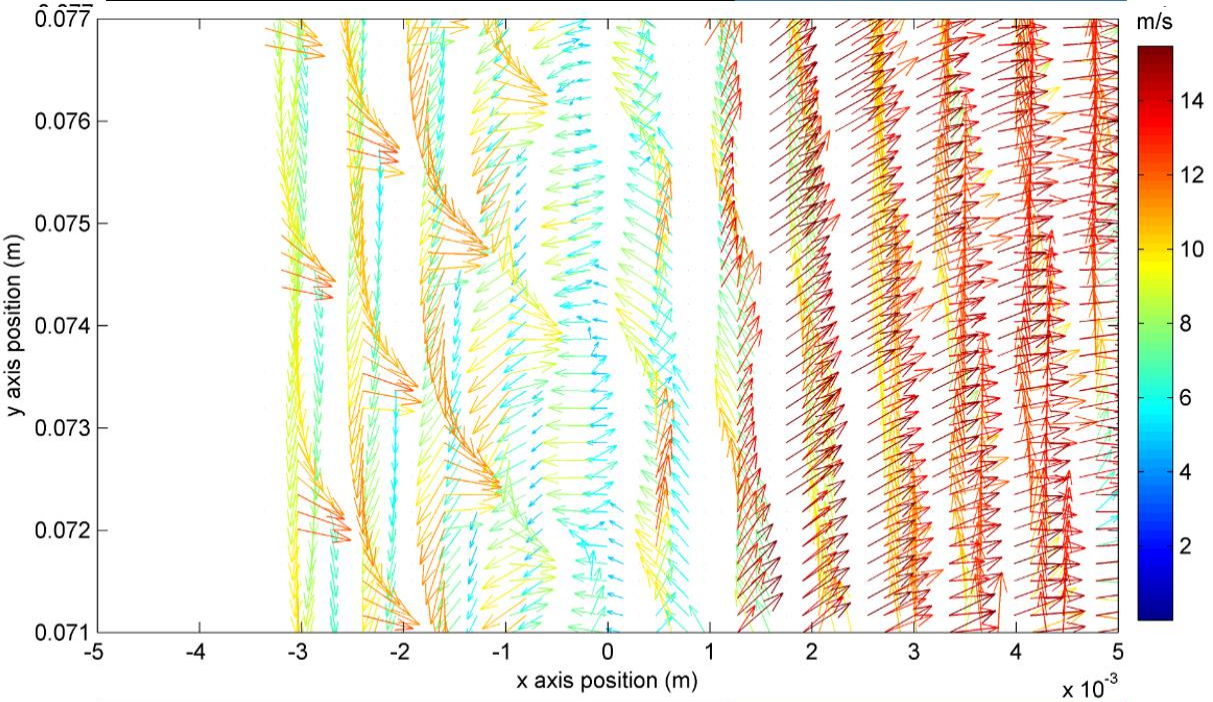

PIV

Rotor Tooth | Rotor Slot

Mesh level 2, N = 26 rps, θ = +7°

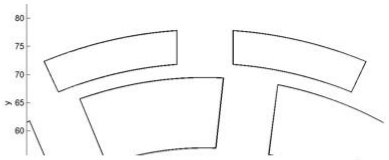

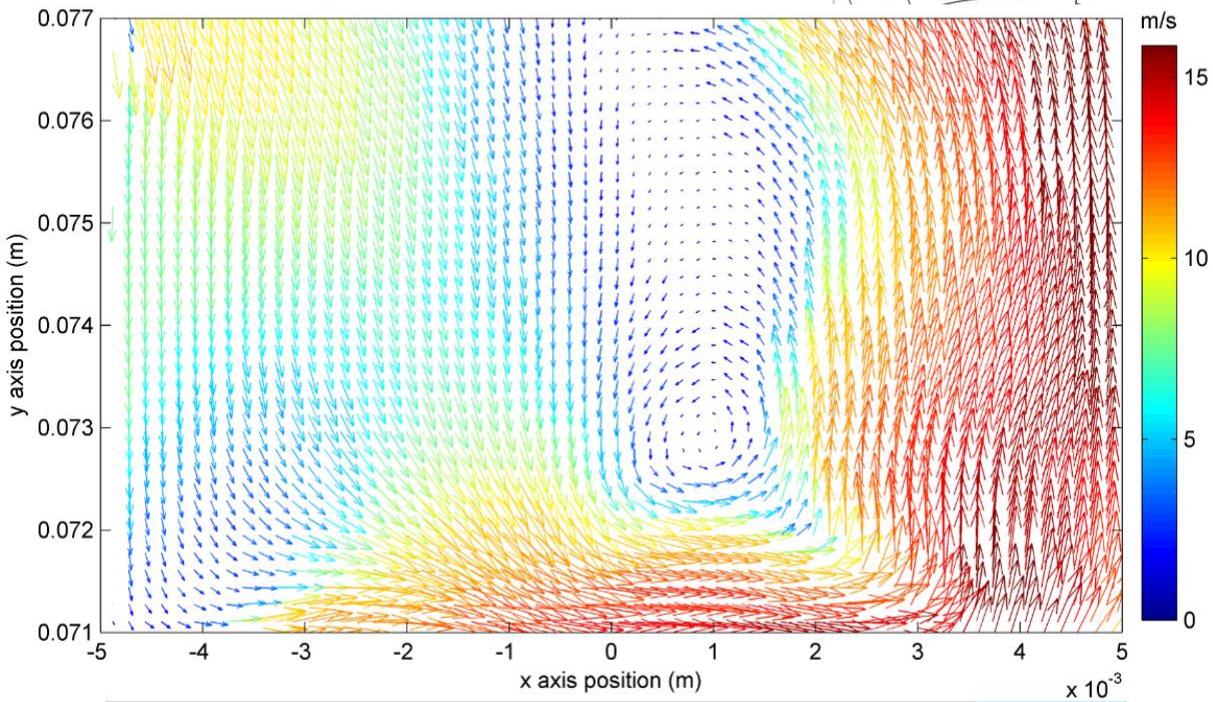

CFD

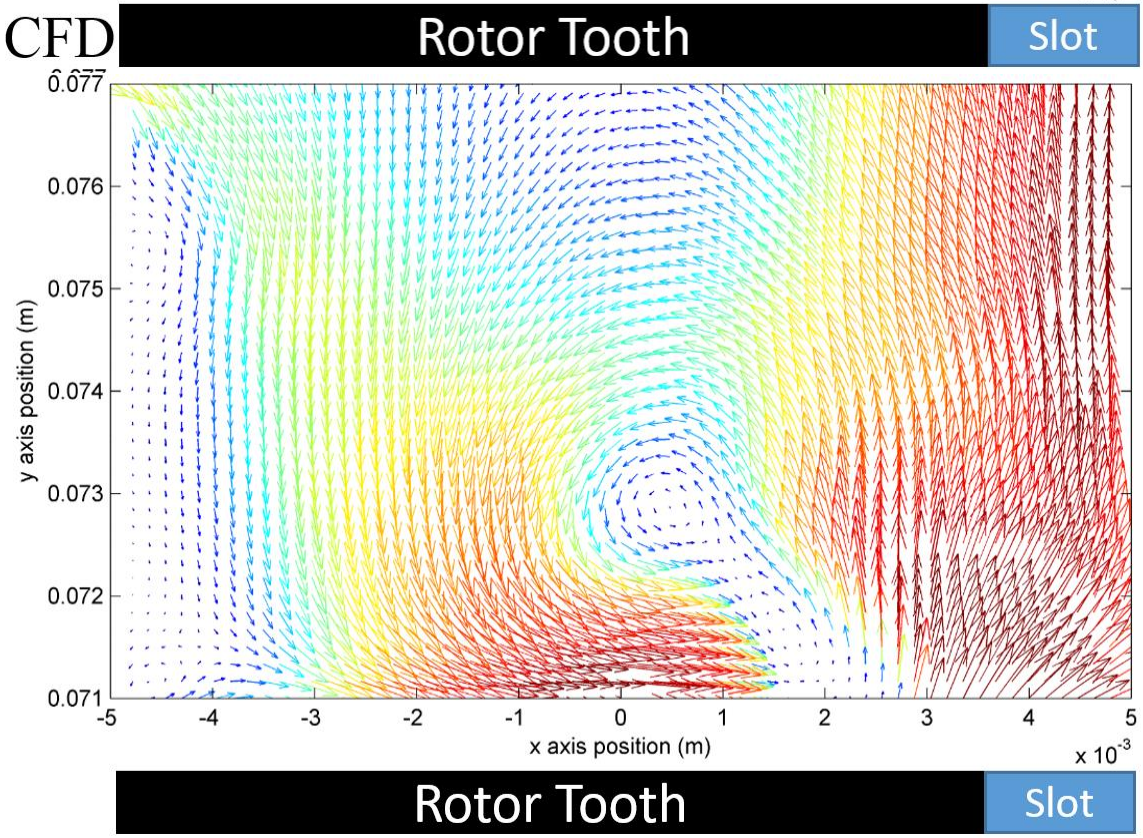

Mesh level 2, N = 26 rps, θ = +9°

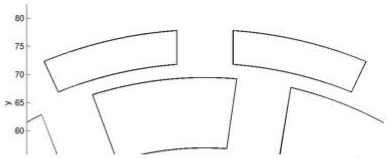

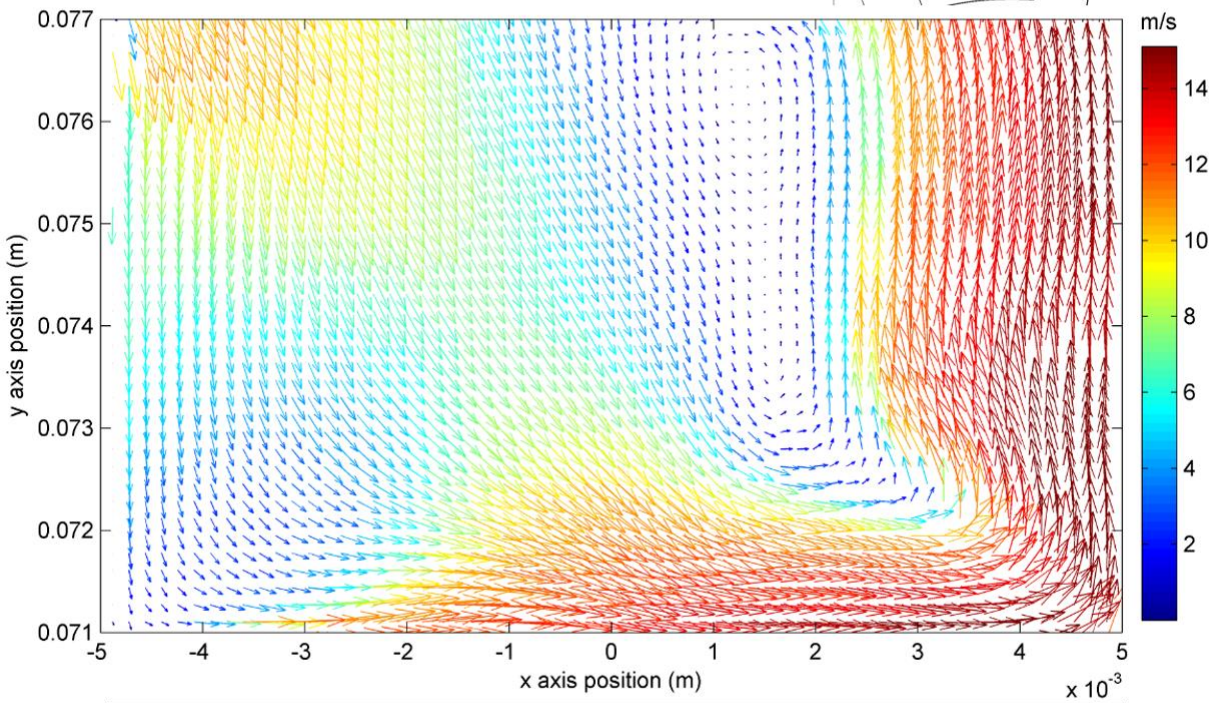

CFD Rotor Tooth

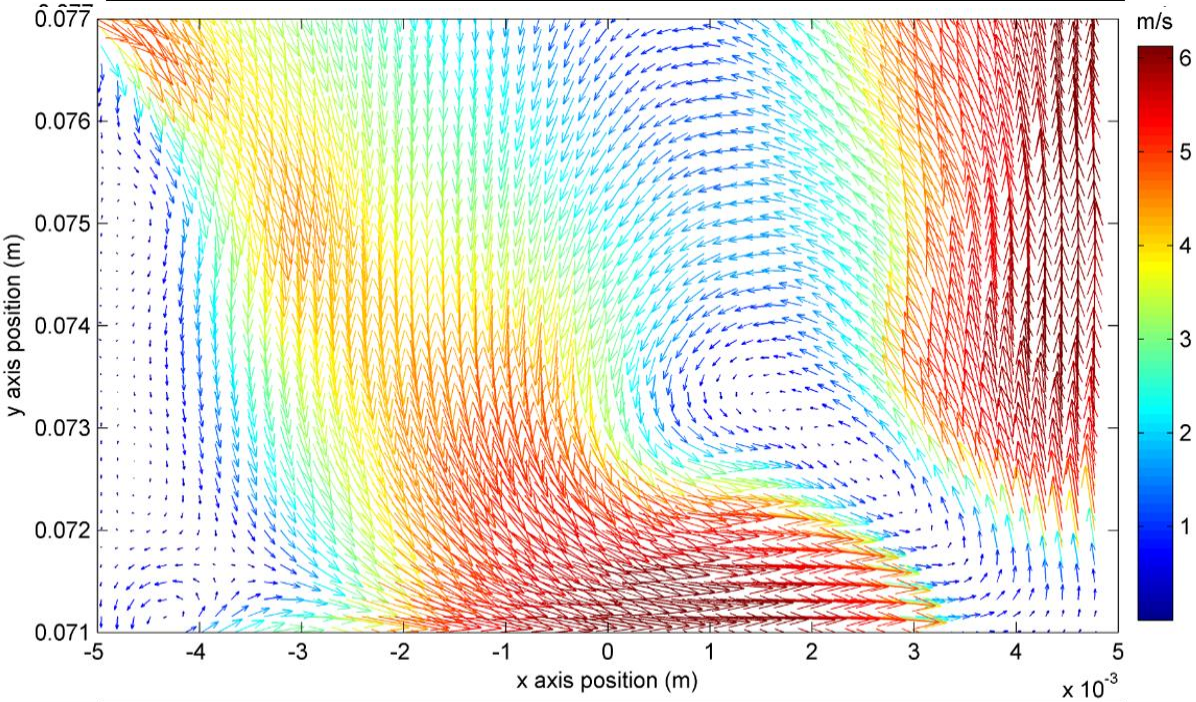

PIV Rotor Tooth

7.2. CFD Mesh Level 2 vs 3 XY-Plane Velocity Vector Plots of Slot 1

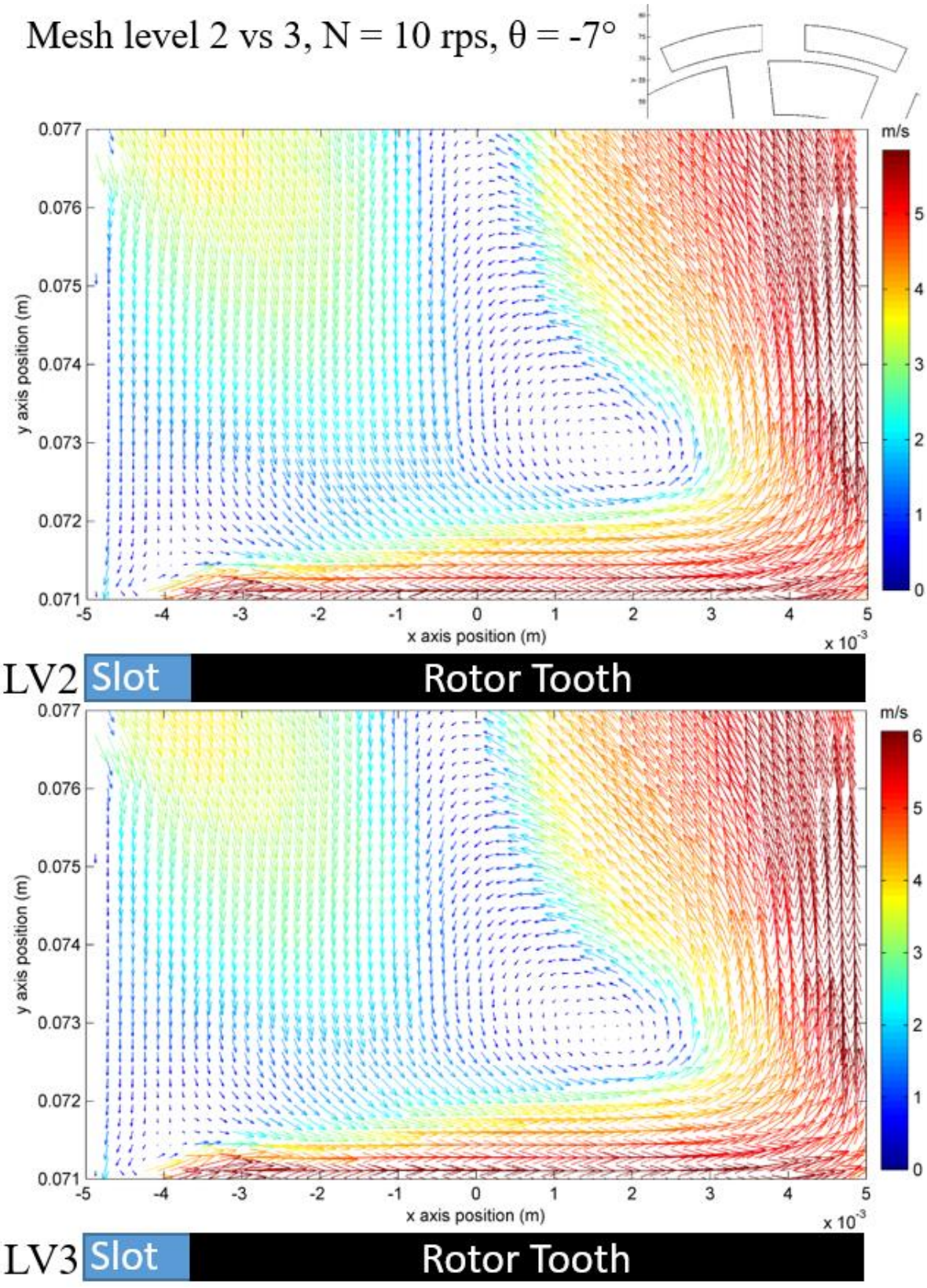

Mesh level 2 vs 3, N = 10 rps, θ = -5°

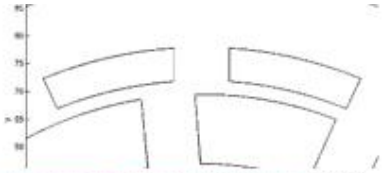

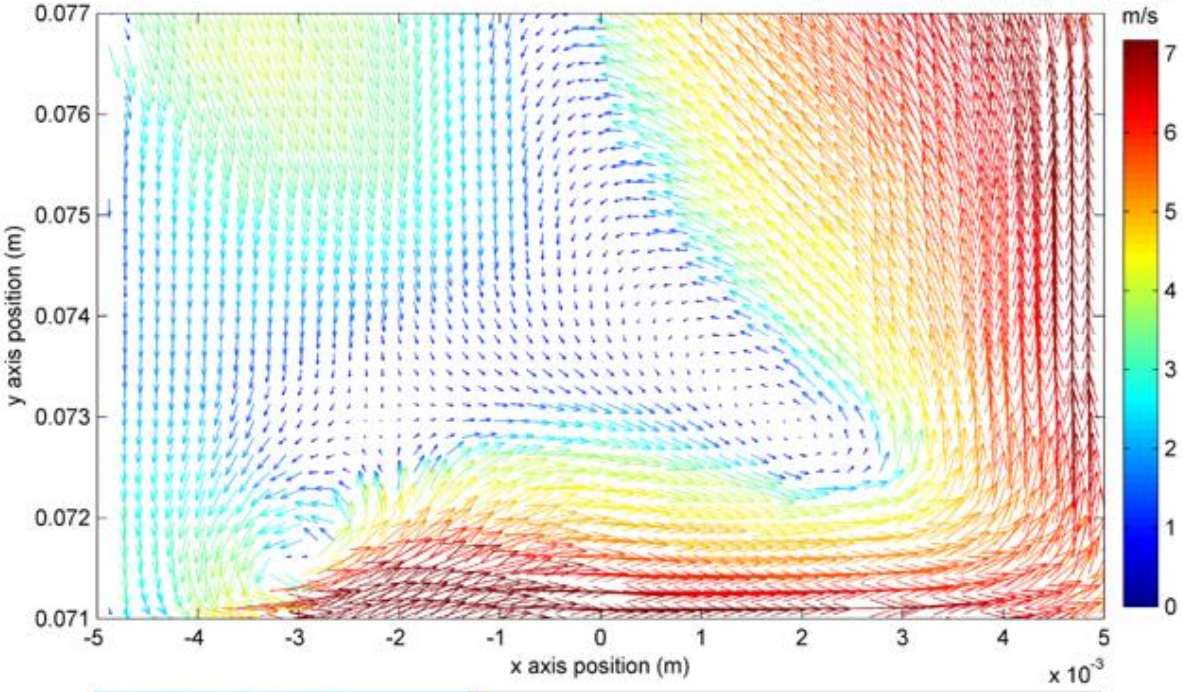

LV2 Rotor Slot Rotor Tooth

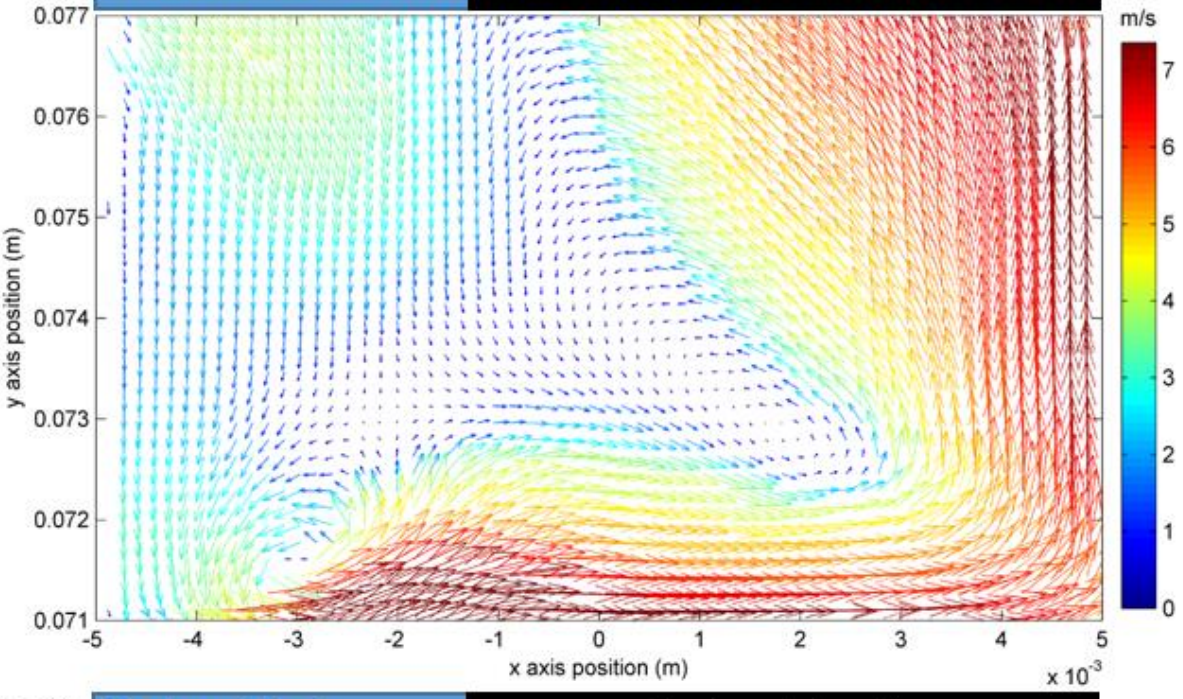

LV3 Rotor Slot Rotor Tooth

Mesh level 2 vs 3, N = 10 rps, θ = -3°

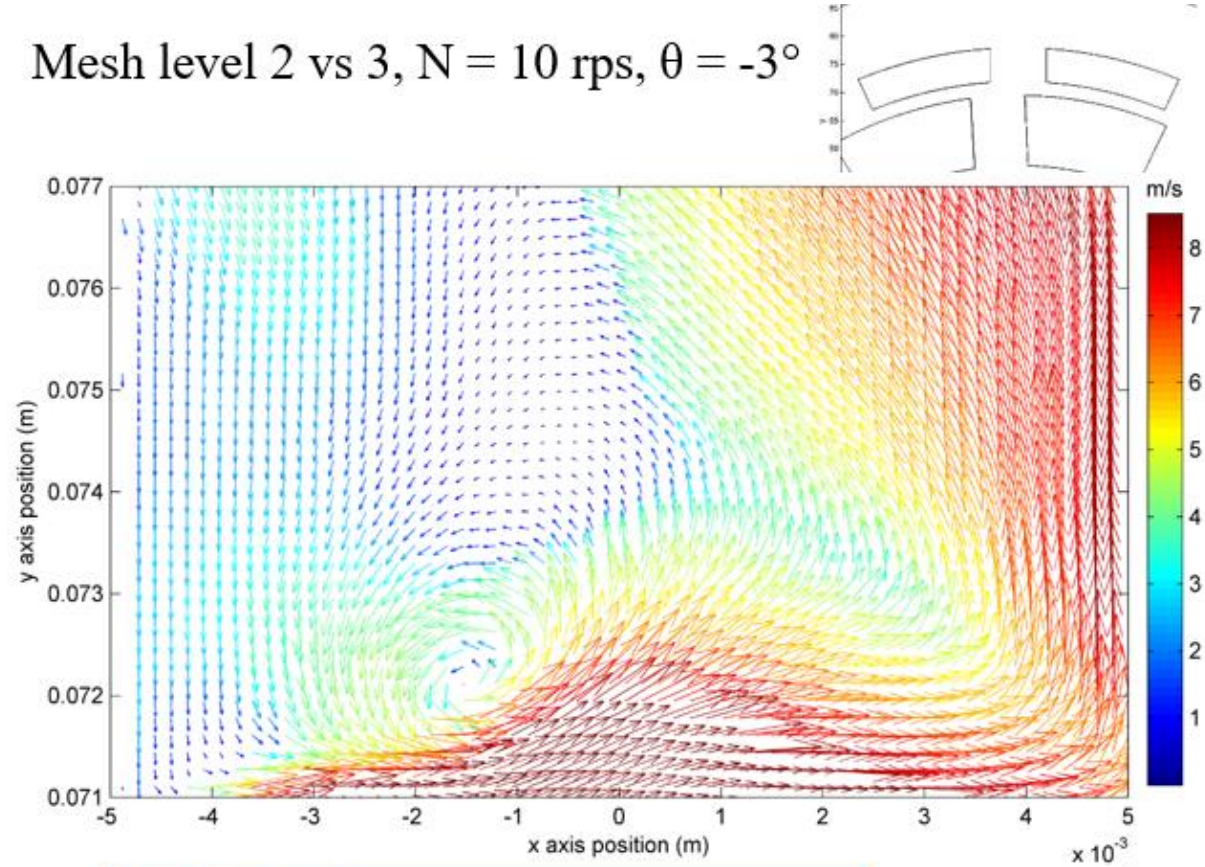

LV2 Rotor Slot Tooth

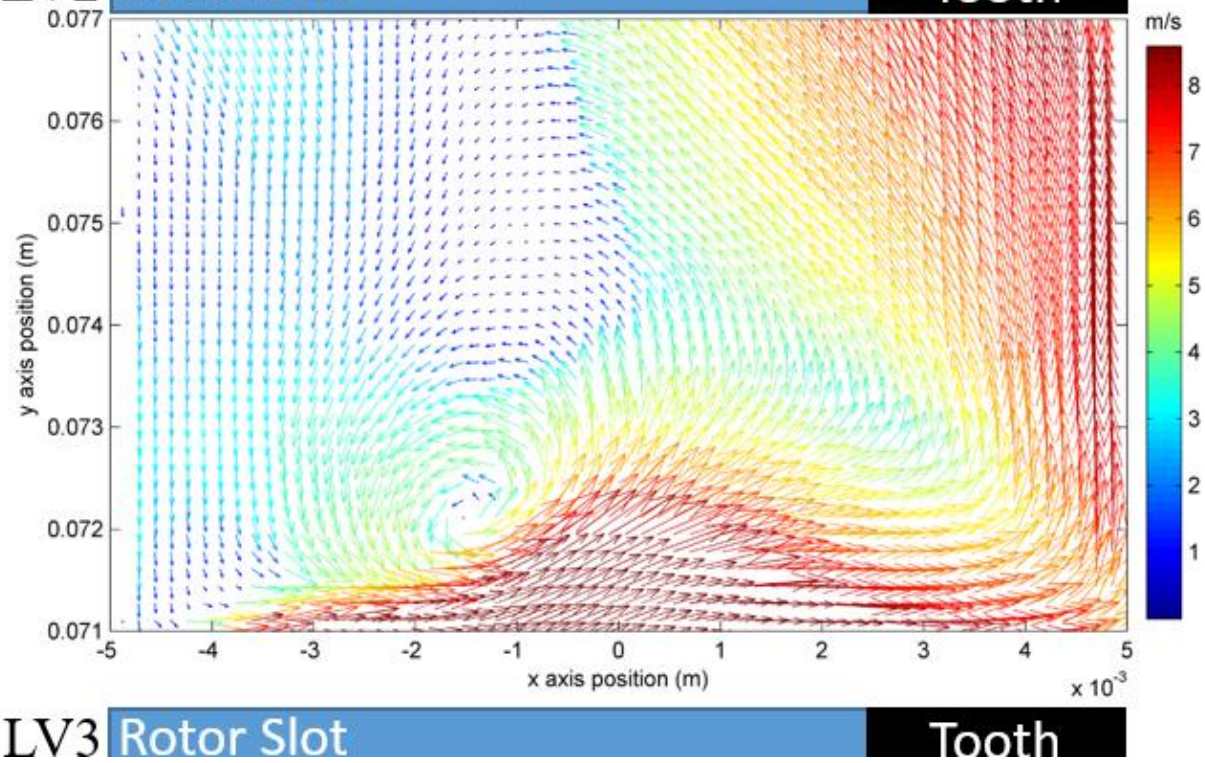

LV3 Rotor Slot Tooth

Mesh level 2 vs 3, N = 10 rps, θ = -1°

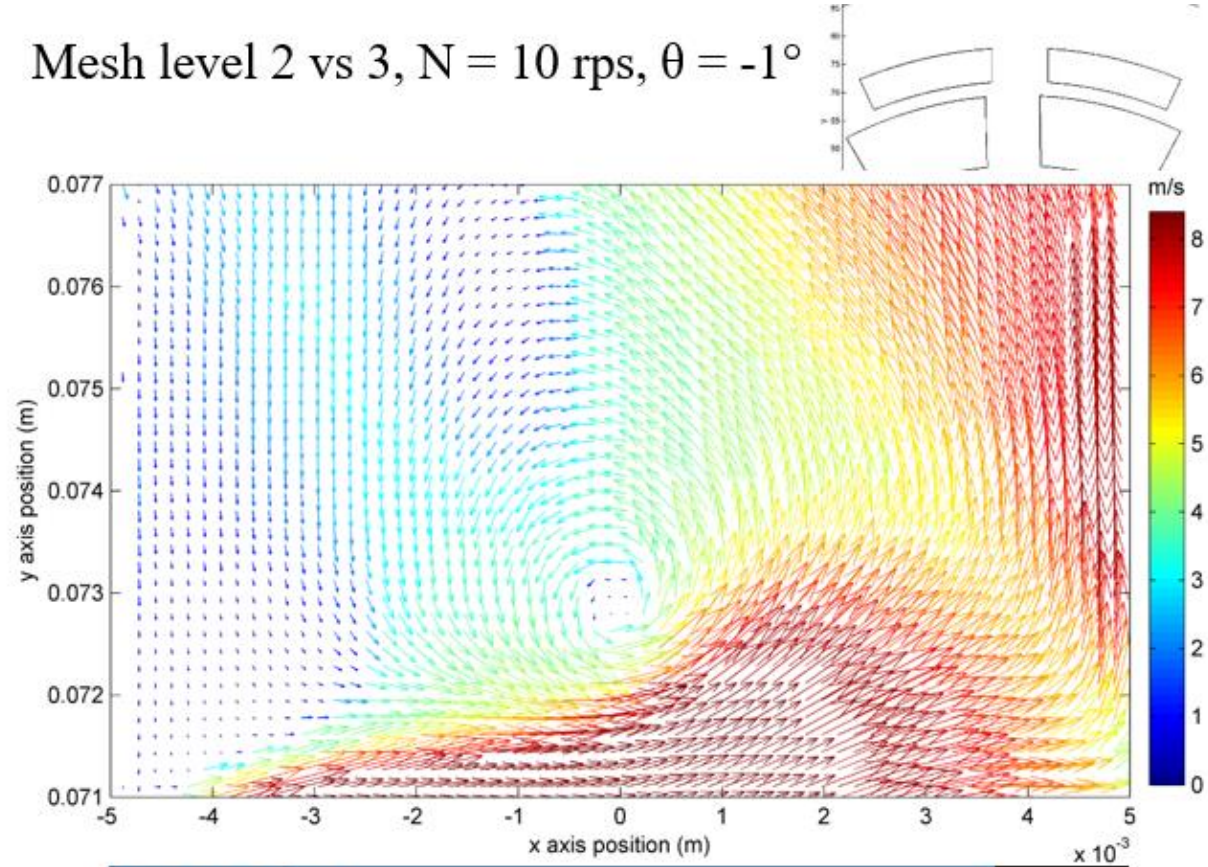

LV2 Rotor Slot Tooth

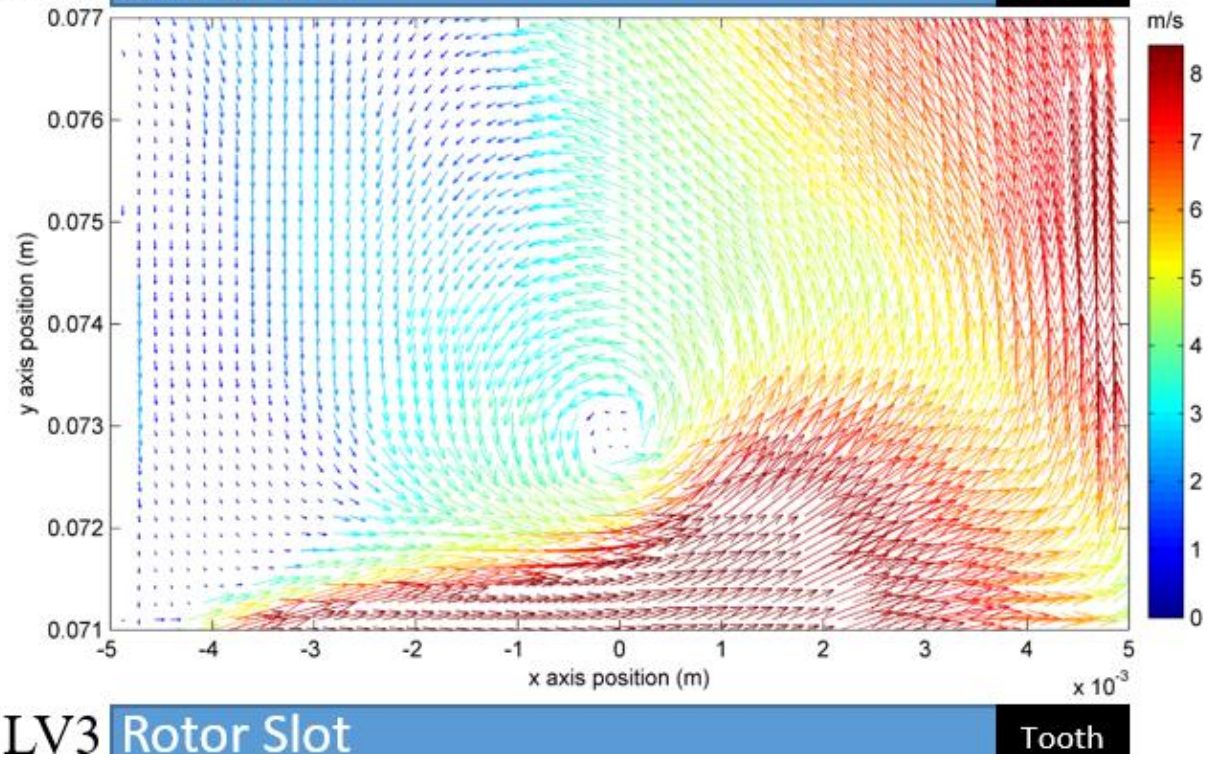

LV3 Rotor Slot Tooth

Mesh level 2 vs 3, N = 10 rps, θ = +1°

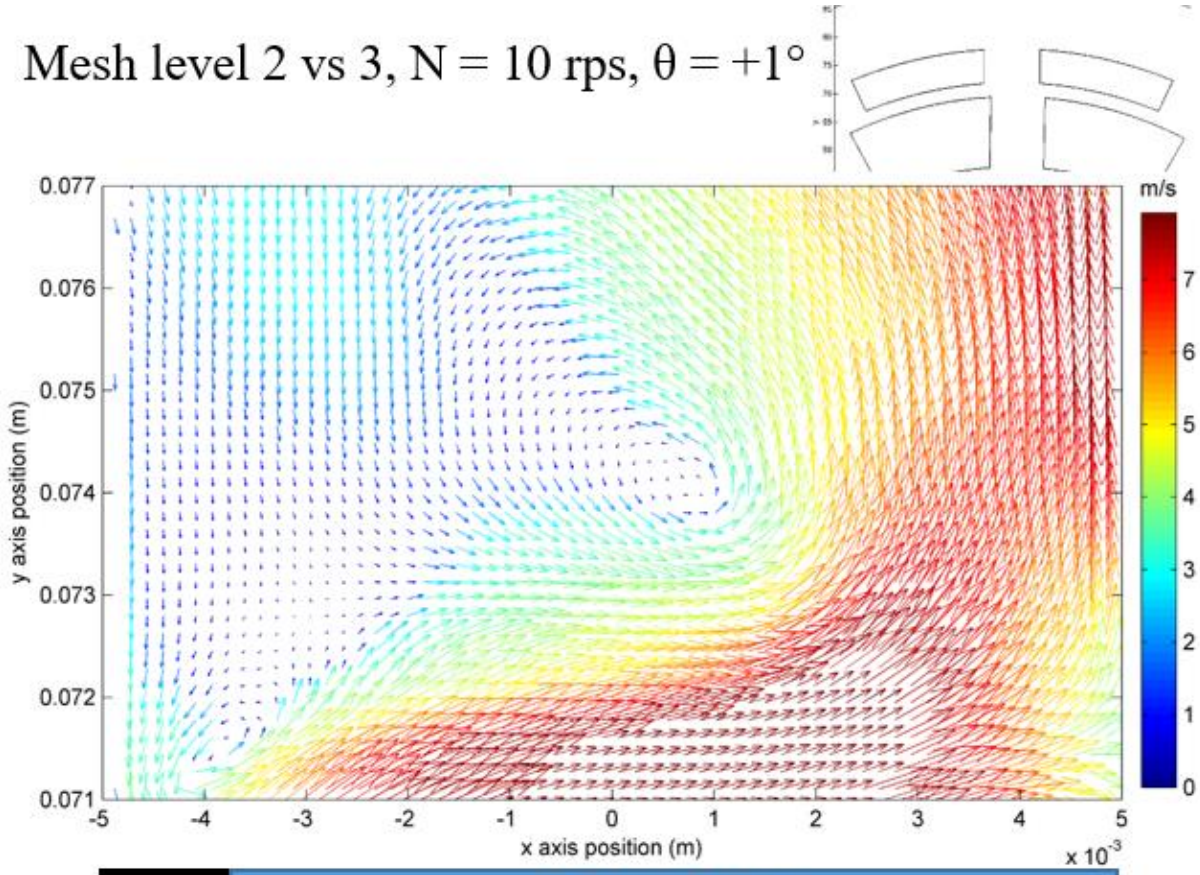

LV2 Tooth Rotor Slot

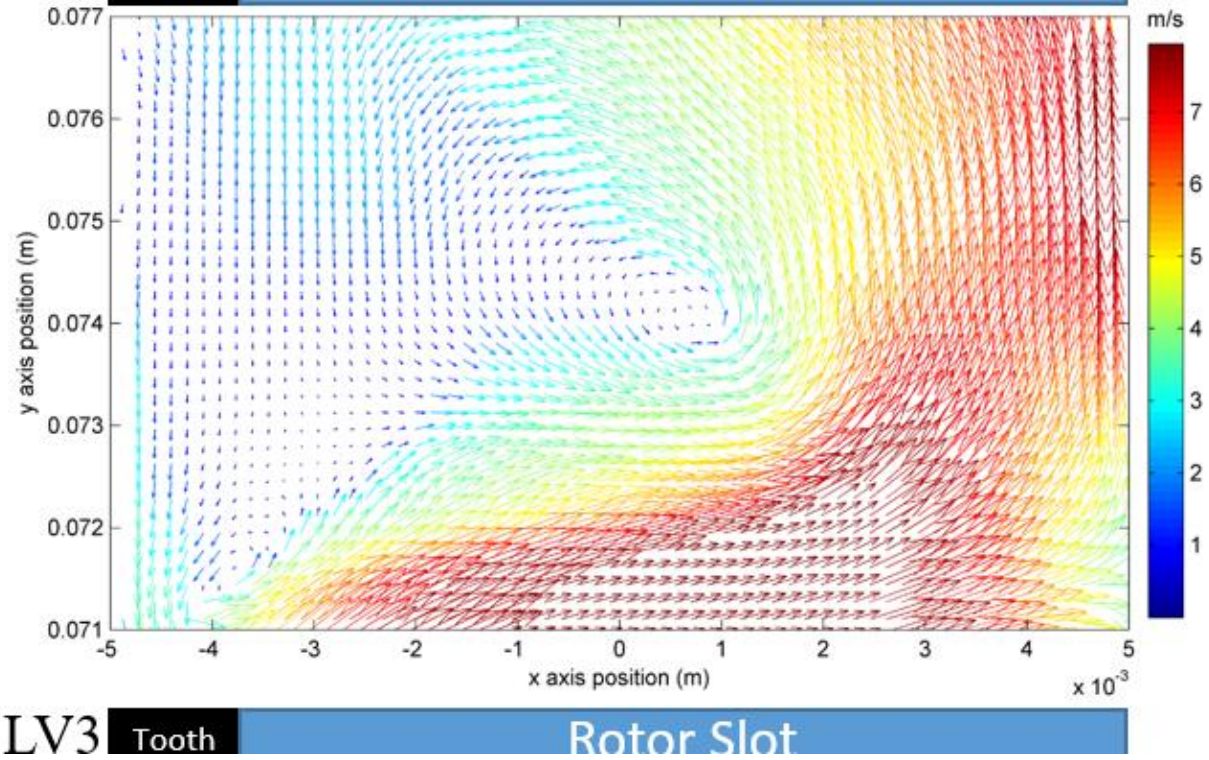

LV3 Tooth Rotor Slot

Mesh level 2 vs 3, N = 10 rps, θ = +3°

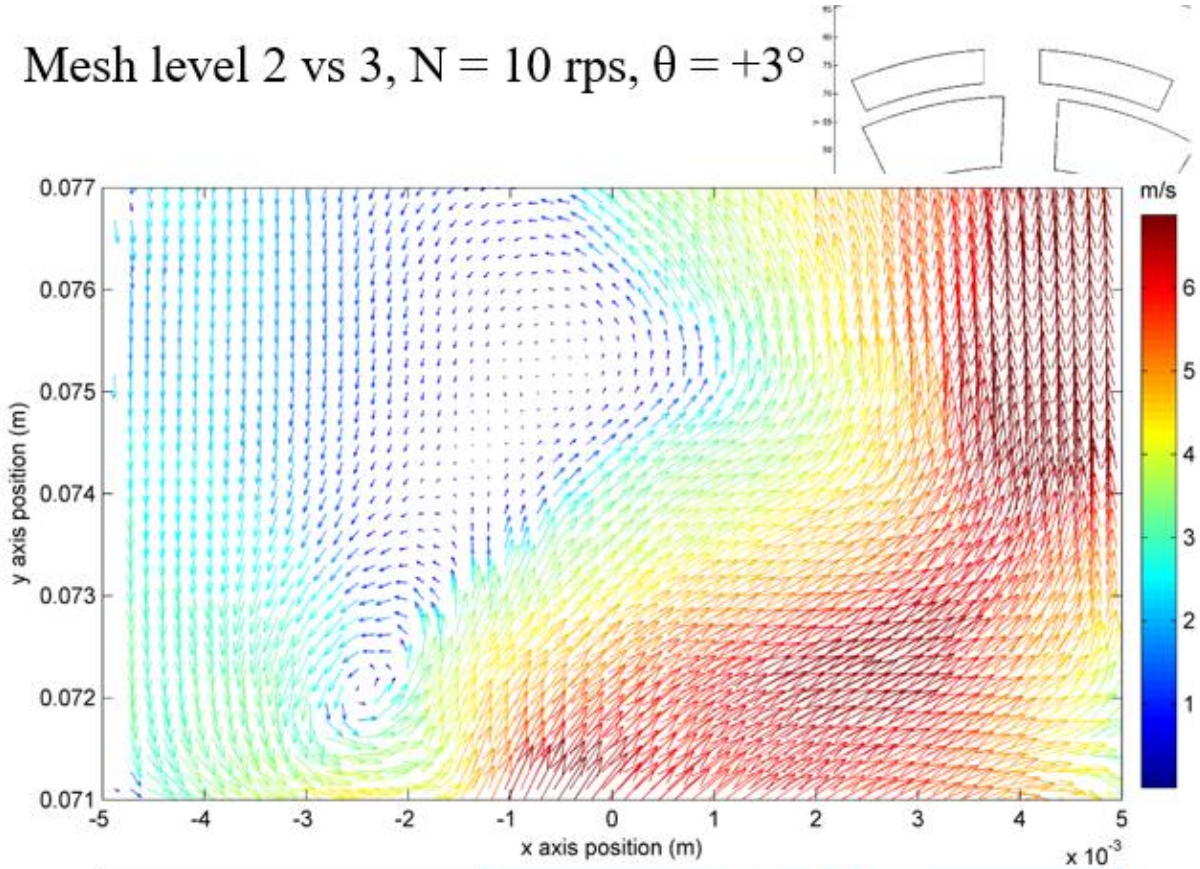

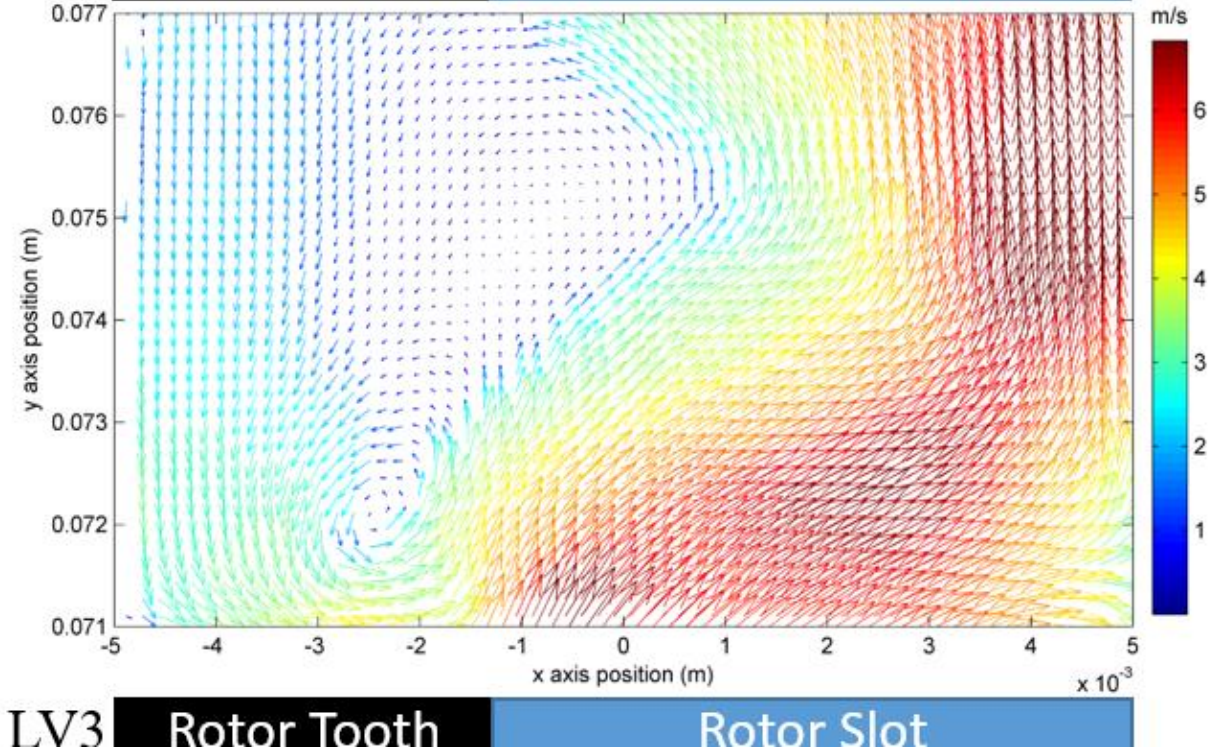

Mesh level 2 vs 3, N = 10 rps, θ = +5°

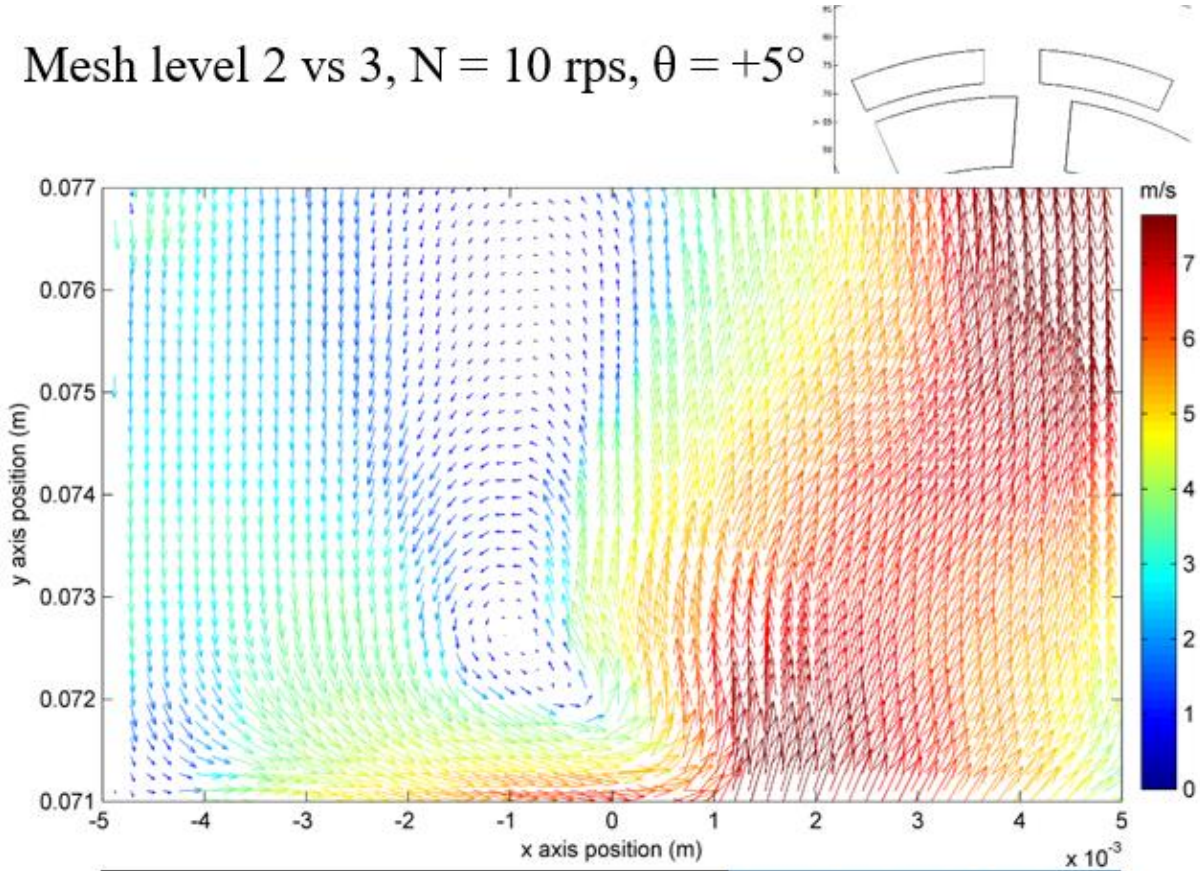

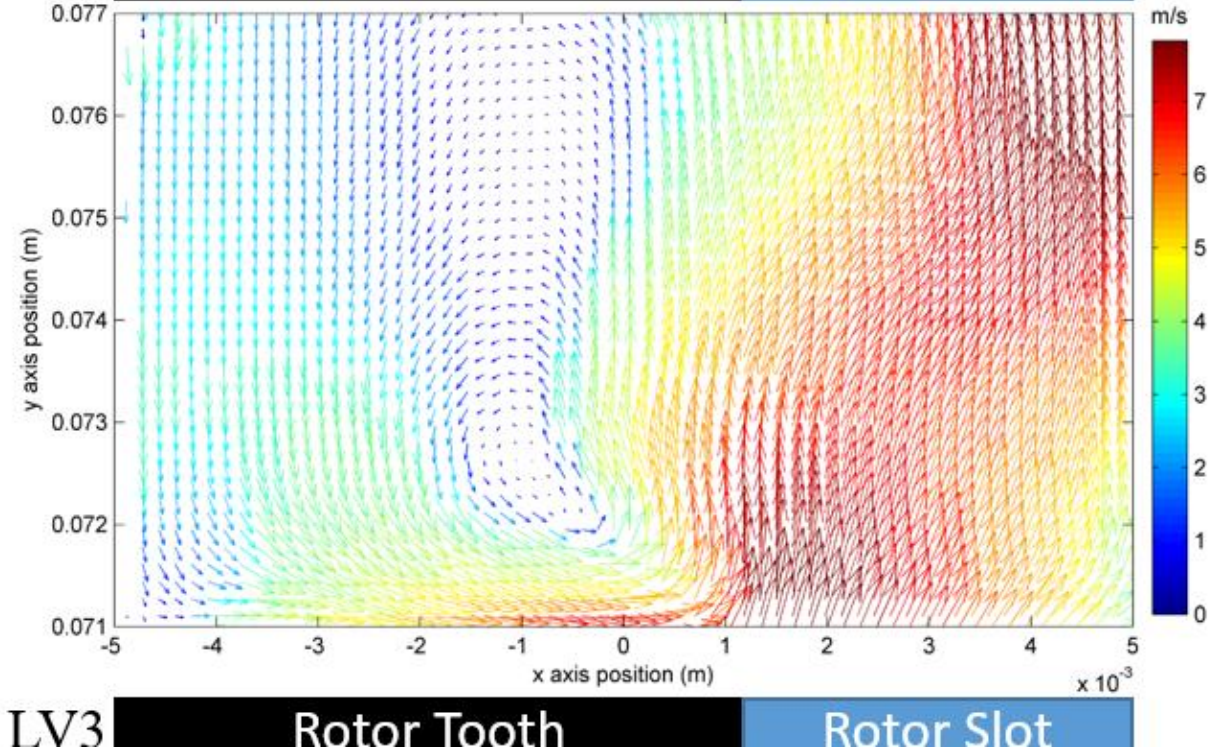

Mesh level 2 vs 3, N = 10 rps, θ = +7°

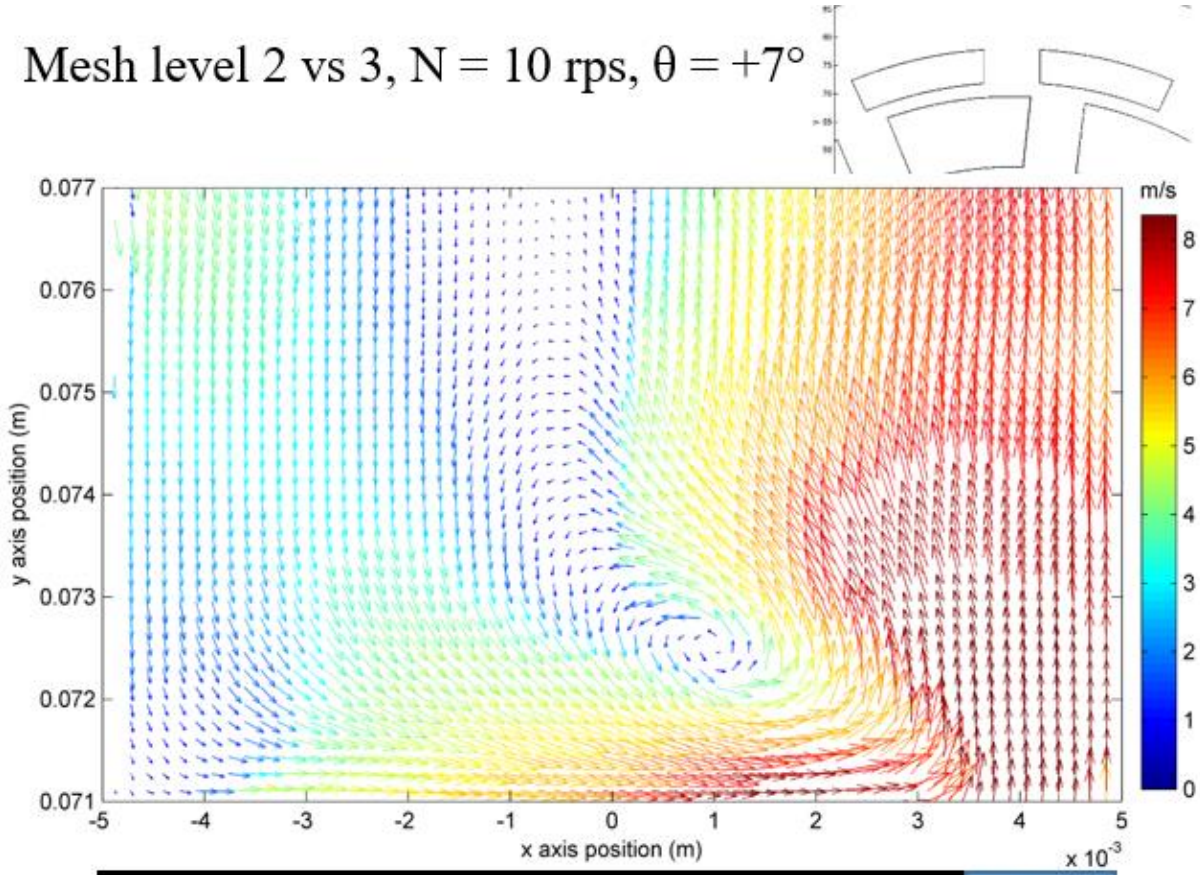

LV2

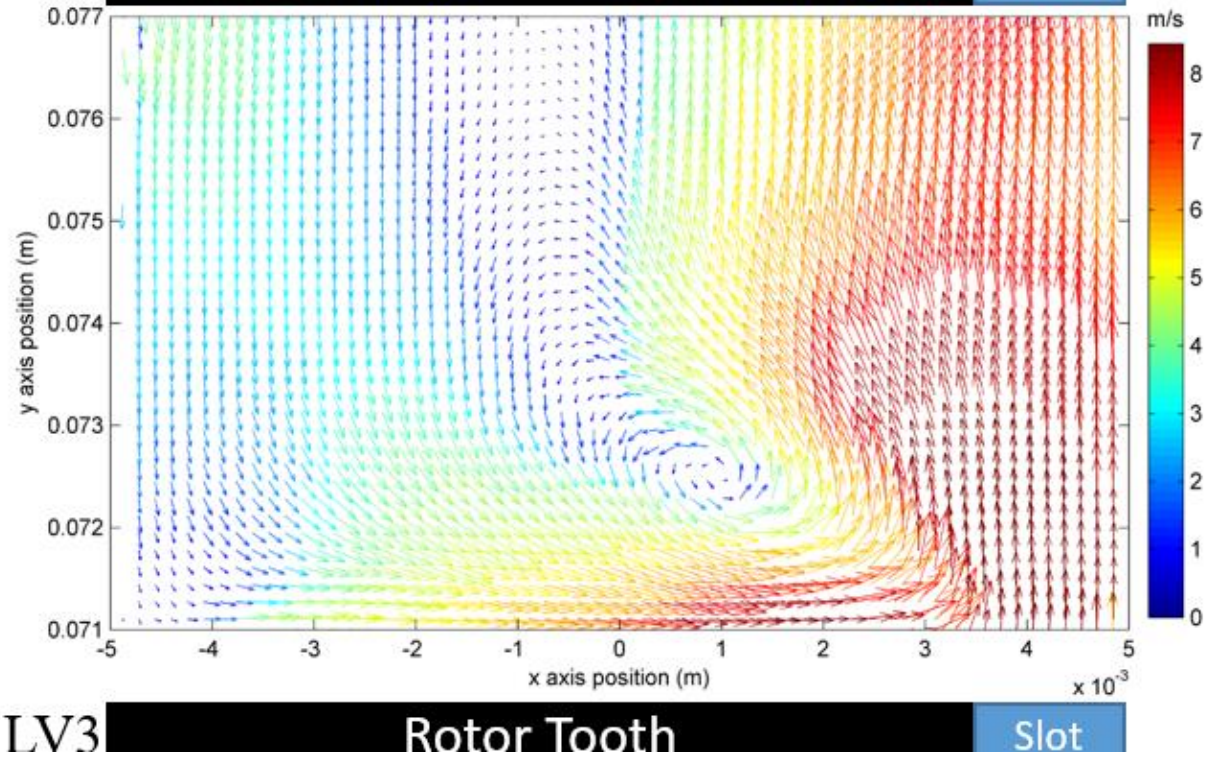

LV3

Mesh level 2 vs 3, N = 10 rps, θ = +9°

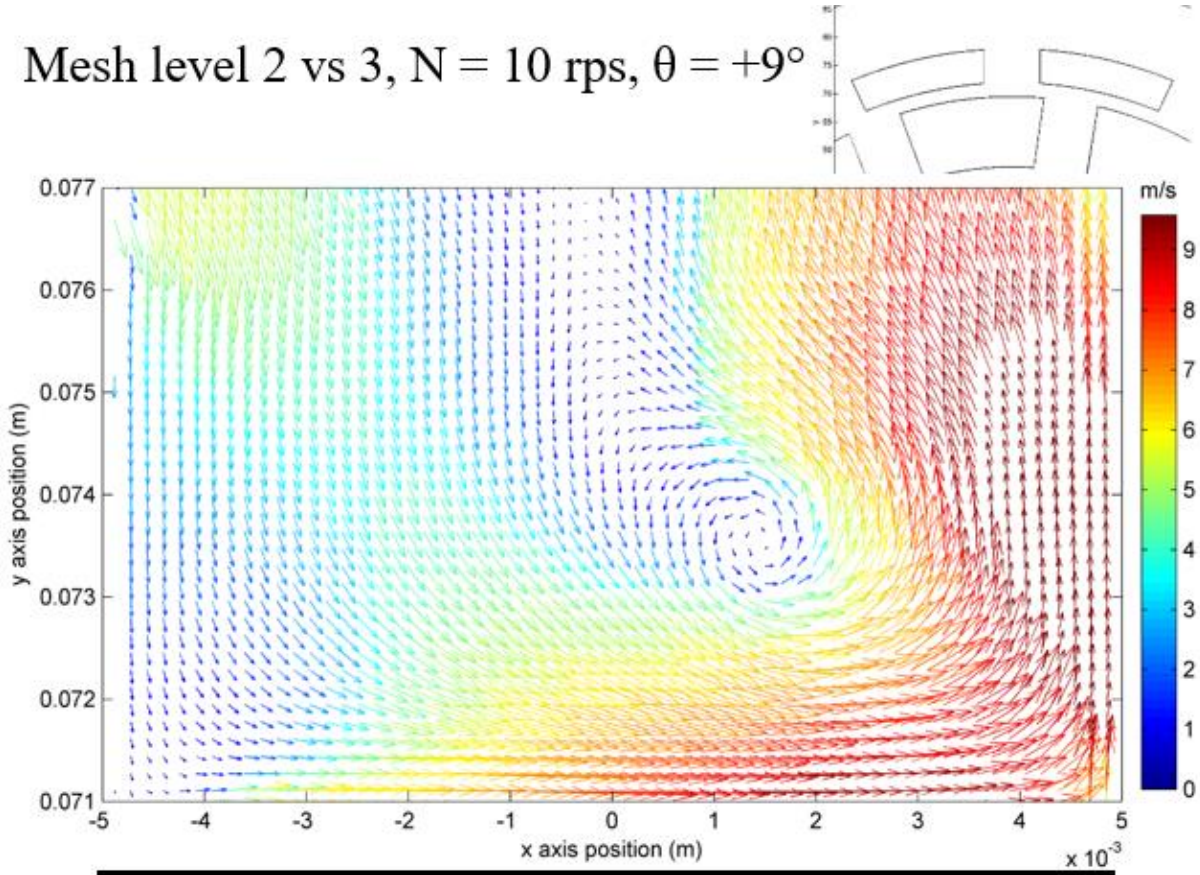

LV2 Rotor Tooth

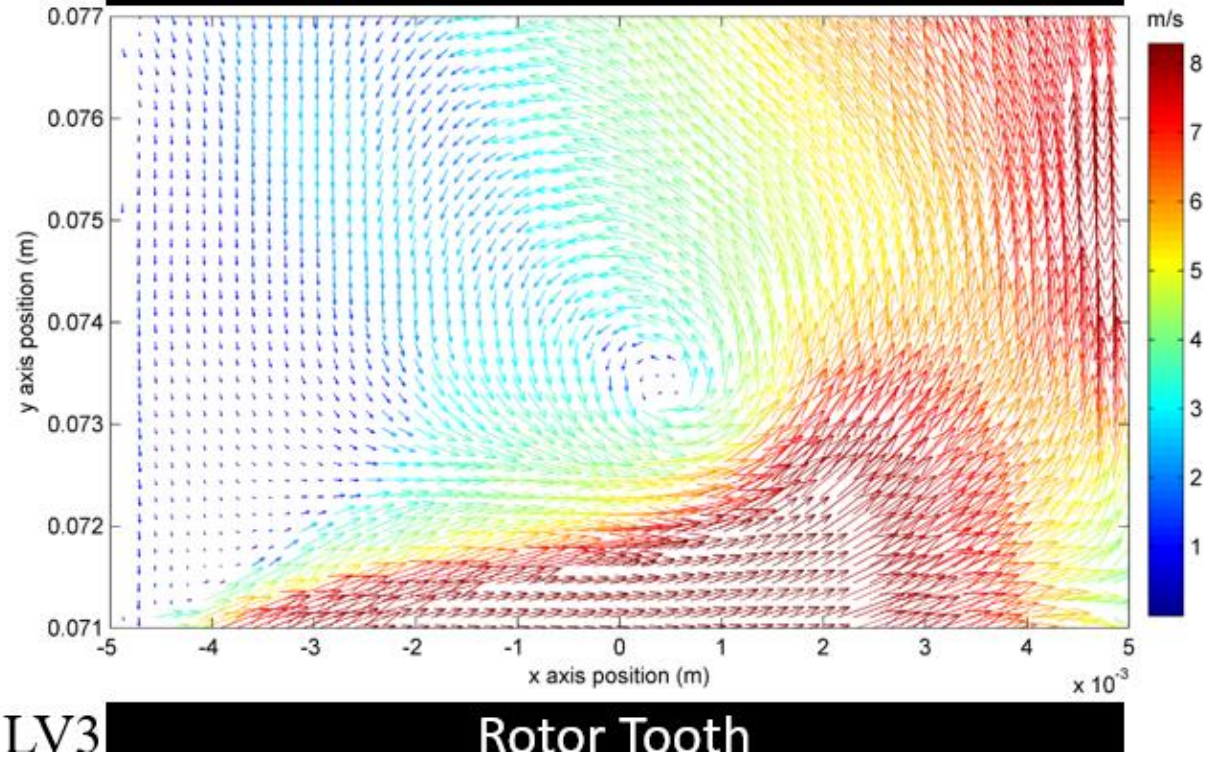

LV3 Rotor Tooth

7.3. Large Print of Exit Y-velocity in Different Depths (Figure 31)

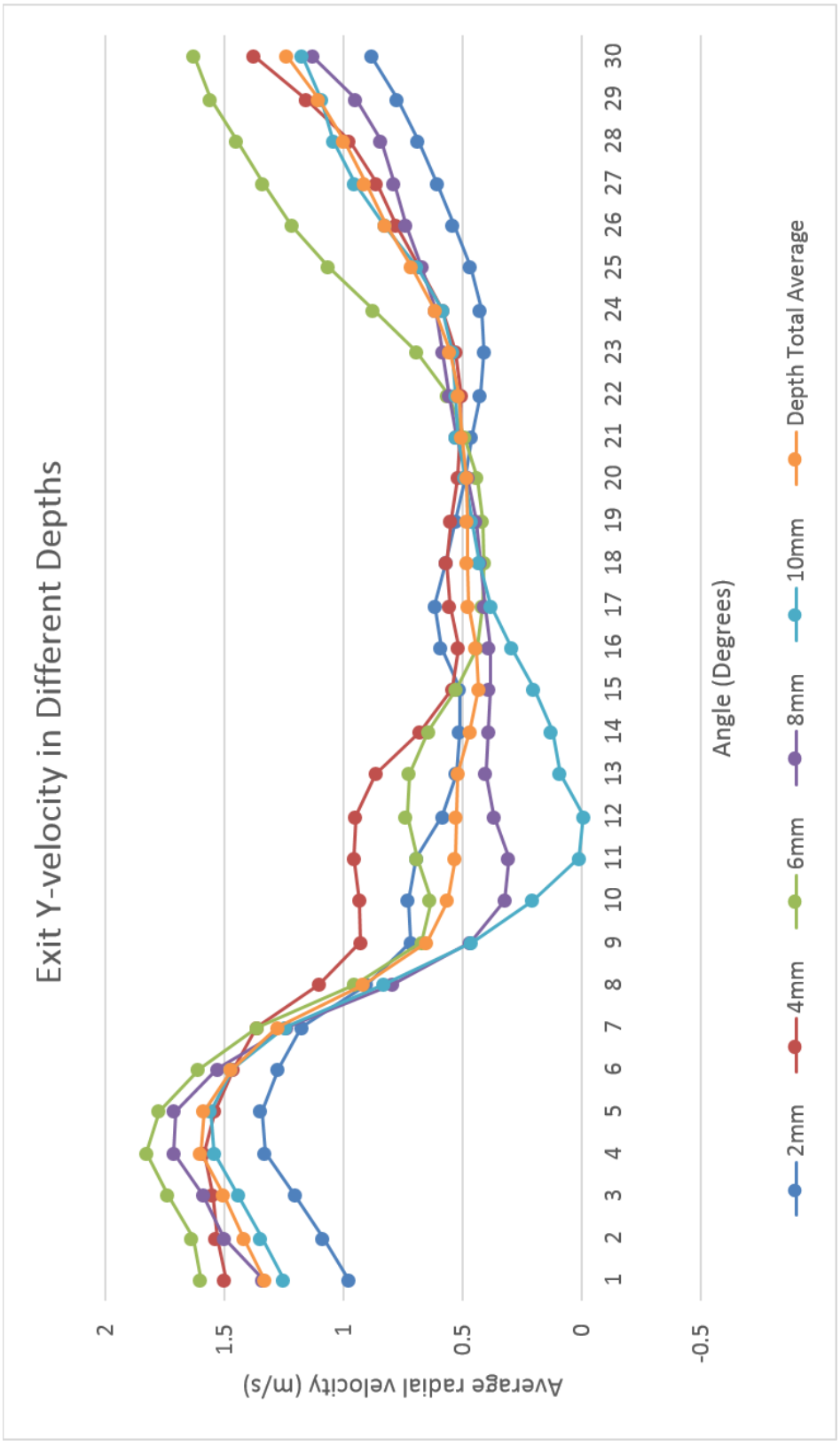

7.4. XZ-Plane Velocity Vector Plots of Slot 1

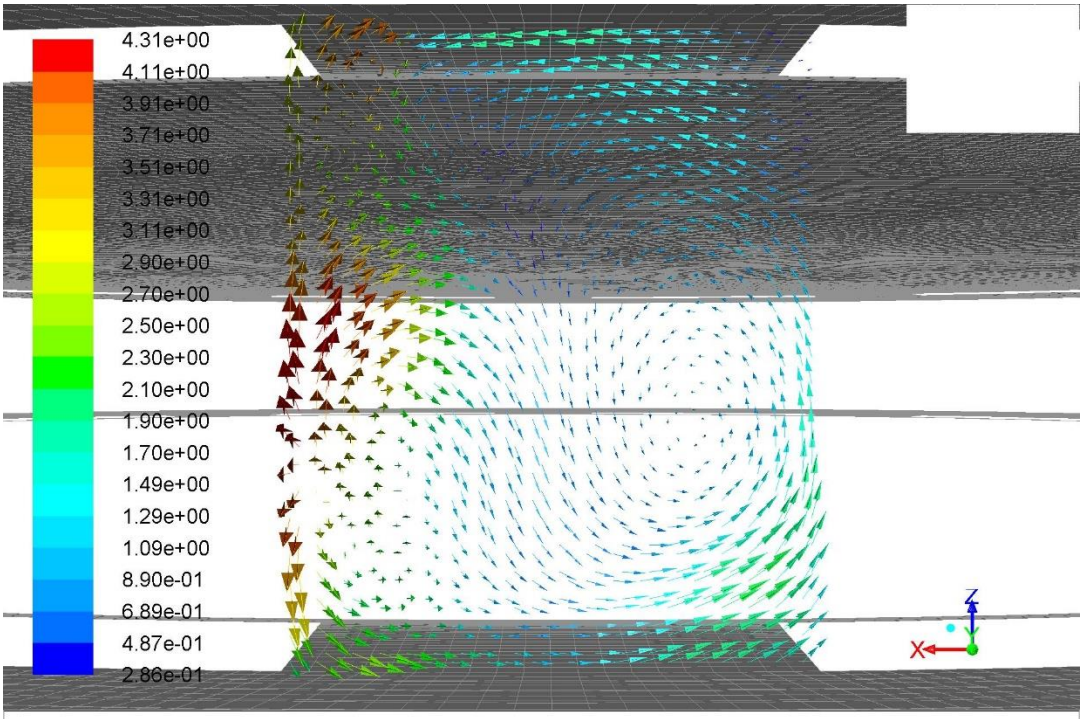

θ = -7°

N = 10 rps

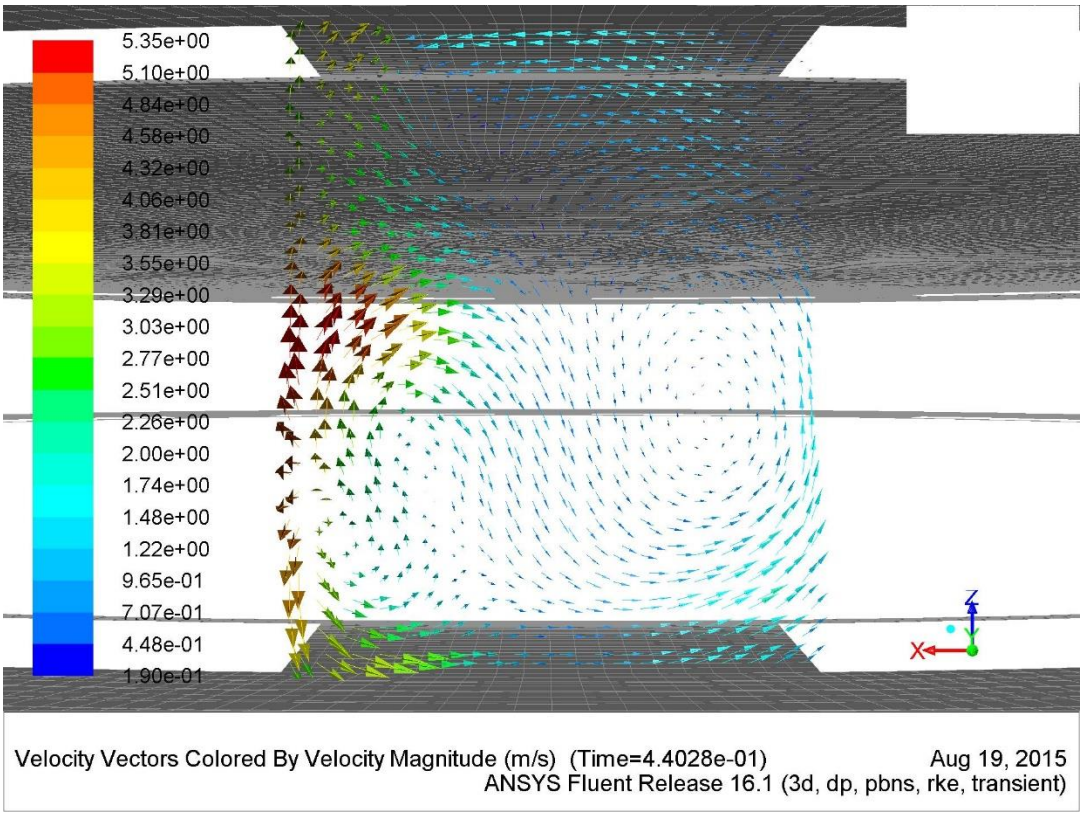

θ = -5°

N = 10 rps

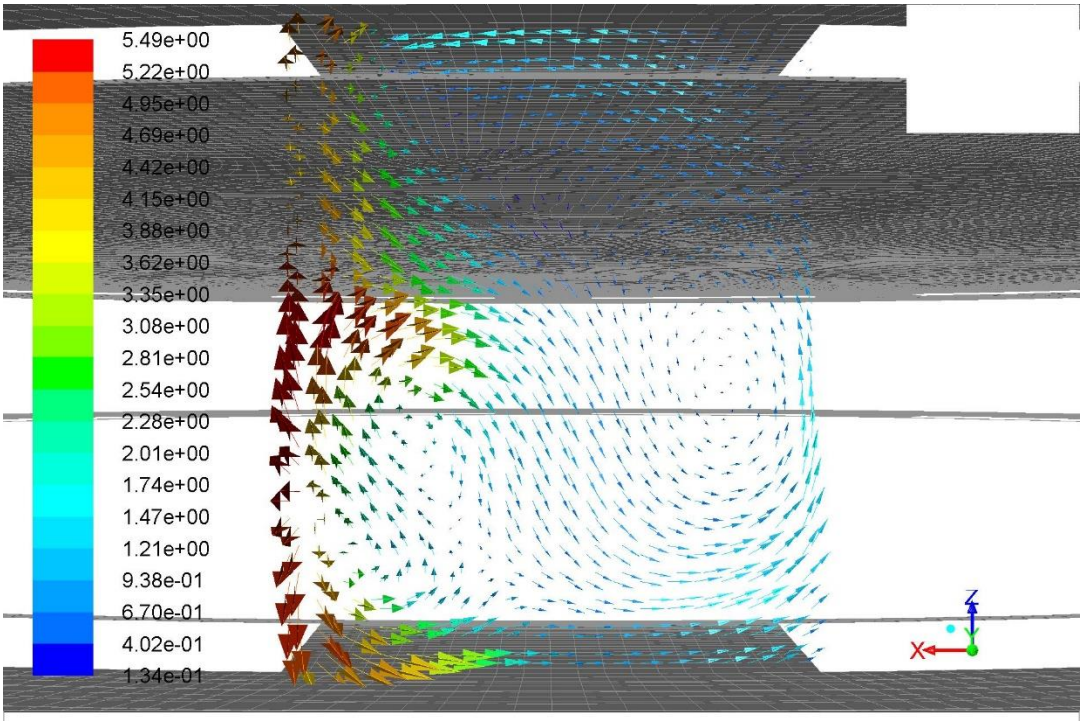

θ = -3°

N = 10 rps

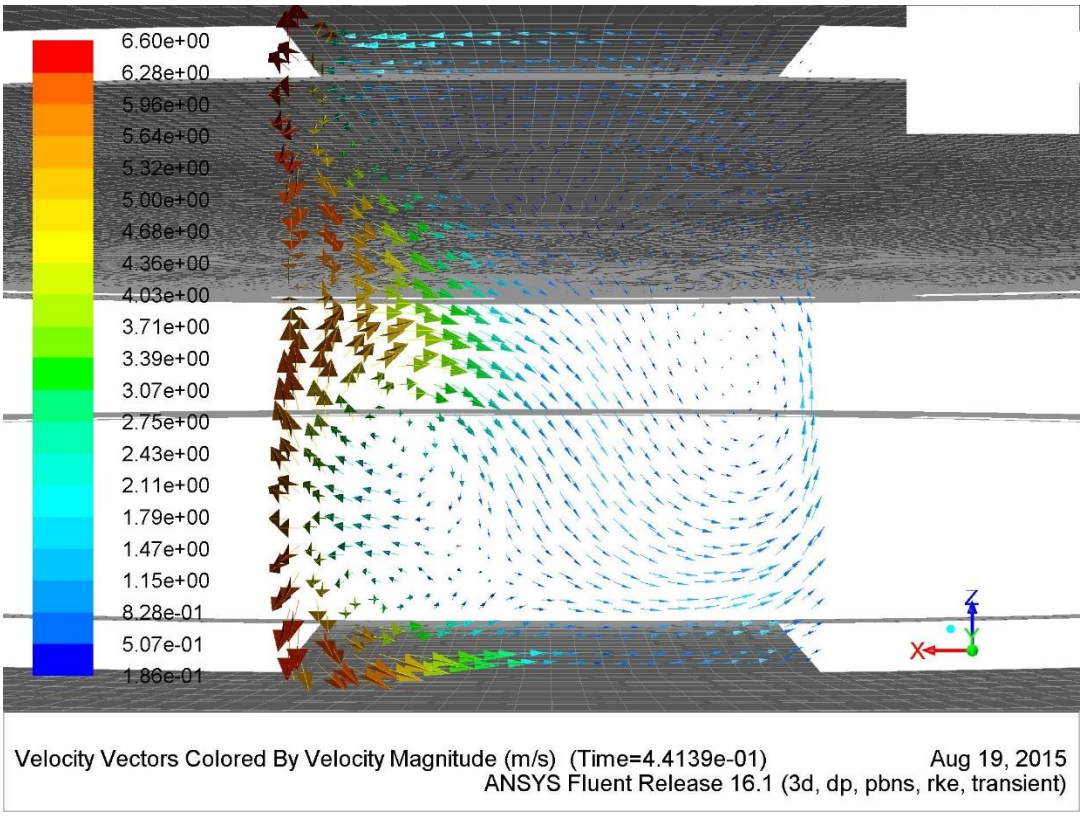

θ = -1°

N = 10 rps

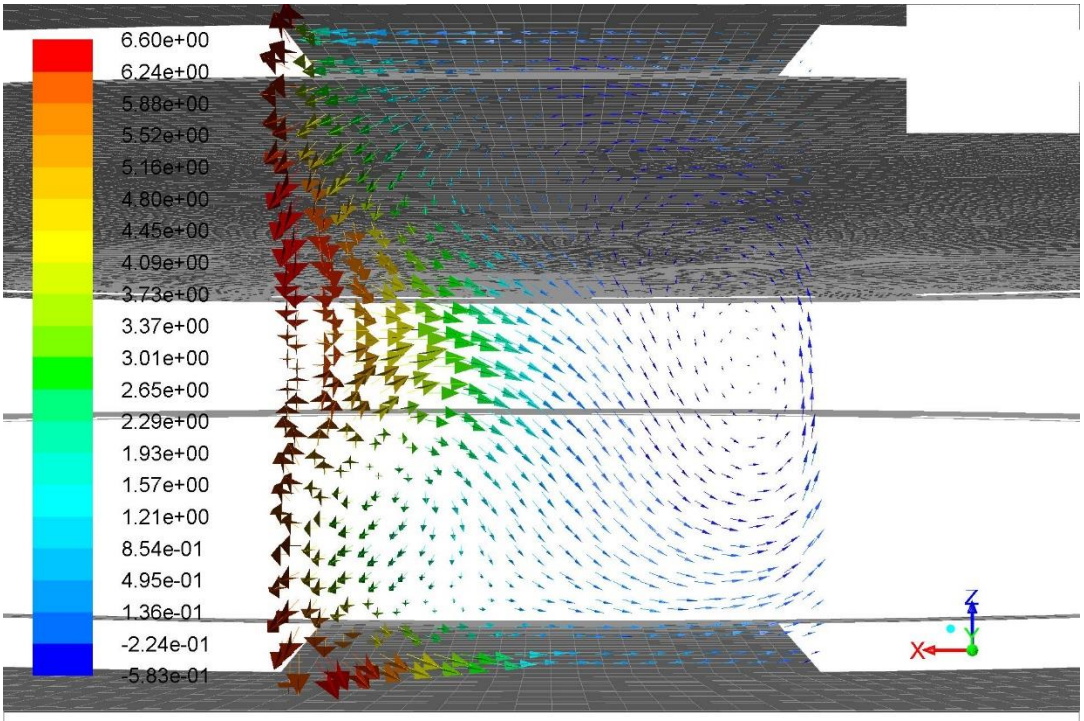

θ = +1°

N = 10 rps

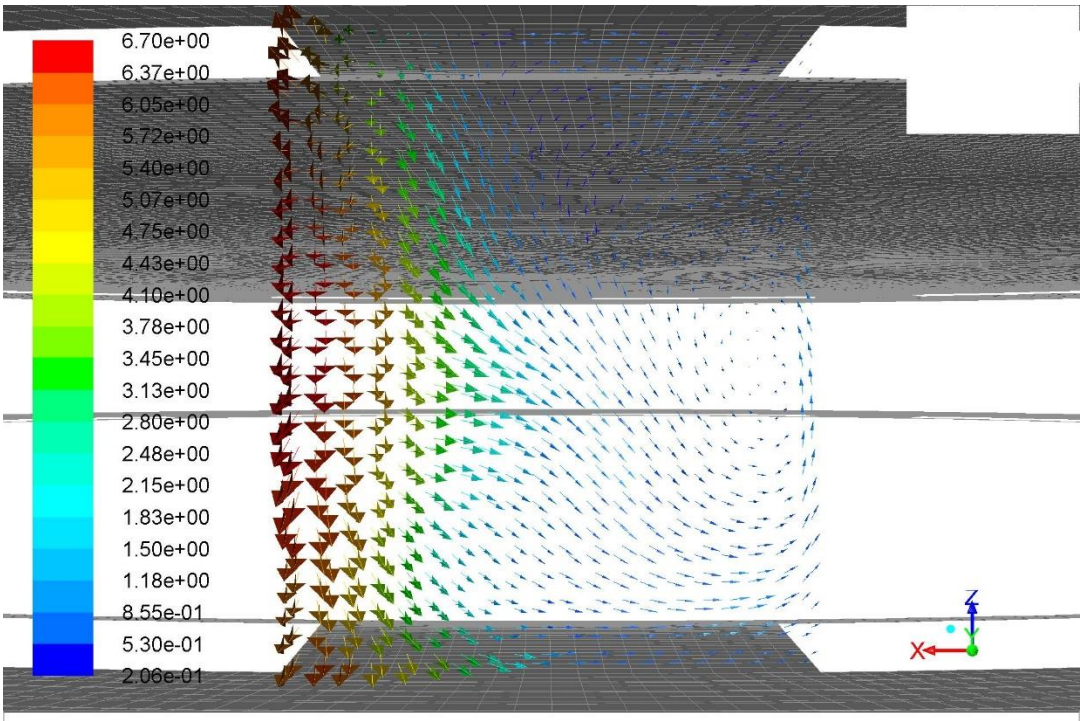

θ = +3°

N = 10 rps

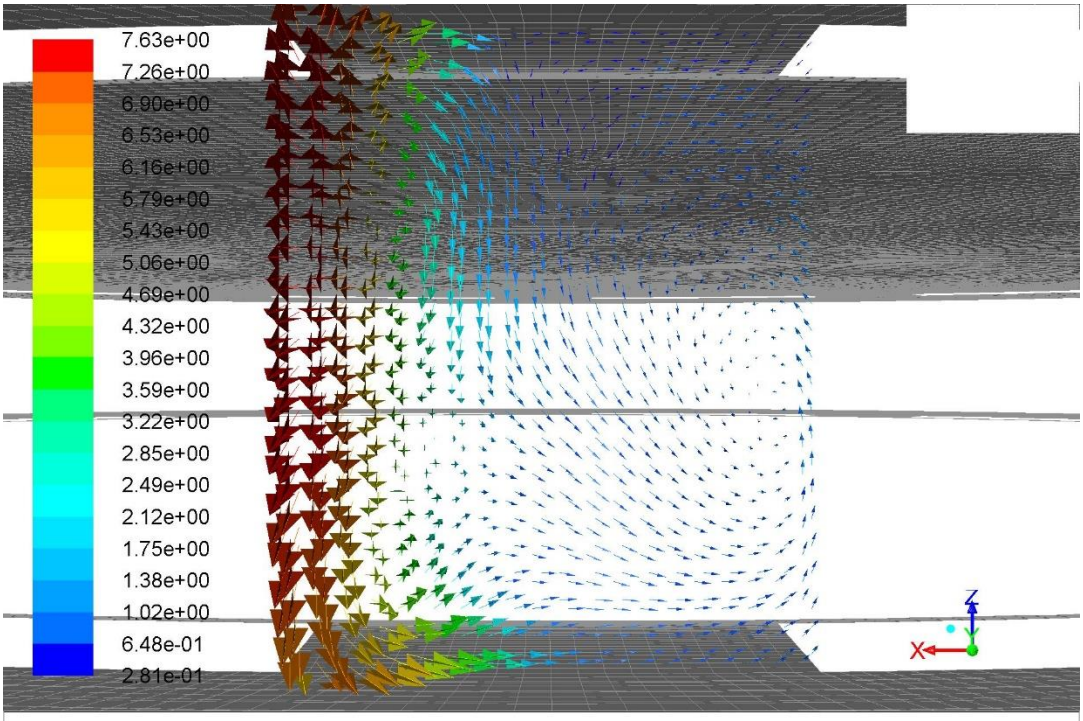

θ = +5°

N = 10 rps

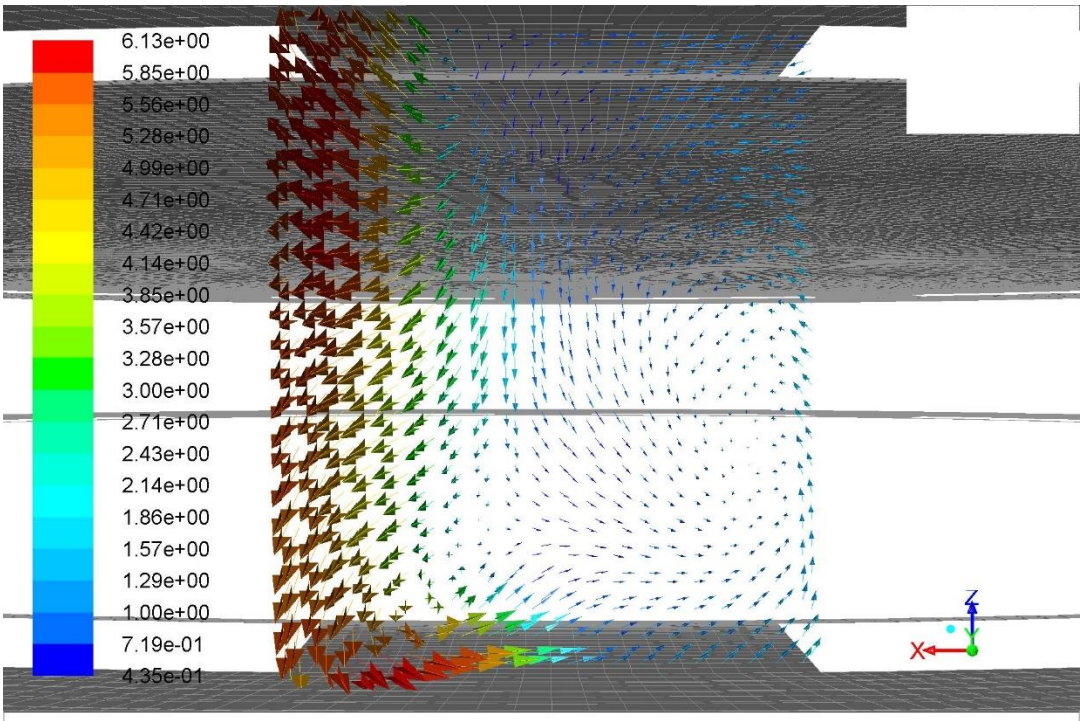

θ = +7°

N = 10 rps

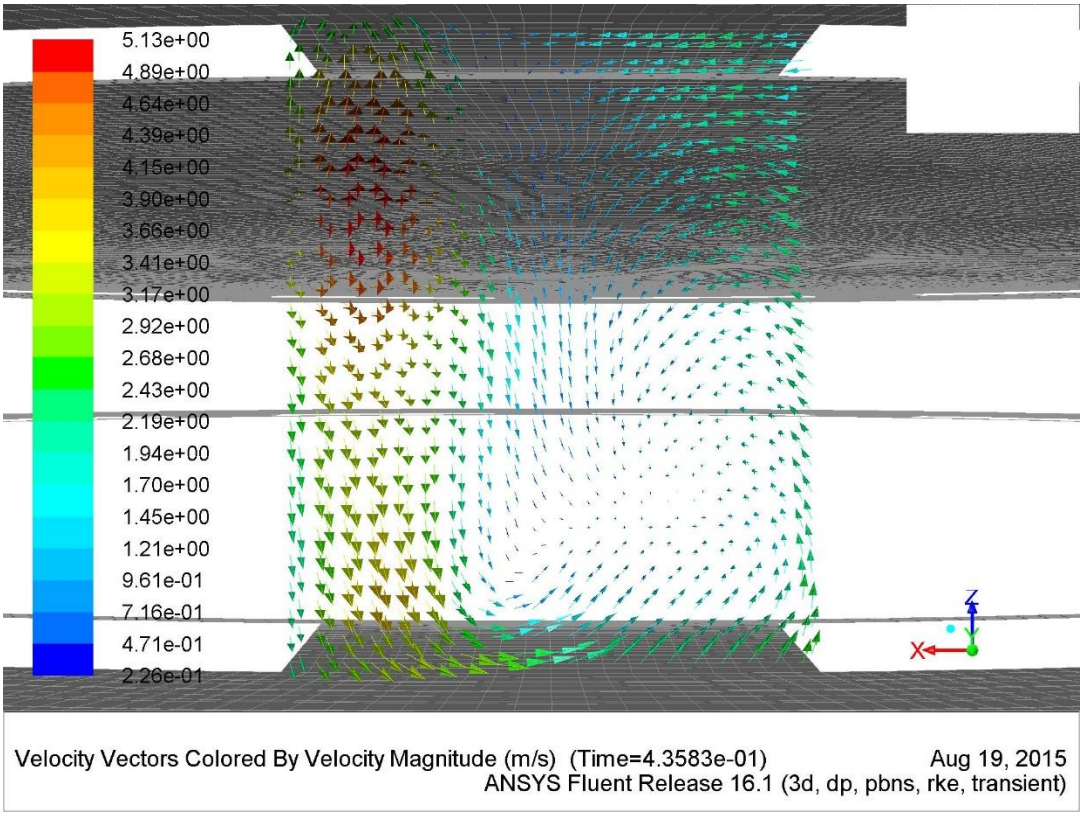

$\theta = +9°$

N = 10 rps

8.5 Extended CFD Mesh Level 2 vs PIV XY-Plane Velocity Vector Plots

*Both PIV and CFD plots have the same vector magnitude scaling of arrow length.

N = 10 rps, CFD Mesh level 2, θ = -7°

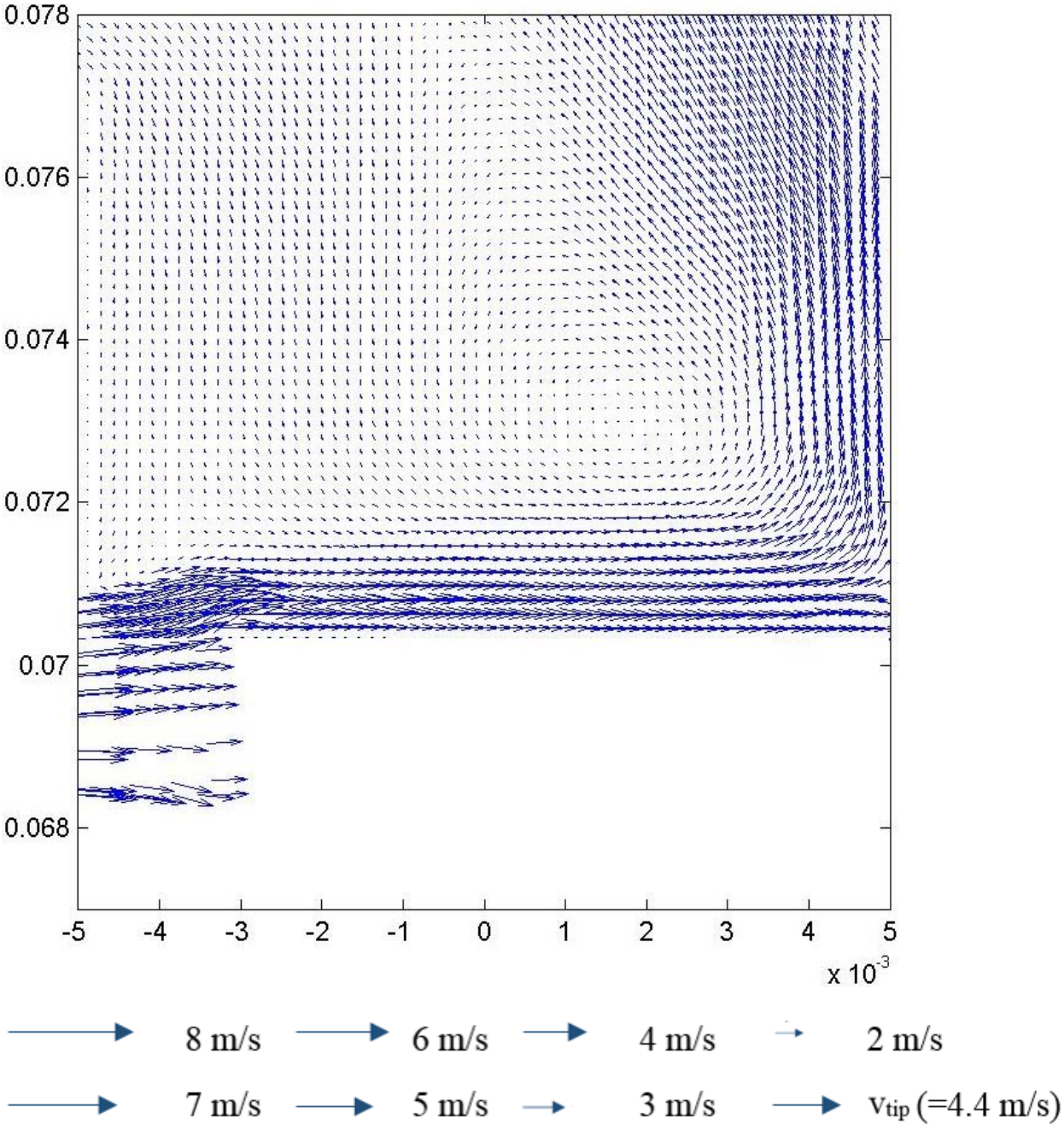

N = 10 rps, PIV, θ = -7°

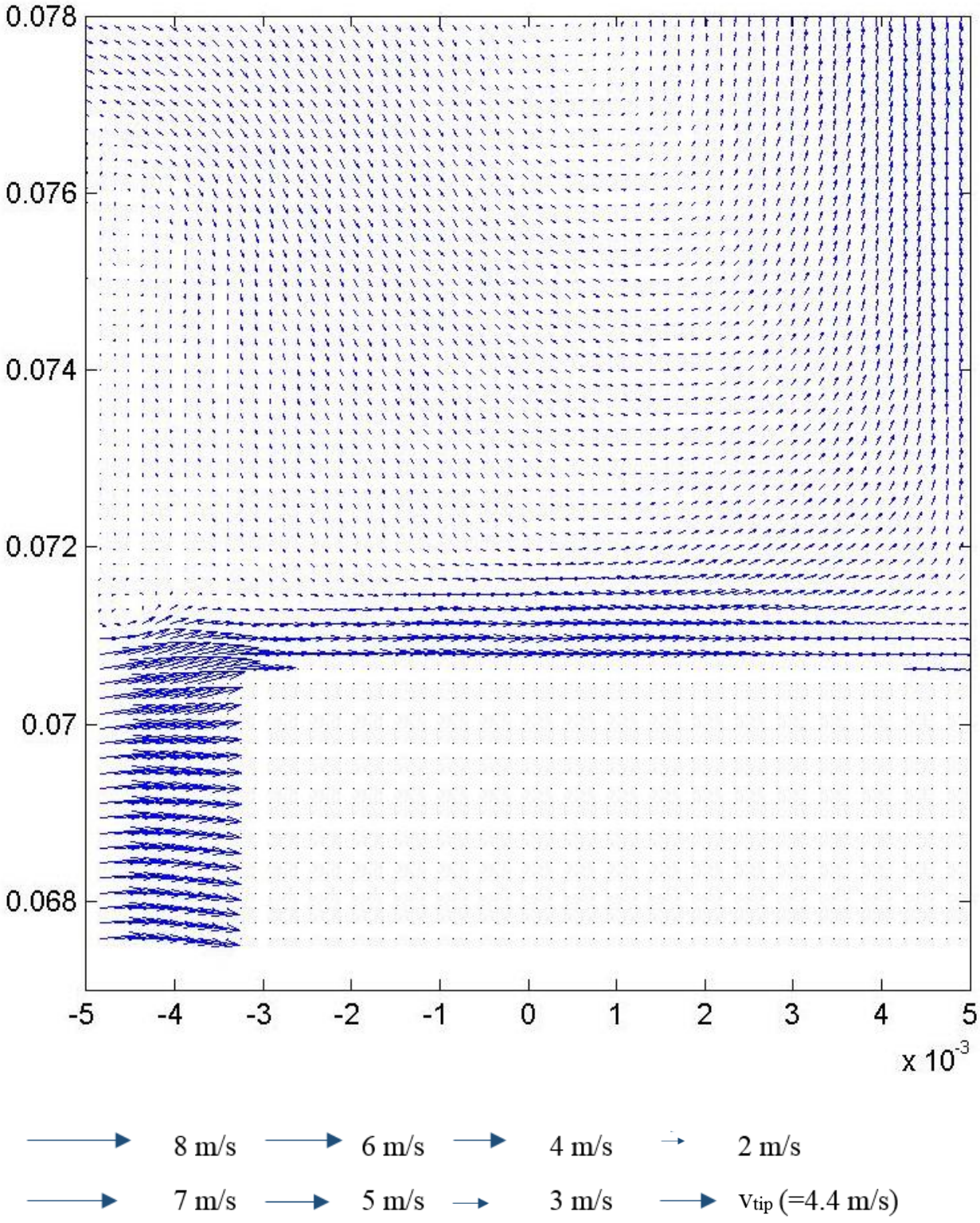

N = 10 rps, CFD (Mesh level 2), θ = -5°

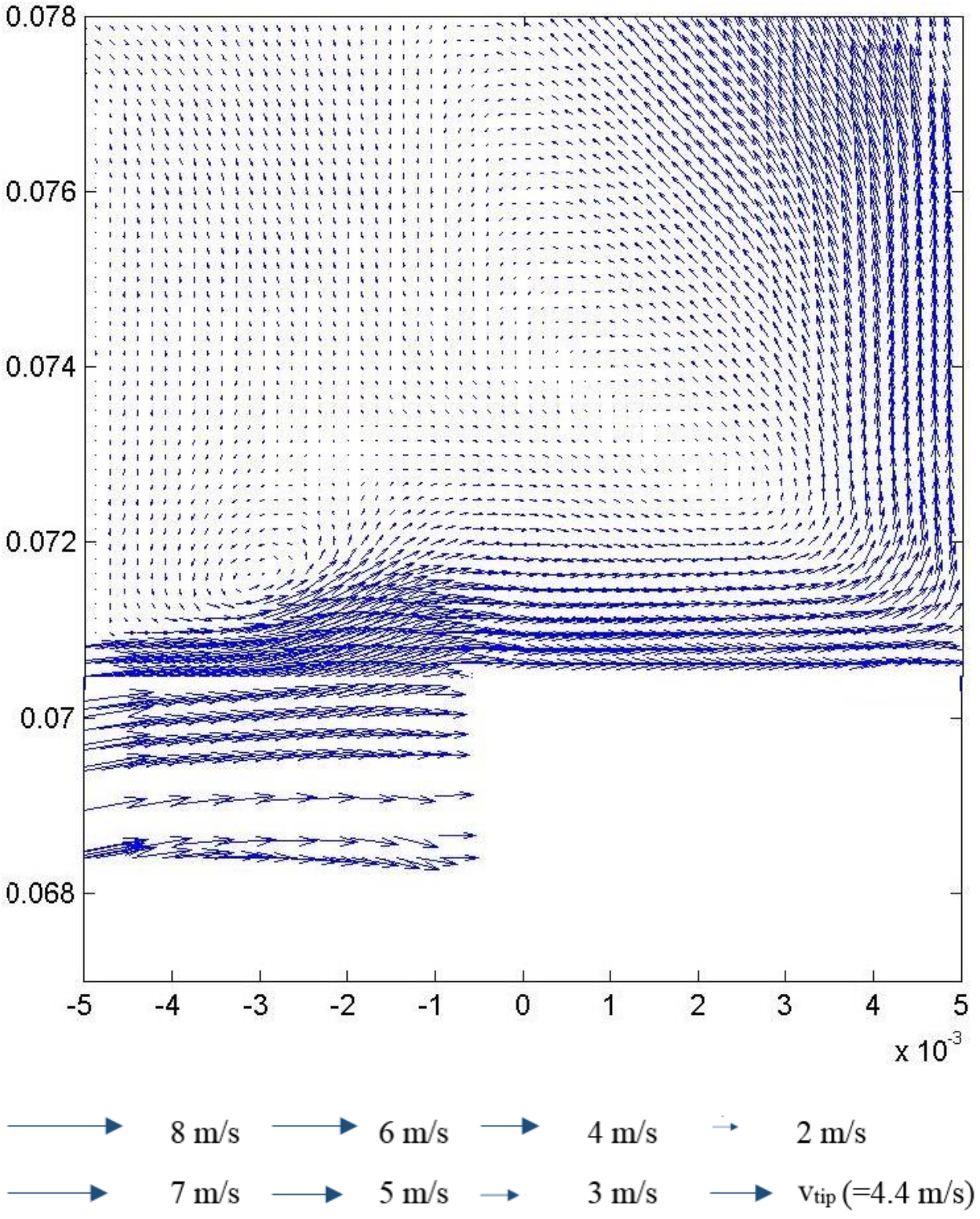

N = 10 rps, PIV, θ = -5°

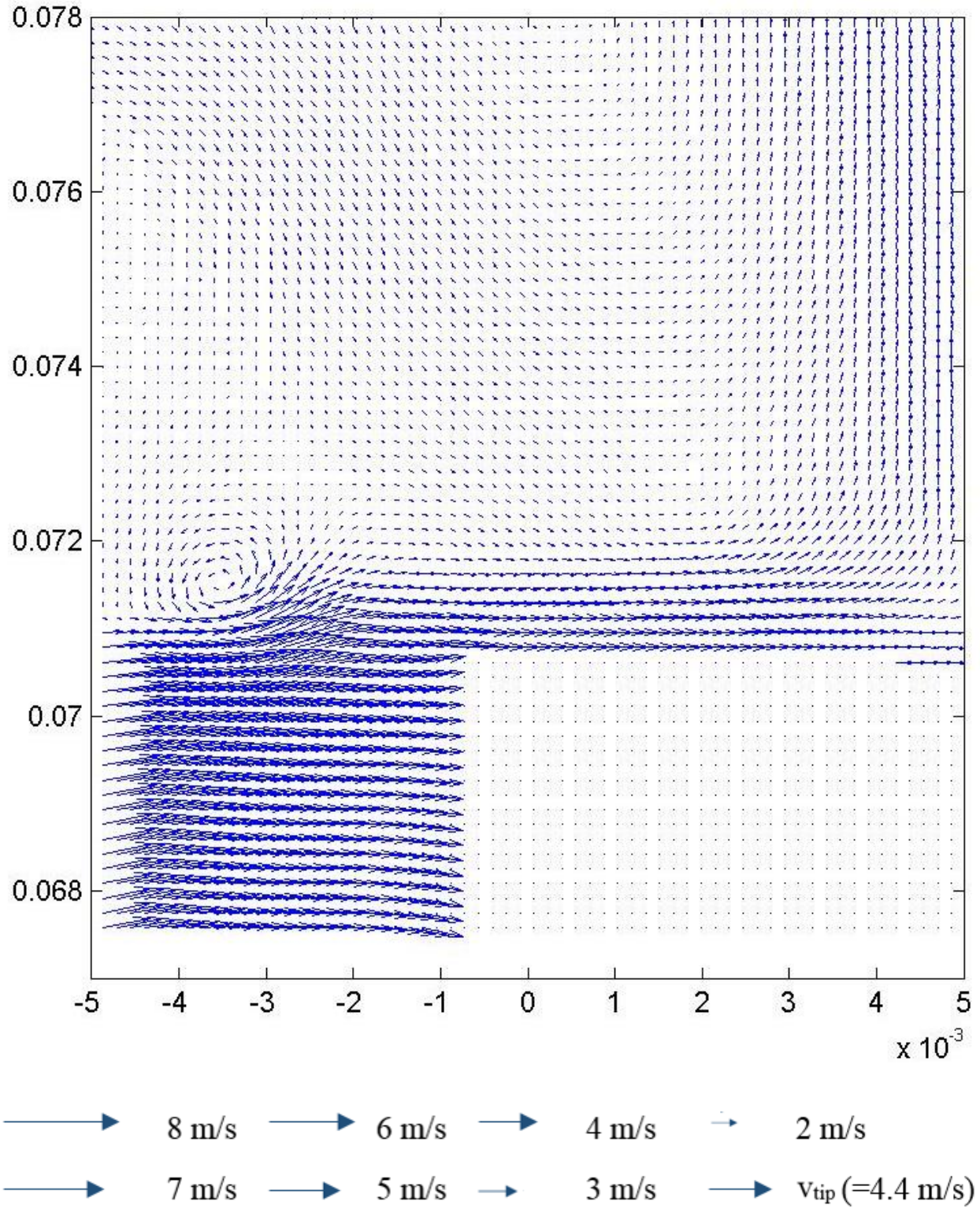

N = 10 rps, CFD (Mesh level 2), θ = -3°

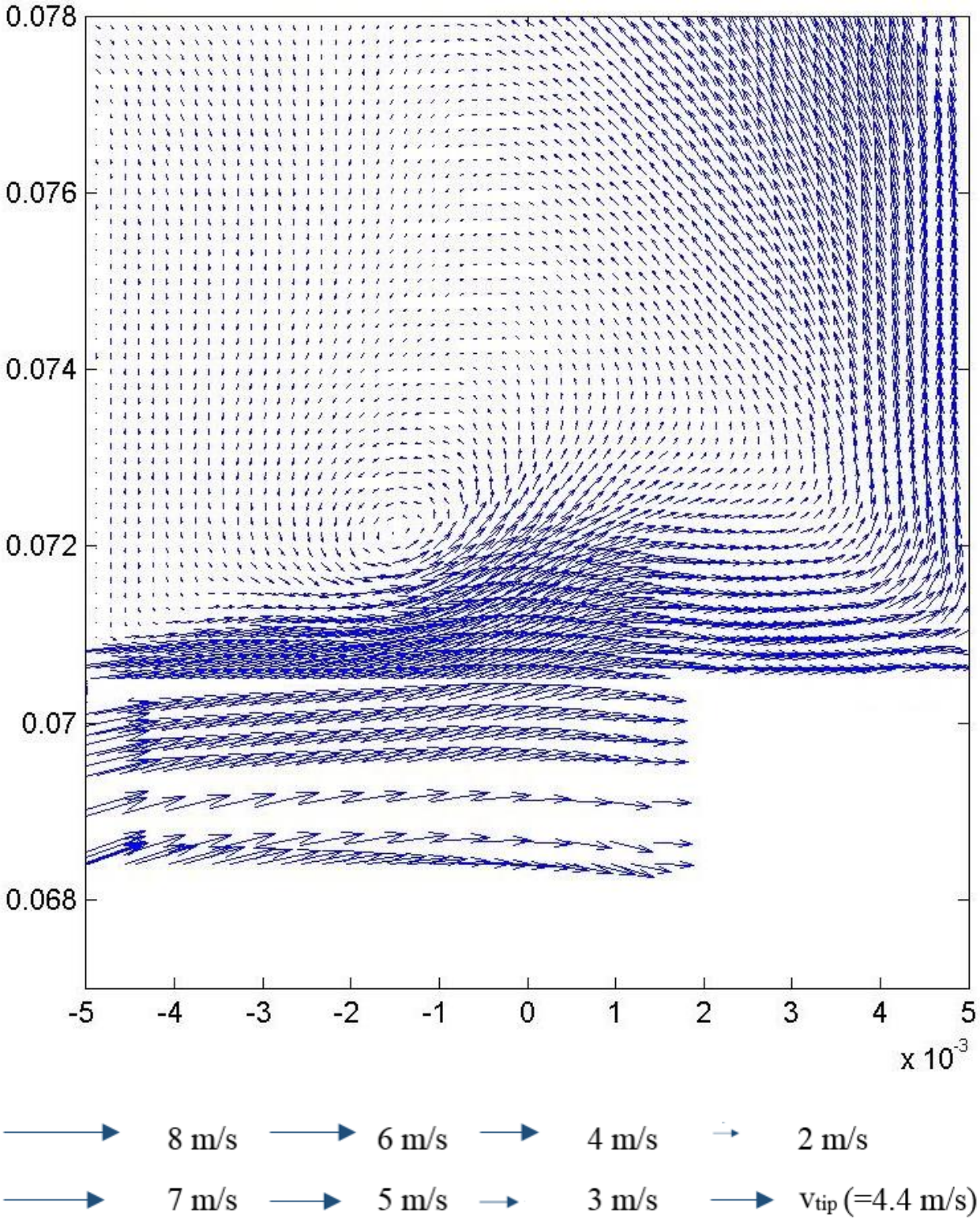

N = 10 rps, PIV, θ = -3°

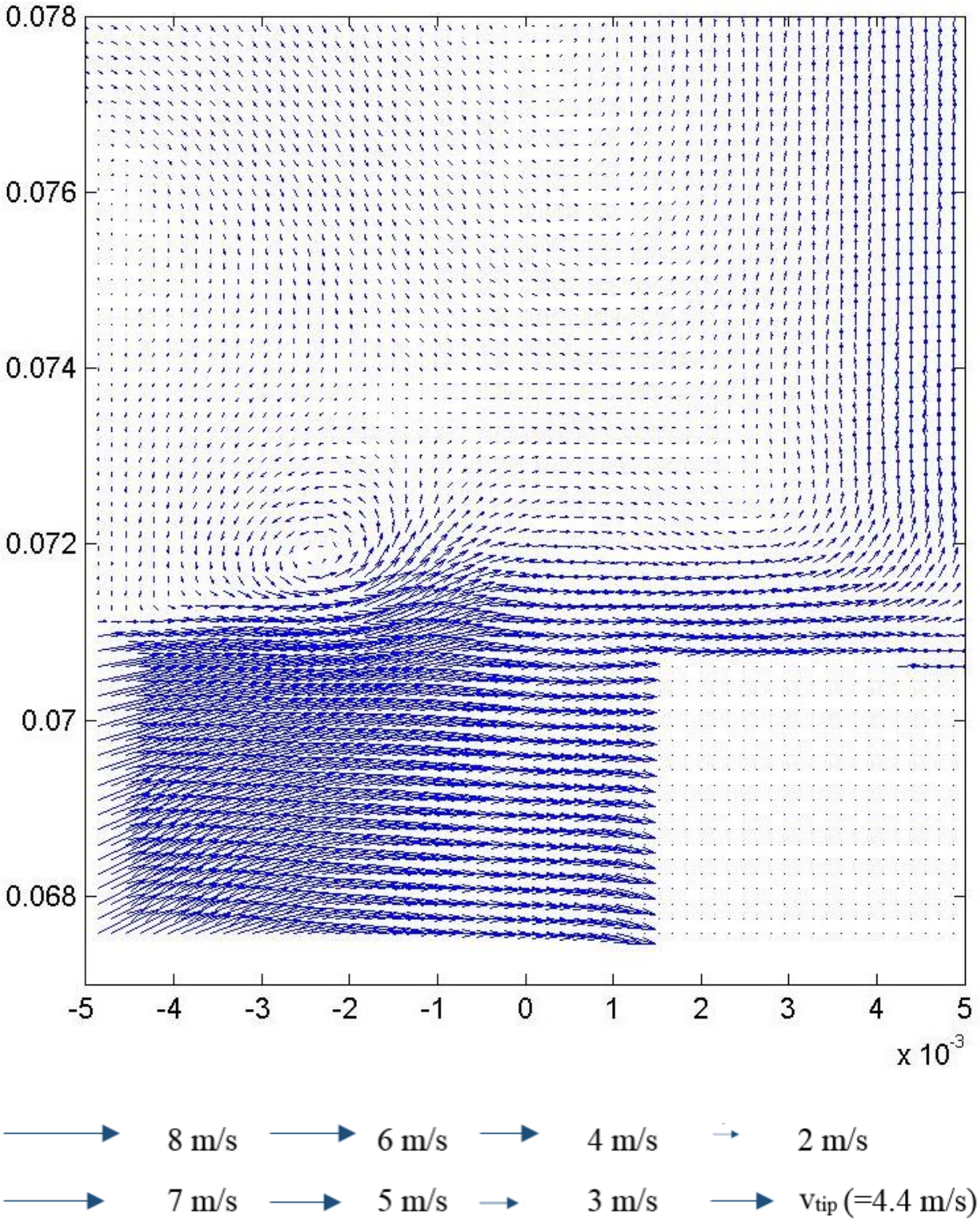

N = 10 rps, CFD (Mesh level 2), θ = -1°

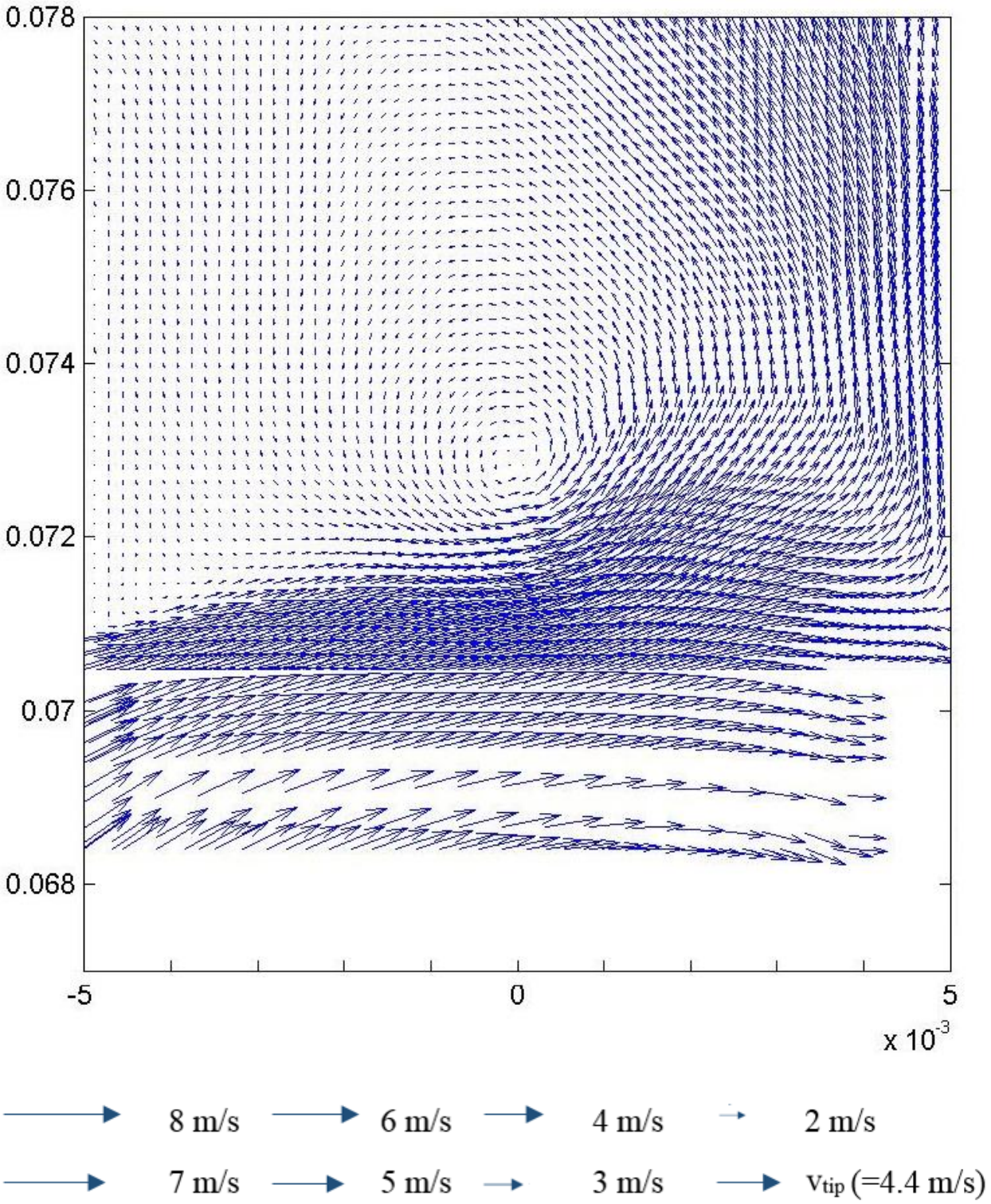

N = 10 rps, PIV, θ = -1°

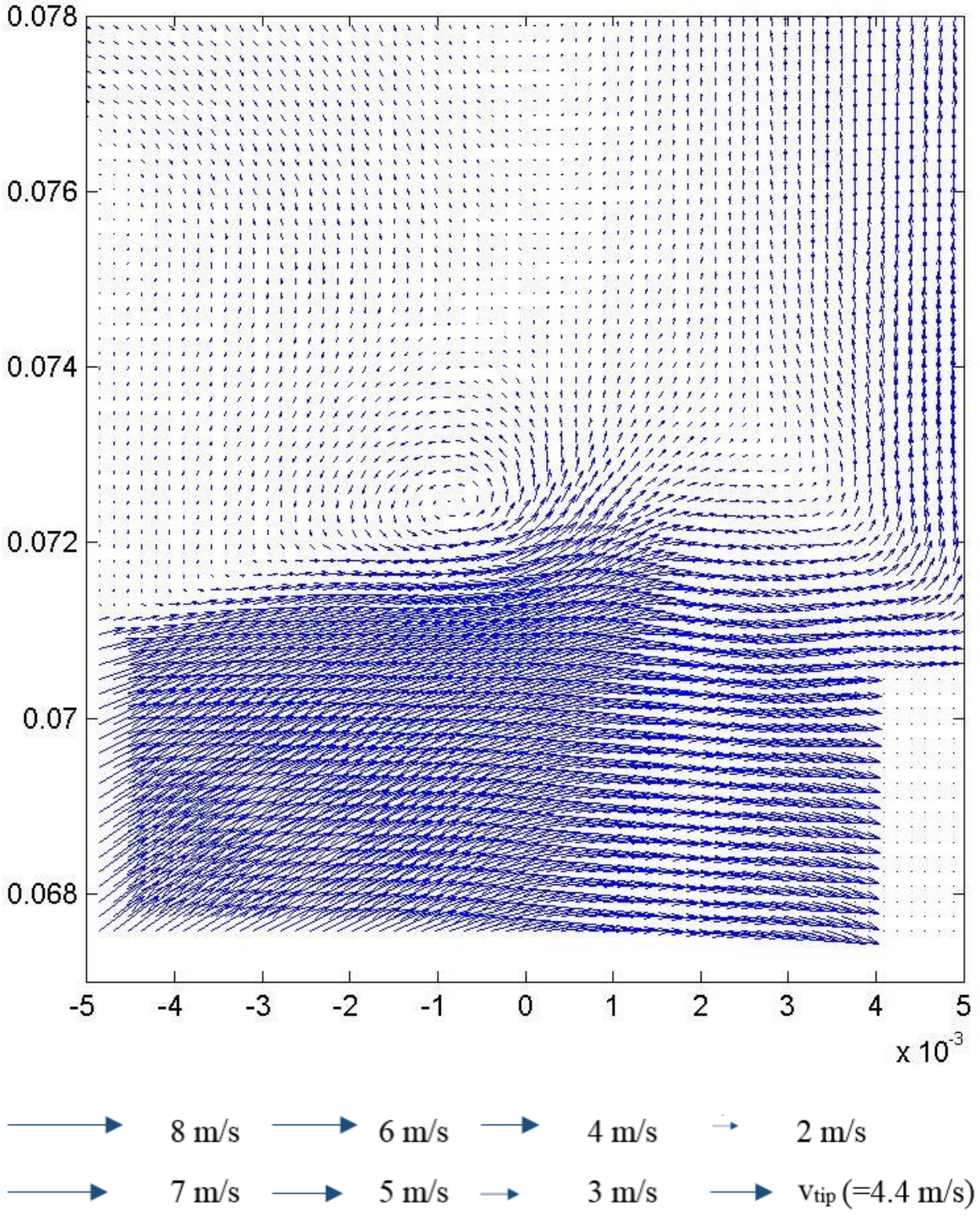

N = 10 rps, CFD (Mesh level 2), θ = +1°

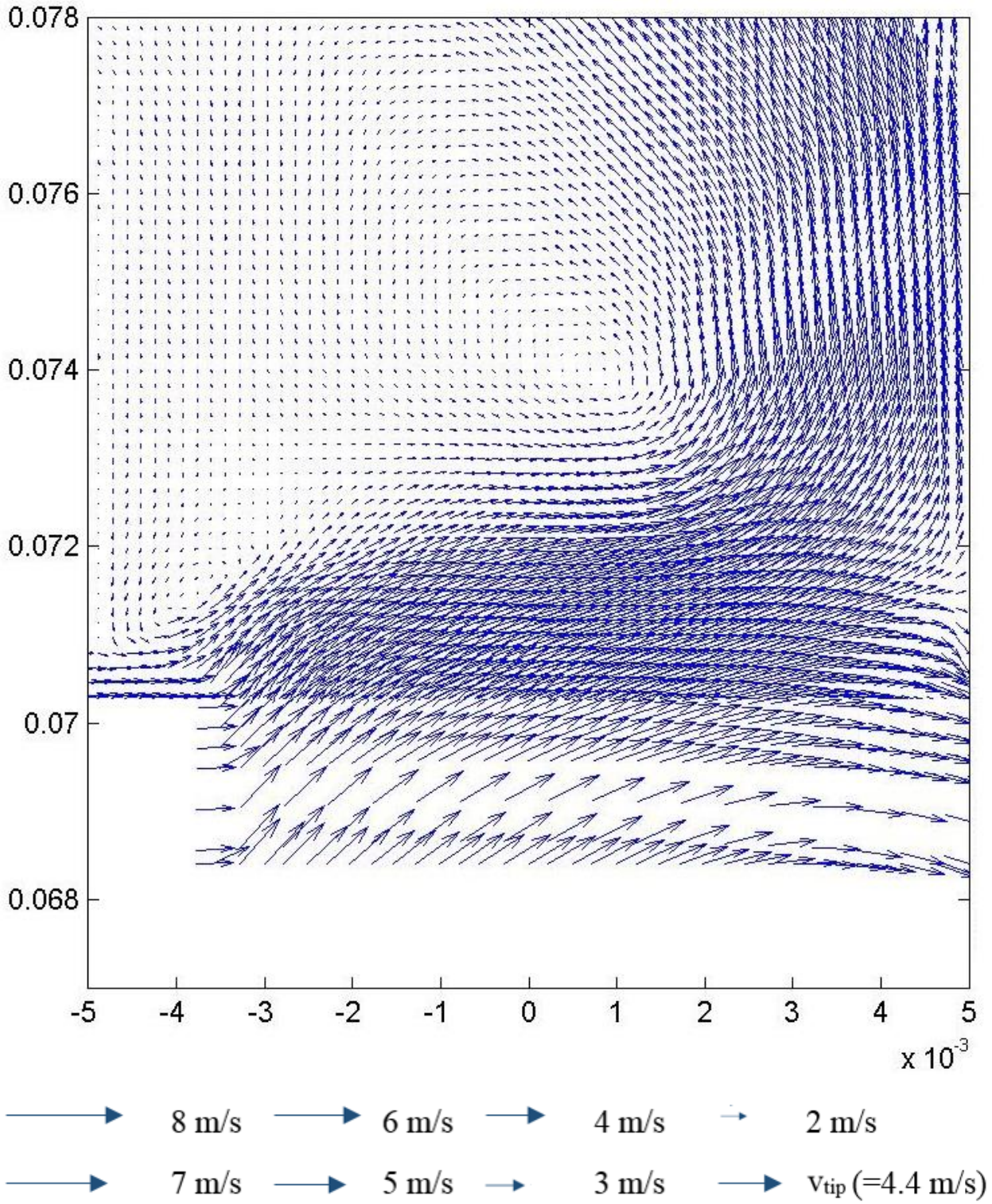

N = 10 rps, PIV, θ = +1°

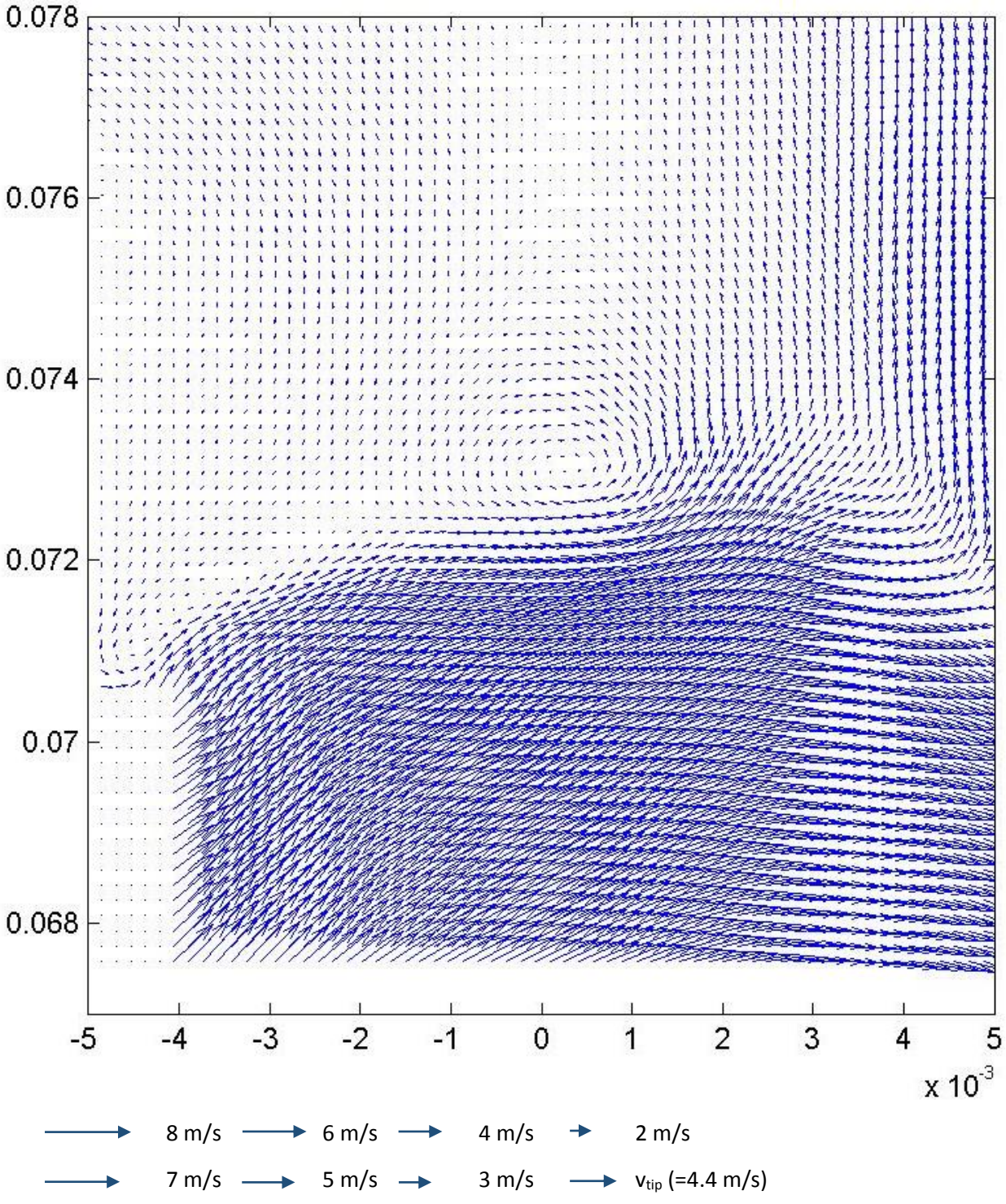

N = 10 rps, CFD (Mesh level 2), θ = +3°

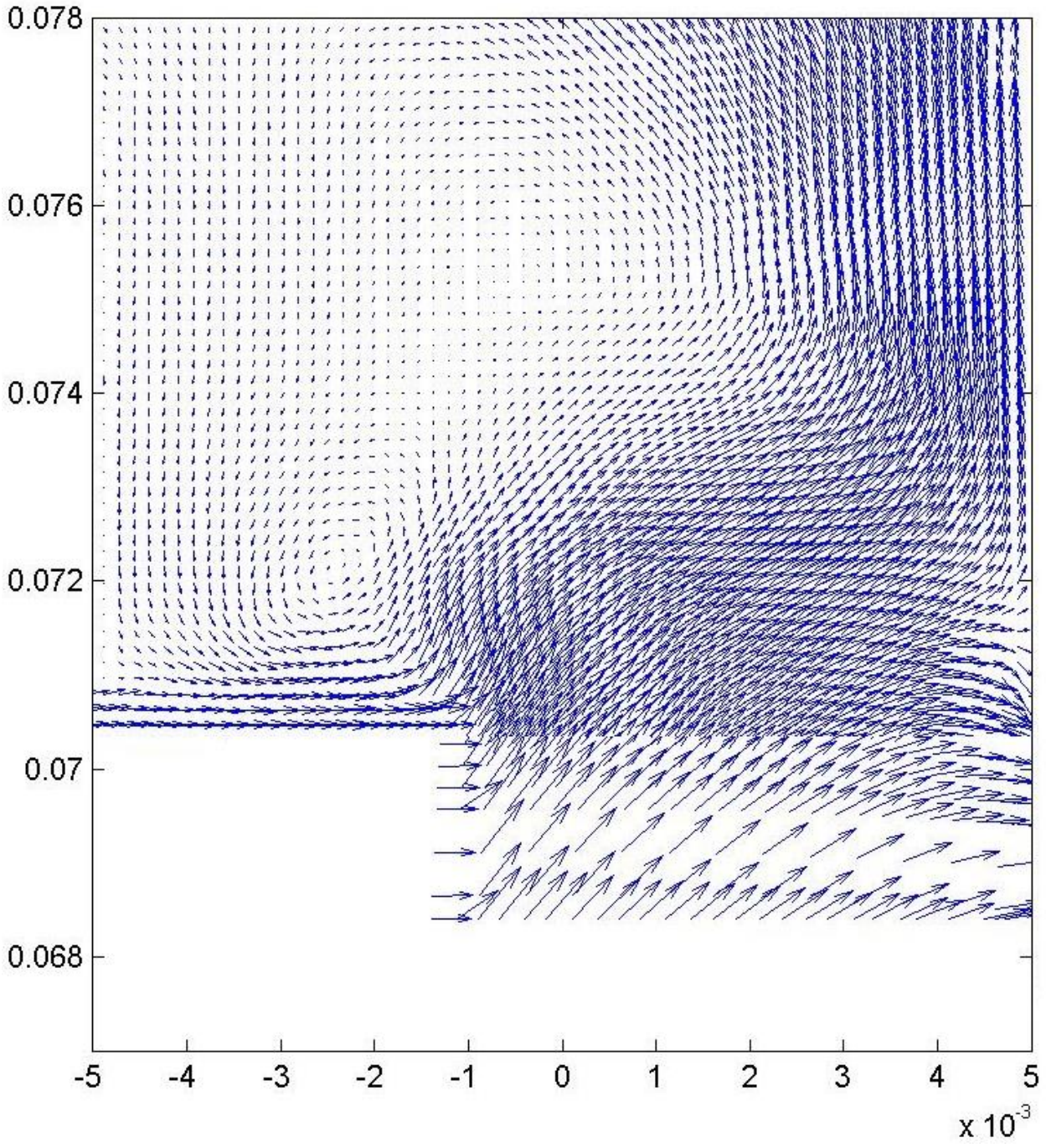

N = 10 rps, PIV, θ = +3°

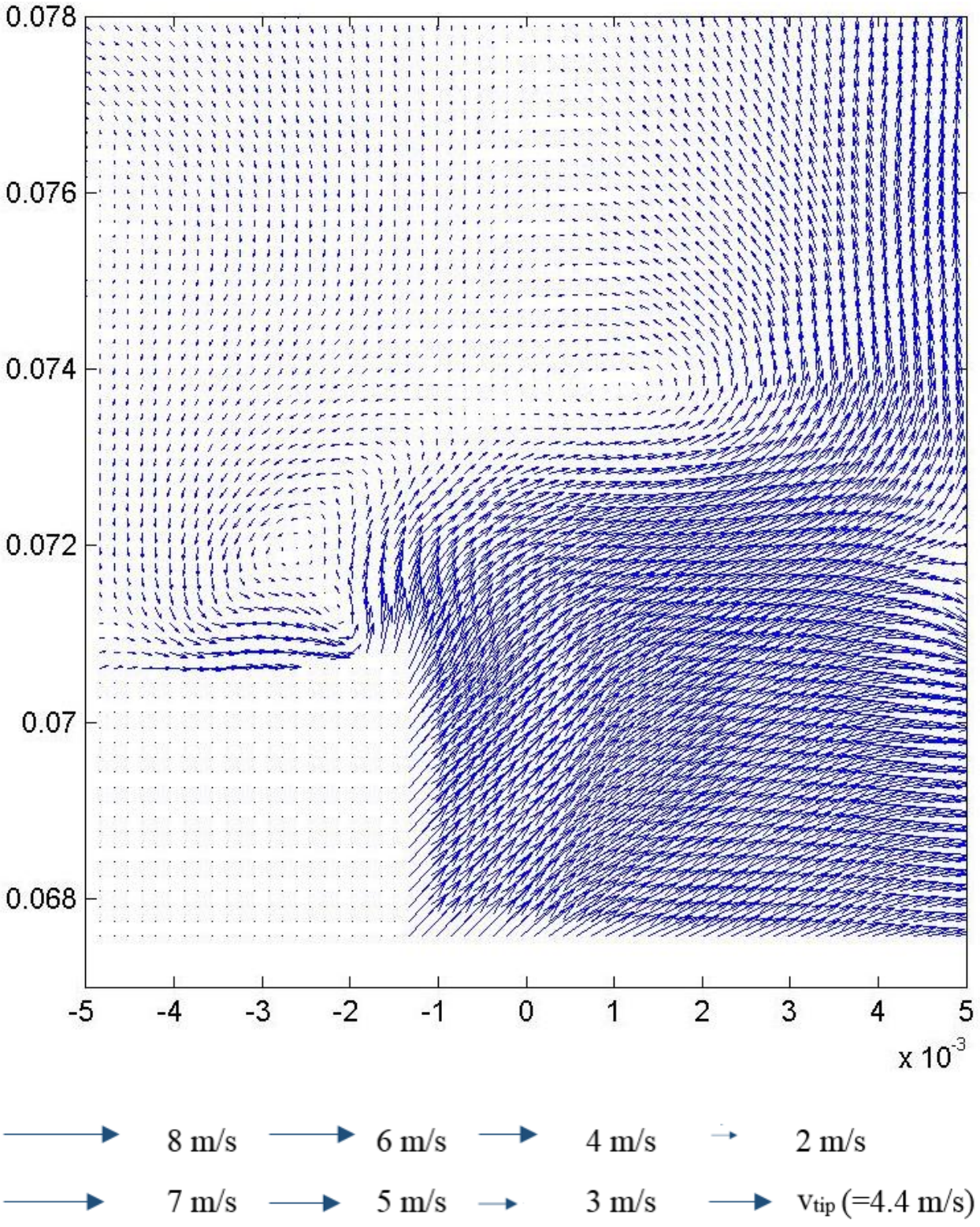

N = 10 rps, CFD (Mesh level 2), θ = +5°

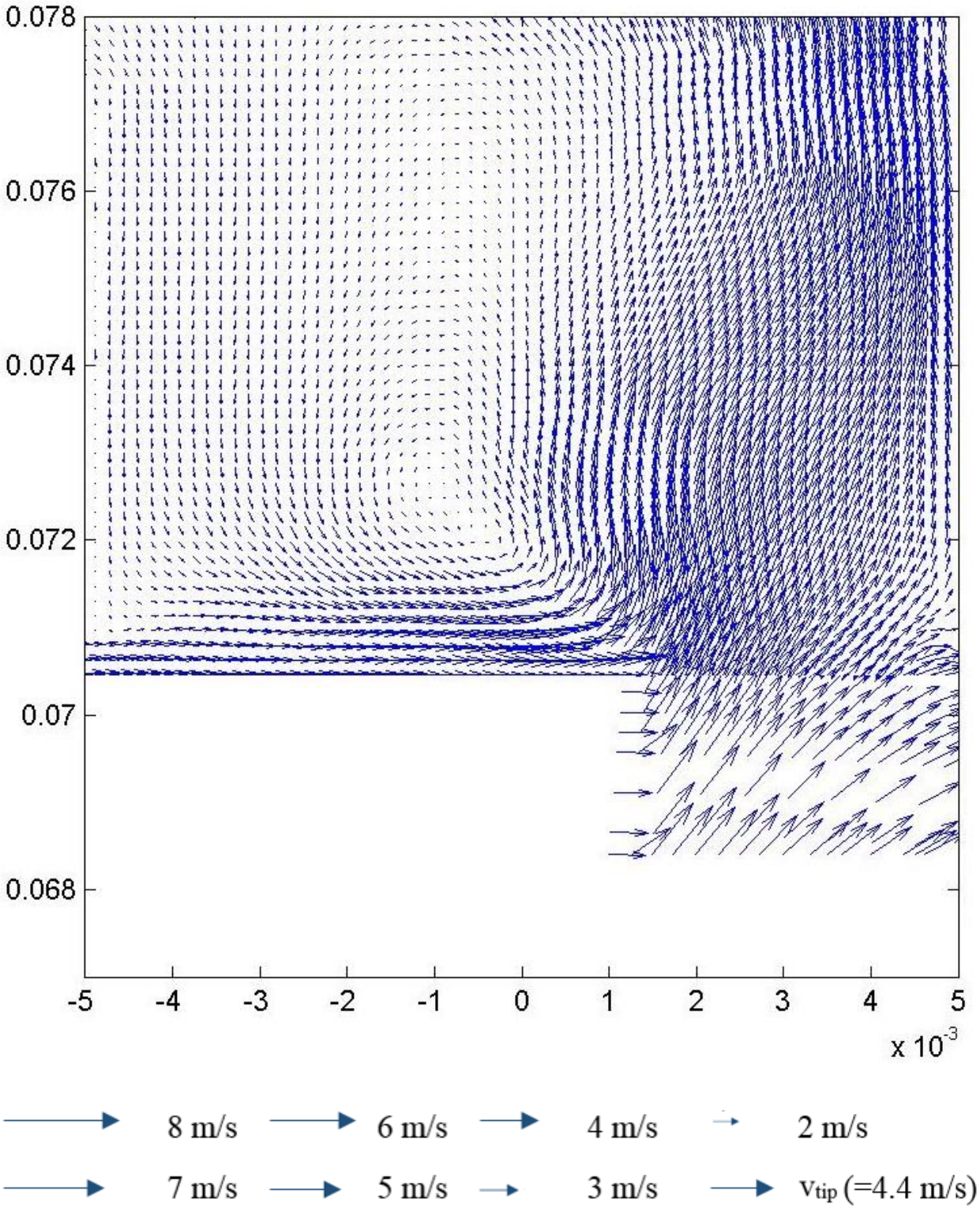

N = 10 rps, PIV, θ = +5°

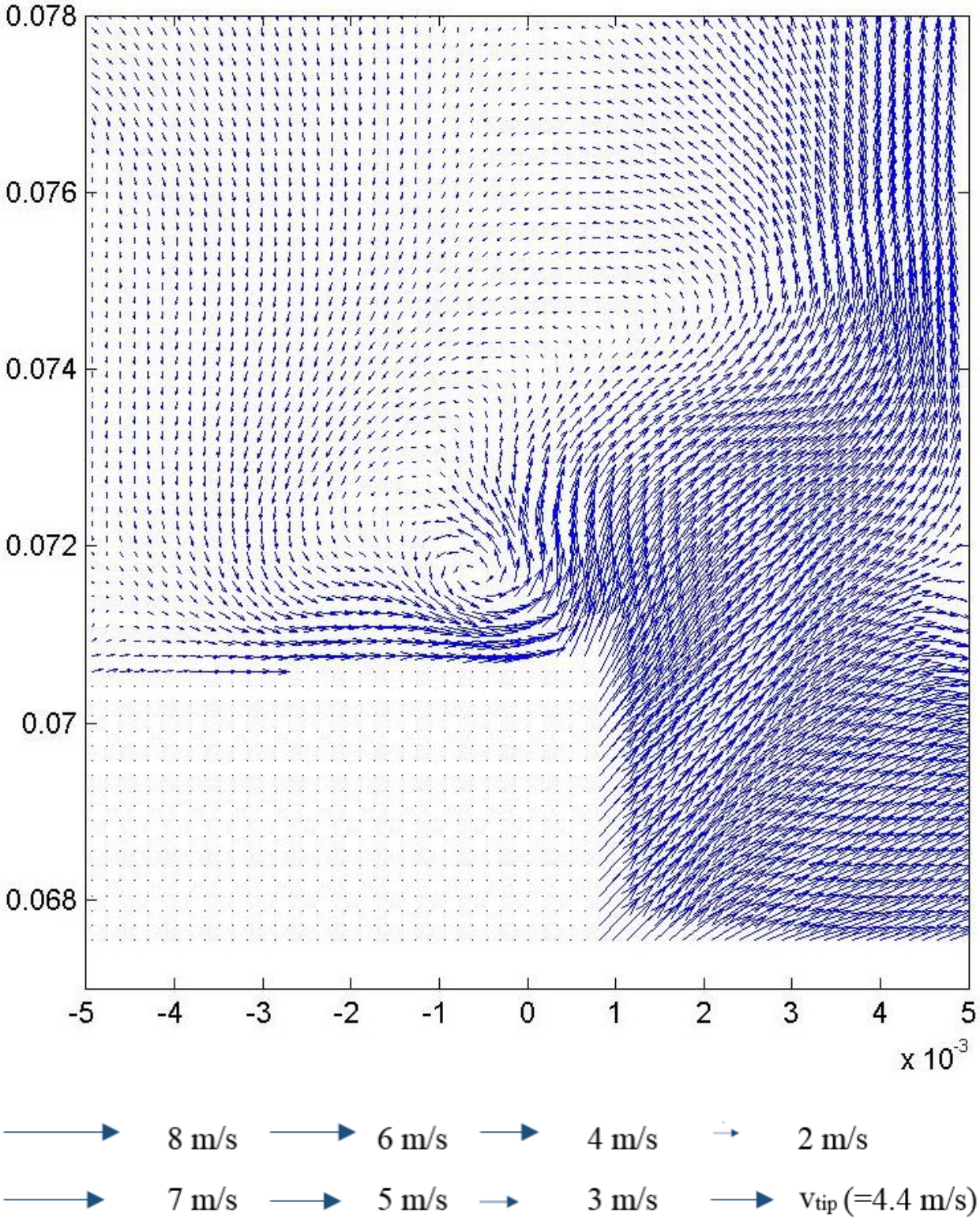

N = 10 rps, CFD (Mesh level 2), θ = +7°

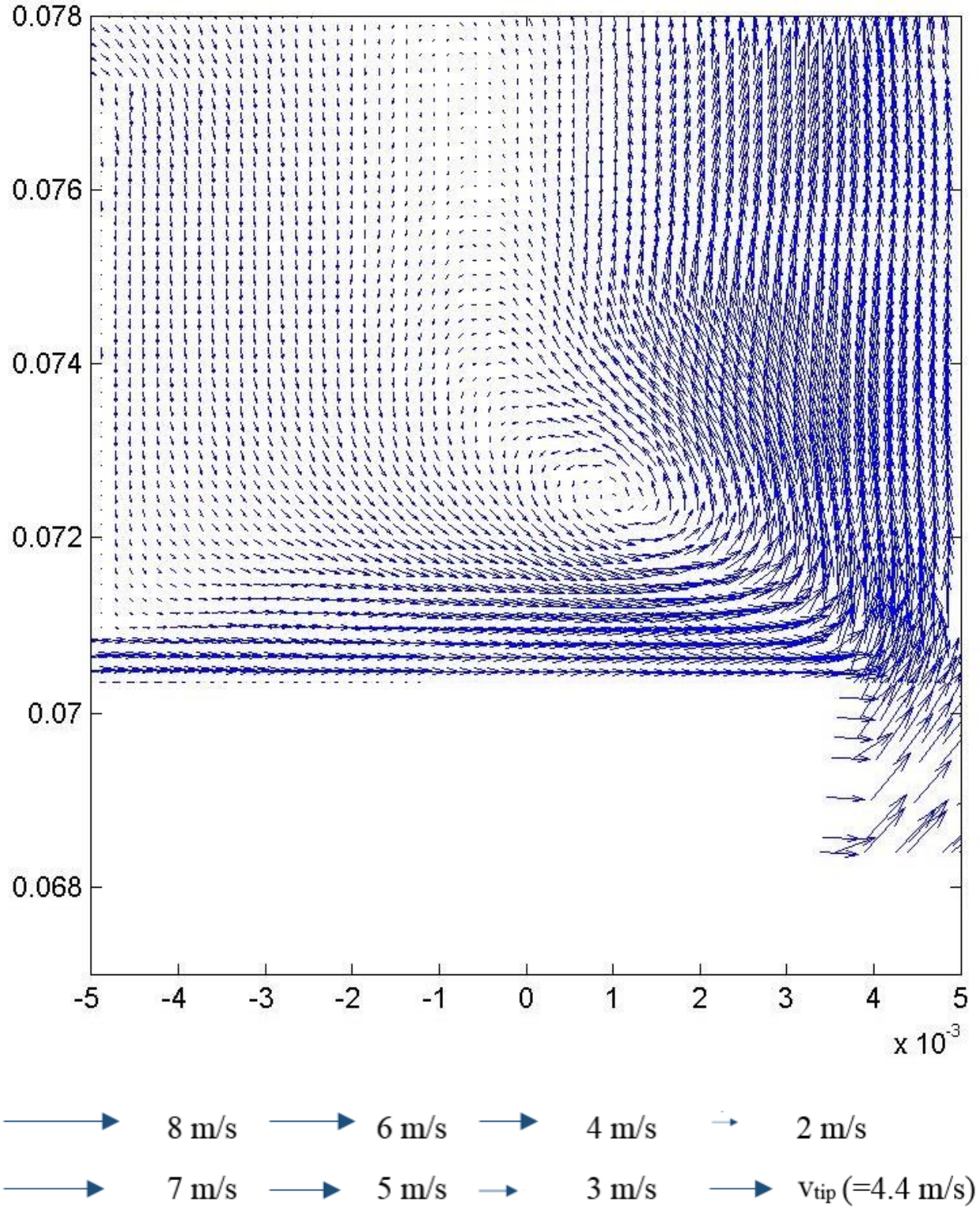

N = 10 rps, PIV, θ = +7°

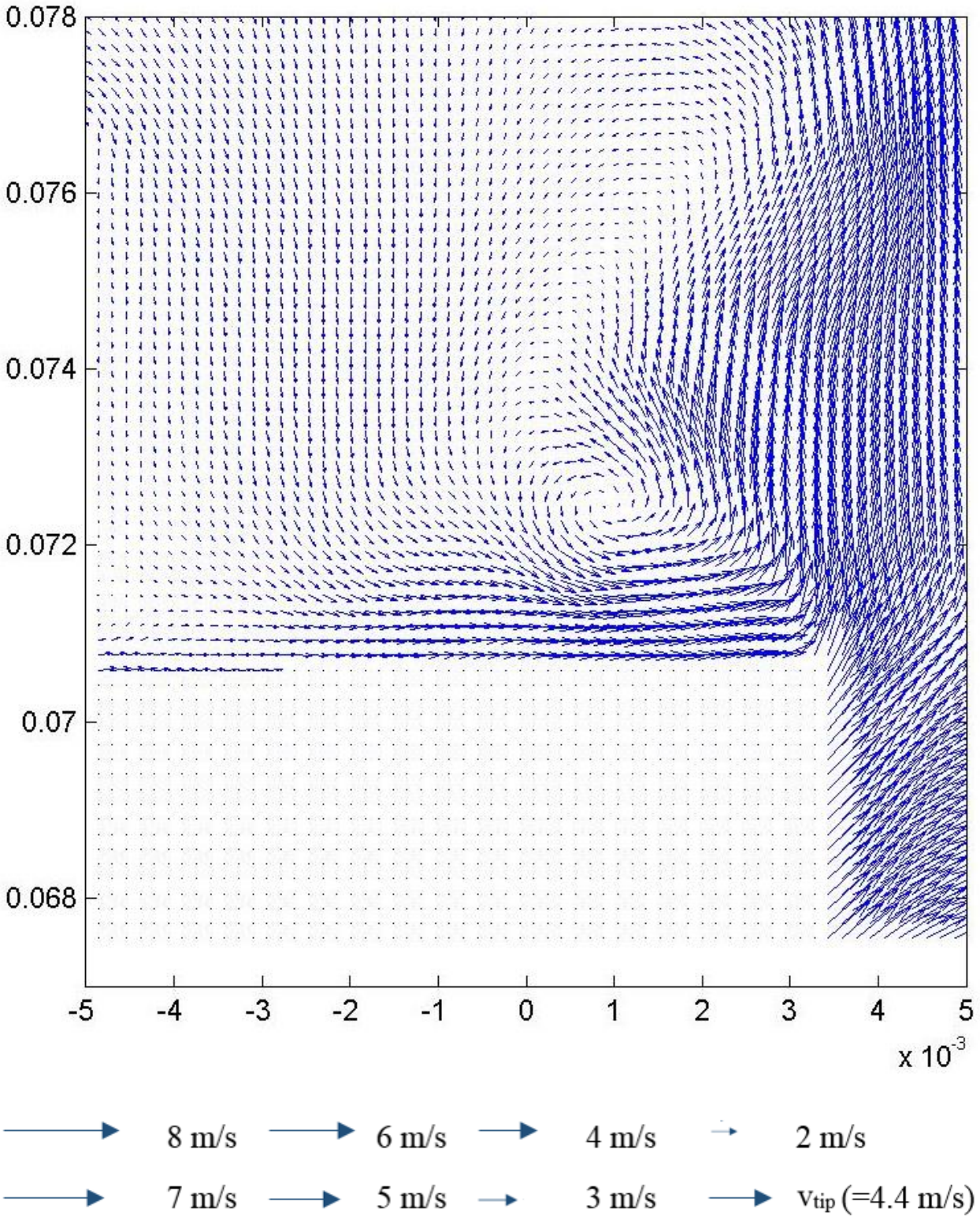

N = 10 rps, CFD (Mesh level 2), θ = +9°

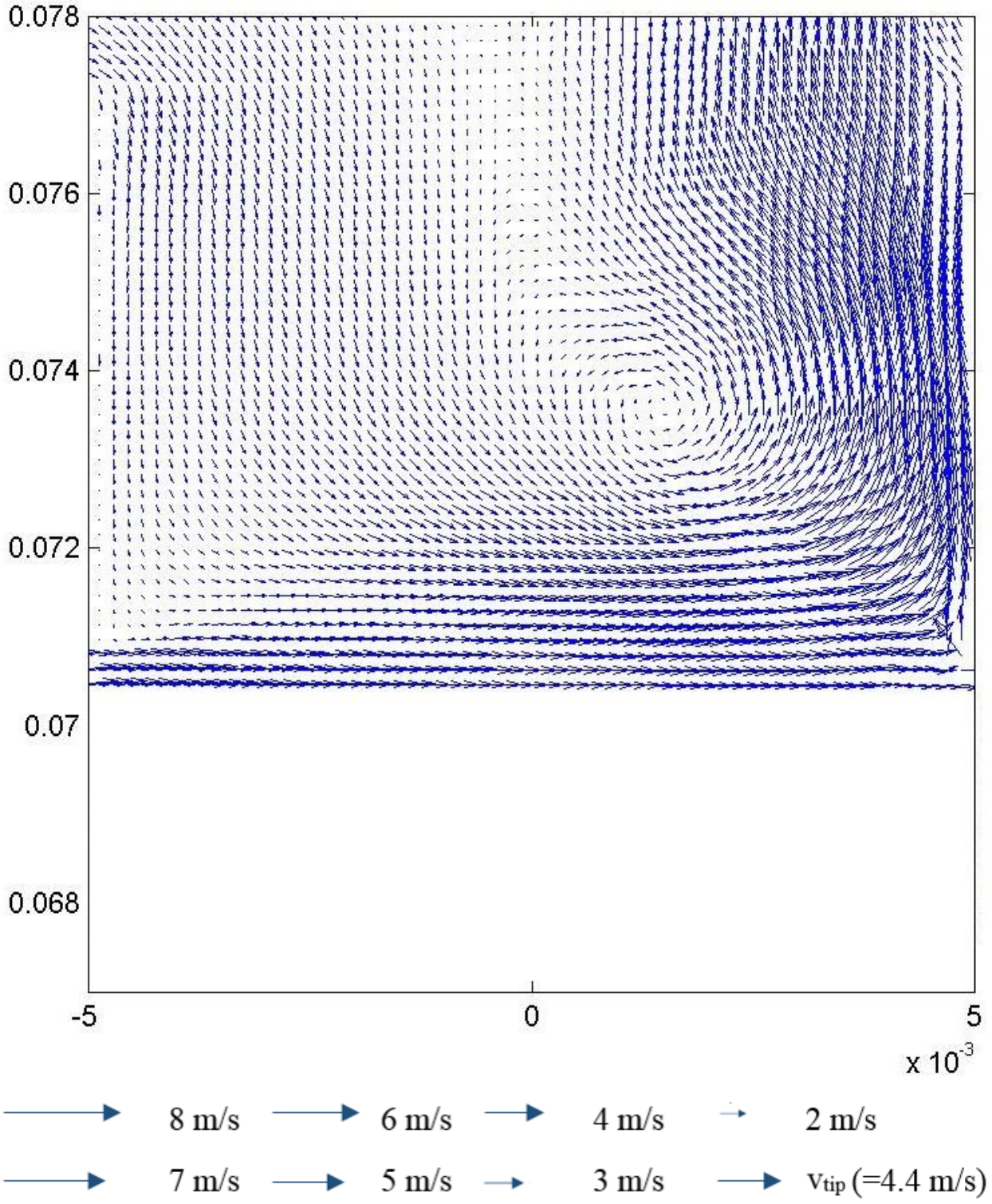

N = 10 rps, PIV, θ = +9°

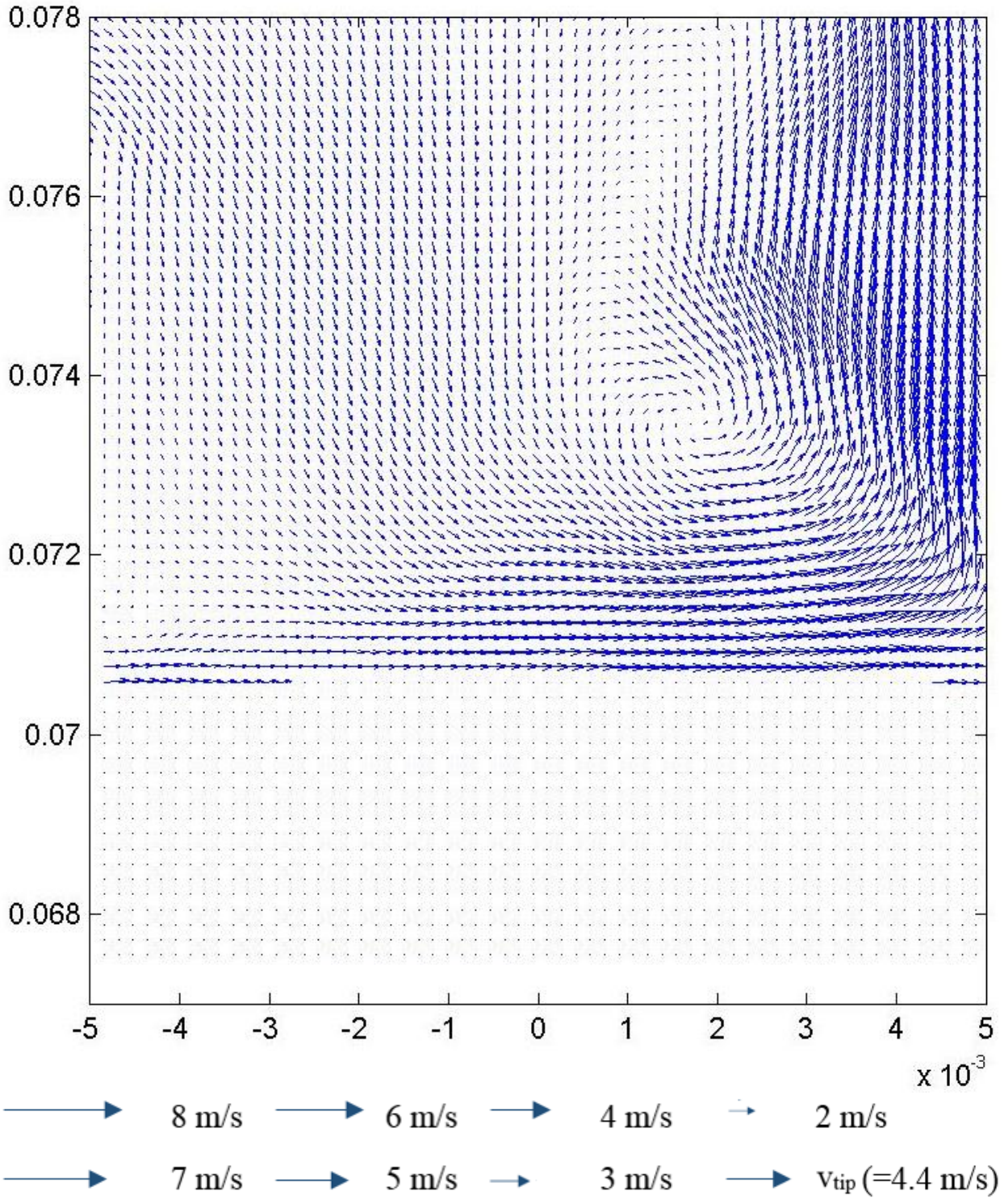

8. References

Amano, R. S. (1983). DEVELOPMENT OF A TURBULENCE NEAR-WALL MODEL AND ITS APPLICATION TO SEPARATED AND REATTACHED FLOWS. *Numerical Heat Transfer*, 59-75.

ANSYS. (n.d.). The Multiple Reference Frame Model. In ANSYS, *Fluent User Guide.*

ANSYS,INC. (2013). *Ansys Fluent Documents Page.* Retrieved from Ansys Fluent: http://148.204.81.206/Ansys/150/ANSYS%20Fluent%20Users%20Guide.pdf

Ariff, M., Salim, S. M., & Cheah, S. C. (2009, December). Wall y+ approach for dealing with turbulent flow over a surface mounted cute: part 1 - low reynolds number. *Seventh International Conference on CFD in the Minerals and Process Industries*, (pp. 9-11). Melbourne.

Banaszek, C. (2009). *The Art of High Shear Mixing.* Retrieved from Charles Ross & Son Company: http://www.mixers.com/whitepapers/The%20Art%20of%20High%20Shear%20Mixing%200824 2007.pdf

Barailler, F., Mourad, H., & Philippe, T. (2006). CFD analysis of a rotor-stator mixer viscous fluids. *Chemical Engineering Science*, 2888-2894.

Borzenski, F. (2007). *Process machinery: advancement in mixing technologies--part1*. Rubber World.

Charles, S. G., Abid, R., & Anderson, E. C. (1992). Critical evaluation of two-equation models for near-wall turbulence. *AIAA Journal*, 324-331.

Edward, P. L., Atiemo-Obeng, V. A., & Kresta, S. M. (2003). *Handbook of Industrial Mixing: Science and Practice.* Wiley.

Fletcher, C. A. (1994). *Computational Techniques for Fluid Dynamics, Vol. 1.*

Ford, M. (2008, April). PIV-measured versus CFD-predicted flow dynamics in anatomically realistic cerebral aneurysm models. *J Biomech Eng, 130*(2), 130-139.

Ko, D. I. (2013). Computational fluid dynamics simulations of an in-line slot and tooth rotor-stator mixer.

Launder, B. E., & Sharma, B. I. (1974). Application of the energy-dissipation model of turbulence to the calculation of flow near a spinning disc. *Letters in Heat and Mass Transfer*, 131-137.

Luo, J. Y., Issa, R. I., & Gosman, A. D. (1994). Prediction of Impeller-Induced Flows in Mixing Vessels Using Multiple Frames of Reference. *I ChemE Symposium Series*, 549-556.

Melling, A. (1997). Tracer particles and seeding for particle image velocimetry. *Measurement Science and Technology*, 12.

Pacek, A., Baker, M., & Utomo, A. (2007). Characterisation of Flow Pattern in a Rotor Stator High Shear Mixer. *Proceedings of European Congress of Chemical Engineering.* Copenhagen: ECCE-6.

Pollman, A. K. (2009, June 6). Get your slurry in a hurry with high shear mixer. *Engineer Live*.

Rodgers, T. L. (2011). Rotor-Stator Mixers. *Chem Eng Trans, 24*, 1411-1416.

Shih, T. (1995). *A New - Eddy-Viscosity Model for High Reynolds Number Turbulent Flows - Model Development and Validation.* Cleveland: NASA STI.

Ullman, F. (2005). *Chemical Engineering and Plant Design.* John Wiley & Sons.

Utomo, A., Baker, M., & Pacek, A. (2008). Flow pattern, periodicity and energy dissipation in a batch rotor-stator mixer. *Chemical Engineering Research and Design*, 1397-1409.

Wilcox, D. C. (1998). *Turbulence Modeling for CFD.* DCW Industries.